

Investigation of the properties of iron-bearing alloys and silicates and their implications for the Earth's lower mantle and core

Von der Fakultät für Biologie, Chemie und Geowissenschaften
der Universität Bayreuth

zur Erlangung der Würde eines Doktors der Naturwissenschaften
- Dr. rer. nat. -
Genehmigte Dissertation

vorgelegt von

Olga Narygina

aus Ekaterinburg (Russland)

Bayreuth, 2009

Vollständiger Abdruck der von der Fakultät für Chemie/Biologie/Geowissenschaften der Universität Bayreuth genehmigten Dissertation zur Erlangung des Grades eines Doktors der Naturwissenschaften (Dr. rer. nat.).

Prüfungsausschuß:

Prof. Dr. Falko Langenhorst, Universität Bayreuth	(Vorsitzender)
Prof. Dr. Leonid Dubrovinsky, Universität Bayreuth,	(1. Gutachter)
Prof. Dr. Vladimir Dmitriev, European Synchrotron Radiation Facility	(2. Gutachter)
Prof. Dr. David Rubie, Universität Bayreuth	
Prof. Dr. Jürgen Senker, Universität Bayreuth	

Tag der Einreichung: 2 Oktober 2009

Tag der wissenschaftlichen Kolloquiums: 18 März 2010

Table of contents

Summary	1
Zusammenfassung	4
1. Introduction	8
1.1. Origin and structure of the Earth	8
1.2. (Mg,Fe)Si,AlO ₃ majorite and perovskite as the dominant components of the Earth's transition zone and lower mantle	11
1.3. Fe-Ni-light element(s) alloy as the main component of the Earth's core	15
2. Motivation	18
2.1. Spin state of iron in (Mg,Fe)(Si,Al)O ₃	18
2.2. Effect of carbon on the phase relations in Fe-Ni system	19
3. Experimental techniques	21
3.1. Creation of high pressure high temperature conditions	21
3.1.1. Diamond anvil cell technique	21
3.1.1. Large-volume press technique	22
3.2. <i>In situ</i> sample analyses	25
3.2.1. X-ray diffraction spectroscopy	25
3.2.2. Conventional Mössbauer spectroscopy	26
3.2.3. X-ray absorption near-edge structure spectroscopy	27
4. Scope of the thesis	29
4.1. Spin state of iron in lower mantle perovskite	29
4.2. Fe-Mg partitioning between (Mg,Fe)SiO ₃ perovskite and (Mg,Fe)O ferropericlae	34
4.3. Fe-Ni-C system at high pressures and temperatures: LH-DAC vs. LVP	38
4.3.1. Phase relations in Fe _{1-x} Ni _x (0.10 < x < 0.22) alloys at pressures to 52 GPa and temperatures to 2600 K	38
4.3.2. Carbon solubility in Fe-Ni alloys at elevated pressure and temperatures and its effect on the phase relations in this system	41
5. Results	43
5.1. Stable intermediate-spin ferrous iron in lower-mantle perovskite	43
5.1.1. Abstract	43
5.1.2. Introduction	44
5.1.3. Experimental details	44
5.1.4. Results and discussion	47
5.1.5 Acknowledgements	54
5.1.6. Supplementary figures	55

5.2. High-pressure experimental and computational XANES studies of the Earth's lower mantle (Mg,Fe)(Si,Al)O ₃ perovskite and (Mg,Fe)O ferropericlae	61
5.2.1. Abstract	61
5.2.2. Introduction	61
5.2.3. Experimental	64
5.2.3.a Sample preparation and characterization	64
5.2.3.b Experimental method	66
5.2.4. Results and discussion	67
5.2.4.a Effect of oxidation state	67
5.2.4b.2. (Mg,Fe)(Si,Al)O ₃ perovskite	77
5.2.4b.2.i Experimental	77
5.2.4b.2.ii <i>Ab initio</i> calculation of X-ray absorption spectra	79
5.2.5. Conclusion	84
5.2.6. Acknowledgments	85
5.3. XANES study of spin crossover in Fe-bearing silicate perovskite	86
5.3.1. Abstract	86
5.3.2. Introduction	86
5.3.3. Sample description and preparation	88
5.3.4. Experimental method	89
5.3.5. Results and discussion	90
5.3.5a Oxidation state of iron	90
5.3.5b Spin state of iron	92
5.3.6. Conclusion	94
5.3.7. Acknowledgements	94
5.4. Electronic state of Fe ²⁺ in (Mg,Fe)(Si,Al)O ₃ perovskite and (Mg,Fe)SiO ₃ majorite at pressures up to 86GPa and temperatures up to 800K	95
5.4.1. Abstract	95
5.4.2. Introduction	95
5.4.3. Experimental procedure	97
5.4.4. Results	99
5.4.4a (Mg,Fe)SiO ₃ perovskite	99
5.4.4a.i Pressure effect	99
5.4.4a.ii Temperature effect	102
5.4.4b (Mg,Fe)SiO ₃ majorite	103
5.4.4b.i Pressure effect	103
5.4.4b.ii Temperature effect	104
5.4.5 Discussion	105
5.4.5a (Fe,Mg)SiO ₃ majorite	105

5.4.5b (Fe,Mg)SiO ₃ perovskite	108
5.4.6. Conclusions	109
5.4.7. Acknowledgments	109
5.5. Development of micro-XANES mapping in the diamond anvil cell	109
5.5.1 Abstract	110
5.5.2 Introduction	110
5.5.3 Experimental details	112
5.5.3. Results and conclusions	116
5.6. Hyperspectral -XANES mapping in the diamond-anvil cell: analytical procedure applied to the decomposition of (Mg,Fe)-ringwoodite at the upper/lower mantle boundary	118
5.6.1 Abstract	118
5.6.2. Introduction	118
5.6.3. Experimental details	120
5.6.4. Analytical procedure	121
5.6.5. Results	126
5.6.6. Conclusion	128
5.6.7. Acknowledgements	129
5.7. Chemically homogenous spin transition zone in the Earth's lower mantle	130
5.7.1. Abstract	130
5.7.2. Introduction	130
5.7.3. Results and discussion	131
5.7.4. Supplementary materials	135
5.7.4a Experimental details	135
5.7.4b Effect of starting material	136
5.7.4c Supplementary figures	139
5.8. Phase relations in Fe-Ni-C system at high pressures and temperatures: implication for the Earth's Core	140
5.8.1. Abstract	140
5.8.2. Introduction	140
5.8.3. Experimental details	142
5.8.4. Experimental results	144
5.8.4a XRD study of FeNi alloys, employing LH-DAC	144
5.8.4a.i Fe _{0.9} Ni _{0.1} alloy at pressures to 30 GPa	144
5.8.4a.ii Fe _{0.78} Ni _{0.22} at pressures to 52 GPa and temperatures to 2600 K	145
5.8.4b Comparative study of Fe _{1-x} Ni _x (0.10 < x < 0.22) at high pressures and temperatures by means of LH-DAC and LVP techniques	148
5.8.5. Discussion	149

5.8.5a $\text{Fe}_{1-x}\text{Ni}_x$ ($0.1 < x < 0.22$ wt%) alloys at pressures to 45 GPa and temperatures to 2500 K: LH-DAC vs. multianvil experiments	149
5.8.5b Effect of carbon on the phase relations in Fe-Ni system at elevated pressures and temperatures. Martensitic transformation	151
5.8.5c Carbon solubility in Fe-Ni system at elevated pressures and temperatures	153
5.8.6. Conclusion	156
5.8.7. Acknowledgments	157
References	158

Acknowledgments

The project, which eventually became my doctoral dissertation, was financially supported by funds from the Eurocores EuroMinSci Programme, German Science Foundation (DFG) Priority Programme SPP1236 under project Mc 3/16-1 and Elitenetzwerk Bayern, International Graduate School program. The administration of the Bayerisches Geoinstitut is acknowledged with thanks for providing me with the necessary facilities to pursue my work. Use of the Advanced Photon Source (beamline 13-ID-D) was supported by the U.S. Department of Energy, Office of Science, Office of Basic Energy Sciences, under Contract No. DE-AC02-06CH11357.

I thank my scientific advisor Prof. Dr. Leonid Dubrovinsky (Bayerisches Geoinstitut) for his outstanding tutor skill, patience and optimism. I thank him for his generous help and fruitful discussions throughout my PhD studies. Without his strict and attentive supervision the present work would not have been possible.

I also thank Dr. Catherine McCammon (Bayerisches Geoinstitut) for her assistance with piston-cylinder experiments, comprehensive help with Mössbauer measurements and interpretation of the data; for the critical reviewing of my scientific papers and current manuscript.

My deepest gratitude is to Dr. Sakura Pascarelli (European Synchrotron Radiation Facility) for her assistance with XANES measurements, for the valuable advice regarding the data analyses and for the significant contribution to my first Physical Review B paper.

I am grateful to Dr. Giuliana Aquilanti, Dr. Manuel Muñoz, Dr. Aleksandr Chumakov, Dr. Ilya Sergeev, Dr. Vladimir Dmitriev (European Synchrotron Radiation Facility) and Dr. Vitali Prakapenka (Applied Photon Source) for the assistance with synchrotron radiation experiments.

Special appreciation goes to Dr. Nobuyoshi Miyajima (Bayerisches Geoinstitut) for hours spent at the TEM with my magnetic samples containing too many phases. Dr. Daniel Frost and Dr. Gudmundur Gudfinnsson and Dr. Shantanu Keshav are acknowledged for the help with the piston-cylinder and multianvil experiments. My heartfelt thanks to Maurizio Mattesini, who spent quite a bit of time trying to confirm theoretically intermediate spin ferrous iron in silicate perovskite.

I am thankful to Hubert Schulze and Uwe Dittmann (Bayerisches Geoinstitut). Without their prompt craftsmanship in the preparation of my samples, most of the present work would not have been successful. Detlef Krauß, Heinz Fischer, Gerti Göllner, Kurt Klasinski, Sven

Linhardt, and Stefan Übelhack are warmly thanked for their skills and tenacity, and for their assistance in the labs. Particularly I would like to thank Petra Buchert, Lydia Kison-Herzing, Nicole Behringer and Stefan Keyssner for their great support and help with all non-scientific, but still important aspects of my daily life in Bayreuth. Many thanks are given to my Russian colleagues Innokenty Kantor, Anastasia Kantor, Polina Gavrilenko and Alexander Kurnosov, who helped me not only with scientific work, but also gave a hand in solving many daily life problems. I thank all PhD students and other colleagues in Bayerisches Geoinstitut, who have constructed a very friendly atmosphere for working, especially Coralie Weigel and Micaela Longo.

And finally I thank heartily my mother, Galina A. Narygina, who has made significant efforts to provide me with a good education. Without her support and wise advice I would not be able to make any success in my life. Мамочка, спасибо тебе огромное за твои любовь, понимание и поддержку!

Summary

1. Spin state of ferrous iron in lower mantle silicate perovskite

(Mg,Fe)(Si,Al)O₃ perovskite comprises about 80% of the Earth's lower mantle by volume, leaving ~ 15% to (Mg,Fe)O ferropericlasite and ~ 5% to CaSiO₃ perovskite. Therefore characteristics of the lower mantle (seismic and chemical heterogeneity, density, electrical and thermal conductivity, oxidation state, etc.) would be determined mostly by the elastic, thermal, electronic, etc. properties of the silicate perovskite and ferropericlasite. The question regarding the electronic state of iron in the lower mantle phase assemblage has been addressed by numerous theoretical and experimental works. In recent years the spin transitions in ferropericlasite and silicate perovskite, predicted to occur at the lower mantle conditions almost 50 years ago, were observed experimentally. While high-spin – low-spin crossover in (Mg,Fe)O is nicely described in literature ([Badro et al., 2003](#); [Lin et al., 2005, 2006a, 2007](#); [Speziale et al., 2005](#); [Kantor et al., 2006a](#), [Goncharov et al., 2006](#)), the electronic state of iron in silicate perovskite at high pressures and temperatures remains controversial. Conclusions derived from the results of X-ray emission and nuclear forward scattering spectroscopic studies of Fe-bearing silicate perovskite are not in agreement on the pressure and temperature conditions of the transition and on whether Fe²⁺ or Fe³⁺ or both iron cations are involved ([Badro et al., 2004](#); [Jackson et al., 2005](#); [Li et al., 2004, 2006](#)). We undertook an alternative study of (Mg,Fe)(Si,Al)O₃ perovskite at a wide pressure and temperature range using a number of different spectroscopic techniques (conventional Mössbauer, X-ray absorption near edge structure with micron resolution (μ -XANES), nuclear forward scattering (NFS, which is the synchrotron analogue of Mössbauer spectroscopy) and X-ray diffraction (XRD) spectroscopies), in order to get a rather complete picture regarding the spin state of iron in this compound. Desirable pressures relevant to those in the Earth's lower mantle were achieved by means of diamond anvil cells, equipped with miniature external resistive heaters, providing homogeneous heating up to 1000 K, which enables us to estimate the effect of temperature as well.

Our Mössbauer and μ -XANES data, collected at pressures to 110 GPa and temperatures to 1000 K for silicate perovskite, revealed a gradual transition involving Fe²⁺, which at room temperature occurs over a rather wide pressure range, from 35(1) GPa to 70(2) GPa, but becomes narrow at high temperatures. This observation coincides with the previously reported drop in spin number revealed by X-ray emission spectroscopy ([Badro et al., 2004](#); [Li et al., 2004](#)). Taking this

into account and based on the fact that our X-ray diffraction measurements, performed at the corresponding pressure-temperature conditions, do not suggest any appreciable structural change in perovskite, we conclude that the origin of the observed transition is fully electronic. Considering the simplified energy diagram of ferrous iron, sitting in 8-12 fold coordinated polyhedra in the perovskite structure, and by analysing the effect of pressure on the distribution of valence electrons over the energy levels, we propose stabilization of intermediate spin Fe^{2+} in magnesium silicate perovskite at pressures over 35(1) GPa.

The gradual character of high-spin – intermediate spin crossover in silicate perovskite does not assume any abrupt changes of the lower mantle properties. However due to the negative Clapeyron slope of the transition in some areas in the uppermost lower mantle, located in the vicinity of subducting slabs or hot mantle upwellings, they would have slightly different properties (namely electrical and thermal conductivity, element partitioning) with respect to the surrounding mantle. Therefore the presence of the spin transition in silicate perovskite is essential for reliable evaluation of the composition, geophysics and dynamics of the Earth's lower mantle.

2. Fe-Mg partitioning between $(\text{Mg,Fe})\text{SiO}_3$ perovskite and $(\text{Mg,Fe})\text{O}$ ferropericlasite

Although the effect of spin transitions in lower mantle silicate perovskite and ferropericlasite on the iron partitioning between these two phases has been widely discussed in the literature, the question remains open, mainly due to the lack of *in situ* experiments under the relevant pressure and temperature conditions. We approach this problem using combined *in situ* synchrotron XRD and μ -XANES spectroscopic measurements with laser-heated diamond anvil cell (LH-DAC) technique. The assemblages of $(\text{Mg,Fe})\text{SiO}_3$ perovskite and $(\text{Mg,Fe})\text{O}$ ferropericlasite were synthesized via the breakdown reaction of $(\text{Mg}_{0.88}\text{Fe}_{0.12})_2\text{SiO}_4$ ringwoodite or a natural $(\text{Mg}_{0.88}\text{Fe}_{0.12})_2\text{SiO}_4$ San Carlos olivine, induced by laser heating over 1800 K at pressures above 26 GPa.

Our data, collected from 22 GPa to 115 GPa, after laser heating to 1950 K and 2300 K, confirmed previously reported preferred partitioning of iron in low-spin ferropericlasite with respect to high or intermediate spin perovskite. Increase of temperature from 1950 K to 2300 was shown to slightly increase the amount of Fe in perovskite (by 10%). We also showed that one needs to be cautious with the choice of starting material for this kind of partitioning experiment, since laser heating-induced decomposition of ringwoodite and olivine results in the formation of

different phase assemblages. In the last case along with silicate perovskite and ferropericlase we detected the formation of a significant amount of metallic iron.

3. Phase relations in Fe-Ni-C system at high pressures and temperatures

The phase diagram of Fe-enriched FeNi alloy at elevated pressures and temperatures comparable to those in the Earth's core as well as the effect of the potential light element in the core (Si, S, O, H, C, etc.) on the system remains under debate. The reason is very simple: the necessary pressure-temperature range (300-350 GPa and 5,000-7,000 K) is hardly achieved in the laboratory. Conditions close to those in the core can be created in LH-DAC experiments; however the main disadvantage of the technique is a lack of control on the system under study. In contrast, the large-volume press (LVP) provides rather equilibrated and controllable experimental conditions, although at significantly lower pressures. Therefore we carried out a "cross-checking" study of phase relations in $\text{Fe}_{1-x}\text{Ni}_x$ ($0.10 < x < 0.22$) and $\text{Fe}_{0.90}\text{Ni}_{(0.10-x)}\text{C}_x$ ($0.01 < x < 0.05$) systems at pressures to 52 GPa and temperatures to 2600 K, using LH-DAC and LVP high pressure techniques. *In situ* and *ex situ* sample analyses were done by means of XRD, Mössbauer spectroscopy, and scanning and transmission electron microscopies.

We showed that laser heating in the DAC can promote undesired reactions between the sample (FeNi alloy in our case) and carbon, which upon laser heating diffuses from the diamond anvils through the pressure-transmitting layers. Therefore we suggest that results obtained in LH-DAC experiments should be interpreted very carefully in general.

We investigated the mechanism of carbon incorporation into the structure of FeNi alloy at high pressures and temperatures, and showed that rapid cooling of *fcc*-structured carbon-bearing FeNi alloy to room temperature (either in the case of LH-DAC or LVP quenched experiments) results in the formation of the metastable solid solution of *bcc*-FeNi, *bct*-Fe-Ni-C (known in metallurgy as martensite) and a certain amount of preserved *fcc* Fe-Ni-C. We also showed that carbon solubility in the Fe-Ni system at high temperatures decreases with pressure. At 2300 K as much as 0.9(2)wt% carbon can be dissolved in Fe-Ni at pressures to 9 GPa, while at 20 GPa the upper limit is 0.7(2) wt%.

Zusammenfassung

1. Spin Zustände des zweiwertigen Eisens in silikatischen Perovskiten des unteren Erdmantels

Der untere Erdmantel besteht aus ca. 80% $(\text{Mg,Fe})(\text{Si,Al})\text{O}_3$ Perovskiten, wobei $\sim 15\%$ des Gesamtvolumens aus $(\text{Mg,Fe})\text{O}$ Ferroperiklas und $\sim 5\%$ CaSiO_3 Perovskit besteht. Daher sind die charakteristischen Eigenschaften des unteren Mantels (seismische und chemische Heterogenität, Dichte, elektrische und thermische Leitfähigkeit, Oxidationszustand, usw.) hauptsächlich durch elastische, thermische, elektronische, usw. Eigenschaften der silikatischen Perovskite und Ferroperiklase bestimmt. Zahlreiche theoretische und experimentelle Studien befassen sich mit der Frage des Elektronenzustandes des Eisens in den Phasen des unteren Erdmantels. Bereits vor 50 Jahren wurde ein Spin Übergang in Ferroperiklasen und silikatischen Perovskiten unter Bedingungen des unteren Erdmantels vorausgesagt und konnte vor wenigen Jahren erstmals experimentell beobachtet werden. Während der high-Spin – low-Spin Übergang in $(\text{Mg,Fe})\text{O}$ vielfach in der Literatur beschrieben wird ([Badro et al., 2003](#); [Lin et al., 2005, 2006a, 2007](#); [Speziale et al., 2005](#); [Kantor et al., 2006a](#), [Goncharov et al., 2006](#)) ist der Elektronenzustand von Eisen in silikatischen Perovskiten bei hohen Drücken und Temperaturen immer noch umstritten. Aussagen, die auf Ergebnisse aus Röntgen-Emissions-Spektroskopie und Kernresonanz-Streuungs-Spektroskopie von eisenhaltigen silikatischen Perovskiten beruhen, stimmen nicht mit den Druck-Temperatur Bedingungen des Übergangs überein, weiterhin sind weder Fe^{2+} , Fe^{3+} noch beide Eisenkationen berücksichtigt ([Badro et al., 2004](#); [Jackson et al., 2005](#); [Li et al., 2004, 2006](#)). Wir haben mit verschiedensten spektroskopischen Methoden (Mössbauer-Spektroskopie, Röntgen-Nahkanten-Absorptions-Spektroskopie mit einer Auflösung im Mikrometerbereich (μ -XANES), Kern-Resonanz-Streuungs-Spektroskopie (NFS, das Synchrotrongegenstück zur Mössbauer-Spektroskopie) und Röntgenbeugung (XRD)) eine alternative Studie an $(\text{Mg,Fe})(\text{Si,Al})\text{O}_3$ Perovskiten in einem weiten Druck-Temperatur Bereich durchgeführt, um ein möglichst komplettes Bild in Bezug auf den Spin Zustand des Eisens in dieser Komponente zu erstellen. Vergleichbare Drücke, wie die im unteren Erdmantel, konnten mit Hilfe von Diamant-Stempel-Zellen erreicht werden. Die Diamant-Stempel-Zellen waren zusätzlich mit externen Miniatur-Widerstands-Heizern ausgerüstet, durch die homogene Temperaturen, von bis zu 1000 K, erreicht werden konnten.

Mössbauer- und μ -XANES-Daten bei einem Druck von 110 GPa und Temperaturen bis zu 1000 K zeigen für silikatische Perovskite einen schrittweisen Übergang von Fe^{2+} , der bei Raumtemperatur über einen weiten Druckbereich (35(1) – 70(2) GPa) auftritt, nicht aber bei hohen Temperaturen. Diese Beobachtung stimmt mit dem vorher, über Röntgen-Emissions-Spektroskopie ermittelten Fall ([Badro et al., 2004](#); [Li et al., 2004](#)), überein. Diese Ergebnisse einbezogen und basierend darauf, dass unsere unter gleichen Bedingungen durchgeführten Röntgenbeugungs-Messungen keinerlei strukturelle Änderung der Perovskite anzeigen, schlussfolgern wir, dass die beobachteten Übergänge gänzlichst einen elektronischen Ursprung haben. Wird das vereinfachte Energie Diagramm des zweiwertigen Eisens, das in den 8-12 fach koordinierten Polyedern der Perovskitstruktur sitzt, berücksichtigt, und wird der Effekt des Drucks auf die Verteilung der Valenzelektronen über die Energieniveaus analysiert, so vermuten wir eine Stabilisierung des intermediären Spins von Fe^{2+} in magnesiumreichen, silikatischen Perovskiten bei Drücken über 35(1) GPa.

Durch den schrittweisen Charakter des high-Spin – intermediär-Spin Übergangs in silikatischen Perovskiten, kann keine abrupte Änderung der unteren Mantel Eigenschaften angenommen werden. Allerdings würde der negative Clapyronpfad des Übergangs in einigen Regionen des obersten unteren Erdmantels, genauergesagt in der Umgebung von subduzierten Platten oder heißen Mantelplums, leichte Veränderungen in den Eigenschaften (elektrische und thermische Leitfähigkeit, Elementverteilung), gegenüber dem umgebenden Mantel, erzeugen. Daher ist die Anwesenheit des Spin Übergangs in silikatischen Perovskiten essentiell für eine zuverlässige Einschätzung der Zusammensetzung, der geophysikalischen und der dynamischen Eigenschaften des unteren Erdmantels.

2. Fe-Mg Verteilung zwischen $(\text{Mg,Fe})\text{SiO}_3$ Perovskiten und $(\text{Mg,Fe})\text{O}$ Ferroperiklasen

Auch wenn in der Literatur vielfach der Effekt von Spin Übergängen im unteren Mantel in Bezug auf die Eisenverteilung zwischen silikatischem Perovskit und Ferroperiklas diskutiert wird, so bleibt diese Frage, durch das Fehlen von *in situ* Experimenten unter den relevanten Druck-Temperatur Bedingungen, doch offen. Wir gehen dieses Problem an, indem wir *in situ* Synchrotron Röntgenbeugungs-Spektroskopie und μ -XANES Messungen mit der Laser-Geheizten-Diamant-Stempel-Zellen-Technik (LH-DAC) kombinieren. $(\text{Mg,Fe})\text{SiO}_3$ Perovskite und $(\text{Mg,Fe})\text{O}$ Ferroperiklase wurden via der Zerfallsreaktion von $(\text{Mg}_{0.88}\text{Fe}_{0.12})_2\text{SiO}_4$

Ringwoodit, oder von natürlichem $(\text{Mg}_{0.88}\text{Fe}_{0.12})_2\text{SiO}_4$ San-Carlos Olivin, bei 26 GPa und 1800 K (Laserstrahl) synthetisiert.

Nach dem Erreichen hoher Temperaturen, 1950 und 2300 K, wurden die Daten bei Drücken von 22 GPa bis 115 GPa aufgenommen. Eine Vorzugsverteilung von low-Spin Eisen in Ferroperiklas und high- bzw. intermediär-Spin Eisen in Perovskit, was bereits in früheren Arbeiten beschrieben wurde, konnte bestätigt werden. Die Erhöhung der Temperatur von 1950 auf 2300 K zeigte eine leichte Anreicherung von Eisen in Perovskit ($\sim 10\%$). Wir konnten ebenfalls zeigen, dass die Zusammensetzung des Ausgangsmaterials von großer Bedeutung für diese Art von Verteilungsexperimenten ist, da die Laserheizung einen Zerfall von Ringwoodit induziert und Olivin bei der Bildung verschiedener Phasenzusammensetzungen entsteht. Schließlich konnten wir in den Experimenten mit silikatischem Perovskit und Ferroperiklas die Bildung von signifikanten Mengen an metallischem Eisen beobachten.

3. Phasen Beziehungen im System Fe-Ni-C bei hohen Drücken und Temperaturen

Das Phasendiagramm von eisenreichen FeNi-Legierungen bei erhöhten Drücken und Temperaturen (vergleichbar mit denen im Erdkern), sowie der Effekt der potentiellen leichten Kernkomponenten (Si, S, O, H, C, usw.), bleiben weiterhin in starker Diskussion. Der Grund ist ein einfacher: der nötige Druck-Temperatur Bereich (300-350 GPa und 5000 – 7000 K) ist im Labor schwer nachstellbar. Diese Bedingungen können mittels LH-DAC erreicht werden, allerdings ist das System unter diesen Bedingungen schlecht kontrollierbar. Im Gegensatz dazu bieten Groß-Volumen-Pressen (LVP) die Möglichkeit Experimente unter annähernden Gleichgewichts- und experimentell kontrollierbaren Bedingungen durchzuführen, allerdings bei wesentlich geringern Drücken. Daher sind mit LH-DAC und LVP Mehrfachprüfungen der Phasenbeziehungen in den Systemen $\text{Fe}_{1-x}\text{Ni}_x$ ($0.10 < x < 0.22$) und $\text{Fe}_{0.90}\text{Ni}_{(0.10-x)}\text{C}_x$ ($0.01 < x < 0.05$) bei Drücken bis 52 GPa und Temperaturen bis 2600 K durchgeführt worden. *In situ* und *ex situ* Probenanalysen wurden mittels Röntgenbeugung, Mössbauer-Spektroskopie, Raster- und Transmissions-Elektronen-Mikroskopie durchgeführt.

Es konnte gezeigt werden, dass die Laserheizung in DAC eine unerwünschte Reaktion zwischen der Probe (FeNi-Legierung) und Kohlenstoff begünstigt, welche von den Diamant-Stempeln ausgehend durch die druckübertragenden Lagen diffundiert. Daher sollten die mit der LH-DAC-Technik ermittelten Daten mit Vorsicht interpretiert werden.

Weiterhin wurde der Mechanismus der Kohlenstoffaufnahme in die Struktur der FeNi-Legierung bei hohen Drücken und Temperaturen untersucht. Dabei konnte gezeigt werden, dass, bei rascher Kühlung der *fcc*-strukturierten, kohlenstoffhaltigen FeNi-Legierung auf Raumtemperatur, eine metastabile Mischung von *bcc*-FeNi, *bct*-Fe-Ni-C (Martensit) und *fcc* Fe-Ni-C entsteht. Es konnte auch eine Abnahme der Löslichkeit von Kohlenstoff in dem System Fe-Ni, mit Abnahme des Drucks bei hohen Temperaturen, gezeigt werden. Bei einer Temperatur von 2300 K und einem Druck von 9 GPa sind 0.9(2)gw% Kohlenstoff in der Fe-Ni Phase gelöst, bei 20 GPa konnte ein Maximum von 0.7(2) gw% beobachtet werden.

1. Introduction

1.1. Origin and structure of the Earth

Knowledge of the Earth's structure, composition and dynamics are crucial for tracing of the planet's evolution and understanding of the global geological processes. The general constraints on the chemical and physical properties of the Earth's interior come from geophysical and seismic observations, geochemical analyses of natural rocks and minerals, as well as from experimental and theoretical studies of phases present in the Earth's interior, their physical properties and behaviour.

According to generally accepted models, the Solar system and Earth (as a part of the system) accreted from a swirling disk resulting from the angular momentum of the cloud of gas and dust that collapsed to form the Sun. The nebular cloud went through an early high-temperature stage during which all the material was in the gas phase. As the system cooled, solids and perhaps liquids started to condense. The first phases to condense (at about 1850-1400 K) would be the highly refractory lithophile (Ca, Al, and silicates associated with trace elements) and siderophile elements (W, Os, Ir) condensing as multicomponent alloys. At 1350-1250 K the most abundant elements heavier than oxygen, Si, Mg and Fe, condensed. In the reducing environment of the solar nebula, iron condensed almost entirely as metal, while magnesium and silicon formed forsterite (Mg_2SiO_4). At temperatures between 1230 K and 640 K, moderately volatile elements condensed: S (in the form of FeS), Na, K, Zn, etc. Finally below 640 K highly volatile Cl, H, O, N, etc., formed ([Palme and Jones, 2003](#)). The earliest stages of planetary formation are the most poorly understood at present. The most widely accepted model of terrestrial planet formation is planetesimal theory ([Chambers, 2003](#)). According to the model, in the first stage (with a timescale of thousands of years) nebular dust settles to form a relatively dense plane of material from which the planets grow. In the second stage either via gravitational instabilities ([Safranov, 1969](#); [Goldreich and Ward, 1973](#); [Goodman and Pindor, 1999](#)) or through the collisions of dust grains, growth of 1-km sized bodies, "planetesimals", occurred. In the third stage of accretion ("runaway growth"), gravity starts to play a role and builds 1-km sized objects into 1000-km sized objects – planetary embryos, the ultimate size of which depends on the amount of available material (bodies of the size of Moon or Mars could have formed at this stage; [Wetherill and Stewart, 1993](#)). The last stage of accretion ("oligarchic growth") was the slowest

1. Introduction

and the most violent, marked by giant collisions between bodies the size of the Moon or Mars. Giant impacts were common at the final stage of accretion (Agnor et al., 1999). The energy released from impacts, along with heat from the decay of radioactive isotopes, would have been sufficient for the partial melting of protoplanets in the inner part of the nebular disk that promoted their differentiation (Tonks and Melosh, 1992). Iron and siderophile elements (Pt, Pd and Au) preferentially sank to the center to form a core, while the lighter lithophile elements formed a mantle. Differentiation resulting in metallic core formation implies significant depletion of the mantle in siderophiles (Holzheid et al., 2000). However Pd, Pt and other siderophile elements are present in the Earth's mantle and crust. In the framework of the most widely accepted "late veneer" hypothesis (Kimura et al., 1974), this fact is explained by the addition of a thin veneer of chondritic material at the last stages of Earth's accretion (after the core-formation event), delivered as a single Moon-sized body which impacted the Earth, or as several late arriving planetesimals. The series of processes and events described above led to the formation of the Earth with chemically distinct metallic core and silicate mantle and crust (Fig. 1.1-1).

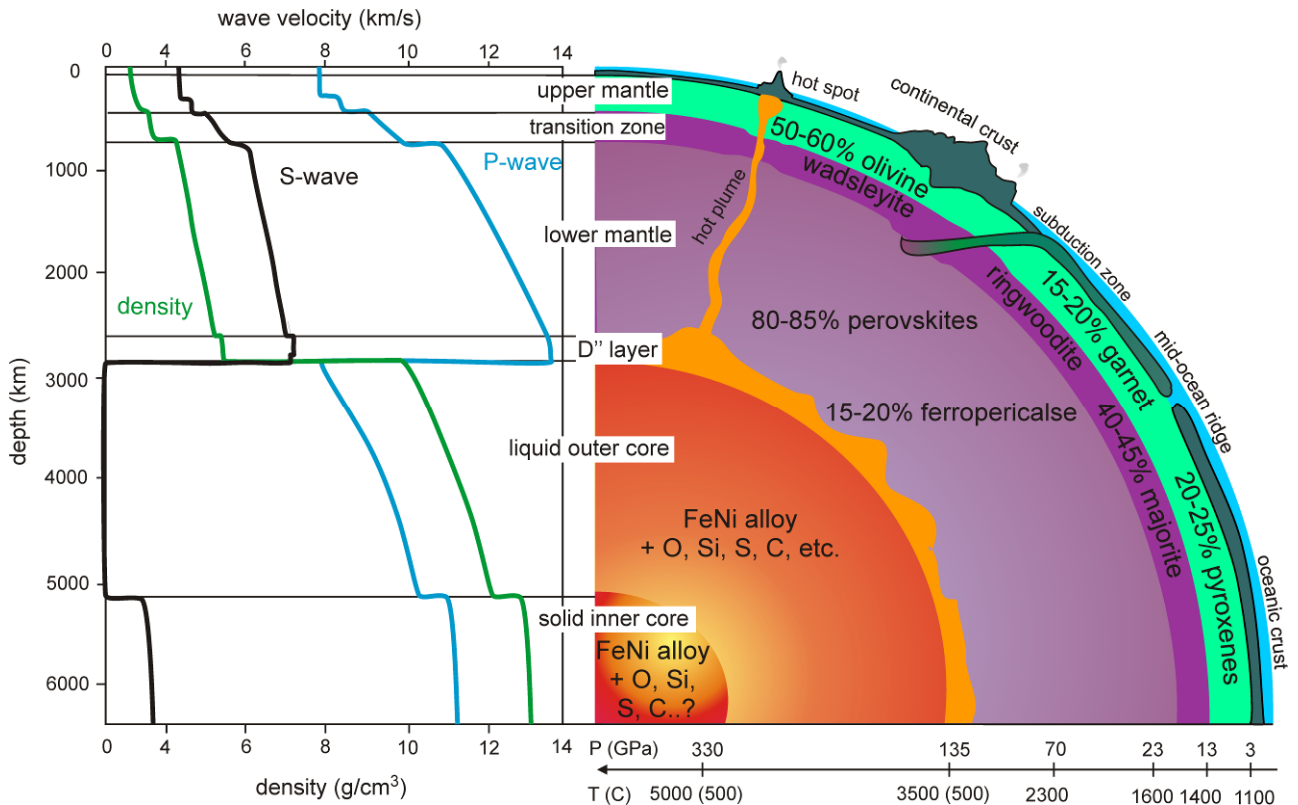


Figure 1.1-1 Summary of the average seismic-wave velocity and density profiles through the Earth according to the PREM model (Dziewonski and Anderson, 1981). Alterations with depth of the compressional (P-wave) and shear (S-wave) wave velocities are given on the top, density is on the bottom. Volume fractions of mineral phases are taken from the pyrolite model (Ringwood, 1975, 1989, 1991; Stixrude and Lithgow-Bertelloni 2005).

1. Introduction

The bulk composition of the Earth is determined both by the chemical composition of the solar nebula from which the sun and planets were formed, and by the nature of the physical processes that concentrated materials to form the planets. Since the composition of the sun was found to be similar to the majority of stars in our galaxy, the relative abundances of the elements in the sun are referred to as “cosmic abundances”. Additional constraints on the bulk solar nebula composition come from studies of meteorites, which, being small bodies with a simple history, provide insight into the early stages of the Solar system evolution. Some meteorites, the *chondrites*, are chemically primitive, having compositions similar to that of the sun. The *nonchondritic meteorites* experienced in their history partial (*primitive achondrites*) or entire melting (*differentiated achondrites*), and therefore to some extent reflect chemical processing similar to that which affected terrestrial and lunar rocks (Krot et al., 2003). But using only cosmic abundances cannot provide a well constrained bulk chemical composition of the Earth – significant differentiation inside the planet that caused formation of the chemically isolated silicate outer part (crust and mantle) and metallic core must be also taken into account. Currently the bulk chemical silicate Earth (crust and mantle) composition is relatively well constrained, although a small scatter between different estimations exist (see Table 1.1-1) (Palme and O’Neill, 2003).

Table 1.1-1 Major element composition of the bulk silicate Earth (crust and mantle)

	Ringwood (1979)	Jagoutz et al. (1979)	Wänke et al. (1984)	Palme and Nickel (1985)	Hart and Zindler (1986)	McDonough and Sun (1995)	Allégre et al. (1995b)	O’Neill and Palme (1998)
MgO	38.1	38.3	36.8	35.5	37.80	37.8	37.77	36.77
Al ₂ O ₃	3.3	4.0	4.1	4.8	4.06	4.4	4.09	4.49
SiO ₂	45.1	45.1	45.6	46.2	46.00	45.0	46.12	45.40
CaO	3.1	3.5	3.5	4.4	3.27	3.5	3.23	3.65
FeO [†]	8.0	7.8	7.5	7.7		8.1	7.49	8.10
Total	97.6	98.7	97.5	98.6		98.8	98.7	98.41

FeO[†] – all Fe as FeO

(* Table is taken from [Palme and O’Neill, 2003](#))

1. Introduction

Since the core is isolated from the mantle, its chemical composition can be only indirectly estimated based on the global mass balance between the composition of the entire Earth, deduced from cosmic abundances, and the composition of silicate part of the Earth. In other words, the difference between the cosmic abundance of an element and its amount in the silicate part provides a rough estimation of the amount of this element in the core. Modelling of the mineral assemblage of the silicate Earth is constrained by both its bulk chemical composition (Table 1.1-1) and seismic profiles, providing the most detailed information regarding the structure of the Earth's interior. Analyses of seismic waves profiles revealed the presence of the two major discontinuities within the mantle: (i) the so-called *transition zone* at a depth from 410 to 660 km, which defines the boundary between the upper and lower mantle; (ii) and the *D'' layer* that lies just above the core-mantle boundary (Fig. 1.1-1). The origin of the mantle discontinuities will be discussed in the following section.

1.2. (Mg,Fe)Si,AlO₃ majorite and perovskite as the dominant components of the Earth's transition zone and lower mantle

In the framework of the widely accepted “pyrolite model” ([Ringwood 1975](#)), the nature of mantle heterogeneities is related to the depth-varying behavior of (Mg,Fe)₂SiO₄ olivine, which composes about 60% of the Earth's upper mantle. The upper boundary of the transition zone (the layer in the lowermost upper mantle, characterized by anomalous behavior of seismic wave velocities) is defined by the phase transition of (Mg,Fe)₂SiO₄ olivine to its high pressure polymorph – β -phase or wadsleyite with a modified spinel structure, which occurs at around 14 GPa (410-km depth) (see Fig. 1.2-1). At about 17 GPa (500-550 km depth) wadsleyite transforms to a more densely packed spinel-structured phase – (Mg,Fe)₂SiO₄ ringwoodite, disproportionation of which to (Mg,Fe)SiO₃ perovskite and (Mg,Fe)O ferropericlase – the lower mantle assemblage, defines the bottom of transition zone, which is the 660-km discontinuity. The measured Clapeyron slopes of the transitions ([Bina and Helffrich, 1994](#)) imply upward deflection of the olivine - wadsleyite transformation in the cold environment of subduction zones ($dP/dT=3\text{MPa/K}$), while breakdown of ringwoodite should be deflected downwards ($dP/dT=-2\text{MPa/K}$). This causes local thickening of the transition zone. Alternatively, in anomalous warm

1. Introduction

environments (in the vicinity of hot plumes) the opposite deflection should locally thin the transition zone region.

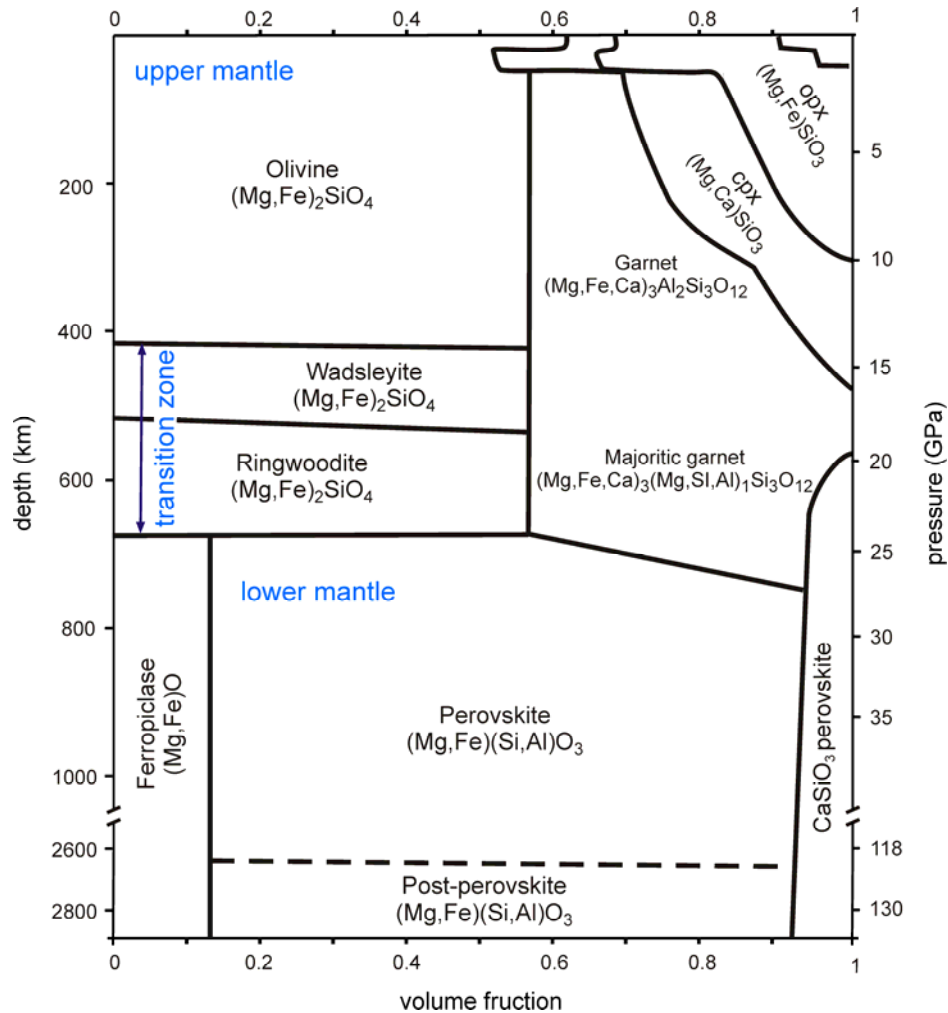


Figure 1.2-1 Mineral volume fraction of the pyrolite model mantle (Ringwood 1989, 1991; Stixrude and Lithgow-Bertelloni 2005). Opx and cpx are acronyms for orthopyroxene and clinopyroxene respectively. Modified after Frost 2008.

The remaining non-olivine components: orthopyroxene, clinopyroxene and garnet, undergo gradual transitions at the depth from 350 to 450 km: pyroxene dissolves in garnet via $^{[6]}\text{MgSi} \rightarrow \text{Al}_2$ substitution, resulting in the formation of Al-depleted garnet (majorite) at pressures above 16 GPa (Irifune and Ringwood, 1987), which eventually also transforms to silicate perovskite (at 23 – 26 GPa or 660 - 750 km depth) with exsolution of Ca-bearing silicate perovskite (Fig. 1.2-1). Since the dissolution of pyroxenes in garnet is “smeared out” over more than 100 km, it leads to changes in slope of the curves of seismic velocity versus depth rather than causing discrete discontinuities.

1. Introduction

Thus majorite (garnet enriched in MgSiO₃-component) comprises a significant part of the transition zone. It forms through the dissolution of (Mg,Fe)SiO₃ and (Mg,Ca)SiO₃ pyroxenes in ^[8-12](Mg,Fe,Ca)₃^[6]Al₂^[4]Si₃O₁₂ garnet, which introduces a ^[8-12](Mg,Fe)₃^[6](Mg,Fe,Si)₂^[4]Si₃O₁₂ majorite component. In this majorite component silica also occupies an octahedral site along with magnesium and iron, while in upper mantle garnet silica exclusively sits in a tetrahedral site. The MgSiO₃ end-member of majorite has tetragonal symmetry, with a slightly deviation from cubic symmetry due to the almost complete ordering of Mg and Si cations among octahedral sites ([Angel et al., 1989](#)). Introducing Al into the structure increases disorder of the cations on the octahedral site and therefore stabilizes cubic symmetry ([Kato, 1986](#); [Hatch and Ghose, 1989](#)). The FeSiO₃ end-member of majorite is unstable. However in solid solution with MgSiO₃ the molar amount of FeSiO₃ can achieve 34% ([Kato, 1986](#)). As was shown by O'Neill ([1993a](#)), even at its minimum oxygen fugacity limit in equilibrium with metallic iron, (Mg,Fe)SiO₃ majorite contains appreciable amount of Fe³⁺ in the octahedral site, and the amount increases with increase of oxygen fugacity. However introducing aluminum into the system does not have any effect on the redox ratio ([McCammon and Ross, 2003](#)). The ability of all dominant phases in the transition zone (wadsleyite, ringwoodite, majorite) to accommodate a certain amount of Fe³⁺ ([O'Neill et al., 1993a](#), [McCammon and Ross, 2003](#)) that is comparable or greater than the Fe³⁺ content of the upper mantle ([O'Neill 1993b](#)) would then imply a low value of oxygen fugacity in the transition zone ([McCammon 2005a, 2005b](#)).

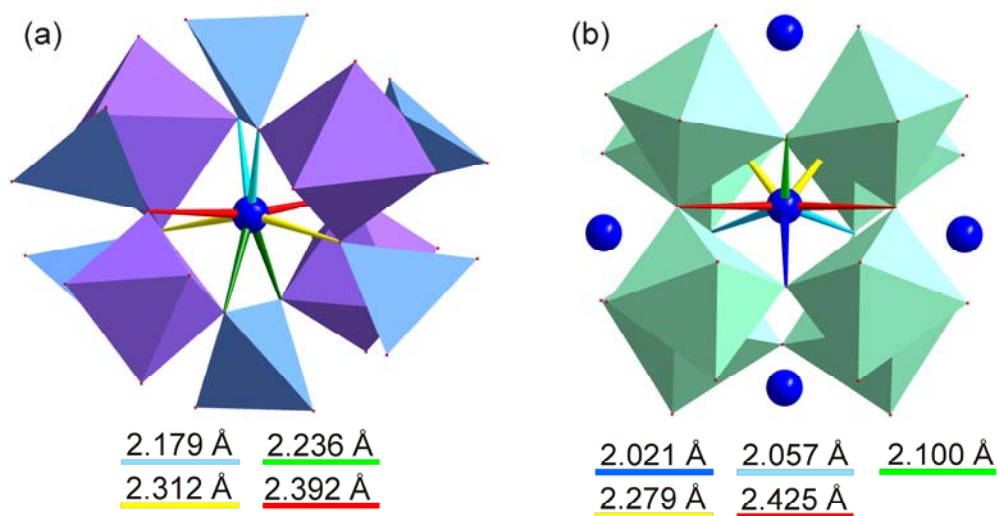


Figure 1.2-2 Polyhedral models of (a) majorite ([Angel, 1989](#); [McCammon and Ross, 2003](#)) and (b) perovskite ([Ross and Hazen, 1989](#)). Solid blue spheres correspond to Fe²⁺/Mg²⁺ in dodecahedral sites; purple octahedra represent Si⁴⁺/Al³⁺/Mg²⁺ site and blue tetrahedra correspond to the Si⁴⁺ site in the majorite structure. Si⁴⁺/Al³⁺ octahedra in the perovskite structure are shown in green.

1. Introduction

Summarizing all of the above, mantle transition zone (Mg,Fe)(Si,Al)O₃ majorite has cubic symmetry with Fe²⁺ and Mg²⁺ cations (blue spheres in Fig. 1.2-2) in the dodecahedral (or distorted cubic) site; the octahedral site (colored in purple in Fig. 1.2-2) is shared by Si⁴⁺, Al³⁺, Mg²⁺, Fe²⁺ and Fe³⁺ cations, and finally the tetrahedral site (colored in blue in Fig. 1.2-2) is occupied by Si⁴⁺. At pressures about 23-26 GPa and temperatures higher than 1300 K, majorite transforms to silicate perovskite.

(Mg,Fe)(Si,Al)O₃ perovskite along with (Mg,Fe)O comprises the major part of the Earth's lower mantle, defining its seismic and density profiles, electrical and thermal conductivity, oxidation state, etc. The ideal cubic ABX₃ perovskite crystal structure with space group *Pm3m* consists of a three-dimensional network of corner connected octahedra (B-site) and the cavities between octahedra form the dodecahedral site (A-site). Lower mantle (Mg,Fe)(Si,Al)O₃ perovskite has the GdFeO₃ structure type, which is distorted from the ideal cubic symmetry by tilting of octahedra and has space group *Pbnm* ([Horiuchi et al. 1987](#)). The large distorted 8- to 12-fold coordinated A-site in orthorhombic perovskite is occupied by Mg²⁺ or Fe²⁺ (solid blue spheres in Fig. 1.2-2 and Fig. 1.2-3) ([Horiuchi et al. 1987](#), [McCammon et al. 1992](#)); and the smaller nearly symmetrical octahedral B-site (colored in green in Fig. 1.2-2 and Fig. 1.2-3) is occupied by Si⁴⁺ and Al³⁺ cations.

(Mg,Fe)SiO₃ perovskite is known to contain a measurable amount of Fe³⁺ even at its minimum oxygen fugacity limit ([McCammon et al., 1992, 1998](#); [Jephcoat et al., 1999](#)). Addition of aluminum into the system increases the Fe³⁺/Fe²⁺ redox ratio due to the favorable energetics of coupled substitution ([McCammon, 1997](#); [Lauterbach et al., 2000](#)), which could significantly affect the radioactive component of the thermal conductivity of lower mantle perovskite ([Goncharov et al., 2008](#)).

In 2004 [Murakami et al.](#) reported a structural transition of orthorhombic magnesium silicate perovskite (space group *Pnmm*) into the post-perovskite phase (space group *Cmcm*) at pressures and temperatures close to those of the core-mantle boundary. The structure of post-perovskite is similar to that of CaIrO₃ and composed of [SiO₆-] octahedra which share an edge and form a chain, where these chains are arranged in layers by connecting through common apices. Mg²⁺ and Fe²⁺ cations are located in between Si-O layers (Fig. 1.2-3 on the right). This transition is believed to be “responsible” for the D'' seismic discontinuity at 2600-km depth (Fig. 1.1-1 and Fig. 1.2-1).

1. Introduction

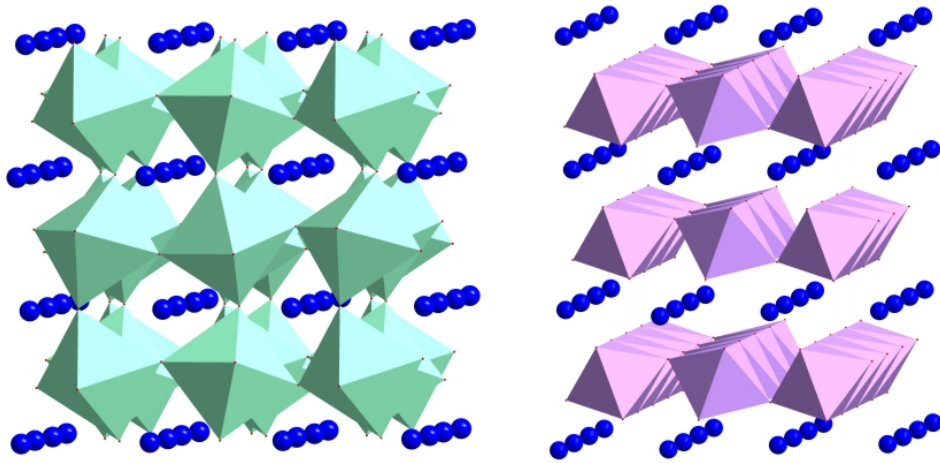


Figure 1.2-3 Polyhedral model of the crystal structures of (Mg,Fe)(Si,Al)O₃ perovskite (left) and (Mg,Fe)(Si,Al)O₃ post-perovskite (right). Solid blue spheres correspond to Mg²⁺/Fe²⁺ cations, while green and purple octahedra represent Si⁴⁺/Al³⁺ cations in the perovskite and post-perovskite structures, respectively.

An essential role in the modelling of lower mantle properties is played by iron, since this transition element influences chemical partitioning and reactions among mantle minerals and with core material, as well as thermal, electrical, and mechanical properties at depth ([Fyfe, 1960](#); [Burns, 1970](#); [Gaffney and Anderson, 1973](#); [Sherman, 1988](#); [Lin et al., 2005, 2006a](#); [Goncharov et al., 2006](#); [Keppler et al., 2007](#)). A spin-pairing transition of iron was predicted to occur within the lower mantle by [Fyfe \(1960\)](#) and recently it was experimentally observed in ferropericlase ([Badro et al., 2003](#); [Lin et al., 2005, 2006a](#); [Speziale et al., 2005](#); [Kantor et al., 2006a](#)) and silicate perovskite ([Badro et al., 2004](#); [Jackson et al., 2005](#); [Li et al., 2006](#)). The presence of a so-called “Spin transition zone” within the lower mantle could explain such phenomena as small seismic heterogeneities ([Hedlin et al., 1997](#); [Kaneshima et al., 1999](#)). The nature of these heterogeneities is related to small fluctuations in Mg/Fe or (Mg,Fe)/Si ratios ([Bina 2003](#)), which in turn can be caused by spin transitions in the lower mantle assemblage ([Lin et al., 2007b](#)).

1.3. Fe-Ni-light element(s) alloy as the main component of the Earth’s core

According to seismic profiles the Earth’s core consists of two parts (see Fig. 1.1-1): (i) outer liquid core, that does not transport shear waves (S-wave), and (ii) solid inner core, which in turn shows anisotropy: longitudinal waves (P waves) spread faster in the direction of the Earth’s rotational axis than in the equatorial directions. The origin of the Earth’s inner core anisotropy is not yet understood; however some possible mechanisms have been proposed: solidification

1. Introduction

texturing (preferred orientation of iron crystals along the direction of dominant flow) ([Bergman, 1997](#)); anisotropic growth of the inner core ([Yoshida et al., 1996](#)); magnetic field induced squeezing of iron crystal from the outer part toward the rotational axes ([Karato, 1999](#)); and partial melting of the inner core ([Vocadlo, 2007](#)).

Based on the bulk silicate earth composition (Table 1.1-1), meteoritic records and calculated density of the core, $\text{Fe}_{1-x}\text{Ni}_x$ ($0.5 \text{ wt}\% \leq x \leq 20 \text{ wt}\%$) alloy is suggested to be the main constituent of the Earth's core. However the calculated densities of the outer and inner core are slightly lower than those of $\text{Fe}_{1-x}\text{Ni}_x$ at the required conditions. Estimates for the density deficit relative to solid iron vary from 6% to 10% for the outer core ([Stevenson, 1981](#); [Anderson and Isaak, 2002](#)), and $2 \pm 1\%$ for the inner core ([Jephcoat and Olson, 1987](#); [Shearer and Masters, 1990](#); [Stixrude et al., 1997](#); [Dubrovinsky et al., 2000](#)). In order to fulfil the density deficit a certain amount of light element(s) in the core (5 to 15%) is required. Candidate element(s) (i) should be cosmically abundant; (ii) should readily alloy with Fe under high pressure-temperature conditions; and (iii) should strongly partition into liquid Fe. Based on these requirements H, O, C, S, Si, N, etc. can be marked as suitable candidates ([Allégre et al., 1995b](#); [McDonough and Sun, 1995](#)). Which alloying element or elements occur in the core is ultimately linked with the various models proposed for the origin and evolution of the core. The chemical composition of the core would directly determine its structural phase, and it would as well put constraints on the Earth's geotherm, the high-temperature part of which is defined by the temperature of the molten outer core.

The phase diagram of iron based on static experiments is presented in Fig. 1.3-1. Upon heating at ambient pressure, the structure of metallic iron changes from body-centered cubic (*bcc*) α -phase to the face-centered cubic (*fcc*) γ -phase. The *fcc* phase transforms to the *bcc* δ -phase just before melting at 1700 K ([Strong, 1959](#); [Claussen, 1960](#); [Omel'chenko et al., 1969](#); [Strong et al., 1973](#), [Mirwald and Kennedy, 1979](#)). Upon compression both the α -phase and γ -phase transform to the hexagonal closed packed (*hcp*) ε -phase ([Akimoto, 1987](#); [Boehler, 1986](#); [Mao et al., 1987](#); [Manghnani and Syono, 1987](#); [Dubrovinsky et al., 1998](#); [Schen et al., 1998](#); [Funamori et al., 1996](#)). According to the phase diagram of iron (Fig. 1.3-1), the *hcp*-structured phase of iron is supposed to be stable at the Earth's core conditions. However since the core is not made out of pure iron, the effect of other elements (Ni, O, S, Si, etc.) must be taken into account.

1. Introduction

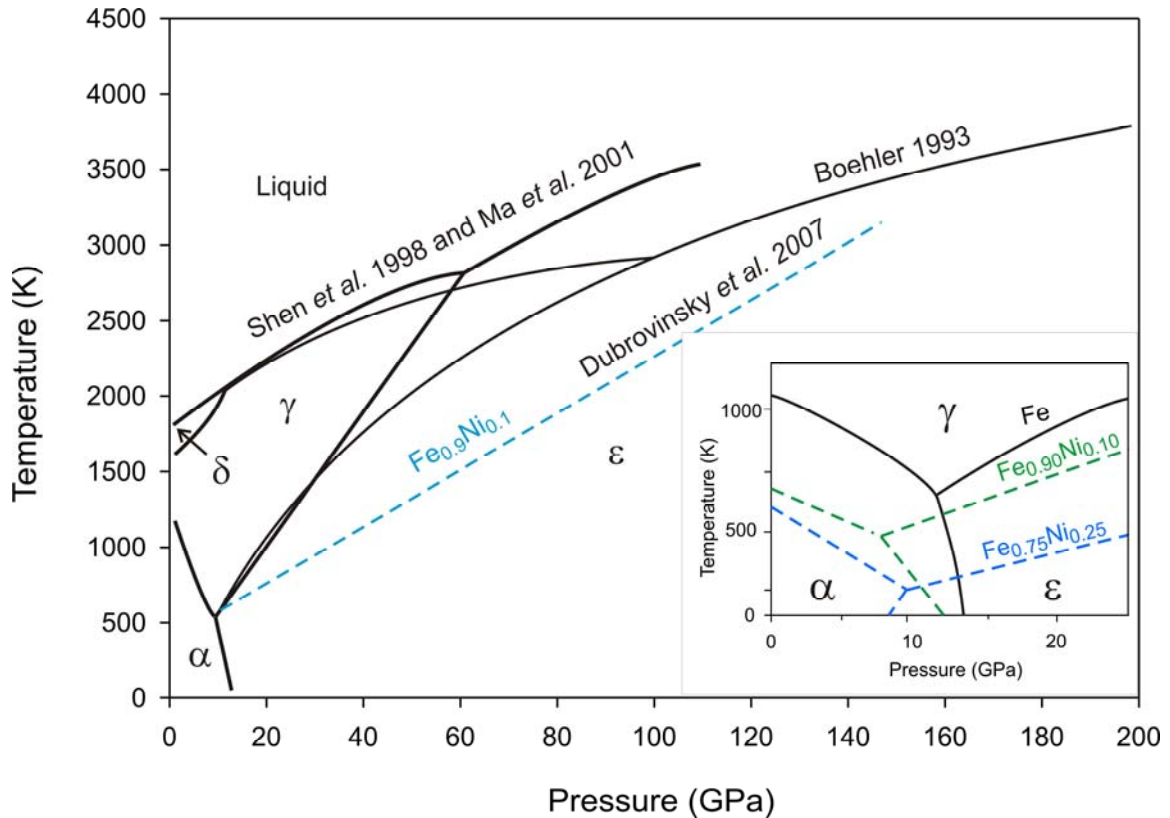


Figure 1.3-1 Phase diagram of iron based on static experiments (black solid curves). The blue dashed line representing the $\gamma - \epsilon$ - phase boundary for $\text{Fe}_{0.9}\text{Ni}_{0.1}$ alloy (Dubrovinsky et al., 2007) and the inset plot (modified after Huang, Bassett and Weathers, 1988) illustrates the effect of Ni on the P-T area of the stability of the γ -phase.

Alloying of iron with a relatively small amount of Ni (10-15%) significantly enlarges the P-T stability region of the *fcc*-structured phase (Huang, Bassett and Weathers, 1988; 1992;) (inset in Fig. 1.3-1), which motivated a number of studies of the effect of Ni on the structural properties of $\text{Fe}_{1-x}\text{Ni}_x$ alloy at conditions comparable with those of the Earth's core (Lin et al., 2002a; 2003; Dubrovinsky et al. 2007; Mao et al., 2006; Vocadlo et al., 2003). Mao et al. (2006) suggested that 15% of Ni would be enough to stabilize the *fcc*-structured phase at the pressures relevant for the outer core. Our group revealed the appearance of a so-called “high-pressure *bcc* phase” at pressures above 230 GPa and temperatures over 3000 K (Dubrovinsky et al., 2007). Possible stabilization of *bcc*-iron was also suggested before by theory (Belonoshko et al., 2003; 2008; Vocadlo et al., 2003). However the question is still open and requires further investigations, accounting also for the possible effect of light element(s) on phase relations in the Fe-Ni system.

2. Motivation

2.1. Spin state of iron in (Mg,Fe)(Si,Al)O₃

For the reliable modelling of the Earth's lower mantle (composition, dynamics, heat transport, etc.), it is essential to constrain the properties of the spin transition zone. The main question is the spin state of iron in silicate perovskite and ferropericlasite at the relevant pressure and temperature conditions and its effect on lower mantle properties. It is known that in (Mg,Fe)O ferropericlasite (second most abundant component in the lower mantle), ferrous iron undergoes a spin-pairing transition at about 50 GPa (in the case of geologically relevant compositions, where about 20% of magnesium is substituted by iron), which affects density, compressibility, sound velocities, radiative thermal conductivity and electrical conductivity of ferropericlasite ([Badro et al., 2003](#); [Lin et al., 2005, 2006a, 2007](#); [Speziale et al., 2005](#); [Kantor et al., 2006a](#), [Goncharov et al., 2006](#)). A change of the spin state of iron in silicate perovskite was also reported ([Badro et al., 2004](#); [Jackson et al., 2005](#); [Li et al., 2004, 2006](#)). However the results are not in agreement on the P-T conditions of the transition and on whether Fe²⁺ or Fe³⁺ or both iron cations are involved. Badro et al. ([2004](#)), using K_β X-ray emission spectroscopy (XES), suggested that iron in perovskite undergoes a spin-pairing transition at 120 GPa, passing through an intermediate-spin state at 70 GPa. Jackson et al. ([2005](#)), applying nuclear forward scattering (NFS), detected a spin-pairing transition in ferric iron at 70 GPa, while ferrous iron remains in the high-spin state up to at least 120 GPa (which is just about the pressure of the transition to the post-perovskite phase). Combining these two techniques (XES and NFS), Li et al. ([2006](#)) suggested that in silicate perovskite Fe²⁺ alone, or concurrently with Fe³⁺, undergoes a gradual spin-pairing transition over quite a large pressure region, from 20 to 100 GPa, which covers almost the entire lower mantle.

Since the spin state of iron in lower mantle perovskite has not been well constrained by XES and NFS techniques, we decided to apply conventional Mössbauer, X-ray diffraction (XRD) and X-ray absorption near edge structure (XANES) spectroscopies to study iron behavior in (Mg,Fe)(Si,Al)O₃ perovskite at high pressures and temperatures, employing diamond anvil cells (DACs) with external resistive heating. In order to have a reference point for the interpretation of Mössbauer spectra of silicate perovskite, we performed an analogue study of (Mg,Fe)SiO₃ majorite, which has quite a similar oxygen environment of iron atoms (see Fig. 1.2-2) and

2. Motivation

therefore one can expect some common features in the behaviour of perovskite and majorite at high pressures and temperatures.

One of the plausible effects that spin crossovers in $(\text{Mg,Fe})(\text{Si,Al})\text{O}_3$ perovskite and $(\text{Mg,Fe})\text{O}$ ferropericlasite may have is a change of the chemical composition of the lower mantle assemblage, primarily the Fe/Mg ratio in co-existing minerals ([Badro et al., 2003, 2005](#); [Lin et al., 2007b](#); [Lin and Tsuchiya, 2008](#)). It was suggested that Fe would partition into low-spin $(\text{Mg,Fe})\text{O}$ relative to high-spin or intermediate-spin silicate perovskite, which would significantly affect lower mantle properties ([Badro et al., 2003; 2005](#)). However, due to the lack of *in situ* partitioning experiments under the relevant pressure and temperature conditions, the effect of the spin state of iron in silicate perovskite and ferropericlasite on the Fe-Mg partitioning is not conclusively constrained ([Mao et al., 1997](#); [Kobayashi et al., 2005](#); [Auzende et al. 2008](#); [Sinmyo et al., 2008](#)). Therefore we performed an *in situ* study of iron partitioning between $(\text{Mg,Fe})\text{SiO}_3$ perovskite and $(\text{Mg,Fe})\text{O}$ ferropericlasite in a laser-heated DAC, combining synchrotron XRD and micro-XANES spectroscopy.

2.2. Effect of carbon on the phase relations in Fe-Ni system

As seen from Section 1.3, the question regarding the structural phase of $\text{Fe}_{1-x}\text{Ni}_x$ ($0.5 \text{ wt}\% \leq x \leq 20 \text{ wt}\%$) alloy, comprising the Earth's core, remains open. This is mainly due to the lack of experiments under the relevant pressure and temperature conditions. Most of the current experimental records on this subject are extrapolations of high pressure data collected at room temperature to the temperatures of the core-mantle boundary. Nowadays P-T conditions close to those in the core can be achieved in DAC experiments with *in situ* laser heating ([Boehler, 1993](#), [Murakami et al., 2005](#); [Mao et al., 2006](#); [Dubrovinsky et al., 2007](#); [Ohta et al., 2008](#); etc.) However this kind of experiment is highly demanding in terms of sample preparation, stability and alignment of the laser spot, maintaining of an acceptable temperature gradient, measurements of temperature itself, etc. For these reasons one should be very cautious in the interpretation of the results obtained with a laser heated DAC (LH-DAC). In contrast to LH-DACs, the large-volume press (LVP) technique allows more homogeneous heating, which can be maintained for a several hours, providing more equilibrated conditions but at significantly lower pressures.

2. Motivation

We decided to combine the advantages of both of the above mentioned high-pressure techniques and perform a comparative study of Fe-Ni-C alloys (with Ni content varying from 6 to 22 wt%, and carbon from 0.2 to 1.1 wt%) at pressures from 0.5 to 60 GPa and temperatures up to 2600 K using a LH-DAC and LVPs (multi-anvil and piston-cylinder). Carbon was chosen first of all as a plausible candidate for the light component in the Earth's core ([Wood, 1993](#); [Scott et al., 2001](#); [Huang et al., 2005](#)), the alloying effect of which on the phase relations in the Fe-Ni system at elevated pressure and temperatures might be essential for the modelling of the Earth's core structure and composition. The second reason arises from recent reports on the possible carbon contamination which can occur during laser heating in a DAC ([Prakapenka et al., 2003-2004](#); [Rouquette et al., 2008](#)).

3. Experimental techniques

3.1. Creation of high pressure high temperature conditions

Diamond anvil cell (DAC) and large-volume press (multianvil and piston-cylinder) techniques allow investigation of matter under a static pressure-temperature regime. A marked advantage of multianvil and piston-cylinder apparatus over the DAC is a much larger sample volume, which makes it possible to conduct experiments under precisely controlled pressure-temperature conditions and to apply some advanced design of the capsule ([Frost et al., 2001, 2004b](#); [Liebske et al., 2005](#)). On the other hand the maximum attainable pressure is limited to roughly 4 GPa in the piston-cylinder and to 25 GPa in the multianvil press (if anvils are made of tungsten carbide; [Kubo and Akaogi, 2000](#)). An additional limitation of multianvil experiments is the reduced number of *in situ* techniques which can be applied. In contrast, with the DAC static pressure as high as 300 GPa (Earth's core conditions) can be reached and, thanks to the transparency of the anvils and miniature design of the diamond anvil cell itself, performing of *in situ* measurements is quite straightforward (X-ray diffraction, X-ray absorption and Mössbauer spectroscopies, Raman and infra-red spectroscopies, etc.)

3.1.1. Diamond anvil cell technique

We employed an opposed-plate four-pin ($\varnothing=50$ mm) DAC (modified Merrill-Bassett DAC). The main body of a DAC (opposed plates) is made out of either Republica or Nimonic alloys, which are hard, mechanically stable and non-magnetic materials. The principal mechanism of the DAC is simple. Tightening the screws forces together two opposed anvils with flawless, brilliant-cut diamonds with flat faces (the culets), which pressurize a μm -size sample, embedded in a gasket along with a pressure-transmitting medium (Fig. 3.1-1a). The gasket is a thin metal sheet (we used rhenium) with a micro-drilled hole somewhat smaller than the culet (e.g. 125 μm hole for 300 μm culet size). We used two types of diamond-anvil culet design (Figs.3.1-1b,c): (i) simple flat ($\varnothing=250\div 300$ μm) and (ii) with polished bevels ($\varnothing=70\div 120$ μm). The size of the culet determines the achievable pressure range (from 80-90 GPa with 250 μm -culet up to 150-170 GPa with 70 μm -culet). For pressure measurements and evaluation of the pressure gradient we mainly employed small ruby chips that were loaded into the cell along with

3. Experimental techniques

the sample. The ruby fluorescence calibration developed by Mao et al. (1986) with temperature corrections from Rekhvi et al. (1999) was used. In synchrotron radiation X-ray diffraction experiments (see Sec. 3.2.1.) pressure was determined from the equation of states of LiF, MgO and Ne.

For studies of matter under geologically relevant conditions not only pressure but also temperature is an issue. We used two ways of heating in a DAC: (i) external resistive heating (up to 1000 K) and (ii) internal laser heating (2500-3000 K). Resistive heating gives the advantage of homogenous, quite stable (more than 24 h) and controlled heating of any material placed in a DAC. It is designed in the following way. A heater, ceramic plate wound with Pt wire of 0.5mm in diameter and isolated from both sides by thin mica sheets or a layer of high-temperature ceramic glue, is fixed to one of the DAC opposed plates by the ceramic glue as shown in Fig. 3.1-1a. A S-type thermocouple (90%Pt10%Rh/Pt) is glued to another DAC opposed plate in such a way that the thermocouple head is as close to the sample as possible (Fig. 3.1-1a).

Laser heating, in contrast, provides substantially higher temperatures (up to 3000 K), but requires thermal isolation of the sample from the anvil surfaces (*e.g.* by pressure-transmitting medium: NaCl, LiF, Ne and He), has a higher temperature gradient and poses some difficulties on the maintenance of a stable temperature regime. As a source of laser light we use a Nd:YAG Quantronix 117 two-head laser (CW TEM00 mode, $\lambda = 1064$ nm) with a maximum power of 70 W, installed in Bayerishes Geoinstitut (BGI).

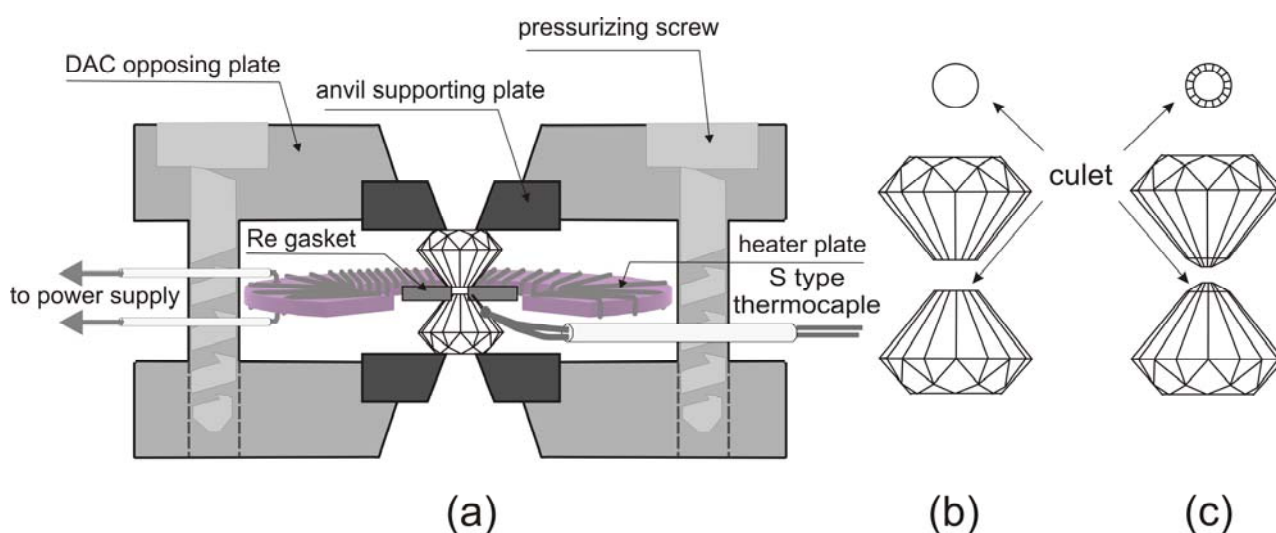


Figure 3.1-1 Schematic drawing of the four-pin modified Merrill-Bassett DAC equipped with an internal resistive heater (a); simple flat (b) and bevelled (c) diamond-anvil culet design.

3. Experimental techniques

3.1.1. Large-volume press technique

In order to study the effect of carbon on the Fe-Ni system a series of quenched experiments were performed by means of large-volume presses (LVP): the piston-cylinder and multianvil apparatus at BGI. The end-loaded piston-cylinder apparatus consists of a tungsten carbide pressure vessel supported by a steel ring (bomb) ([Boyd and England, 1960](#)). The pressure vessel is end-loaded during a run with a thrust delivered by a hydraulic press (see Fig. 3.1-2, left). The pressure is applied to the sample via pressure amplification from a small force on a large piston to a large force on a small piston, driven by a second hydraulic press. The load is transferred from the ram to the tungsten carbide piston which is pushed into the bomb applying pressure to the sample. The pressure in the sample assembly is controlled automatically by a hydraulic pump.

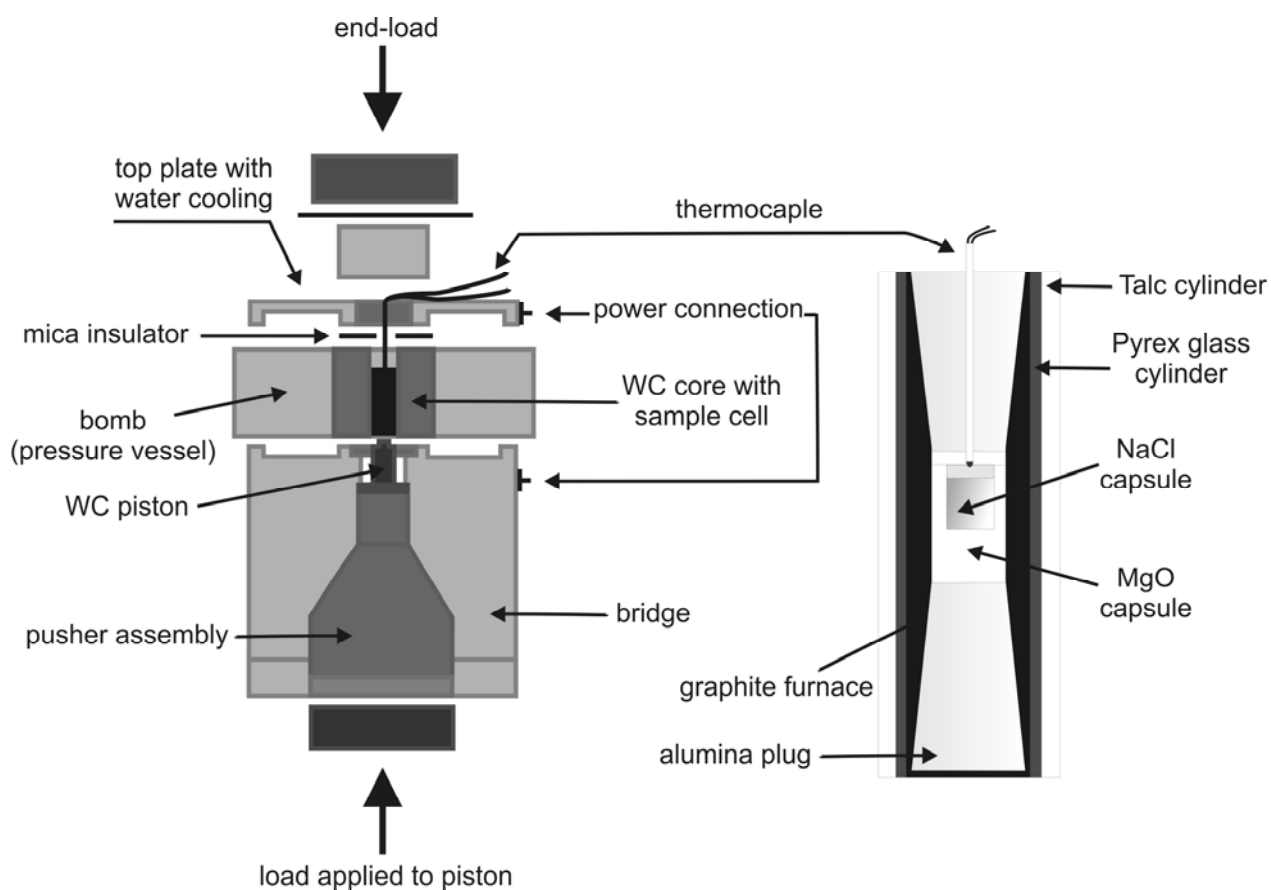


Figure 3.1-2 Schematic drawing of an end-loaded piston-cylinder apparatus and a half inch sample assembly. Modified after Mierdel ([2006](#)) and Gavrilenko ([2008](#)).

3. Experimental techniques

Two types of capsule were used: (i) “simple” cylinder of $\text{Ø}=6$ mm and 12 mm in height (capsule and cup) made out of MgO compressed powder; and (ii) “composite” capsule, which is a single crystal of NaCl (5 mm \times 5 mm \times 3 mm) placed inside the MgO cylinder with the same dimensions, 6 mm \times 12 mm, where the cavities were filled by MgO powder. NaCl was used in order to eliminate oxygen from the system. Temperature was controlled by a $\text{W}_{75}\text{Re}_{25}/\text{W}_{97}\text{Re}_3$ thermocouple (type D) (wire $\text{Ø}=0.25$ mm) within a 4-hole Al_2O_3 sleeve. In all of the runs the samples first were fully pressurized and then isobarically heated up to 1750 °C. The duration of the runs varies from 4 to 14 h, depending on the cooling procedure: (i) isobaric quenching from 1750 °C to room temperature (~ 30 seconds); and (ii) “graded” isobaric cooling from 1750 °C to 1000 °C during 10h followed by quenching to room temperature (~ 15 sec).

Another set of experiments was carried out on a 6-8 Kawai-type multi-anvil press ([Kawai and Endo, 1970](#)). A detailed description of the multi-anvil technique and experimental procedure can be found in work from Rubie ([1999](#)). Schematically, the details of the multi-anvil apparatus are shown in Fig. 3.1-3.

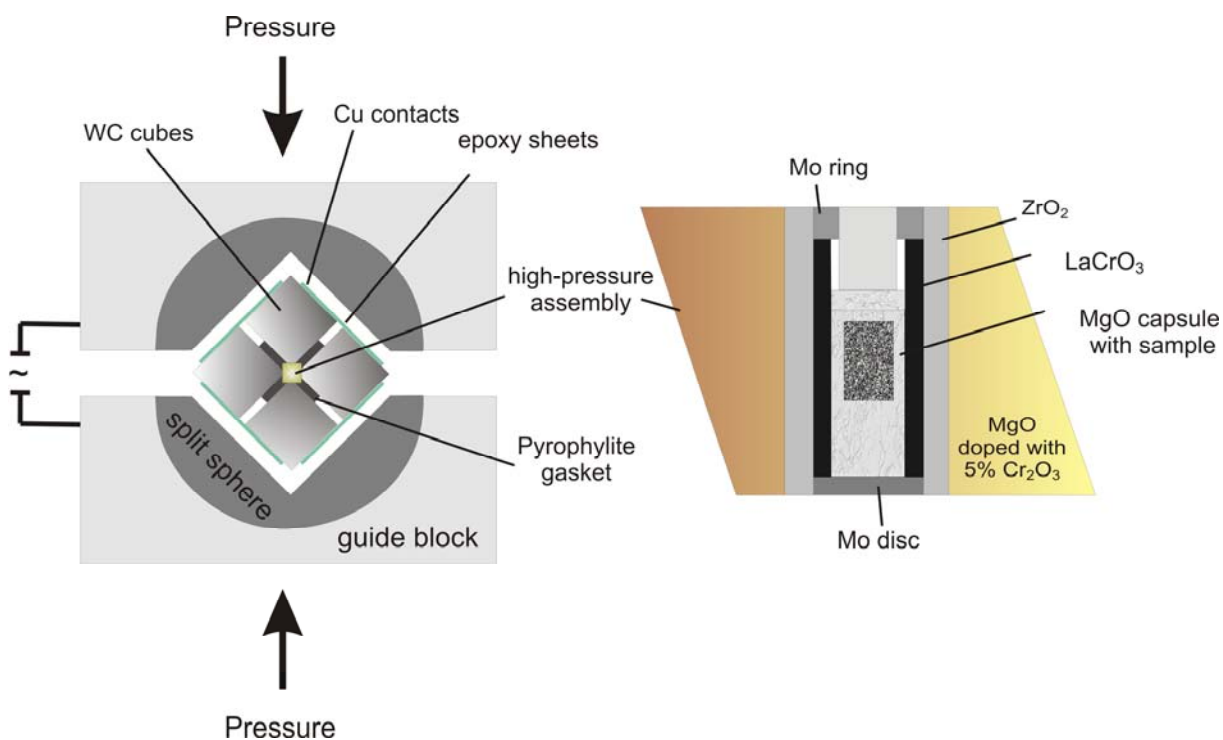


Figure 3.1-3 Schematic drawing of 6-8 Kawai-type apparatus: two guide blocks enclosing six anvils forming a cubic cavity for eight tungsten-carbide anvils enclosing a 10/5 multi-anvil pressure assembly, shown on the right. Modified after Stoyanov ([2006](#)) and Rubie ([1999](#)).

3. Experimental techniques

The 10/5 (octahedral edge length / tungsten-carbide anvil truncation in mm) assembly was employed in the 1200 tonne press. The pressure cells consist of a cylindrical LaCrO₃ heater, a cylindrical zirconia sleeve around the heater providing thermal insulation ([Rubie, 1999](#)), and a MgO capsule. The capsule was placed inside an octahedron of MgO doped with 5% Cr₂O₃ to reduce heat loss by radiation. The octahedral sample assembly was compressed by a set of eight corner-truncated tungsten-carbide cubes (first stage anvils). Pyrophyllite gaskets were used between the cubes. The cubes were packed all together using epoxy-impregnated fiberglass laminate sheets which also insure electrical insulation from the six guide block anvils. The set of cubes is then compressed by the six outer tool-steel anvils (second stage), which are driven by a hydraulic press in a uniaxial direction (see Fig. 3.1-3). The calibration for the 10/5 assembly was based on the calibration curve developed by Frost et al. ([2001](#)). In all multi-anvil runs, the samples first were fully pressurized, then heated up to the desired temperatures (during ~10 min), kept at the conditions for 5-10 minutes, and then isobarically quenched to room temperature by shutting off the power (~ 20 sec.).

3.2. *In situ* sample analyses

Experimental results presented in this work were mainly obtained by means of X-ray diffraction, X-ray absorption near edge structure and conventional Mössbauer spectroscopies. In the case of DAC experiments these techniques were applied *in situ*, while products of LVP runs were analysed *ex situ*. Also scanning and transmission electron microscopy techniques (SEM and TEM) were used for the characterization of the recovered samples.

3.2.1. X-ray diffraction spectroscopy

X-ray diffraction (XRD) is the most direct probe of the crystal structure of the material. In this work we used XRD mainly for phase analyses in both DAC and LVP experiments. Angle-dispersive XRD measurements were mainly performed at the synchrotron facilities (European Synchrotron Radiation Facility (ESRF) in Grenoble, France; and Applied Photon Source (APS) in Chicago, USA). For the preliminary analyses of the recovered samples the High-brilliance X-ray diffractometer installed in BGI was used. Some experimental parameters are listed in Table

3. Experimental techniques

3.2-1. Two dimensional XRD scans were integrated using Fit2D software ([Hammersley, 1997, 1998](#)) and then processed by means of the GSAS package ([Larson and Von Dreele, 2004](#)).

Table 3.2-1 Experimental parameters of the angle-dispersive X-ray diffraction measurements

	λ (Å)	focal spot FWHM (μm)	2θ range (deg)	Detector
high –pressure ID27 beamline (ESRF)	0.3738	10x9	2-19	MAR345
high –pressure ID09A beamline (ESRF)	0.4141	10x10	2-22	MAR345
Swiss-Norwegian high pressure beamline (ESRF)	0.7002	40x40	0-50	MAR345
CARS high pressure beamline (APS)	0.3344	5x5	2-22	MAR345
high-brilliance X-ray diffractometer with Mo anode (BGI)	0.7108	40x40	0-35	SMART APEX 4K CCD

3.2.2. Conventional Mössbauer spectroscopy

Mössbauer spectroscopy is based on the emission and absorption of γ -ray photons without loss of energy due to recoil of the nucleus and without thermal broadening ([Mössbauer, 1958](#)). The Mössbauer absorption spectrum, characterized by the hyperfine parameters (central shift (CS), quadrupole splitting (QS) and hyperfine magnetic field (HBF)), provides information on magnetic interactions in the sample, oxidation and electronic states of the absorbing atom (in our case Fe), its coordination and degree of distortion of the crystallographic site. Due to the high sensitivity of the hyperfine parameters to the state of iron, the spectral contributions from ferrous and ferric iron can be clearly distinguished, which allows quite precise measurements of the redox ratio ($\text{Fe}^{3+}/\Sigma\text{Fe}_{\text{tot}}$), and also provides the opportunity to study the behaviour of iron species separately. Analyses of the temperature effect on the central shift and quadrupole splitting provides an estimation of some parameters which cannot be probed directly. From CS(T) the

3. Experimental techniques

Debye temperature can be extracted ([Mössbauer, 1958](#)), while QS(T) is related to the energy splitting between valence electron levels ([Ingalls, 1964](#); [Huggins, 1975](#)).

Mössbauer spectra presented in this work were recorded in transmission mode on a constant acceleration Mössbauer spectrometer with a point ^{57}Co source (500 μm in diameter). The design of the transmission Mössbauer spectrometer, adapted for measurements in the DAC, is shown in Fig. 3.2-1. It consists of a drive with vibrating holder, on the tip of which a ^{57}Co point source is fixed; a sample in a DAC or in a lead holder (in the case of experiments in air); and the detector.

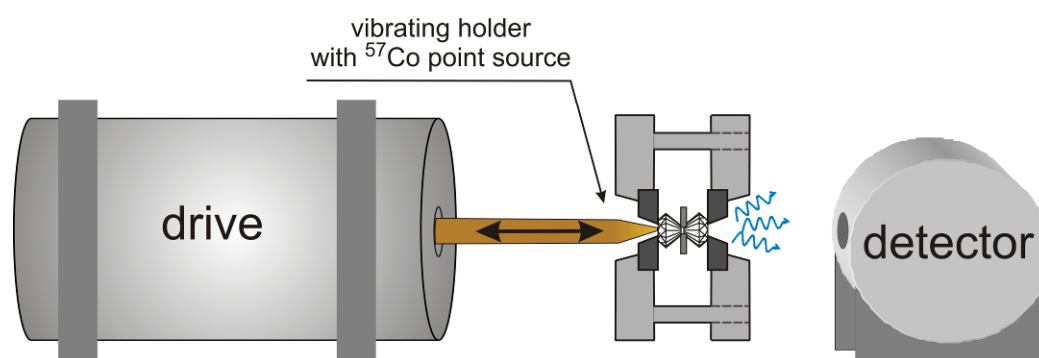


Figure 3.2-1 Schematic drawing of the experimental setup for conventional Mössbauer spectroscopic measurements in the DAC.

Due to the μm -size of a sample enclosed in a DAC and the absorption of γ -photons by the diamond anvils, all samples used for DAC experiments were enriched in ^{57}Fe . The velocity scale was calibrated relative to 25 μm Fe foil. The average duration of a single run was 24-48 h. The spectra were fitted to Lorentzian lineshapes using NORMOS ([Brand, 1990](#)) and Recoil ([Lagarec and Rancourt, 1998](#)) program packages.

3.2.3. X-ray absorption near-edge structure spectroscopy

X-ray absorption near edge structure (XANES) covers the low energy part of absorption spectra, extending 50-100 eV beyond the absorption edge. It is a powerful element-specific probe of local atomic and electronic structure, and it is particularly sensitive to the geometrical arrangement of nearest neighbors of the absorbing atom ([Bianconi, 1988](#); [Brown Jr. et al., 1988](#)). Element selectivity of the method and its sensitivity to the chemical and orbital moment of a

3. Experimental techniques

target atom provides useful information that complements results obtained by the other techniques (e.g. XRD, Mössbauer spectroscopy, etc.).

XANES measurements at the Fe K-edge were performed at the energy dispersive X-ray absorption beamline ID24. Detailed description of the experimental setup is given elsewhere (Pascarelli et al., [2004](#) [2006](#)). The conventional optical scheme for XANES is given in Fig.3.2-2. The beam is focused horizontally using a curved polychromator Si (220) crystal in Bragg geometry and vertically with a bent Si vertical mirror 2 placed at 2.8 mrad with respect to the direct beam, providing the beam size of $4\ \mu\text{m} \times 5\ \mu\text{m}$ in the focal plane of the sample (Pascarelli et al. [2006](#)). The Bragg diffraction peaks arising from the diamond anvils were removed from the energy range of interest by changing the orientation of the diamond anvil cell and following in real time the intensity of the transmitted beam on a two-dimensional detector.

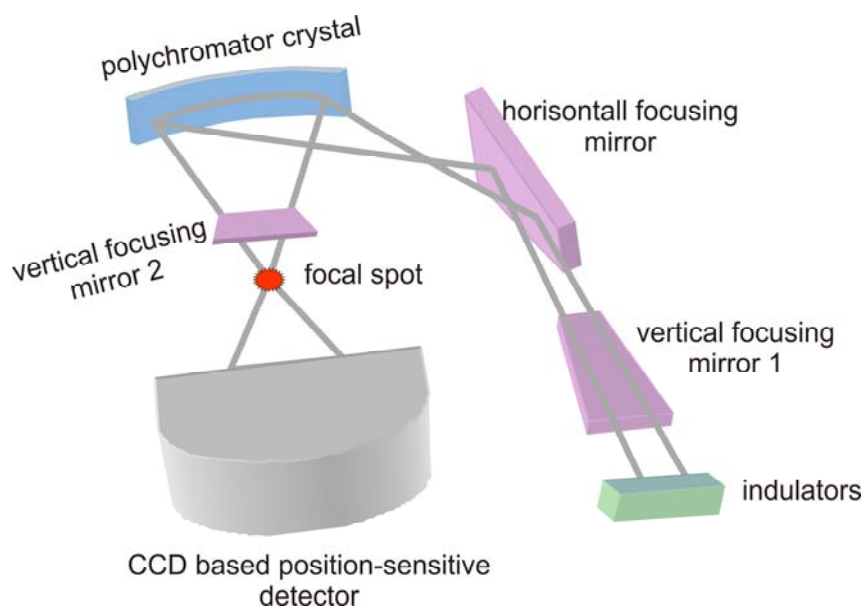


Figure 3.2-2 The conventional optical scheme for XANES measurements. Redrawn from Pascarelli et al. ([2004](#)).

Micro-resolution achieved by the setup allows two dimensional mapping of the sample area enclosed in the DAC with a $5\ \mu\text{m}$ step. Every pixel of such a map contains the full XANES information. 2D maps were processed by means of the XASMAP package (Muñoz et al., [2006](#)). The measured XANES spectra were analyzed using the VIPER program (Klementev [2001](#)). The flat part of the pre-edge region of the spectrum was fitted to the Victoreen function ($F = a + bE^3$, where E is the absorption energy and a and b are fit parameters) and this baseline was extended over the entire energy region. The post-edge jump in X-ray absorption was then normalized to 1.

4. Scope of the thesis

This chapter provides a summary of the results presented in eight manuscripts comprising Chapter 5, which is organized in the following way. Sections 5.1-5.4 report on the spin state of Fe^{2+} in silicate perovskite; Sections 5.5-5.6 provide a description of the developed XANES mapping technique; Section 5.7 is devoted to the Fe-Mg partitioning between silicate perovskite and ferropericlasite; and finally Section 5.8 presents a study of phase relations in the Fe-Ni-C system at high pressures and temperatures. Three manuscripts out of eight (Sections 5.1, 5.5 and 5.6) were not written by me as a first author; however I took an active part in the experimental measurements, data analyses and writing of the manuscripts.

4.1. Spin state of iron in lower mantle perovskite

Using diamond anvil cells (DAC) with external resistive heating (Section 3.1.1.) we carried out a systematic Mössbauer and XANES spectroscopic study of iron behaviour in $(\text{Mg}_{0.88}^{57}\text{Fe}_{0.12})\text{SiO}_3$ and $(\text{Mg}_{0.86}^{57}\text{Fe}_{0.14})(\text{Si}_{0.98}\text{Al}_{0.02})\text{O}_3$ perovskites at pressures to 110 GPa in the temperature range 295-1000 K. A detailed description of the study can be found in [Sections 5.1.-5.4](#). The summarized result is presented in Fig. 4.1-1. All spectra collected at pressure below 30-35 GPa were fitted to two quadrupole doublets with Lorentzian line shape, corresponding to (i) high-spin Fe^{2+} in the dodecahedral site, HS $^{[8-12]}\text{Fe}^{2+}$ (component colored in gray in Fig. 4.1-1a with central shift, CS, close to 1 mm s^{-1} and quadrupole splitting, QS, around 2 mm s^{-1}), and (ii) Fe^{3+} (small black doublet in Fig. 4.1-1a), a certain amount of which (in our case 10-12% of the total iron content) is known to be present in magnesium silicate perovskite in the octahedral site ([McCammon et al., 1992, 1998](#); [Jephcoat et al., 1999](#)). At pressures above 35(2) GPa a new component (colored in blue in Fig. 4.1-1a) with $\text{QS} \sim 3.7 \text{ mm s}^{-1}$ and CS close to that of HS $^{[8-12]}\text{Fe}^{2+}$ appeared (hereafter this component will be referred as the “high-QS component”). The amount of the high-QS component increases with both pressure and temperature, balanced by a decrease of the amount of HS $^{[8-12]}\text{Fe}^{2+}$, which finally approaches zero at about 72 GPa (Fig. 4.1-1e; temperature data can be found in [Section 5.4](#), Fig. 5.4-6). The component shaded in light gray (with $\text{CS} \sim 0.6 \text{ mm s}^{-1}$) we attributed to rapid charge transfer between ferric and ferrous iron.

4. Scope of the thesis

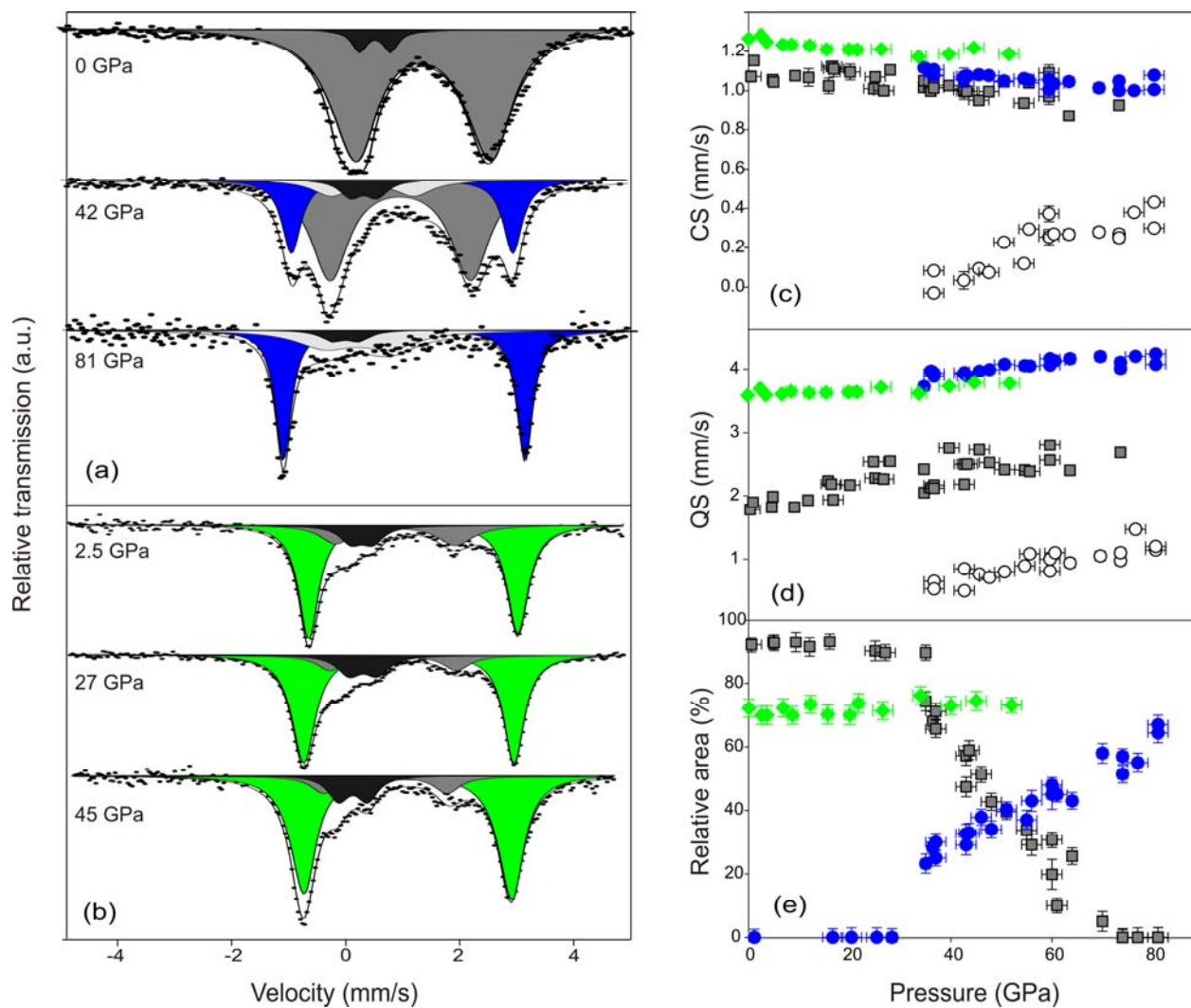


Figure 4.1-1 Selected room temperature Mössbauer spectra of $(\text{Mg}_{0.88}\text{Fe}_{0.12})\text{SiO}_3$ perovskite **(a)** and $(\text{Mg}_{0.82}\text{Fe}_{0.18})\text{SiO}_3$ majorite **(b)** fitted to the three Lorentzian line shape quadrupole doublets. On the right side the hyperfine parameters of some of these components: CS **(c)**, QS **(d)** and relative area **(e)**, are plotted as a function of pressure. Blue closed circles and dark gray closed squares correspond respectively to high-QS and HS $^{[8-12]}\text{Fe}^{2+}$ components in the perovskite Mössbauer spectra, while the charge transfer component in perovskite is shown by open white circles. For comparison hyperfine parameters for the HS $^{[8-12]}\text{Fe}^{2+}$ component in the majorite Mössbauer spectra (green closed diamonds) are given.

Note that Mössbauer spectra collected for Al-bearing perovskite (see [Section 5.1](#), Fig. 5.1-4 and [Section 5.3](#), Fig. 5.3-2d) demonstrate the same behaviour of $^{[8-12]}\text{Fe}^{2+}$; however spectral lines are broader, and due to the significant amount of Fe^{3+} (20-25%) the contribution from $\text{Fe}^{2+} - \text{Fe}^{3+}$ charge transfer is higher.

4. Scope of the thesis

Using nuclear forward scattering (NFS) spectroscopy (the synchrotron analogue of conventional Mössbauer spectroscopy), we extended the experimental data set to 110 GPa and 1000 K. NFS data confirmed the result obtained by conventional Mössbauer and suggest that the high-QS component remains dominating up to 110 GPa (for details see Section 5.1).

XANES spectra collected at pressures up to 87 GPa at ambient temperature also suggest some peculiarities in the behaviour of iron in both Al-free and Al-bearing perovskite at 30-70 GPa, revealing changes in the white-line region of the XANES spectra (the region just after the Fe K edge (7121 eV), the shape of which is mainly determined by the electronic state of iron) and in the high energy part of the spectra (7170 eV), defined primarily by the local environment of Fe atoms (see Fig. 5.2-12 in [Section 5.2](#)). A detailed description of the XANES study of silicate perovskite at the Fe K-edge is given in [Section 5.2](#) and [5.3](#).

Our Mössbauer and XANES data on silicate perovskite suggest a transition involving Fe²⁺ above 30-35 GPa, which coincides with the previously reported drop in spin number revealed by XES ([Badro et al., 2004](#); [Li et al., 2004](#)). Therefore the reason for the high QS value might be related to the electronic transition. The magnitude of QS is determined by the structural factor, related to the charge distribution surrounding the absorbing nucleus (lattice contribution, F_{lat}) and the electronic state of the absorbing nucleus itself, which is defined by the distribution of electrons over the valence energy levels associated with the absorbing nucleus (valence contribution, F_{val}). High-resolution XRD (see [Section 5.1](#)) does not suggest any significant structural change in both Al-free and Al-bearing perovskite at the considered P-T conditions; consequently the appearance of the high-QS component cannot be accounted for by a change of the lattice contribution – it must be related to F_{val} .

It should be mentioned that such a high value of QS, 3.7 mm s⁻¹ (that we obtained for the new component), is not common for iron containing compounds, except for garnets where QS of the ferrous iron component is ~ 3.6 mm s⁻¹ at ambient conditions ([Murad and Wagner, 1987](#); [McCammon and Ross 2003](#)). Since the oxygen environment of ferrous iron in majorite (garnet enriched in MgSiO₃-component) is similar to that in the perovskite structure (see Fig. 1.2-1), we decided to compare the behaviour of the high-QS component in these two phases at elevated pressures and temperatures. Majorites with two slightly different compositions, (Mg_{0.82}⁵⁷Fe_{0.18})SiO₃ and (Mg_{0.89}⁵⁷Fe_{0.11})SiO₃, were studied by means of Mössbauer spectroscopy at pressures to 52 GPa in the temperature range from 296 to 800 K (for details see [Section 5.4](#)). In the entire P-T studied region the Mössbauer spectra of majorite were fitted to three quadrupole

4. Scope of the thesis

doublets with Lorentzian line shape (Fig. 4.1-1b). The main component, representing dodecahedral ferrous iron, $^{[8-12]}\text{Fe}^{2+}$, colored in green in Fig. 4.1-1b, has QS $\sim 3.6 \text{ mm s}^{-1}$ and CS $\sim 1.2 \text{ mm s}^{-1}$ at ambient conditions. Upon compression the value of QS gradually increases while CS decreases (closed green diamonds in Figs. 4.1-1c,d) due to the decrease of Fe^{2+} -ligand distances. Upon heating to 800 K both CS and QS decrease. Finally the relative area of the $^{[8-12]}\text{Fe}^{2+}$ component does not change either with pressure or temperature (Fig. 4.1-1e; note temperature data are given in [Section 5.4.](#), Fig. 5.4-8f), which is different from the perovskite case, where both pressure and temperature significantly increase the amount of high-QS component (Fig. 4.1-1e; temperature data are in [Section 5.4.](#), Fig. 5.4-6)

The temperature effect on the hyperfine parameters can provide essential information regarding the system under study. The high quality of data collected for majorite samples allowed us to extract the value of splitting between the two low energy 3d electron levels of HS $^{[8-12]}\text{Fe}^{2+}$, Δ_1 , (Fig. 4.1.-2, on the left) using the following equation suggested by Huggins ([1975](#)):

$$\text{QS}(T) = (\text{QS}(0) + F_{\text{lat}}) \left(\frac{1 - e^{-\Delta_1/kT}}{1 + e^{-\Delta_1/kT}} \right) - F_{\text{lat}}, \quad (4.1-1)$$

where QS(0) is the quadrupole splitting (in mm s^{-1}) at 0 K, Δ_1 is the separation of e_g levels (Fig. 4.1-2, on the left), k is Boltzmann's constant and F_{lat} is the lattice contribution (in mm s^{-1}) to the QS. This equation is based on the premise that in the case of HS $^{[8-12]}\text{Fe}^{2+}$, the valence contribution to the QS value is determined by the electron transitions between e_g levels. A fit of our temperature data with equation (4.1-1) gives the following values of Δ_1 at 20 GPa: 1500 (50) cm^{-1} and 1680 (70) cm^{-1} for $(\text{Mg}_{0.82}^{57}\text{Fe}_{0.18})\text{SiO}_3$ and $(\text{Mg}_{0.89}^{57}\text{Fe}_{0.11})\text{SiO}_3$ majorites, respectively (Fig. 4.1-2 on the right). For comparison, the reported value of Δ_1 for ferrous iron in silicate almandine (mineral belonging to the garnet group) is 1100 (50) cm^{-1} at ambient conditions ([Huggins, 1975](#); [Burns, 1993](#)). Thus, in the case of majorite the high value of QS for the $^{[8-12]}\text{Fe}^{2+}$. Mössbauer component can be attributed to the valence contribution defined by the specific energy splitting between the lower energy levels, e_g ; and QS(T) in this case can be nicely described in the framework of the Huggins ([1975](#)) model. Taking the last statement into account as well as the fact that the high-QS components in perovskite and majorite behave differently with pressure and temperature, we conclude that the origin of the high QS value in these two phases is different.

4. Scope of the thesis

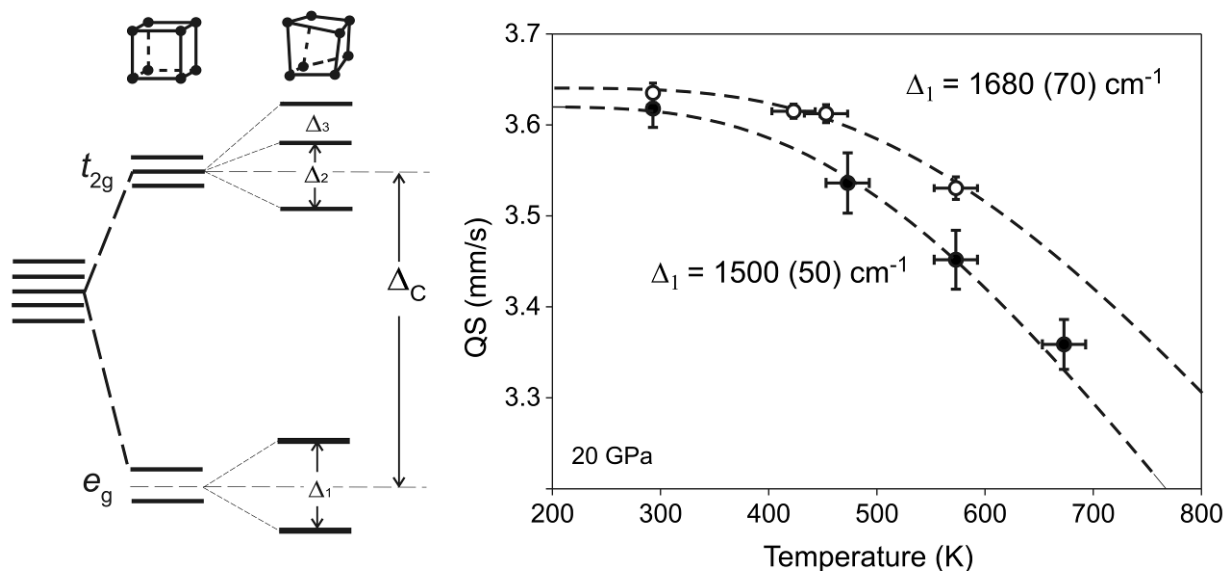


Figure 4.1-2 (left) Simplified energy diagram for $^{[8-12]}\text{Fe}^{2+}$ (redrawn after Burns, [1993](#)). Δ_C is the crystal field splitting energy. (right) Temperature dependences of QS collected at 20 GPa for $(\text{Mg}_{0.82}\text{Fe}_{0.18})\text{SiO}_3$ (closed circles) and $(\text{Mg}_{0.89}\text{Fe}_{0.11})\text{SiO}_3$ (open circles) majorites. Dashed lines represent fits of the corresponding temperature data with equation (4.1-1).

Applying the same simplified energy diagram for $^{[8-12]}\text{Fe}^{2+}$ in perovskite (Fig. 4.1-2, on the left), we considered the effect of spin configuration on the value of F_{val} . In the high spin, HS, state (four unpaired electrons) as we just discussed, F_{val} is determined by the splitting between e_g levels, Δ_1 ; in the intermediate spin, IS, state (two unpaired electrons on t_{2g}) consequently F_{val} is defined by the splitting between t_{2g} levels Δ_2 , Δ_3 , and finally in the low spin (LS) state (all electrons are paired) it is zero. Upon compression the value of crystal field splitting, Δ_C , increases and at some point starts to dominate over the spin-pairing energy, leading to the stabilization of the IS state, followed by the LS state with further compression. According to Keppler et al. ([1994](#)), in the case of $^{[8-12]}\text{Fe}^{2+}$ in silicate perovskite $\Delta_2, \Delta_3 \gg \Delta_1$; consequently the transition to IS would enhance the valence contribution to QS. Therefore we suggest that the effect that we observed by Mössbauer and XANES reflects a gradual high-spin (HS) – intermediate-spin (IS) state crossover that occurs in iron-bearing silicate perovskite over a wide pressure range, 35-70 GPa, at ambient temperature, and becomes narrower at higher temperatures. Considering the current thermal models ([Brown and Shankland, 1981](#); [Billen, 2008](#); [Leng and Zhong, 2008](#)), the last statement implies that the HS-IS transition in perovskite occurs in the uppermost lower mantle. Recently published work of Lin et al. ([2009](#)) suggests that ferrous iron in silicate

4. Scope of the thesis

perovskite remains in the IS state at 110 GPa and temperatures up to 3000 K. Consequently the major part of the lower mantle is dominated by IS silicate perovskite (see [Section 5.1](#)). Therefore for the proper modelling of the bulk lower mantle composition and thermal structure derived from seismic profiles, systematic measurements of the shear moduli of silicate perovskite containing IS ferrous iron are required.

Due to the negative Clapeyron slope, the area of the spin transition is broader in the cold environment of subducting slabs, whereas in the vicinity of hot mantle upwellings it is thinner. According to recent measurements ([Ohta et al., 2008](#)), the electrical conductivity of silicate perovskite transforming to the IS state drops by almost two orders of magnitude, which implies higher electrical conductivity in subducting slabs relative to the surrounding mantle, and consequently lower conductivity in areas of mantle upwelling. Thermal conductivity of perovskite is expected to increase due to a change of the spin number ([Badro et al., 2003; 2005](#)). Crossover to the IS state in perovskite also might affect element partitioning in the lower mantle assemblage ([Badro et al., 2003; 2005](#)), which would then cause chemical heterogeneities, particularly in the vicinity of hot plumes and subducting slabs in the uppermost lower mantle. Thus, although the gradual character of HS-IS crossover in silicate perovskite does not produce any abrupt changes of lower mantle properties, considering the presence of the transition is essential for reliable evaluation of the composition, geophysics and dynamics of the Earth's lower mantle.

4.2. Fe-Mg partitioning between (Mg,Fe)SiO₃ perovskite and (Mg,Fe)O ferropericlasite

Combining XRD and micro-XANES spectroscopies, we measured the Fe-Mg partition coefficient between (Mg,Fe)SiO₃ perovskite and (Mg,Fe)O ferropericlasite *in situ* in a LH-DAC at temperatures to 2300 K in the pressure range 28-115 GPa. The key idea of the method is the following. Parameters of a XANES spectrum are defined by an electronic state of a target atom (iron in our case) and its geometrical environment; therefore its (spectrum) shape is unique for a given Fe-bearing compound (Fig. 4.2-1).

The XANES signal from a mixture is the superposition of the unique XANES signals from the constituents. Consequently the deconvolution of a XANES spectrum of a mixture to the

4. Scope of the thesis

sub-XANES spectra of the constituents enables the amount of iron in each constituent to be estimated relative to the total iron content. Combining this information with XRD data, one can obtain the iron partition coefficient between phases comprising the mixture under study. Thanks to the experimental setup developed at ID24 (ESRF) (see [Sections 5.5-5.6](#)), this method can be combined with the DAC technique.

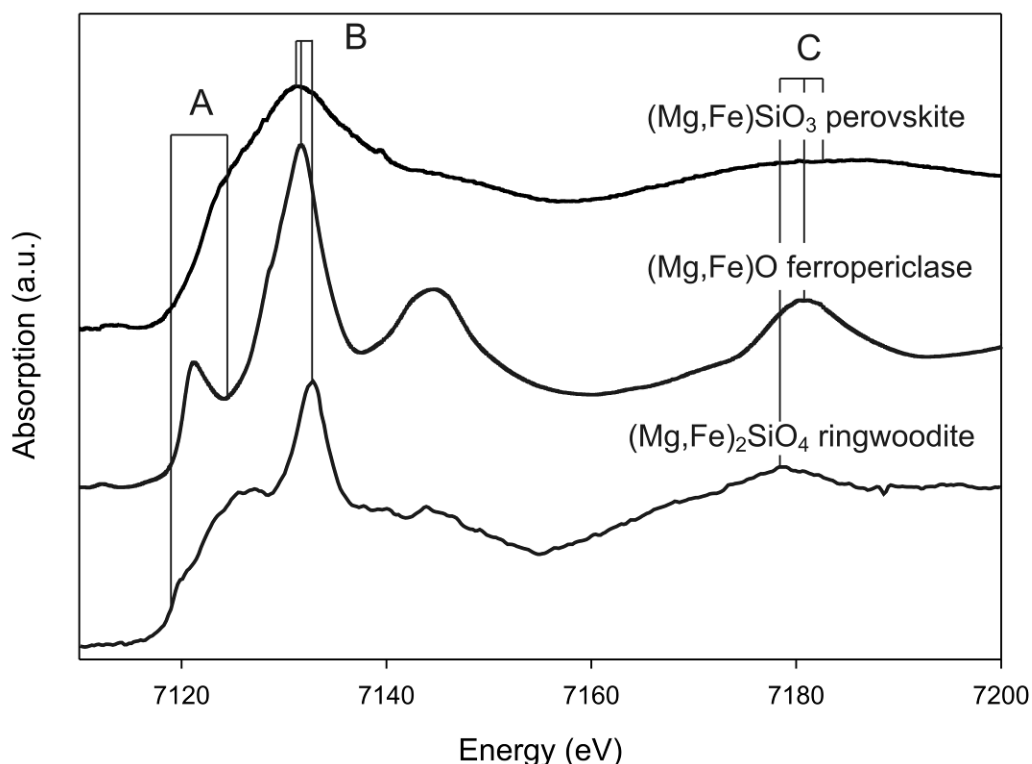
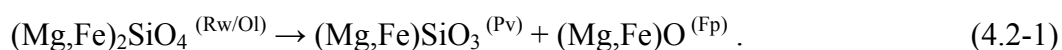


Figure 4.2-1 Fe K-edge XANES spectra collected at 26 GPa and ambient temperature for $(\text{Mg,Fe})\text{SiO}_3$ perovskite, $(\text{Mg,Fe})\text{O}$ ferropericlasite and $(\text{Mg,Fe})_2\text{SiO}_4$ ringwoodite. Characteristic features are highlighted.

The assemblages of $(\text{Mg,Fe})\text{SiO}_3$ perovskite (Pv) and $(\text{Mg,Fe})\text{O}$ ferropericlasite (Fp) for the partitioning experiments were obtained in a LH-DAC via the following breakdown reactions of $(\text{Mg}_{0.88}\text{Fe}_{0.12})_2\text{SiO}_4$ ringwoodite (Rw) or a natural $(\text{Mg}_{0.88}\text{Fe}_{0.12})_2\text{SiO}_4$ San-Carlos olivine (Ol), induced by laser heating over 1800 K at pressures above 26 GPa:



4. Scope of the thesis

Full transformation of Rw (or Ol) to Pv and Fp within the laser heated area was verified by synchrotron XRD (with the beam size $10\ \mu\text{m}\times 10\ \mu\text{m}$) as well as by the 2D micro-XANES map (with $5\ \mu\text{m}$ step) collected before and after laser heating. As an example, pre-normalized 2D micro-XANES absorbance and edge-jump maps along with the photo image of the laser heated ringwoodite are presented in Fig. 4.2-2.

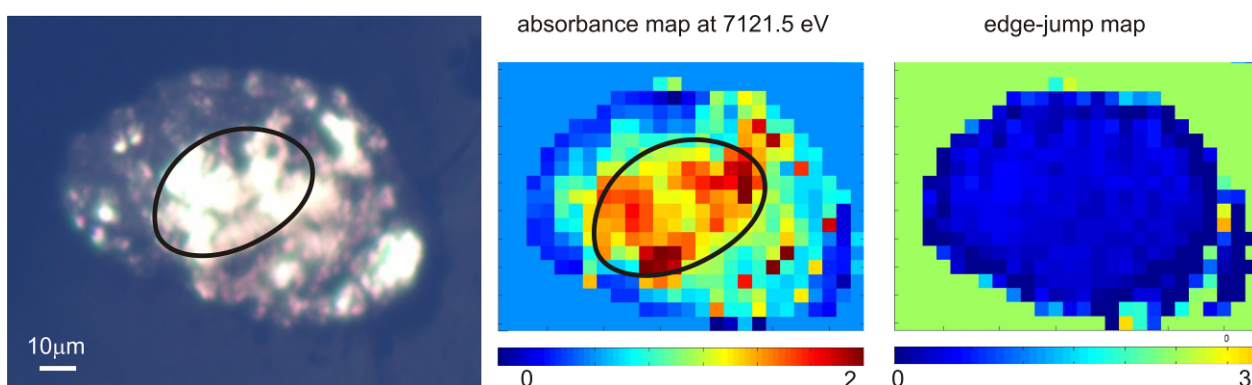


Figure 4.2-2 Photo image of $(\text{Mg}_{0.88}\text{Fe}_{0.12})_2\text{SiO}_4$ ringwoodite, laser heated in the central part to 2300 K at 40 GPa (left) and its pre-normalised absorbance and edge-jump maps collected after laser heating at 40 GPa (right). The laser heated spot is marked by the black line.

The pre-normalized absorbance map (Fig. 4.2-2) plotted at $7121.5\ \text{eV}$ (position of the characteristic peak of $(\text{Mg,Fe})\text{O}$ XANES spectrum at 40 GPa; see feature A in Fig. 4.2-1) clearly shows the contrast between the laser heated spot (where Rw was fully transformed to the assemblage of Pv and Fp as revealed by XRD) and the rest (non-transformed) area of the sample. Each pixel of the pre-normalized XANES edge-jump map (Fig. 4.2-2, on the right) provides information regarding the average “height” of the Fe absorption edge-jump from a $5\times 5\ \mu\text{m}^2$ area of the sample. According to the Beer-Lambert absorption law, this parameter (edge-jump) for a constant density and thickness of the sample is defined by the iron content. Therefore the homogeneity of the edge-jump map (Fig. 4.2-2, on the right) suggests that laser heating of the sample to 2300 K does not induce significant migration of iron within the precision of the measurements. Thus XANES mapping allows us to control (i) the rate of Rw decomposition to Pv and Fp (whether or not the full transformation occurred), and (ii) the possible iron migration due to the thermal gradient.

In order to optimize the conditions for the *in situ* XANES-XRD study of Fe-Mg partitioning, we performed a series of experiments on the decomposition of Rw and Ol to the assemblage of Pv and Fp, changing the thickness of the starting material (Rw or Ol), the

4. Scope of the thesis

thickness of the diamond anvils, and the P-T conditions of the breakdown reaction (4.2-1) (details can be found in [Sections 5.5-5.7](#)). The result of one of the experiments on the decomposition of $(\text{Mg}_{0.88}\text{Fe}_{0.12})_2\text{SiO}_4$ ringwoodite, described in Section 5.7, is presented in Fig. 4.2-3. Three different areas of the Rw enclosed in the DAC were fully transformed to Pv + Fp assemblages by laser heating at 27(1) GPa to three different temperatures: 1750 (50) K, 1950 (50) K and 2300 (50) K. Upon step-by-step compression to 115 GPa, 2D micro-XANES maps and XRD patterns were collected. From each map the average XANES spectrum from the laser heated area was extracted and then deconvoluted to the Pv and Fp sub-spectra (the detailed procedure is described in [Sections 5.6.-5.7.](#)). Deconvolution coefficients give the percentage amount of iron in Fp and Pv relative to the total iron content, normalized to unity. These values, corrected to the amount of the phases obtained by XRD (performed at the same P-T conditions), enable us to calculate the Fe-Mg partition coefficient between Pv and Fp, K_D :

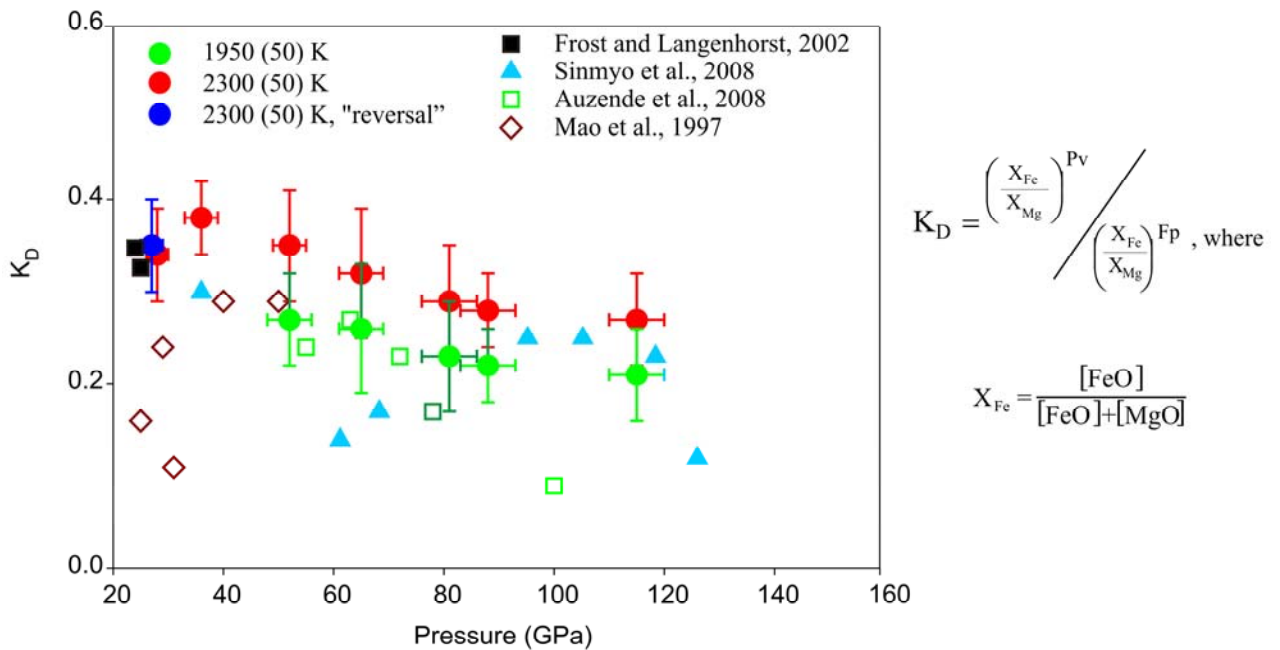


Figure 4.2-3 Mg-Fe partition coefficient between $(\text{Mg,Fe})\text{SiO}_3$ perovskite and $(\text{Mg,Fe})\text{O}$ ferropericlasite as a function of pressure obtained after laser heating of $(\text{Mg}_{0.88}\text{Fe}_{0.12})_2\text{SiO}_4$ ringwoodite to 1950(50) K (closed green circles) and to 2300 (50) K (red closed circles); the value obtained on decompression is also given (blue closed circle). For comparison some of previously published results are also shown.

As seen from Fig. 4.2-3, increasing of temperature enhances iron partitioning into Pv relative to Fp. Upon compression from 37 to 86 GPa the partition coefficient decreases, which is likely caused by the gradual spin-pairing transition occurring in Fp at the corresponding

4. Scope of the thesis

conditions (iron preferably partitions to LS Fp relative to HS or IS Pv; [Badro et al., 2003, 2005](#)). Values of K_D calculated at 115 GPa for both isotherms (1950 K and 2300 K) lie slightly higher than the main trends, which could be a sign of the “saturation” regime due to the complete spin-pairing transition in Fp. However in order to make such a conclusion, more data points above 86 GPa are required.

Although our data on iron partitioning between Pv and Fp coincide with those obtained by Frost and Langenhorst ([2002](#)), there is a substantial discrepancy with other previously reported results. In all studies given in Fig. 4.2-3 for comparison, Ol was used as a starting material, except for Frost and Langenhorst ([2002](#)), where orthopyroxenes was used. We have shown that laser heating of $(\text{Mg}_{0.88}\text{Fe}_{0.12})_2\text{SiO}_4$ San Carlos olivine leads to the precipitation of a significant amount of metallic iron (e.g. about 50% after laser heating to 2300K at 52(1) GPa) along with Pv and Fp (see Section 5.7.4b), while in the case of Rw as a starting material, formation of Fe^0 was not detected (precipitation of metallic iron during the decomposition of Ol in LH-DAC was previously reported elsewhere; [Duba et al., 2007](#); [Auzende et al., 2008](#); [Fialin et al., 2009](#)). Thus, choice of starting material as well as different P-T conditions of the synthesis of the Pv + Fp assemblage can influence the results of Fe-Mg partitioning studies.

To summarize, we have shown that upon compression iron preferably partitions into Fp relative to Pv (which confirmed the previously reported statement that the spin-pairing transition in Fp promotes depletion of Pv in iron; [Badro et al., 2003, 2005](#); [Auzende et al., 2008](#)). The value of K_D decreases only by 0.1 from 37 GPa to 115 GPa at both 1950 (50) and 2300 (50) K, which should not produce any significant effect on the properties of the lower mantle. However, increasing of temperature from 1950 K to 2300 K increases the amount of iron in Pv. Therefore for the proper modelling of lower mantle properties, both the pressure and temperature effect on the Mg-Fe partition coefficient between Pv and Fp must be taken into account.

4.3. Fe-Ni-C system at high pressures and temperatures: LH-DAC vs. LVP

4.3.1. Phase relations in $\text{Fe}_{1-x}\text{Ni}_x$ ($0.10 < x < 0.22$) alloys at pressures to 52 GPa and temperatures to 2600 K

4. Scope of the thesis

The phase diagram of Fe-enriched FeNi alloy at elevated pressures and temperatures remains a subject of debate in geoscience. There have been several theoretical works suggesting that, under pressure and at high enough temperature, a *fcc*- or even a *bcc*- structured phase of iron can become more stable than *hcp* ([Michailyshkin et al., 2007](#); [Belonoschko et al., 2003, 2008](#)). This effect is supposed to be even more pronounced in the case of iron alloyed with a small amount of Ni and/or potential light element(s) (Si, O, H, C, etc) ([Lin et al., 2002b](#); [Vocadlo et al., 2003](#); [Dubrovinsky et al., 2007](#); [Mao et al., 2003](#)). Therefore, not only pressure but also high temperature (on the order of a few thousands of degrees) is considered to be a crucial parameter in experiments addressing the structural phase of the Earth's core. Nowadays LH-DAC techniques are the only tools which can approach core conditions in the static regime. Therefore we undertook an *in situ* XRD study of Fe_{0.90}Ni_{0.1} and Fe_{0.78}Ni_{0.22} alloys, covering the P-T region from ambient conditions to 52 GPa and 2600 K, using a LH-DAC. The details of these experiments are given in Section 5.8.4a. Briefly, upon laser heating at high pressure in both cases (Fe_{0.90}Ni_{0.1} and Fe_{0.78}Ni_{0.22} alloys) we observed formation of the “additional” *fcc*-structured phase (additional to the “main” Fe,Ni phase, which is supposed to be stable at the corresponding conditions in accordance with the equilibrium phase diagram of the Fe-Ni system). This *fcc*-phase appeared to be quenchable to room temperature (Fig. 5.8-1 and Fig. 5.8-3). Although coexistence of Fe-Ni structured polymorphs at certain P-T conditions was previously observed in a LH-DAC experiment ([Lin et al., 2002a](#); [Mao et al., 2003](#)), the stability at room temperature of a *fcc*-structured phase of iron alloy with 10-22 %wt nickel has never been discussed.

In order to understand this phenomenon we undertook a comparative study of the Fe_{1-x}Ni_x (0.10 < x < 0.22) system at pressures to 31 GPa and temperatures to 2600 K using a laser-heated diamond anvil cell (LH-DAC) and multianvil techniques (for details see Section 5.8.4b). In both cases the samples of FeNi alloy were initially compressed to the required pressure (10-31 GPa, depending on the run) and then, after heat treatment during 5-10 min (1700 K - 2600 K, depending on the run), they were quenched to room temperature at high pressure. The recovered samples were analysed by XRD and Mössbauer spectroscopy as well as by scanning and transmission electron microscopies. As an example, Mössbauer spectra and XRD images collected for the quenched products obtained as the result of the paired LVP and LH-DAC runs with Fe_{0.90}Ni_{0.10} are given in Fig. 4.3-1. XRD analyses of FeNi alloys, laser heated in a DAC, detected weak *fcc* reflections along with strong reflections coming from the main *bcc* FeNi phase (Fig. 4.3-1c). Mössbauer spectroscopy also showed the presence of an additional non-magnetic

4. Scope of the thesis

(paramagnetic) Fe-bearing component in the FeNi alloy samples that were laser-heated in a DAC (singlet with central shift around 0 mm s^{-1} in Fig. 4.3-1a). Based on the XRD analyses and taking into account the fact that *fcc* Fe is known to be antiferromagnetic ([Strixrude et al., 1994](#); [Cohen and Mukherjee, 2004](#); [Shallcross et al., 2006](#)), we assigned this additional Mössbauer component to *fcc*-FeNi. The presence of the *fcc* phase was detected in all FeNi alloy samples recovered after laser-heating in the DAC. However the quenched products of multianvil runs, performed with the same samples at the same P-T conditions (covered P-T region is 15 – 20 GPa and 1700 – 2200 K), revealed the presence of only the single initial *bcc*-structured Fe,Ni phase (Figs. 4.3-1b,d).

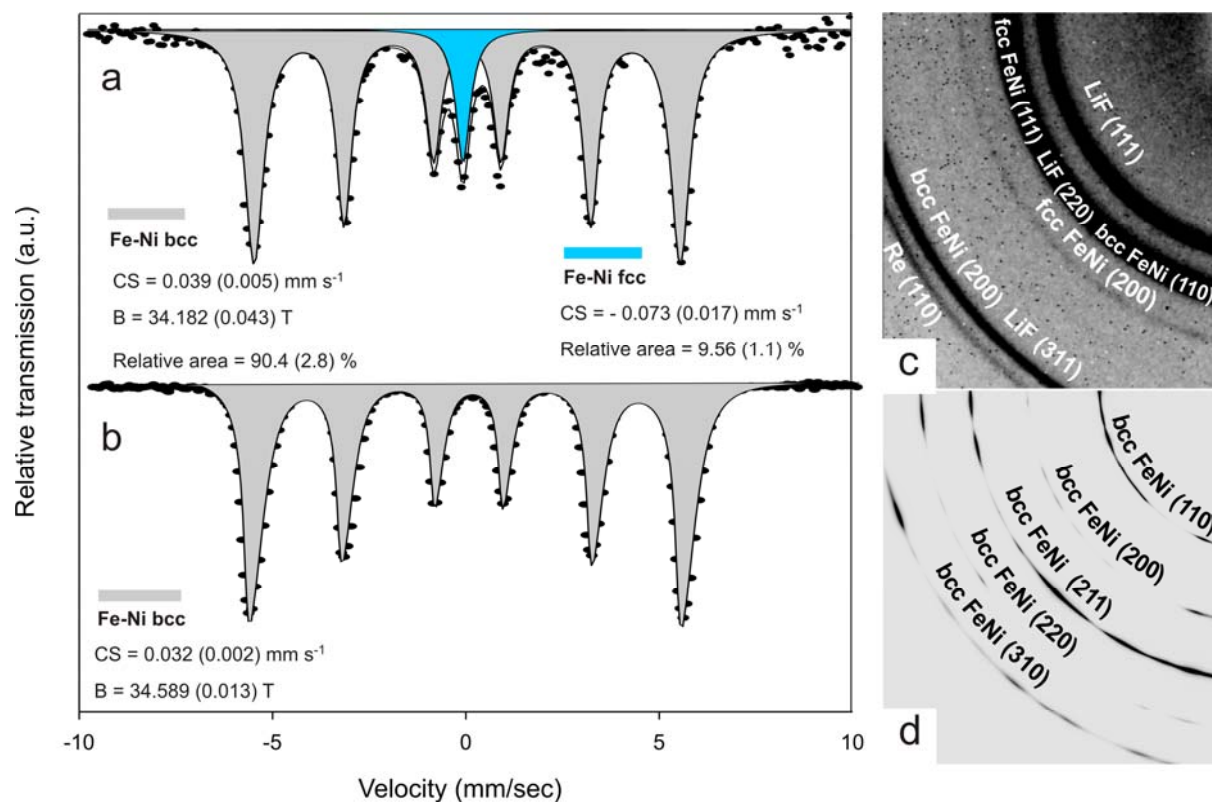


Figure. 4.3-1. Mössbauer spectra and XRD images collected for $\text{Fe}_{0.90}\text{Ni}_{0.10}$ alloy heated to 2000 (50) K at 20 (1) GPa in LH-DAC (top) and in multianvil (bottom).

One possible explanation for the discrepancy between results obtained using the two high pressure techniques is the presence of contaminating material in LH-DAC experiments reacting with the sample. Careful preparation of a DAC experiment enables the elimination of any possible contamination excluding one that cannot be removed by definition –carbon in the form of diamond. Indeed as was previously reported by [Prakapenka et al. \(2003-2004\)](#) and [Rouquette et al. \(2008\)](#), carbon from diamond anvils can react with the sample material during laser heating.

4. Scope of the thesis

We checked this hypothesis by simulating conditions of a DAC experiment in the multianvil press by adding diamond powder into the pressure chamber. Analyses of the recovered samples, heated in multianvil press at 20 GPa to 2100-2200 K in the presence of 1 wt% diamond powder, revealed the formation of the *fcc* phase along with *bcc* Fe₃Ni and Fe₃C carbide (See section 5.8.5a, Fig. 5.8-5), thus confirming our hypothesis regarding carbon contamination in the case of the LH-DAC experiment, which leads to the decomposition of the sample to *bcc* and *fcc* Fe-Ni-C phases, stable at ambient conditions. The reason why we did not observe formation of Fe₃C carbide in the LH-DAC experiments is most probably related to the much smaller amount of dissolved carbon (in comparison with 1 wt% carbon in the case of the DAC-simulating multianvil experiment described above). To summarize, we showed that laser heating in the DAC can induce diffusion of carbon from diamond anvils, which can enter into a reaction with the sample (in our case it was FeNi alloy), and therefore necessarily interfere with the experimental data.

4.3.2. Carbon solubility in Fe-Ni alloys at elevated pressure and temperatures and its effect on the phase relations in this system

In order to explain the stabilization of *fcc* carbon-bearing FeNi alloy to ambient conditions, observed in both LH-DAC and multianvil experiments described above, one needs to address the mechanism of the incorporation of carbon into the structure of Fe₃Ni alloy. It is known that the solubility of carbon in *fcc* iron is significantly larger than that for *bcc* iron (2.0600 wt% at 1400 K vs. 0.0022 wt% at 1000 K, according to the Fe-C phase diagram at ambient pressure). Due to this appreciable difference the *fcc-bcc* phase transition of carbon-bearing Fe-Ni alloy is accompanied by the precipitation of Fe₃C carbide. In the ideal case upon gradual equilibrated cooling of Fe-Ni-C alloy through the *fcc-bcc* phase boundary, a solid solution of *bcc*-FeNi and Fe₃C carbide should form. However, rapid cooling of the *fcc*-Fe-Ni-C system leads to a diffusionless transformation to the body centered tetragonal (*bct*) Fe-Ni-C phase, known in metallurgy as martensite ([Martens, 1878a,b,c; 1880](#)). As was shown experimentally due to its non-equilibrium nature, this transition is usually not complete at room temperature ([Stevens and Haynes, 1956](#); [Gulyaev, 1977](#); [Troiano and Greninger, 1946](#); [Shackelford, 2001](#)), which results in the retaining of a certain amount of the parent *fcc*-Fe-Ni-C in the matrix of the *bct* martensite phase (for the details see Section 5.8.5b). We suggest that the *fcc* phase, which we observed in LH-DAC and multianvil experiments described above, is a consequence of the martensitic

4. Scope of the thesis

transformation induced by rapid cooling of Fe-Ni-C alloy from high temperatures, corresponding to the *fcc*-stability field, down to room temperature.

In order to estimate the solubility of carbon in the Fe-Ni system at high pressures and temperatures, we performed a series of quenched LVP runs with $\text{Fe}_{0.90}\text{Ni}_{(0.10-x)}\text{C}_x$ ($0.01 < x < 0.05$, corresponding to $0.02 < x < 0.11$ wt.% carbon) at pressures of 0.5-20 GPa and temperatures of 2050-2300 K, using multianvil and piston-cylinder presses. The quenched products were analysed by XRD, Mossbauer spectroscopy, and scanning and transmission electron microscopies. Details can be found in Section 5.8.5c. Briefly, we confirmed the previously reported decrease of the carbon solubility in the Fe-Ni system upon compression ([Wood, 1993](#); [Huang et al., 2005](#); [Lord et al., 2009](#)). While at pressures to 9.0(5) GPa and 2300 (20) K *fcc*-FeNi alloy can still incorporate as much as 0.9(2) wt% carbon, at 20 GPa and 2300 K this value drops to 0.7(2) wt%.

5. Results

5.1. Stable intermediate-spin ferrous iron in lower-mantle perovskite

McCammon C.A.¹, Kantor I^{1,3}, Narygina O.¹, Rouquette J.^{1,4}, Ponkratz U.², Sergueev I.², Mezouar M.², Prakapenka V.³, and Dubrovinsky L¹

¹*Bayerisches Geoinstitut, Universität Bayreuth, D-95440 Bayreuth, Germany;* ²*European Synchrotron Radiation Facility, BP 220, F-38043 Grenoble Cedex, France;* ³*Center for Advanced Radiation Sources, University of Chicago, Chicago, Illinois 60637, USA;* ⁴*PMOF, University Montpellier II, Place Eugene Bataillon, cc1504, 34095 Montpellier cedex 5, France (J.R.)*

Nature Geoscience (2008) 1, 684-687

5.1.1. Abstract

The lower mantle is dominated by a magnesium- and iron-bearing mineral with the perovskite structure. Iron has the ability to adopt different electronic configurations, and transitions in its spin state in the lower mantle can significantly influence mantle properties and dynamics. However, previous studies aimed at understanding these transitions have provided conflicting results ([Badro et al., 2004](#); [Jackson et al., 2005](#); [Li et al., 2004, 2006](#)). Here we report the results of high-pressure (up to 110 GPa) and high-temperature (up to 1000 K) experiments aimed at understanding spin transitions of iron in perovskite at lower-mantle conditions. Our Mössbauer and nuclear forward scattering data for two lower-mantle perovskite compositions demonstrate that the transition of ferrous iron from the high-spin to the intermediate-spin state occurs at approximately 30 GPa, and that high temperatures favour the stability of the intermediate-spin state. We therefore infer that ferrous iron adopts the intermediate-spin state throughout the bulk of the lower mantle. Our X-ray data show significant anisotropic compression of lower-mantle perovskite containing intermediate-spin ferrous iron, which correlates strongly with the spin transition. We predict spin-state heterogeneities in the uppermost part of the lower mantle associated with sinking slabs and regions of upwelling. These may affect local properties, including thermal and electrical conductivity, deformation (viscosity) and chemical behaviour, and thereby affect mantle dynamics.

5. Results: iron in silicate perovskite

5.1.2. Introduction

Spin-pairing transitions of iron were predicted to occur within the Earth's interior nearly 50 years ago ([Fyfe, 1960](#)), but only in the past few years has direct experimental evidence for such transitions at lower-mantle conditions been reported. The transition of Fe^{2+} in $(\text{Mg,Fe})\text{O}$ from the high-spin (HS) state (four unpaired d electrons) to the low-spin (LS) state (no unpaired d electrons) is now well established by both experimental and computational data to occur near 50 GPa at room temperature for lower-mantle compositions (recently reviewed [Lin et al., 2007a](#)). However, in the Earth's most abundant phase, $(\text{Mg,Fe})(\text{Si,Al})\text{O}_3$ perovskite, the picture is not so clear. X-ray emission (XES) and nuclear forward scattering (NFS) data present conflicting results on the location, number and sharpness of the transition(s), and on whether Fe^{2+} or Fe^{3+} or both are involved ([Badro et al., 2004](#); [Jackson et al., 2005](#); [Li et al., 2004, 2006](#)). As these parameters influence physical and chemical properties of the mantle, we undertook the first high-pressure high-temperature study of iron-containing silicate perovskite to reconcile these previous conflicting observations using combined Mössbauer and NFS techniques to determine the spin state of iron in the dominant lower-mantle phase.

5.1.3. Experimental details

The present study used two orthopyroxene starting materials with compositions $\text{Mg}_{0.88}\text{Fe}_{0.12}\text{SiO}_3$ and $\text{Mg}_{0.86}\text{Fe}_{0.14}\text{Si}_{0.98}\text{Al}_{0.02}\text{O}_3$ (each 61% enriched in ^{57}Fe) that were synthesised in a pervious study ([Lauterbach et al., 2000](#)). Two methods were used to synthesise silicate perovskite: (1) in a Re capsule using a multianvil press at 25 GPa and 1650 °C; (2) in a laser-heated diamond anvil cell at 30-35 GPa and approximately 2500°C. Run products from both methods were found using X-ray diffraction to consist almost exclusively of $(\text{Mg,Fe})\text{SiO}_3$ or $(\text{Mg,Fe})(\text{Si,Al})\text{O}_3$ perovskite (in a few samples traces of SiO_2 stishovite were detected), and chemical compositions were found using the electron microprobe to be the same as the starting material within experimental uncertainty. Silicate perovksite samples were loaded into Re gaskets preindented to about 30 μm thickness and drilled with a 125 μm diameter hole. Pressure was applied using a three- or four-pin modified Merrill-Bassett diamond anvil cell (DAC) with 300 or 250 μm diameter culet gem-quality diamonds, and temperature was applied using an external

5. Results: iron in silicate perovskite

resistive heater mounted around the DAC ([Dubrovinskaia and Dubrovinsky, 2003](#)). Pressure was measured based on the fluorescence of small ruby chips loaded together with the sample, and temperature was measured using a S-type thermocouple mounted next to the diamonds. To relieve stresses, after nearly all increases or decreases of pressure at room temperature above 30 GPa, samples were annealed at 1700-2000°C using an infrared laser at low power, which is within the stability field of the silicate perovskite. In several loadings the silicate perovskite sample was sandwiched between layers of silica of a few microns thickness.

The ^{57}Fe Mössbauer spectra were collected using a constant-acceleration Mössbauer spectrometer at Bayerisches Geoinstitut equipped with a high specific-activity ^{57}Co point source (500 μm in diameter). The velocity scale was calibrated relative to $\alpha\text{-Fe}$ foil, and spectra were collected over 1–2 days each. The dimensionless effective thicknesses were approximately 6 and 7 for the $\text{Mg}_{0.88}\text{Fe}_{0.12}\text{SiO}_3$ and $\text{Mg}_{0.86}\text{Fe}_{0.14}\text{Si}_{0.98}\text{Al}_{0.02}\text{O}_3$ perovskite samples, respectively, which correspond to 15 and 17 mg unenriched Fe cm^{-2} . NFS data were collected at room temperature on beamline ID18 at the European Synchrotron Radiation Facility (ESRF) during operation in four-bunch mode, with the beam focused to about $4\ \mu\text{m}\times 20\ \mu\text{m}$ using a Kirkpatrick–Baez mirror. High-temperature NFS data were collected on ID18 at ESRF during operation in 16-bunch mode with a beam size of about $20\ \mu\text{m}\times 150\ \mu\text{m}$. Further details of the beamline are given in the literature ([Ruffer and Chumakov, 1996](#)). Pressure was measured *in situ* for all NFS experiments using ruby fluorescence (corrected for temperature where needed), and *in situ* X-ray diffraction patterns for phase identification were collected using either an image plate (four-bunch mode) or an online CCD camera (16-bunch mode). Data collection times were 1–2 h for each NFS spectrum. High-resolution X-ray powder diffraction data were collected at room temperature on beamline ID27 at ESRF during operation in four-bunch mode (MAR CCD detector, wavelength of X-ray radiation $0.3738\ \text{Å}$, beam size $5\ \mu\text{m}\times 7\ \mu\text{m}$). X-ray data of the same sample were collected in the DAC at the same pressure using beamline ID18 either immediately before or following the NFS data collection. Additional high-resolution X-ray powder diffraction data of some of the same DAC sample loadings were collected on beamline 13-ID-D at the Advanced Photon Source (Argonne National Laboratory) (MAR CCD detector, wavelength of X-ray radiation $0.3344\ \text{Å}$, beam size $7\ \mu\text{m}\times 7\ \mu\text{m}$).

Eleven different sample loadings of $\text{Mg}_{0.88}\text{Fe}_{0.12}\text{SiO}_3$ perovskite were made. Each sample loading was subjected to a series of compressions/decompressions, including heating in some cases, and Mössbauer data were collected up to a maximum pressure of 89 GPa and a maximum

5. Results: iron in silicate perovskite

temperature of 800 K. During two of the run series the loaded DAC was taken to ESRF for NFS measurements, and Mössbauer spectra were collected both before and after the NFS experiments. Fifteen NFS spectra were collected during 4-bunch mode operation, and seventeen were collected during 16-bunch mode operation, with a maximum pressure and temperature of 110 GPa and 1000 K. Five different sample loadings of $\text{Mg}_{0.86}\text{Fe}_{0.14}\text{Si}_{0.98}\text{Al}_{0.02}\text{O}_3$ perovskite were also made, with compression/decompression and heating as with the Al-free sample, up to a maximum pressure and temperature of 55 GPa and 700 K. The relative concentration of Fe^{3+} was measured before and after each compression/decompression run, and while the Fe^{3+} concentration varied up a few percent between different synthesis runs, it was found to remain constant for a given sample loading.

Mössbauer spectra were fitted to Lorentzian lineshapes in the thin-absorber approximation using conventional constraints (equal quadrupole component widths and areas). We also tried fits incorporating Voigt line shapes, but found no statistical improvement in the fit to justify the additional parameters as measured with an F-test. We found that the data of all compositions were best described by a three doublet model, consisting of two Fe^{2+} -like doublets and one Fe^{3+} -like doublet. In some cases additional doublets were added to account for broadening of the high-spin Fe^{2+} doublet, but since these were considered to arise from iron in the same site and electronic state, only weighted averages of their hyperfine parameters were used. To explore the influence of thickness effects, we additionally used a full transmission integral fit in fitting some of the Mössbauer data, but found that hyperfine parameters and relative areas were unchanged within experimental uncertainty. A minor component appeared in some of the Mössbauer spectra whose presence was coupled to intermediate-spin Fe^{2+} . However it could not be fitted to a separate component since its hyperfine parameters overlap those of Fe^{3+} . Higher temperatures increased the intensity of this component, particularly in the $(\text{Mg,Fe})(\text{Si,Al})\text{O}_3$ sample; hence we infer that it might arise from Fe^{2+} - Fe^{3+} electron delocalization ([Fei et al., 1994](#)). The intensity of the minor component varied between different synthesis runs, which may be due to factors such as differences in short-range ordering. To enable a meaningful comparison of relative areas between different Mössbauer runs, the Fe^{3+} absorption (assumed to remain constant for a given sample synthesis run) was subtracted from the relative area of the minor component to obtain the relative area of the inferred electron delocalisation absorption. The total spin number was then calculated according to Table 5.1-1. Since the intensity of the inferred electron

5. Results: iron in silicate perovskite

delocalisation absorption is relatively low (less than 15% of the spectrum on average), its interpretation does not affect the conclusions of this study.

NFS spectra were fitted using the kinematical approximation ([Smirnov, 1999](#)), since even at the highest pressures (largest recoil-free fraction) in 4-bunch mode (largest time window), there is no observation of dynamical beats. The 4-bunch mode data could be fitted with a stable model to two quadrupole doublets with parameters that did not vary depending on their initial starting values. For the 16-bunch mode data the fitting was more complicated due to the short time window and overlap of data from different bunches. The most stable model was found to be one with three singlets, which could be interpreted as two overlapping quadrupole doublets. The only stable parameters of the fit are the splitting of the large doublet, the shift of the central line (i.e., the splitting of the small doublet), and the line broadening of all three lines. The relative areas could not meaningfully be extracted from the data due to complications including overlap of bunches in 16-bunch mode. X-ray patterns were analysed by Rietveld refinement using the GSAS package ([Larson and Dreele, 1985](#)).

5.1.4. Results and discussion

We collected 77 ^{57}Fe Mössbauer and 32 NFS spectra of $\text{Mg}_{0.88}\text{Fe}_{0.12}\text{SiO}_3$ perovskite ($\text{Fe}^{3+}/\sum\text{Fe} \sim 15\%$) and 42 Mössbauer spectra of $\text{Mg}_{0.86}\text{Fe}_{0.14}\text{Si}_{0.98}\text{Al}_{0.02}\text{O}_3$ perovskite ($\text{Fe}^{3+}/\sum\text{Fe} \sim 30\%$) using a resistively heated diamond anvil cell at pressures up to 110 GPa and temperatures up to 1000 K, combined with high-resolution X-ray diffraction of many of the same sample loadings. Our low-pressure Mössbauer spectra are similar to those in the literature, and show one broad quadrupole doublet assigned to HS Fe^{2+} in the 8–12-coordinated site, and one quadrupole doublet assigned to HS Fe^{3+} ([Fei et al., 1994](#); [Lauterbach et al., 2000](#)). A new quadrupole doublet appears above ~ 30 GPa that has narrow linewidth, high centre shift ($\sim 1.1 \text{ mm s}^{-1}$ relative to $\alpha\text{-Fe}$) and extremely high quadrupole splitting (QS) ($\sim 4 \text{ mm s}^{-1}$) in both $\text{Mg}_{0.88}\text{Fe}_{0.12}\text{SiO}_3$ perovskite (Fig. 5.1-1a) and $\text{Mg}_{0.86}\text{Fe}_{0.14}\text{Si}_{0.98}\text{Al}_{0.02}\text{O}_3$ perovskite (see Section 5.1.6, Fig. 5.1-4) spectra (hyperfine parameters are plotted in Section 5.1.6, Fig. 5.1-5). The relative area of the high-QS doublet increases with pressure at the expense of the low-QS doublet, indicating that the transition involves Fe^{2+} in the 8–12-coordinated site, and dominates the spectra at the highest pressures reached. Increasing temperature also increases the relative area of the high-QS doublet (Fig. 1a and Fig. 5.1-4 in Section 5.1.6). The presence of the high-QS

5. Results: iron in silicate perovskite

component is also seen in NFS spectra, as recognized by the high quantum beat frequency which is proportional to QS (Fig. 5.1-1b) (hyperfine parameters of NFS spectra are plotted in Fig. 5.1-5 in Section 5.1.6). Elevated-temperature NFS data confirm that the high-QS component is stable at high temperature (Fig. 5.1-1b).

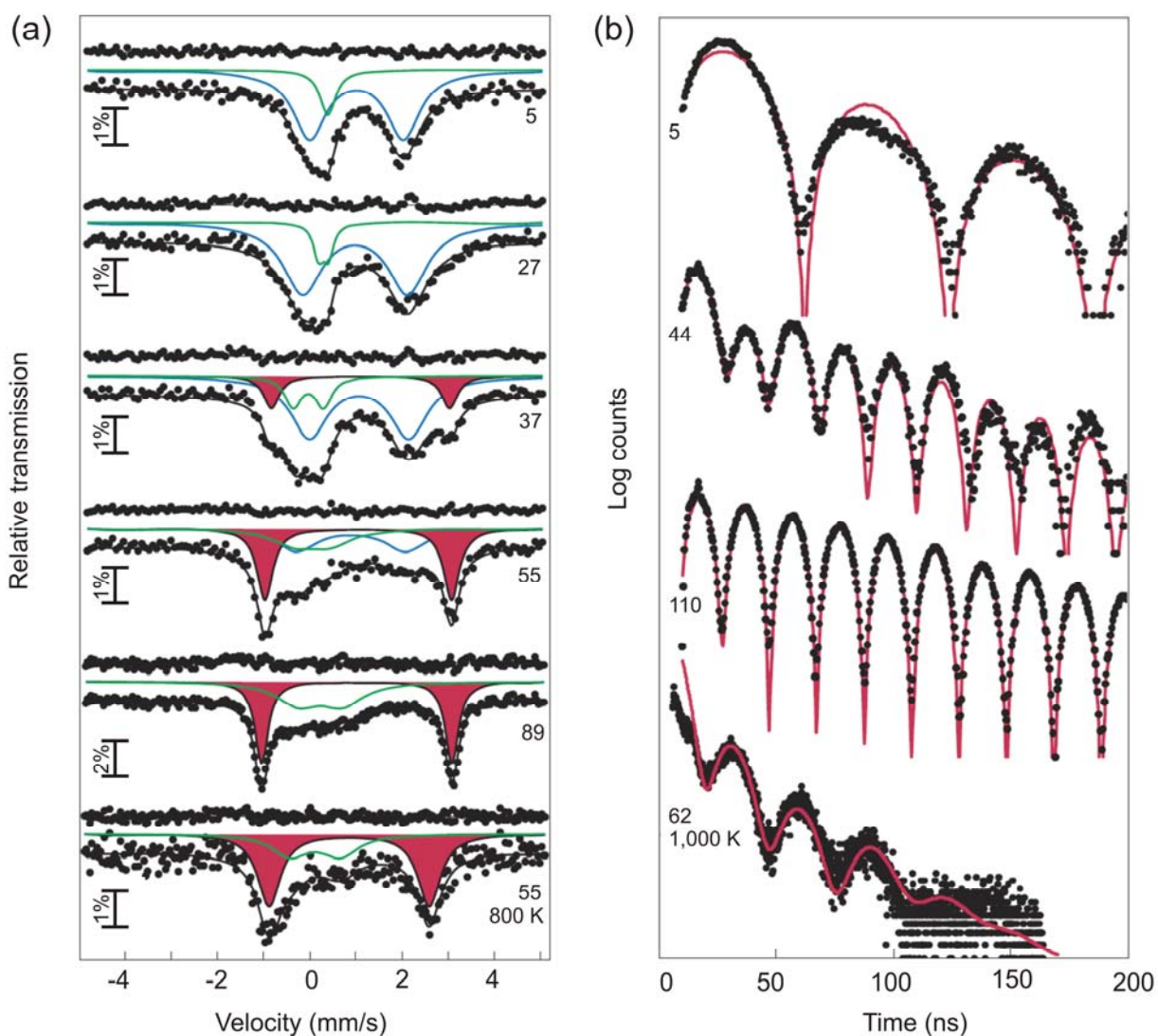


Figure 5.1-1 High-pressure ^{57}Fe spectra of $\text{Mg}_{0.88}\text{Fe}_{0.12}\text{SiO}_3$ perovskite. **(a)**, Mössbauer spectra collected at room temperature (top five spectra) and high temperature (bottom spectrum). Pressures are given in GPa and quadrupole doublets are colored as follows: HS Fe^{2+} , blue; high-QS Fe^{2+} , red; minor component including Fe^{3+} , green. **(b)**, NFS spectra collected at room temperature (top three spectra) and high temperature (bottom spectrum). Pressures are given in GPa.

Detailed comparison of our hyperfine parameters with previous NFS data is equivocal owing to the non-uniqueness of NFS spectra arising from multiple interactions ([Smirnov, 1999](#))

5. Results: iron in silicate perovskite

compounded by the short time separation of X-ray bunches in the previous data (153 ns). Also, the lack of laser heating to relieve stress between compression steps of previous NFS experiments causes line broadening and contributes further uncertainty. Nevertheless, one parameter that can be robustly extracted from NFS data is the QS of the dominant component, because it is largely determined by the frequency of quantum beats. We note that all previous NFS data for (Mg,Fe)SiO₃ and (Mg,Fe)(Si,Al)O₃ perovskite report the increasing abundance of a high-QS component ($\sim 3.5 \text{ mm s}^{-1}$) with increasing pressure ([Jackson et al., 2005](#); [Li et al., 2006](#)), in agreement with our results.

Our Mössbauer and NFS data show a transition involving Fe²⁺ above ~ 30 GPa, which corresponds to the drop in spin number reported previously in XES studies ([Badro et al., 2004](#); [Li et al., 2004](#)). Our high-resolution X-ray data show no evidence for a major structural transition (see Section 5.1.6, Fig. 5.1-6), which is consistent with the high-QS component arising from an electronic transition.

Explanations suggested by previous authors include a transition of HS Fe²⁺ to either intermediate-spin (IS) (two unpaired *d* electrons) or LS Fe²⁺, possibly accompanied by an HS-to-LS transition of Fe³⁺ ([Badro et al., 2004](#); [Jackson et al., 2005](#); [Li et al., 2004, 2006](#)), but as XES data cannot distinguish different contributions to the spin number the nature of the transition has remained unresolved. Mössbauer data can distinguish individual contributions, hence we can test these different possibilities directly by calculating the total spin state of iron, S_T , using the following relation:

$$S_T = \sum S_n \times A_n, \quad (5.1-1)$$

where S_n is the spin number assigned to the n th doublet with relative area A_n , and the sum is over all n doublets. We tested six different models with spin numbers assigned as indicated in Table 5.1-1. The comparison of our data with previous XES data provides a clear resolution of the spin state of Fe²⁺ in silicate perovskite at high pressure (Fig. 5.1-2), where we emphasize that the data were calculated directly from equation (5.1-1) and that no adjustment of the fit was made. The best agreement for both compositions is provided by model 3. To estimate the degree to which the different Fe³⁺ concentrations in the XES studies compared with our samples affected the results, we recalculated the total spin state for model 3 at minimum (0%) and maximum Fe³⁺/ \sum Fe values (30% and 50% for Al-free and Al-containing perovskites, respectively), assuming the

5. Results: iron in silicate perovskite

abundance ratio of IS to HS Fe^{2+} to remain the same (red error bars in Fig. 5.1-2). The results are similar for other models. The best fit is still provided by model 3, hence we conclude that Fe^{2+} undergoes an HS-to-IS transition above 30 GPa, and that the presence of a spin transition in Fe^{3+} is not strongly indicated by the data up to 100 GPa.

Table 5.1-1 Spin number assigned to each quadrupole doublet for total spin number calculation according to Equation. (5.1-1)

	Fe^{2+} QS < 3 mm s ⁻¹	Fe^{2+} QS < 3.5 mm s ⁻¹ ‘high QS’	Fe^{3+}
Model 1	2	2	5/2
Model 2	2	2	1/2
Model 3	2	1	5/2
Model 4	2	1	1/2
Model 5	2	0	5/2
Model 6	2	0	1/2

The assignment of the high-QS component to IS Fe^{2+} enables us to quantify the effect of temperature on its stability. We calculated the total spin number from the high-temperature Mössbauer data according to equation (1), and found that the spin number decreases with increasing temperature at constant pressure for both $(\text{Mg,Fe})\text{SiO}_3$ and $(\text{Mg,Fe})(\text{Si,Al})\text{O}_3$ perovskite (see Section 5.1.6, Fig. 5.1-7). These results are consistent with complementary high-pressure and temperature XES and NFS data that demonstrate the stability of the Fe^{2+} IS state in silicate perovskite under lowermost-mantle pressure and temperature conditions ([Lin et al., 2009](#)).

5. Results: iron in silicate perovskite

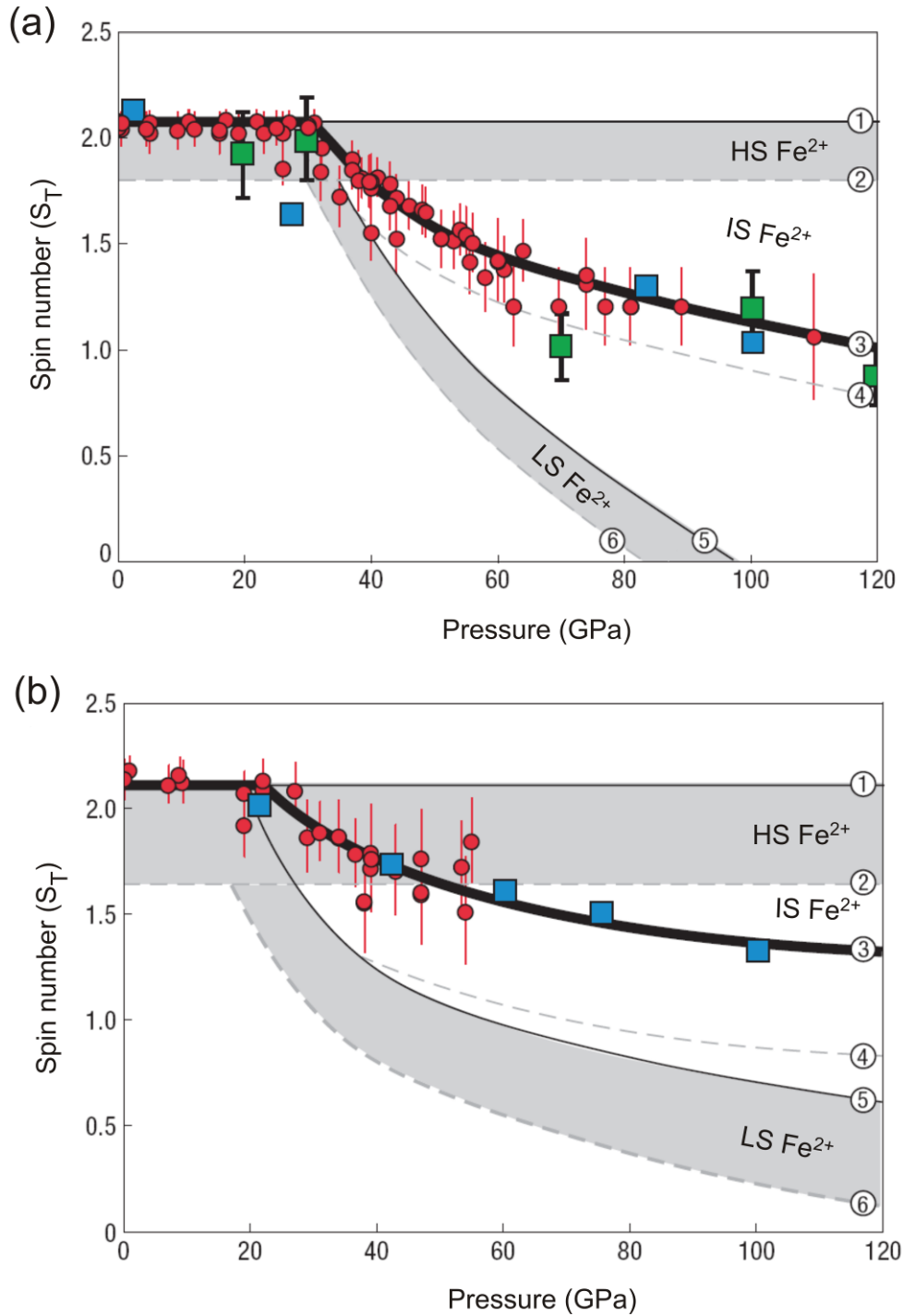


Figure 5.1-2 Total spin number of iron in silicate perovskite. **(a)**, $Mg_{0.88}Fe_{0.12}SiO_3$. **(b)**, $Mg_{0.86}Fe_{0.14}Si_{0.98}Al_{0.02}O_3$. The red circles were derived from room-temperature Mössbauer data on the basis of model 3 (see Table 1), whereas the results of other models are shown as solid lines (models with $HS Fe^{3+}$) or dashed lines (models with $LS Fe^{3+}$). Previous XES data are indicated by green (Badro et al., 2004) and blue (Li et al., 2004) squares. The red error bars indicate the maximum estimated uncertainty in the red data points arising from differences in Fe^{3+} concentration between our samples and those of the previous XES studies.

5. Results: iron in silicate perovskite

Our Mössbauer and NFS data demonstrate that the IS state of Fe^{2+} is stable in the 8–12-coordinated site of silicate perovskite over a wide range of pressures and temperatures. The transition from the HS to the IS state occurs over a large pressure range at low temperature, but over a relatively narrow range at high temperature (see Section 5.1.6, Fig. 5.1-7). This behaviour probably represents a dynamic equilibrium driven by a thermodynamic process similar to the HS–LS states in $(\text{Mg,Fe})\text{O}$ ([Sturhahn et al., 2005](#)). *Ab initio* computations have failed to find that IS Fe^{2+} is stable ([Zhang and Oganov, 2006](#); [Stackhouse et al., 2007](#); [Bengston et al., 2008](#)), and thermodynamic calculations predict that lower-mantle perovskite should contain only HS Fe^{2+} at high temperature ([Hofmeister, 2006](#)). One reason for the discrepancy between theory and experiment may arise from the similar energies and entropies of the different spin states of Fe^{2+} in 8–12 coordination, compared with the large differences for Fe^{2+} in octahedral coordination ([Sturhahn et al., 2005](#)). Our high-resolution X-ray data show that the compression of $\text{Mg}_{0.88}\text{Fe}_{0.12}\text{SiO}_3$ perovskite is strongly anisotropic, with the *b*-axis being 31% less compressible than the *a*-axis (see Section 5.1.7, Fig. 5.1-8), compared with only 20% for the MgSiO_3 perovskite endmember ([Fiquet et al., 2000](#)). Anisotropic compression leads to a large increase in the octahedral tilting angles, whose variation with pressure follows closely the trend of the spin transition (see Section 5.1.6, Fig. 5.1-9). As octahedral tilting also affects the distortion of the 8–12-coordinated site, there may be a cooperative effect that stabilizes the IS state through a Jahn–Teller effect. Such effects, including the influence of temperature, must be taken into account to obtain realistic simulations.

The inferred distribution of Fe^{2+} spin states in lower-mantle silicate perovskite on the basis of current thermal models ([Brown and Shankland, 1981](#); [Billen, 2008](#); [Leng and Zhong, 2008](#)) shows that Fe^{2+} in the bulk lower mantle is predominantly in the IS state (Fig. 5.1-3a). Models to extract lower-mantle thermal structure and bulk chemical composition from seismic profiles depend sensitively on shear moduli and their pressure derivatives ([Mattern et al., 2005](#); [Matas et al., 2007](#)), yet no elastic wave velocities have ever been measured for silicate perovskite containing IS Fe^{2+} . Current mantle-modelling approaches use experimental constraints from the MgSiO_3 endmember, and although it is premature to speculate on the magnitude of the difference in shear modulus behaviour between MgSiO_3 and $(\text{Mg,Fe})(\text{Si,Al})\text{O}_3$ perovskite the inferred coupling between IS-state stability and structure distortion combined with the large observed difference in anisotropic compression between MgSiO_3 and $(\text{Mg,Fe})\text{SiO}_3$ perovskite (see Section 5.1.6, Fig. 5.1-9) suggests that behaviour will be measurably different for the two perovskite

5. Results: iron in silicate perovskite

compositions. Such a difference would affect conclusions regarding lower-mantle compositional homogeneity and observed deviations from an adiabatic geotherm [Matas et al., 2007](#)).

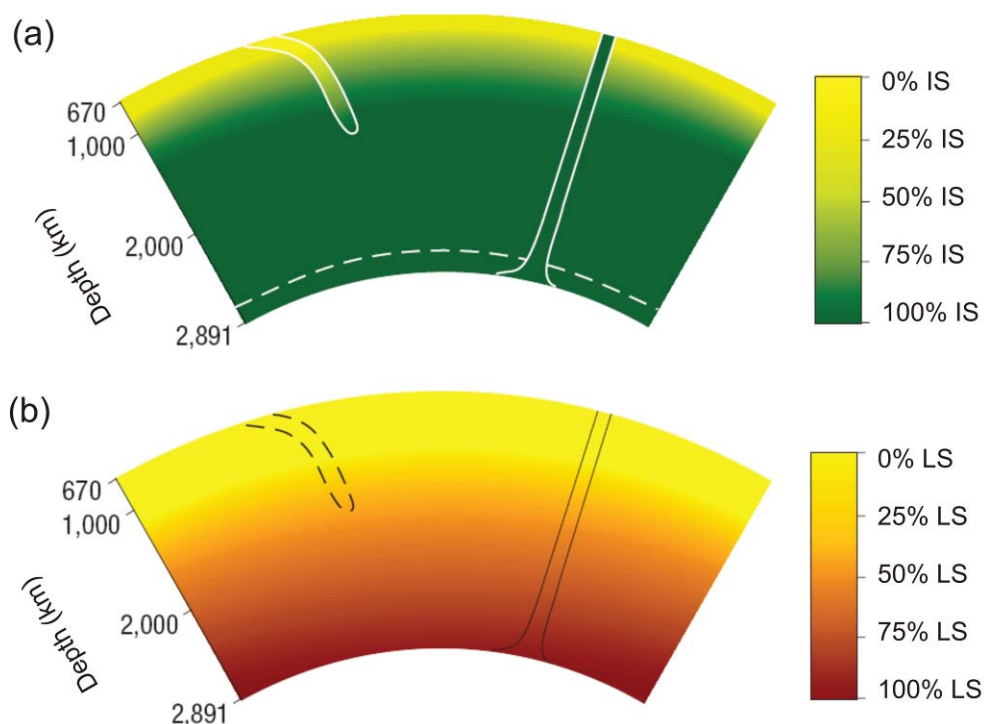


Figure 5.1-3 Estimated Fe^{2+} spin-state distribution in the lower mantle. **(a)** Silicate perovskite variation estimated from our data, previous XES data ([Badro et al., 2004](#); [Li et al., 2004](#)) and current thermal models (Brown and Shankland, 1981; Billen, 2008; Leng and Zhong, 2008). The greatest contrast occurs in the uppermost region, and no spin transition is expected at the base of the mantle in the post-perovskite phase ([Lin et al., 2009](#)). **(b)** (Mg,Fe)O variation on the basis of previous data ([Lin et al., 2007a](#)) shows the greatest contrast in spin state to occur in the middle part of the lower mantle. Slab mineralogy excludes (Mg,Fe)O and the temperature effect is small in the uppermost and lowermost regions of the lower mantle ([Lin et al., 2007b](#)).

The greatest contrast in spin state occurs in the uppermost region of the lower mantle (Fig. 5.1-3a). Temperature seems to have a greater effect on the relative spin population than differences in composition (see Section 5.1.6, Fig. 5.1-7; Fig. 5.1-2). Downgoing slabs in the uppermost lower mantle are predicted to contain more HS Fe^{2+} compared with the surrounding mantle owing to their lower temperatures ([Billen, 2008](#)), whereas areas of mantle upwelling are inferred to contain more IS Fe^{2+} owing to their higher temperatures ([Leng and Zhong, 2008](#)) (Fig. 5.1-3a). Electrical conductivity measurements show a decrease of approximately two orders of magnitude for silicate perovskite in transforming to the IS state ([Ohta et al., 2008](#)), suggesting enhanced electrical conductivity in downgoing slabs compared with the surrounding mantle. Spin

5. Results: iron in silicate perovskite

transitions can affect the radiative contribution to the thermal conductivity ([Badro et al., 2004](#)), and if silicate perovskite follows the behaviour of (Mg,Fe)O as suggested in the literature ([Badro et al., 2005](#)) the thermal conductivity will increase, which implies a decreased Rayleigh number in regions of mantle upwelling. Partitioning of iron between silicate perovskite and (Mg,Fe)O is affected by spin transitions; therefore, the contrast in spin distribution in the uppermost lower mantle, notably in regions of mantle upwelling, could lead to chemical heterogeneity. Plastic deformation of silicate perovskite is strongly influenced by orthorhombic distortions of the unit cell ([Carrez et al., 2007](#)), and as orthorhombic distortions of (Mg,Fe)SiO₃ perovskite are significantly greater than those of the MgSiO₃ endmember parameters such as viscosity may change, hence influencing mantle convection ([Naliboff and Kellogg, 2007](#)).

All of these effects due to the spin transition in silicate perovskite are focused in the uppermost region of the lower mantle, whereas effects due to the spin transition in (Mg,Fe)O are concentrated in the middle part of the lower mantle (Fig. 5.1-3b) ([Lin et al., 2007a](#)). Our study provides an improved map of iron spin state in lower-mantle phases, highlighting those parameters most critical to mantle models that deserve highest priority for measurement (such as elastic wave velocities of silicate perovskite at lower-mantle pressures and temperatures), and should stimulate more detailed *ab initio* calculations that can succeed in reproducing experimental results in order to provide a more realistic parameter database for modelling of lower-mantle properties and dynamics.

5.1.5 Acknowledgements

We acknowledge the European Synchrotron Radiation Facility for provision of synchrotron radiation facilities (ID18 and ID27) and we would like to thank A. Chumakov and R. Rüffer for assistance in using beamline ID18 and V. Dmitriev for additional technical assistance. Use of the Advanced Photon Source (beamline 13-ID-D) was supported by the U.S. Department of Energy, Office of Science, Office of Basic Energy Sciences, under Contract No. DE-AC02-06CH11357. We are grateful to S. Übelhack and S. Linhardt for technical assistance at Bayerisches Geoinstitut. The project was partly supported by funds from the German Science Foundation (DFG) Priority Programme SPP1236 under project Mc 3/16-1.

5. Results: iron in silicate perovskite

5.1.6. Supplementary figures

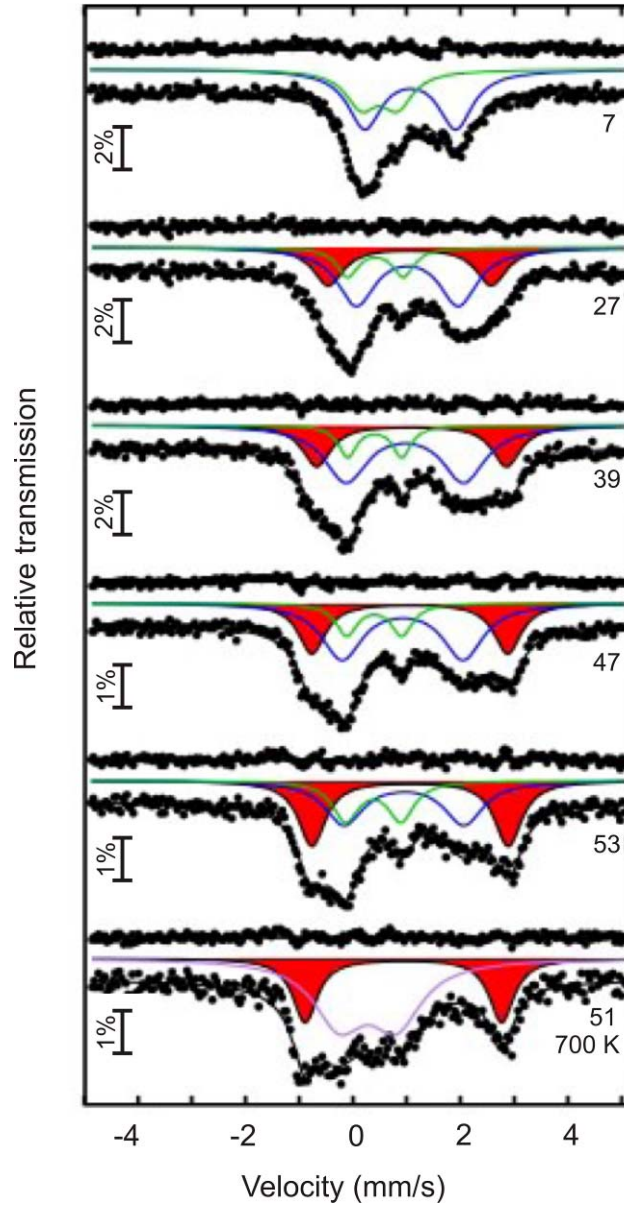


Figure 5.1-4 High-pressure ^{57}Fe Mössbauer spectra of $\text{Mg}_{0.86}\text{Fe}_{0.14}\text{Si}_{0.98}\text{Al}_{0.02}\text{O}_3$ perovskite. Pressures are given in GPa, and were collected at room temperature (top five spectra) and high temperature (bottom spectrum). Doublets are coloured as follows: HS Fe^{2+} (blue); high QS Fe^{2+} (red); minor component including Fe^{3+} (green); temperature-induced Fe^{2+} - Fe^{3+} electron delocalisation (violet).

5. Results: iron in silicate perovskite

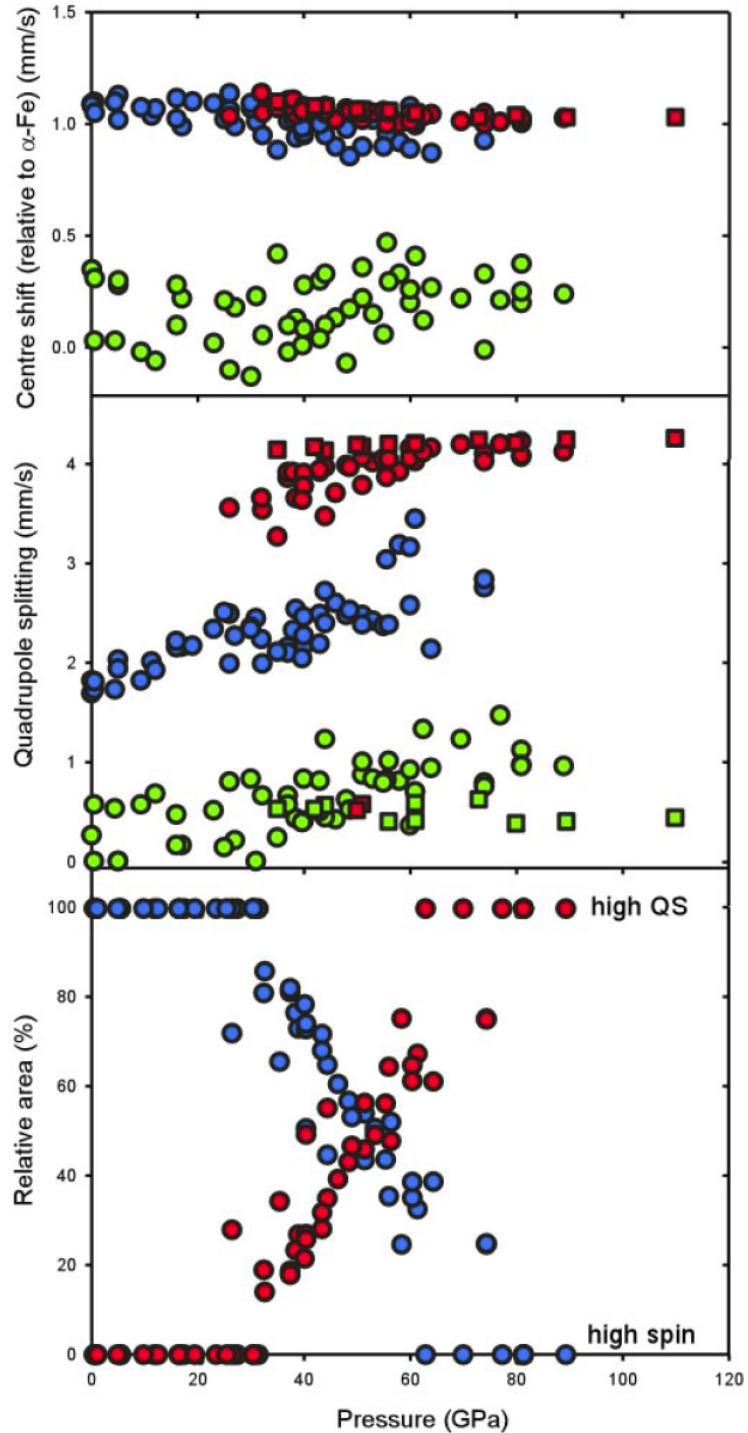


Figure 5.1-5 Effect of pressure on the hyperfine parameters of $\text{Mg}_{0.88}\text{Fe}_{0.12}\text{SiO}_3$ perovskite derived from room temperature Mössbauer (circles) and NFS (squares) spectra. Assignments are as follows: high-spin Fe^{2+} (blue); high QS Fe^{2+} component (red); minor component including Fe^{3+} (green). The centre shift of the high QS Fe^{2+} component was determined relative to an assumed centre shift of the minor component of 0 mm/s, and for clarity the relative areas were renormalised after subtraction of the minor component.

5. Results: iron in silicate perovskite

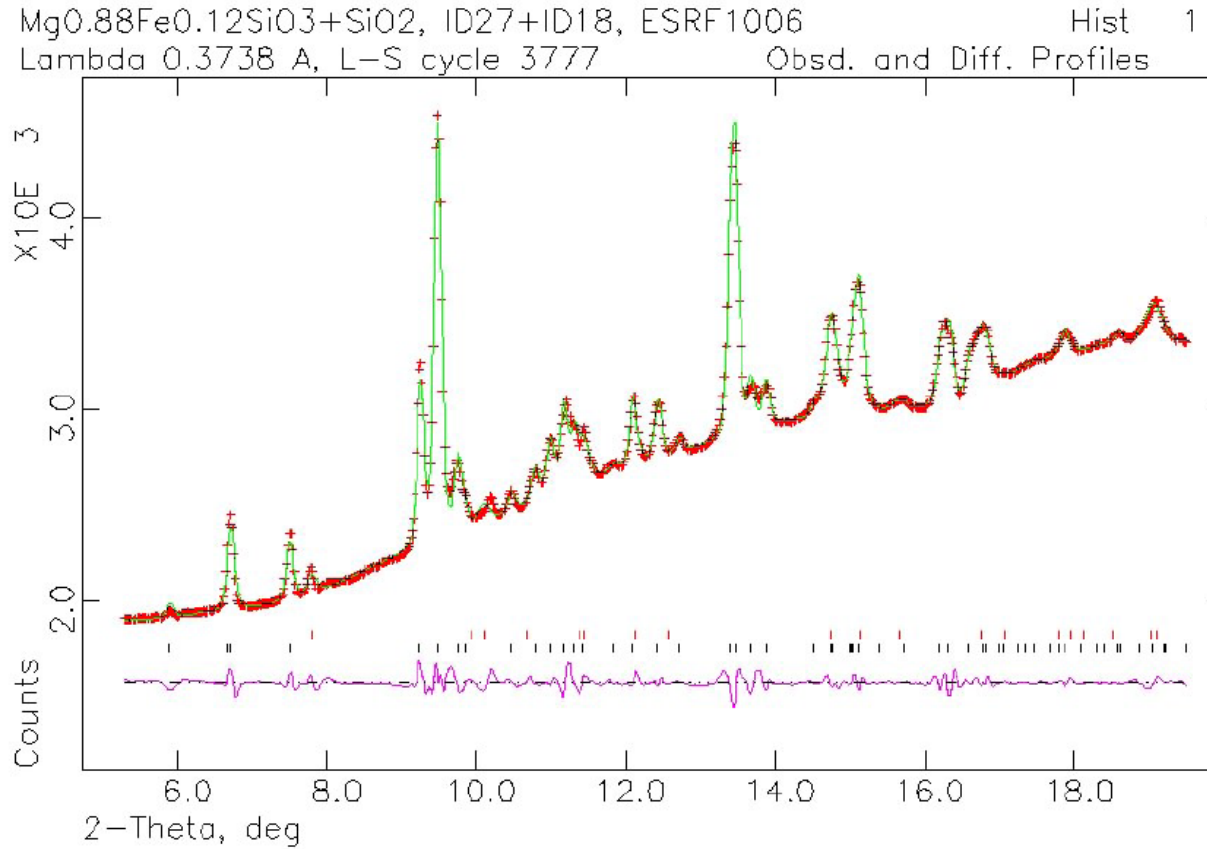


Figure 5.1-6 Room temperature X-ray diffraction pattern of Mg_{0.88}Fe_{0.12}SiO₃ perovskite at 110 GPa after laser heating at 2000 K collected on beamline ID27 (ESRF) for the same sample as shown in Fig. 5.1-1a. Rietveld refinement shows that all reflections are accounted for by orthorhombic perovskite (*Pbnm*, $a = 4.3964(5)$ Å, $b = 4.6301(4)$ Å, $c = 6.4047(4)$ Å, $X_{Me}=0.986$, $Y_{Me}=0.066$, $X_{O1}=0.088$, $Y_{O1}=0.4777$, $X_{O2}=0.691$, $Y_{O2}=0.301$, $Z_{O2}=0.064$) and CaCl₂-type SiO₂ (used as a thermal insulator for laser heating).

5. Results: iron in silicate perovskite

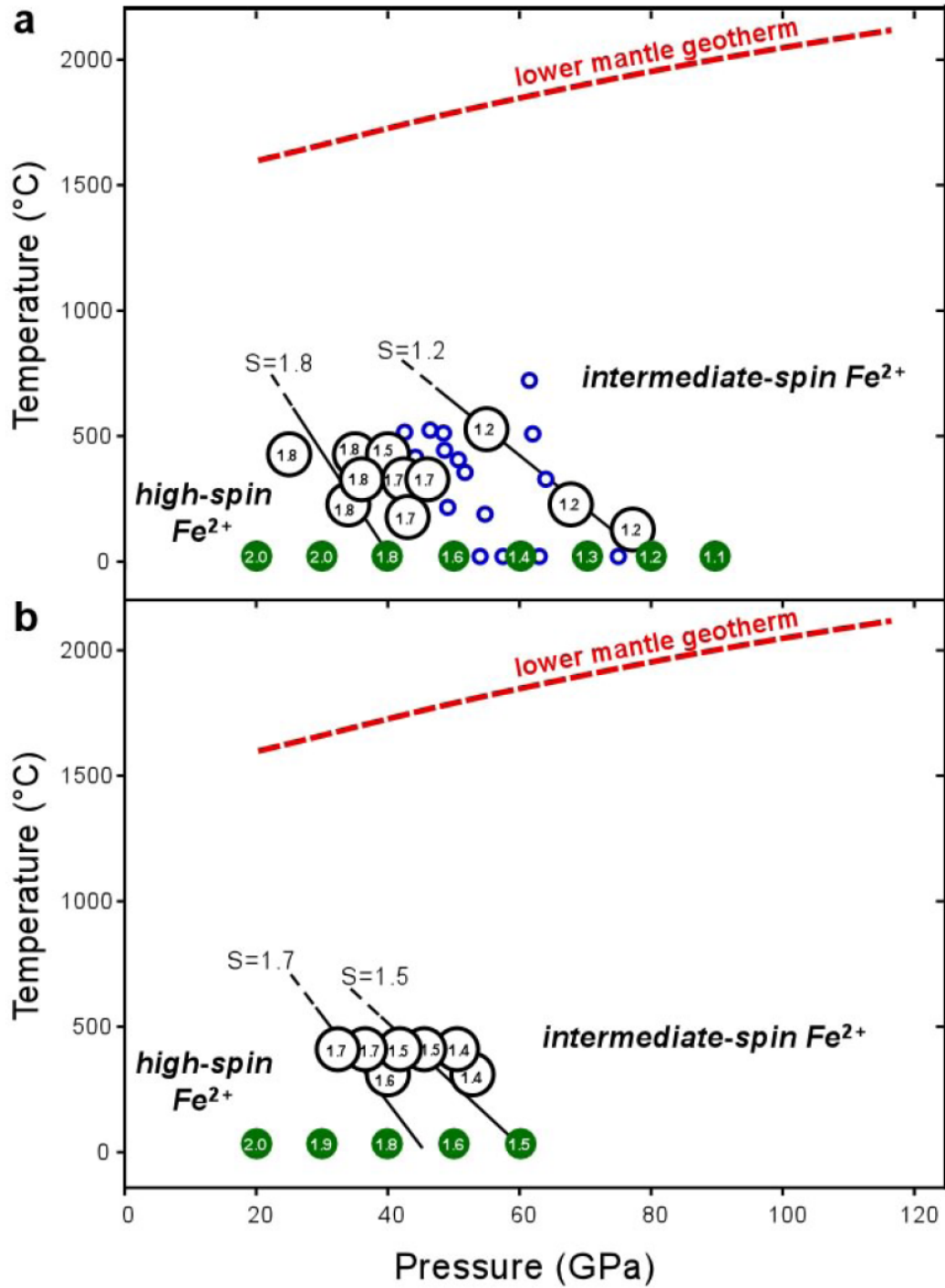


Figure 5.1-7 Effect of pressure and temperature on the total spin number of (a) $\text{Mg}_{0.88}\text{Fe}_{0.12}\text{SiO}_3$ and (b) $\text{Mg}_{0.86}\text{Fe}_{0.14}\text{Si}_{0.98}\text{Al}_{0.02}\text{O}_3$ perovskite. Large open circles (spin number indicated within) correspond to data from Mössbauer spectroscopy, while small blue circles correspond to NFS data. Although accurate spin numbers could not be calculated from NFS data, all spectra were consistent with spin numbers significantly less than 2. Solid green circles give the room temperature values derived from Fig. 5.1-2. Lines of equal spin number have negative slope; hence along the lower mantle geotherm Fe^{2+} is predicted to be predominantly in the IS state.

5. Results: iron in silicate perovskite

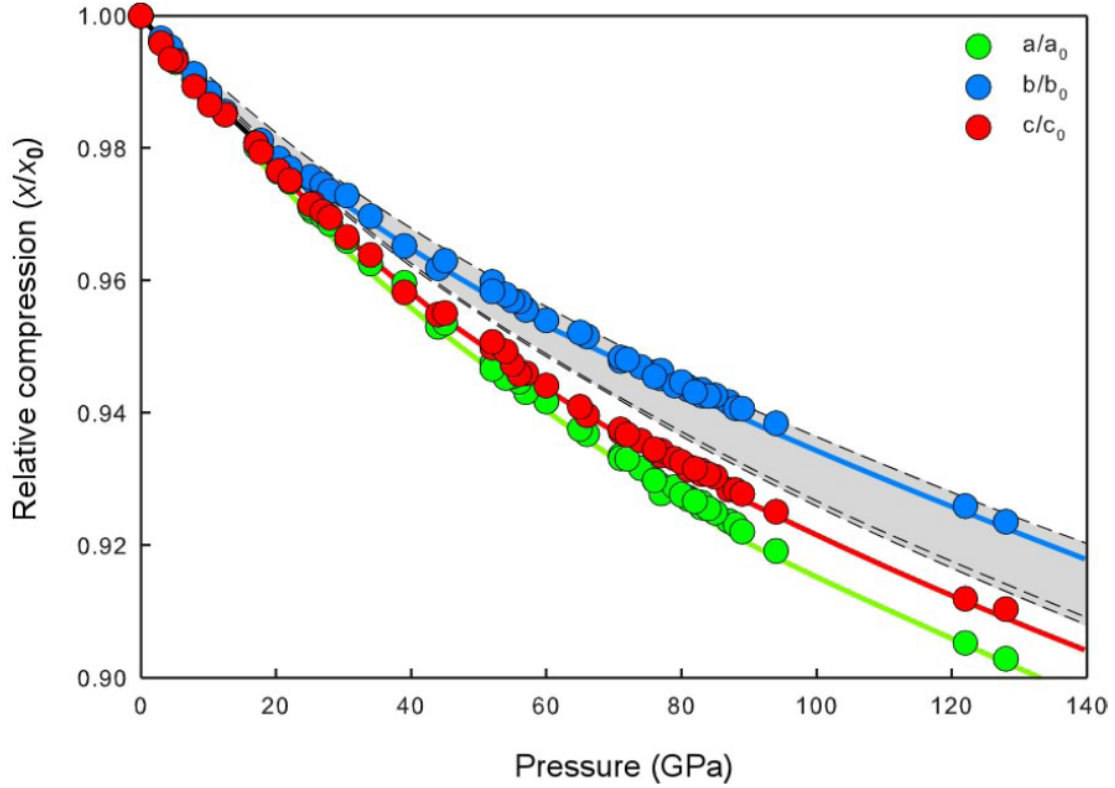


Figure 5.1-8 Relative compression of the unit cell axes of $\text{Mg}_{0.88}\text{Fe}_{0.12}\text{SiO}_3$ perovskite as determined from *in situ* room temperature X-ray powder diffraction using the same sample as shown in Fig. 5.1-1a in the main text. Literature data for MgSiO_3 perovskite (Fiquet et al., 2000) are shown for comparison as dashed lines, with grey shading between the curves of minimum (b/b_0) and maximum (a/a_0) compression for emphasis.

5. Results: iron in silicate perovskite

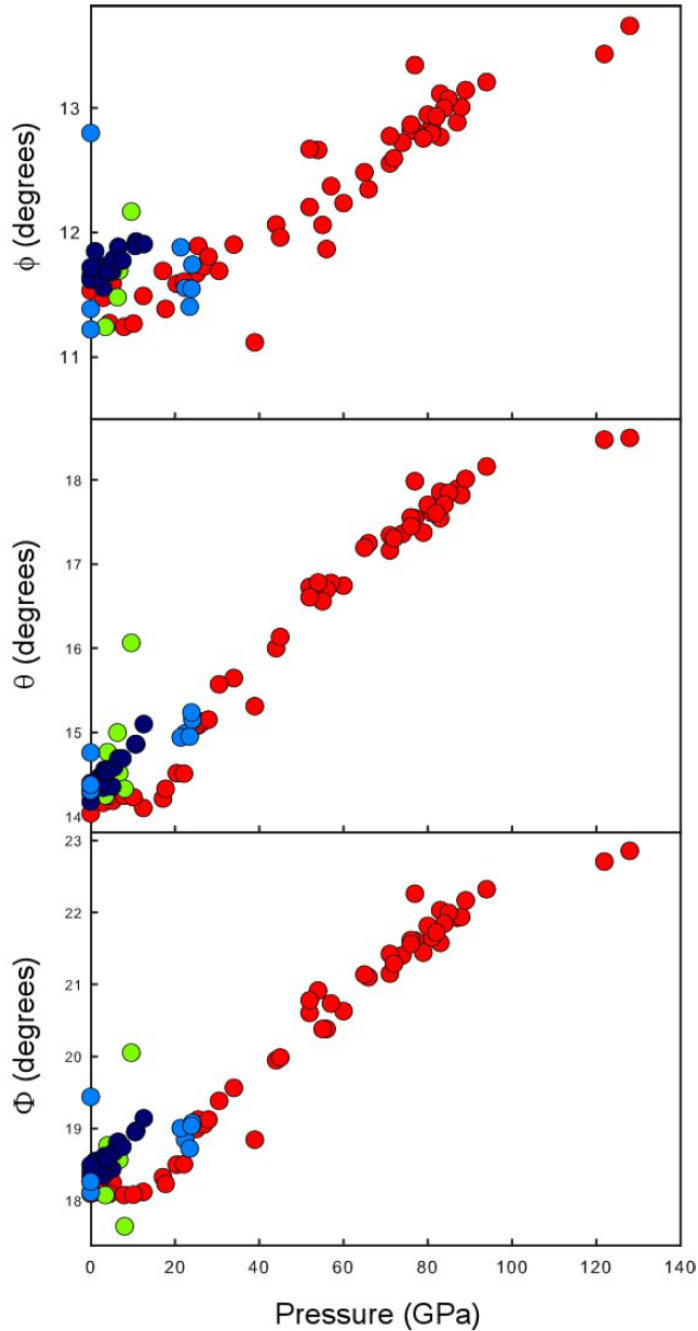


Figure 5.1-9 Variation of octahedral tilting angles (Mitchell, 2002) $\phi = \arccos(a/b)$, $\theta = \arccos(\sqrt{2a/c})$, and $\Phi = \arccos(\sqrt{2a^2/bc})$ shown as red circles calculated from the data in Fig. 5.1-8. Literature data for MgSiO_3 perovskite are shown for comparison in green (Kudoh et al., 1987), dark blue (Ross and Hazen, 1990) and light blue (Funamori et al., 1996).

5.2. High-pressure experimental and computational XANES studies of the Earth's lower mantle (Mg,Fe)(Si,Al)O₃ perovskite and (Mg,Fe)O ferropericlasite

Narygina O.¹, Mattesini M.², Kantor I.⁴, Pascarelli S.³, Wu X.¹, Aquilanti G.³, McCammon C.¹, Dubrovinsky L.¹

¹ Bayerisches Geoinstitut, Universität Bayreuth, Bayreuth D-95440, Germany; ²Departamento de Física de la Tierra, Astronomía y Astrofísica I, Universidad Complutense de Madrid, E-28040 Madrid, Spain; ³ European Synchrotron Radiation Facility, 38043, Grenoble, France; ⁴ CARS, University of Chicago, IL 60437, USA

Physical Review B (2009) 79(17), 174115.1-10

5.2.1. Abstract

Seven iron-containing oxides and silicates including (Mg_{0.88}Fe_{0.12})SiO₃, (Mg_{0.86}Fe_{0.14})(Si_{0.98}Al_{0.02})O₃ perovskites and (Mg_{0.80}Fe_{0.20}) ferropericlasite were studied using Fe K-edge X-ray Absorption Near Edge Spectroscopy (XANES) under pressure up to 85 GPa at ambient temperature. First principles calculations of Fe K-edges of (Mg_{0.88}Fe_{0.12})SiO₃ perovskite and (Mg_{0.80},Fe_{0.20})O ferropericlasite were performed using a spin-dependent method. The amount and quality of the data collected allows to perform for the first time a systematic study of the absorption edge features as a function of pressure in these geophysically important systems, providing direct experimental validation for band-structure calculations. The comparison between experiment and theory allows to analyze in detail the effect of Fe valence and spin state modifications on the spectra, allowing to confirm qualitatively the presence of a pressure induced spin pairing transition in (Mg,Fe)O ferropericlasite and a high spin intermediate spin crossover in (Mg,Fe)(Si,Al)O₃ perovskite.

5.2.2. Introduction

The Earth's lower mantle is believed to consist predominantly of (Mg,Fe)(Si,Al)O₃ perovskite with a smaller amount of (Mg,Fe)O ferropericlasite and CaSiO₃ perovskite. The influence of iron on the properties of these phases is still not fully understood, but it is believed

5. Results: iron in silicate perovskite

that properties such as elasticity, electrical and thermal conductivity, element partitioning between phases, etc. could be significantly affected by the electronic and structural behaviour of iron in minerals under lower mantle conditions.

A number of studies have been carried out to investigate the spin and oxidation state of iron in (Mg,Fe)(Si,Al)O₃ perovskite under high pressures. It is known that in the perovskite structure iron can occur in the ferrous (Fe²⁺) or ferric (Fe³⁺) valence state. It is well established that ferrous iron occupies the large distorted 8-12-fold coordinated polyhedron, while ferric iron might also occupy the smaller octahedral site ([McCammon et al., 1992](#); [McCammon, 1998](#)). Electron energy loss spectroscopy (EELS) and Mössbauer data suggest that the ferric iron fraction in (Mg,Fe)(Si,Al)O₃ perovskite depends on the aluminum content: with increasing aluminum concentration the amount of Fe³⁺ increases almost linearly ([Lauterbach et al., 2000](#); [McCammon et al., 2004](#); [Frost et al., 2004](#)).

Using K_β X-ray emission spectroscopy (XES) Badro et al. ([2004](#)) proposed that iron in (Mg,Fe)SiO₃ perovskite undergoes a spin crossover at 70 GPa, with a transition to the low-spin state at 120 GPa. Jackson et al. ([2005](#)) investigated the iron spin state in (Mg,Fe)SiO₃ perovskite with different iron contents using nuclear forward scattering (NFS), and inferred a high-spin to low-spin transition in Fe³⁺ at 70 GPa, with Fe²⁺ remaining in the high spin state throughout the studied pressure interval. Combining XES and NFS techniques to study (Mg,Fe)(Si,Al)O₃ perovskite, Li et al. ([2006](#)) inferred that Fe undergoes a transition from high-spin to low-spin in the pressure range 20-100 GPa. From these results it appears that the use of only XES and NFS methods was not able to provide a conclusive answer to the question of the iron spin state in magnesium-bearing silicate perovskite at the megabar pressure range.

X-ray absorption near edge spectroscopy (XANES) directly probes the empty density of electronic states above the Fermi level around the absorber atom. Fe K-edge XANES, along with Electron Energy Loss Spectroscopy (EELS), conventional and synchrotron Mössbauer spectroscopies (nuclear forward scattering: NFS), is one of the more precise experimental techniques to follow electronic and local structure around Fe and can be relatively easily combined with the diamond anvil cell (DAC) technique for making *in situ* measurements under high pressure and temperature conditions. In contrast to Mössbauer spectroscopy, XANES does not require ⁵⁷Fe-enrichment of the sample which simplifies the experimental procedure. While conventional Mössbauer spectroscopy gives information over a large region of the sample, it has recently become possible to obtain high quality XANES with the micron resolution enabling the

5. Results: iron in silicate perovskite

analysis of individual regions within the DAC ([Pascarelli et al., 2006](#)). Therefore micro-XANES spectroscopy can be a powerful experimental tool for *in situ* high-pressure and/or high-temperature measurements of the local electronic and crystallographic environment of iron. Consequently Fe K-edge micro-XANES can provide information that complements the results of other methods (XRD, conventional Mössbauer, NFS, and XES) for examining the spin and oxidation states of iron under Earth's lower mantle pressures.

Up to now, no systematic study has been performed on the evolution of Fe K-edge XANES in these geologically relevant systems up to very high pressures. One of the reasons for this is related to the experimental difficulties in obtaining good quality data at such extreme conditions, due to the high absorption of the diamond anvils at low X-ray energy (the Fe K-edge is at ~ 7 KeV), and to the strong constraint on spot size and stability that these studies impose. Many of these difficulties have been overcome with the use of 3rd generation synchrotron sources, coupled to advances in X-ray optics and high pressure techniques.

In parallel, major advances in *ab-initio* codes make it now possible to calculate band structures even in complex systems such as transition metal oxides, and from these obtain theoretical simulations of the absorption spectra, which include both core-hole and spin polarization effects.

The aim of this study was therefore to take advantage of these recent experimental and theoretical advances to perform for the first time a systematic Fe K-edge XANES study of several iron oxides and silicates under pressure in order to establish the strengths and limitations of this technique in complementing information on oxidation and electronic state of iron in these compounds, and to define the abilities of the method to investigate spin transitions, particularly in Fe-bearing silicate perovskites.

The paper is organized as follows. In section 5.2.3 we give experimental details on sample preparation and on preliminary structural and magnetic characterization (5.2.3.a), as well as on the experimental methods used (5.2.3.b). Section 5.2.4 reports the Fe K-edge XANES results for all the studied systems, and emphasizes the discussion on two issues: the effect of oxidation state (5.2.4.a) and the effect of spin state (5.2.4.b) on the absorption spectra. Whereas we discuss the former issue globally for the whole set of samples, the latter issue has been focused only on the ferropericlase (5.2.4.b.1) and on the perovskite systems (5.2.4.b.2). Finally in Section 5.2.5 we report the main conclusions of this work.

5. Results: iron in silicate perovskite

5.2.3. Experimental

5.2.3.a Sample preparation and characterization

Seven samples with different $\text{Fe}^{3+}/\Sigma\text{Fe}$ ratio were studied by means of XANES spectroscopy: Fe_2O_3 (hematite), Fe_3O_4 (magnetite), FeO (wüstite), $(\text{Mg,Fe})\text{O}$ (ferropericlase), FeTiO_3 (ilmenite), $(\text{Mg,Fe})\text{SiO}_3$ and $(\text{Mg,Fe})(\text{Si,Al})\text{O}_3$ (perovskites). All samples are synthetic and enriched with the ^{57}Fe isotope (in order to use the same samples for high-pressure Mössbauer spectroscopy).

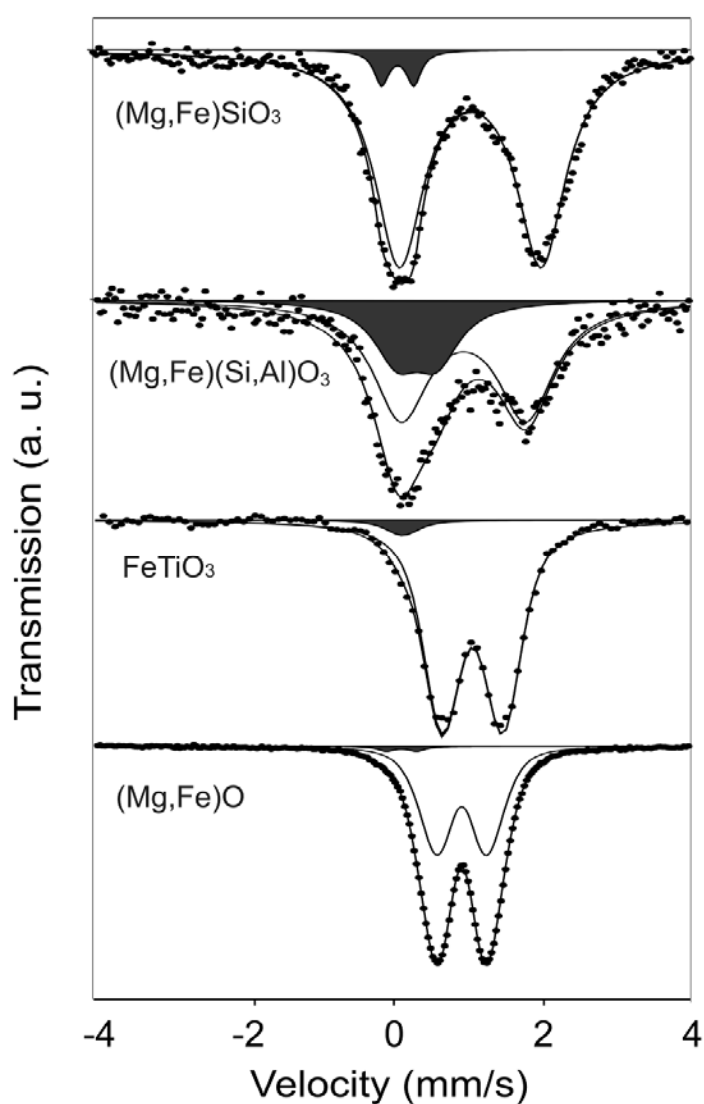


Figure 5.2-1 Mössbauer spectra at ambient conditions of $(\text{Mg,Fe})\text{SiO}_3$ and $(\text{Mg,Fe})(\text{Si,Al})\text{O}_3$ perovskites, FeTiO_3 and $(\text{Mg,Fe})\text{O}$. The spectral area colored in black corresponds to Fe^{3+} .

5. Results: iron in silicate perovskite

Hematite Fe_2O_3 is an iron III oxide with a corundum-like structure, with all iron ions occupying octahedral positions. The sample was a commercially available 99.99 % purity Fe_2O_3 powder. X-ray diffraction and Mössbauer spectroscopic measurements at ambient conditions show that no other phases except hematite are present in the sample. $\text{Fe}^{3+}/\Sigma\text{Fe}$ for this sample is defined to be 1.

Magnetite Fe_3O_4 is a mixed-valence oxide with an inverse spinel structure. The tetrahedral position is fully occupied with Fe^{3+} ions, while the octahedral position is filled with equal amounts of Fe^{2+} and Fe^{3+} ions. Nominally there are two Fe^{3+} ions for every Fe^{2+} ion in the magnetite structure. However magnetite is known to be a nonstoichiometric compound with a small excess or deficit of cations relative to the Fe_3O_4 formula ([Aragón et al., 1985](#)). A polycrystalline sample of magnetite was synthesized by heating metallic ^{57}Fe in air at 1400°C for 24 hours and quenching it into water. Both X-ray diffraction and Mössbauer spectroscopic measurements at ambient conditions show the presence of a pure magnetite phase. It is difficult to measure accurately the degree of nonstoichiometry in magnetite, but based on the relation between magnetite composition, temperature and oxygen fugacity ([Aragón et al., 1985](#)), we estimate that in our sample the nonstoichiometry parameter δ in the $\text{Fe}_{3(1-\delta)}\text{O}_4$ formula is approximately 0.02 (maximum possible value). The corresponding $\text{Fe}^{3+}/\Sigma\text{Fe}$ ratio in our magnetite sample is therefore 0.72.

Wüstite FeO with a rock-salt type structure is known to be a highly nonstoichiometric compound where x in Fe_{1-x}O can reach a value of 0.12. Fe^{2+} ions occupy the octahedral positions. The crystal chemistry of ferric iron in wüstite is complex, involving predominantly octahedral coordination with some minor amount of tetrahedrally coordinated Fe^{3+} . The degree of nonstoichiometry correlates well with the lattice parameter a of the cubic cell, allowing a straightforward determination of ferric iron content using X-ray diffraction at ambient conditions^[11]. The polycrystalline sample of wüstite was synthesized from metallic iron powder in a CO/CO_2 gas-flow furnace at 900°C and $\log(f\text{O}_2) = -16$. The resulting powder sample had a lattice constant a of $4.2959(1)$ Å, corresponding to $\text{Fe}_{0.92}\text{O}$ ([McCammon and Liu, 1984](#)). It is not straightforward to determine the Fe^{3+} content of wüstite from the Mössbauer spectrum due to the number of strongly overlapping and closely spaced absorption lines which arise due to complex defect clustering. The $\text{Fe}^{3+}/\Sigma\text{Fe}$ ratio in our wüstite sample was calculated from its composition to be 0.17 ([McCammon and Liu, 1984](#)).

5. Results: iron in silicate perovskite

Al-bearing and Al-free silicate perovskite phases were synthesized in a laser-heated DAC at 30-35 GPa and approximately 2500°C from two orthopyroxene starting materials with compositions $\text{Mg}_{0.86}\text{Fe}_{0.14}\text{Si}_{0.98}\text{Al}_{0.02}\text{O}_3$ and $\text{Mg}_{0.88}\text{Fe}_{0.12}\text{SiO}_3$ (each 61% enriched in ^{57}Fe) that were described in Lauterbach et al. (2000). Run products were found using X-ray diffraction to consist almost exclusively of $(\text{Mg,Fe})\text{SiO}_3$ or $(\text{Mg,Fe})(\text{Si,Al})\text{O}_3$ perovskite (in aluminium bearing samples traces of SiO_2 stishovite were detected), and chemical compositions were found using the electron microprobe to be the same as the starting materials within experimental uncertainty. The relative concentration of Fe^{3+} was found by means of Mössbauer spectroscopy to be 0.10 (± 0.02) and 0.25 (± 0.07) for the $\text{Mg}_{0.88}\text{Fe}_{0.12}\text{SiO}_3$ and $\text{Mg}_{0.86}\text{Fe}_{0.14}\text{Si}_{0.98}\text{Al}_{0.02}\text{O}_3$ perovskite samples, respectively (Fig. 5.2-1).

Ilmenite (FeTiO_3) was synthesized from a stoichiometric mixture of Fe_2O_3 , TiO_2 and ^{57}Fe heated in an evacuated silica tube at 1200°C for 24 hours. X-ray diffraction and Mössbauer spectroscopy showed no other phase to be present except ilmenite, and Mössbauer data showed the amount of Fe^{3+} to be 0.03 (± 0.01) (Fig. 5.2-1).

Ferropericlase $(\text{Mg,Fe})\text{O}$ is a MgO-FeO solid solution with FeO content less than 50%. We studied a polycrystalline sample with $(\text{Mg}_{0.8}\text{Fe}_{0.2})\text{O}$ composition in this work. The sample was synthesized by mixing stoichiometric amounts of MgO and Fe_2O_3 , heating overnight at 1200°C under reducing conditions ($\log f\text{O}_2 = -17.4$) using a CO/CO_2 gas-flow furnace and quenching into water. The lattice constant a of ferropericlase was measured to be 4.2389(5) Å. The ferric iron content, measured using Mössbauer spectroscopy over a wide pressure range, was found to be 0.05 (± 0.01), and this value was used in the present study (Fig. 5.2-1).

5.2.3.b Experimental method

For *in situ* high pressure micro-XANES and Mössbauer spectroscopy measurements in the DAC we used diamonds with 250 or 300 μm culet size. Samples were loaded into Re gaskets that had been preindented to $\sim 30 \mu\text{m}$ and then drilled with a hole of 125 μm diameter. For pressure calibration and evaluation of the pressure gradient we used small ruby chips that were loaded into the cell along with the sample. At the highest pressures (~ 100 GPa) the uncertainty in pressure measurements was estimated to be 5 GPa, while the pressure difference between the center and the edge of the pressure chamber was a maximum of 5 GPa. After each increase or decrease of pressure with step ~ 5 GPa above 30 GPa samples were annealed at 1700-1900 K by

5. Results: iron in silicate perovskite

laser heating. K-edge XANES measurements were performed at the European Synchrotron Radiation Facility at the energy dispersive XAS beamline ID24. The beam was focused horizontally using a curved polychromator Si(111) crystal in Bragg geometry and vertically with a bent Si mirror placed at 2.8 mrad with respect to the direct beam ([Pascarelli et al., 2004](#)). The Bragg diffraction peaks arising from the diamond anvils were removed from the energy range of interest by changing the orientation of the diamond anvil cell and following in real time the intensity of the transmitted beam on a two-dimensional detector. The measured XANES spectra were analysed using the VIPER program ([Klementev, 2001](#)). The flat part of the pre-edge region of the spectrum was fitted to the Victoreen function ($F = a + bE^{-3}$, where E is the absorption energy and a and b are fit parameters) and this baseline was extended over the entire energy region. The post-edge jump in X-ray absorption was then normalized to 1. Transmission Mössbauer spectra were recorded on a constant acceleration Mössbauer spectrometer at temperatures in the range 300-800 K and pressures in the range from ambient up to above 80 GPa. The experimental procedure is described in detail in McCammon et al. (1992) and Kantor et al. ([2004](#)).

5.2.4. Results and discussion

5.2.4.a Effect of oxidation state

The XANES spectra of all samples at 13 GPa are presented for comparison in Fig. 5.2-2. For magnetite (Fe_3O_4) for example, the pre-edge peak structure is well pronounced, which allows extracting information about $\text{Fe}^{3+}/\Sigma\text{Fe}$ (e.g., in [Berry et al., 2003](#)). However in the case of wüstite (FeO), ferropericlase ($(\text{Mg,Fe})\text{O}$), ilmenite (FeTiO_3), Al-bearing $(\text{Mg,Fe})(\text{Si,Al})\text{O}_3$ and Al-free perovskites $(\text{Mg,Fe})\text{SiO}_3$, the intensity of pre-edge peaks is very weak. In this case the extraction of information about iron oxidation state is challenging, and it is necessary to identify other spectral features that are systematically correlated with the amount of ferric iron. In a previous XANES study of silicate glasses ([Berry et al., 2003](#)), the following features were proposed: (i) the energy of the main absorption edge, normalized to one at a height of 0.9; and (ii) the areas of the derivative peaks associated with the $1s \rightarrow 4s$ and $1s \rightarrow 4p$ transitions. For our XANES experimental data the most well defined and reproducible spectral feature is the energy

5. Results: iron in silicate perovskite

corresponding to the absorption edge, which can be determined from the centroid position of the first peak in the derivative (Fig. 5.2-3).

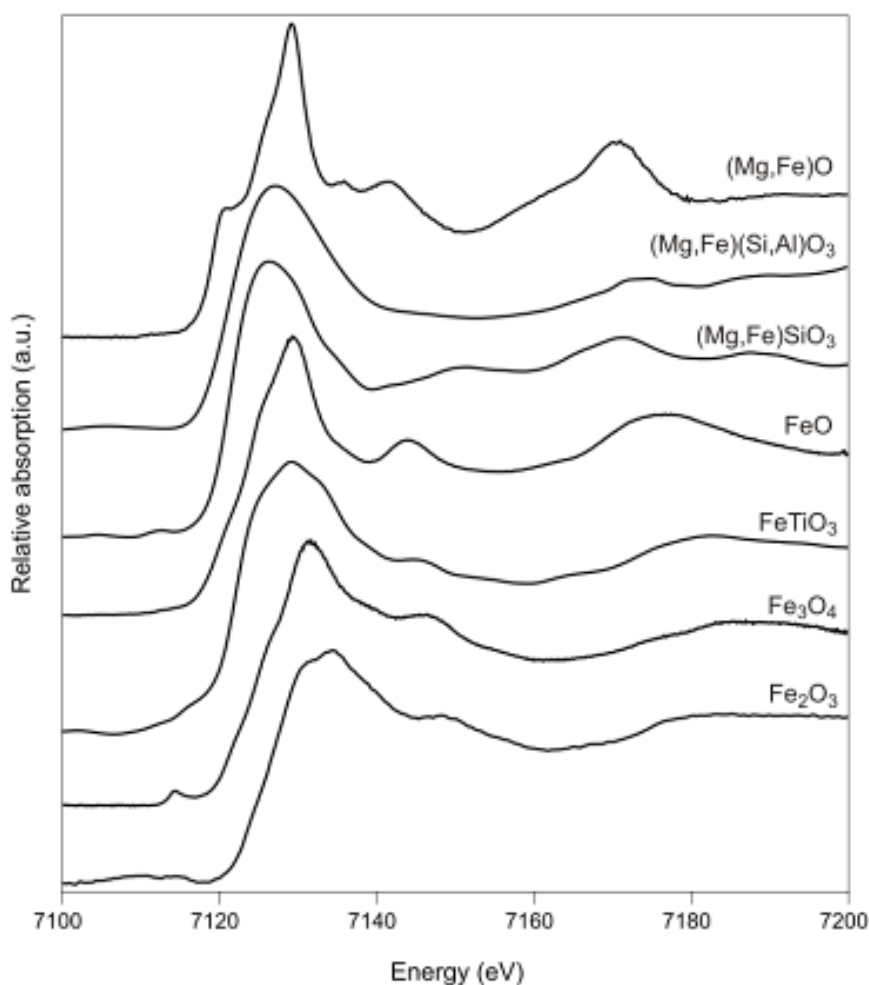


Figure 5.2-2 Normalized XANES spectra taken at 13 GPa from the seven Fe-containing oxides and silicates: (Mg,Fe)O (ferroperricite), (Mg,Fe)(Si,Al)O₃ and (Mg,Fe)SiO₃ (perovskites), FeO (wüstite), FeTiO₃ (ilmenite), Fe₃O₄ (magnetite) and Fe₂O₃ (hematite).

The experimentally obtained edge position energies plotted vs. $\text{Fe}^{3+}/\Sigma\text{Fe}$ at ambient pressure are shown in Fig. 5.2-4. For the pure Fe oxides FeO, Fe₂O₃ and Fe₃O₄ a correlation can be made between $\text{Fe}^{3+}/\Sigma\text{Fe}$ and valence (see dashed line in Fig. 5.2-4). On the other hand, the K-edge position values for ferroperricite, the perovskites and for ilmenite are all systematically shifted towards higher energies with respect to the average slope traced by the values of the pure Fe oxides. The addition of Mg or Ti evidently modifies the density of empty states just above the Fermi level with respect to that of the pure Fe oxides, and this strongly affects the shape of the

5. Results: iron in silicate perovskite

absorption edge. Therefore, whereas the centroid position of the first peak in the derivative is a good fingerprint of Fe valence within the family of pure Fe oxides, it fails when attempting to include Mg and Ti containing Fe oxides.

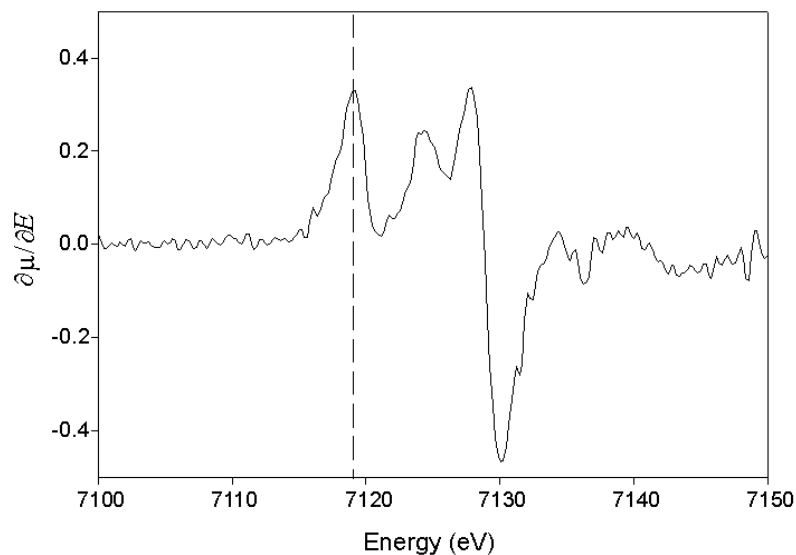


Figure 5.2-3 First derivative of XANES spectrum of (Mg,Fe)O at 1 GPa. The vertical dashed line corresponds to the $1s \rightarrow 4s$ transition peak position that was taken as the absorption edge position.

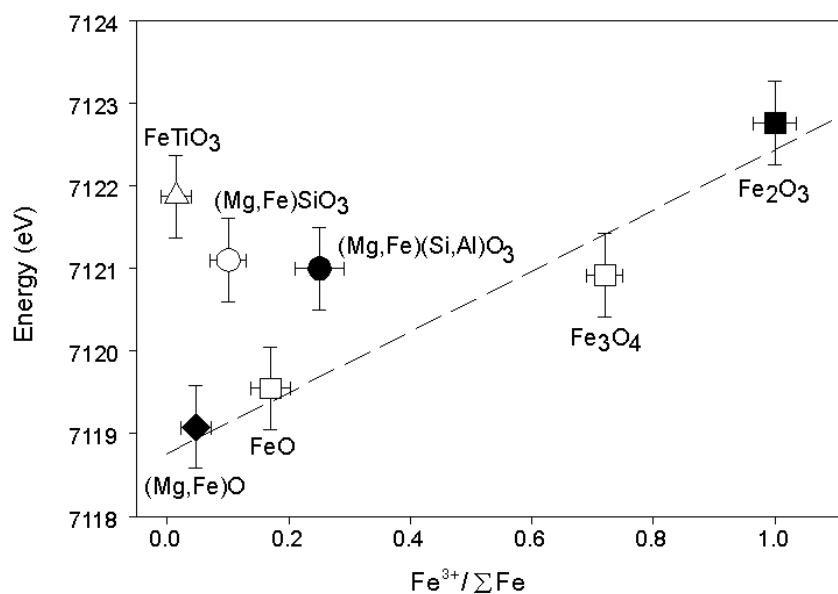


Figure 5.2-4 Absorption edge position energy plotted vs. ferric iron content for Fe_2O_3 (black closed rectangle), Fe_3O_4 (gray closed rectangle), FeO (open rectangle), FeTiO_3 (open triangle), $(\text{Mg,Fe})\text{SiO}_3$ (gray closed circle), $(\text{Mg,Fe})(\text{Si,Al})\text{O}_3$ (black closed circle) and $(\text{Mg,Fe})\text{O}$ (black closed diamonds). Dashed line represents the fit of the pure oxide data.

5. Results: iron in silicate perovskite

The effect of pressure on absorption edge position for all studied systems is presented in Fig. 5.2-5. Except for FeTiO_3 and $(\text{Mg,Fe})\text{O}$ the K-edge position for studied samples does not show any significant change with pressure apart from a gradual shift towards higher energies (Fig. 5.2-5). The pressure evolution of the absorption edge position for FeTiO_3 (Fig. 5.2-5b) shows a peculiarity between 20 and 40 GPa, where the transition to single perovskite phase takes place. This effect is described in detail in [Wu et al. 2009](#). In the case of $(\text{Mg,Fe})\text{O}$ (Fig. 5.2-5b) we observe a discontinuity at ~ 60 GPa, that perfectly coincides with the previously reported spin transition in ferropericlase ([Kantor et al., 2006a](#); [Lin and Tsuchiya, 2008](#)). We will discuss this point again in the following section.

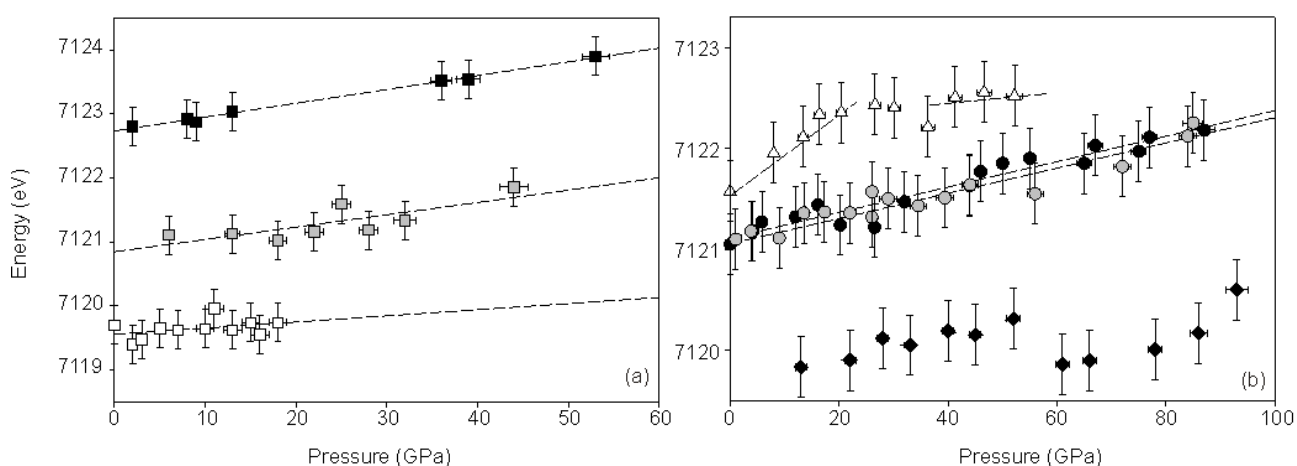


Figure 5.2-5 Evolution of the Fe K-edge position with pressure for seven iron oxides and silicates: (a) Fe_2O_3 (black closed rectangles), Fe_3O_4 (gray closed rectangles) and FeO (open rectangles); (b) FeTiO_3 (open triangles), $(\text{Mg,Fe})\text{SiO}_3$ (gray closed circles), $(\text{Mg,Fe})(\text{Si,Al})\text{O}_3$ (black closed circles) and $(\text{Mg,Fe})\text{O}$ (black closed diamonds). Dashed lines represent the linear fit of the absorption edge positions.

5.2.4.b Effect of spin state

5.2.4.b.1. $(\text{Mg,Fe})\text{O}$ ferropericlase

5.2.4.b.1.i Experimental

The main goal of the study is to examine the ability of XANES to detect spin transitions under high pressure. Therefore $(\text{Mg}_{0.80}\text{Fe}_{0.20})\text{O}$ was chosen as the example system for tracing changes in the absorption of iron through the gradual high spin (HS) – low spin (LS) crossover in the compound.

5. Results: iron in silicate perovskite

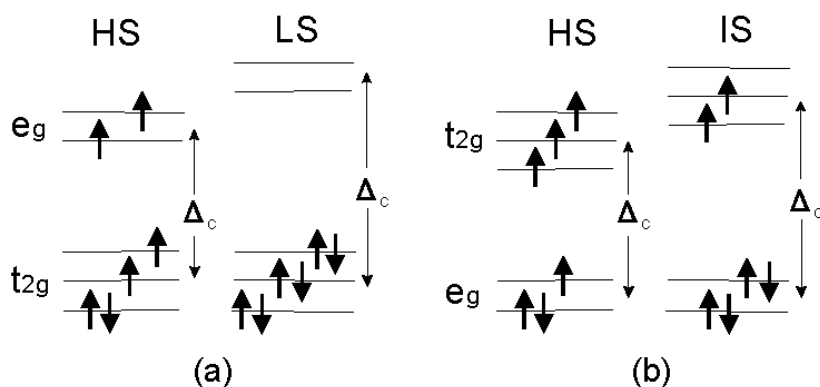


Figure 5.2-6 High spin (HS) and low spin (LS) electronic configurations of Fe²⁺ in the octahedral field (ferropericlase case) – (a); and high spin (HS) and intermediate spin (IS) electronic configurations of Fe²⁺ in the distorted cubic field (perovskite case) – (b). Δ_C is crystal field splitting.

In ferropericlase Fe²⁺ ions occupy octahedral sites, therefore the five 3d energy levels are split in three lower - t_{2g} and two higher - e_g energy levels, separated by the crystal-field splitting energy - Δ_C (Fig. 5.2-6a) (Burns, 1970). At ambient conditions Δ_C is small compared to the spin pairing energy and therefore the high spin configuration (two paired and four unpaired electrons) is the most stable one. But with pressure the crystal-field splitting increases and at a certain point (50 GPa for (Mg_{0.80}Fe_{0.20})O ferropericlase (Kantor et al., 2006a)) Δ_C becomes higher than the spin pairing energy, making the low spin configuration energetically favorable. The crossover to the low spin state modifies not only the electronic field gradient but also the local environment of iron since the Fe-O bond distribution is expected to be modified, and therefore the transition effect on the Fe K- absorption edge in (Mg,Fe)O is expected to be significant.

In fact, a close look at the experimental data shown in Fig. 5.2-7 highlights clear changes in the shape of the absorption spectra starting from the data at 61 GPa, in addition to the above mentioned anomalous behaviour of the absorption edge position: (i) at ambient pressure the main peak in the white line area is formed by two poorly resolved peaks (feature A) which gradually converge with pressure and finally form one peak of higher intensity; (ii) the small peak at ~7135 eV (feature B) gradually shifts towards high energies and merges with feature C forming an intense single peak ~ 7140 eV.

5. Results: iron in silicate perovskite

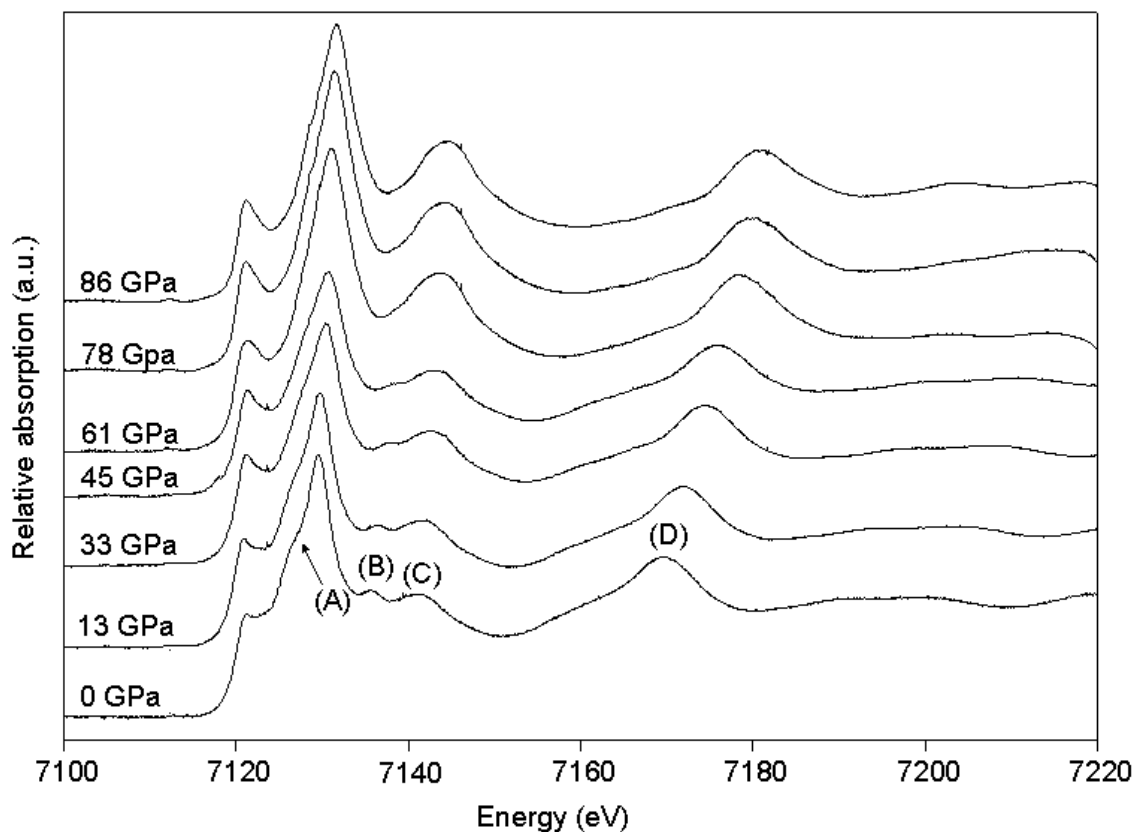


Figure 5.2-7 Experimental XANES spectra of $(\text{Mg}_{0.8}\text{Fe}_{0.2})\text{O}$ ferropericlase as a function of pressure.

We note that the changes in the shape of the spectra starting from the data at 61 GPa are rather abrupt. We can help visualize this important change with pressure by plotting the pressure evolution of specific features, such as the amplitude ratio between feature A (the white line peak, expected to be particularly sensitive to spin state) and feature D, expected to be less sensitive to spin state and more sensitive to local structure. The evolution of this amplitude ratio with pressure obtained from the data of Fig. 5.2-7 is shown in Fig. 5.2-8.

One can clearly see that a significant change occurs between 50-80 GPa, known as the pressure region of the gradual high spin low spin crossover in $(\text{Mg}_{0.80}\text{Fe}_{0.20})\text{O}$ ferropericlase ([Kantor et al., 2006a](#); [Lin et al., 2005](#)). This trend, that highlights the visual changes in the shape of the spectra shown in Fig. 5.2-7, can therefore be taken as evidence of the HS-LS transition in this system.

5. Results: iron in silicate perovskite

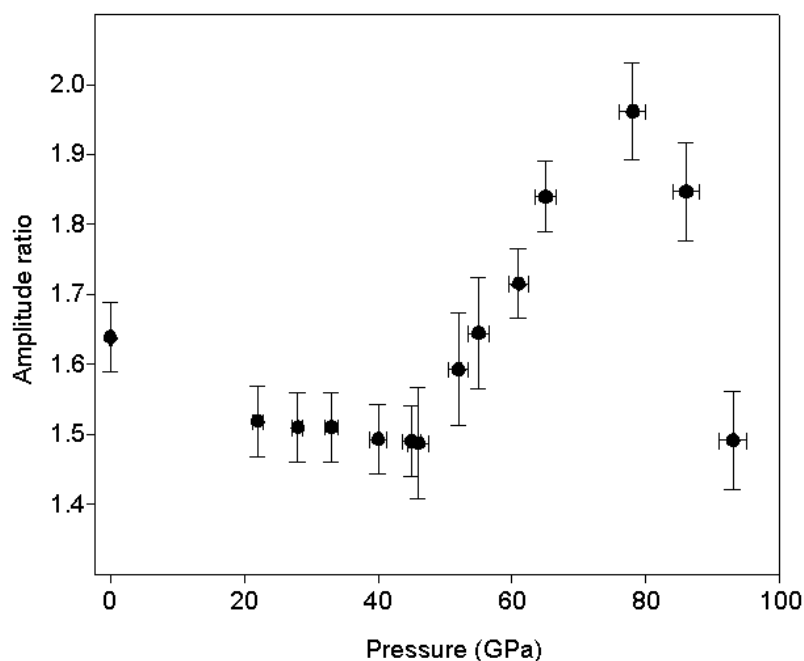


Figure 5.2-8 Pressure evolution of amplitude ratio between the white line peak at 7130 eV (feature A) and the peak at 7170 eV (feature D) of the $(\text{Mg}_{0.80}\text{Fe}_{0.20})\text{O}$ XANES spectra shown in Fig. 5.2-7.

5.2.4.b.1.ii *Ab initio* calculation of X-ray absorption spectra

Ab initio calculations were performed for a $2 \times 2 \times 2$ MgO supercell (B_1 structure) consisting of a 64-atom cubic system with 29 Mg, 32 O and 3 Fe atoms. Theoretical X-ray absorption spectra were computed within the single-particle transition model using the Augmented Plane Wave plus local orbitals (APW+lo) band structure method (Blaha et al., 2001), where the exchange and correlation effects were described by means of the generalized gradient approximation (GGA) (Perdew et al., 1996). The muffin-tin radii (R_{MT}) for Mg and Si were set to $1.80 a_0$; whereas for Fe and O we used $2.0 a_0$ and $1.55 a_0$, respectively.

Calculations were performed with a plane wave cut-off corresponding to $R_{\text{MT}} * K_{\text{max}} = 7$ and by using s , p and d local orbitals in the APW basis set to improve the convergence of the wave function. The valence wave functions inside the non-overlapping muffin-tin spheres were expanded into spherical harmonics up to $l = 10$ and the potential up to $l = 4$.

The total energy was converged with respect to a $4 \times 4 \times 5$ k -point sampling corresponding to 24 inequivalent k -points. Theoretical XAS data were then evaluated at the converged ground-state density by multiplying the angular momentum projected density of states by the transition-

5. Results: iron in silicate perovskite

matrix elements ([Müller and Wilkins, 1984](#)) and accounting for the electric-dipole approximation (*i.e.* $l \rightarrow l \pm 1$ transitions). A direct comparison of the calculated spectra with the measured data was finally achieved by including the instrumental broadening in the form of Gaussian functions corresponding to the experimental resolution of 1.1 eV.

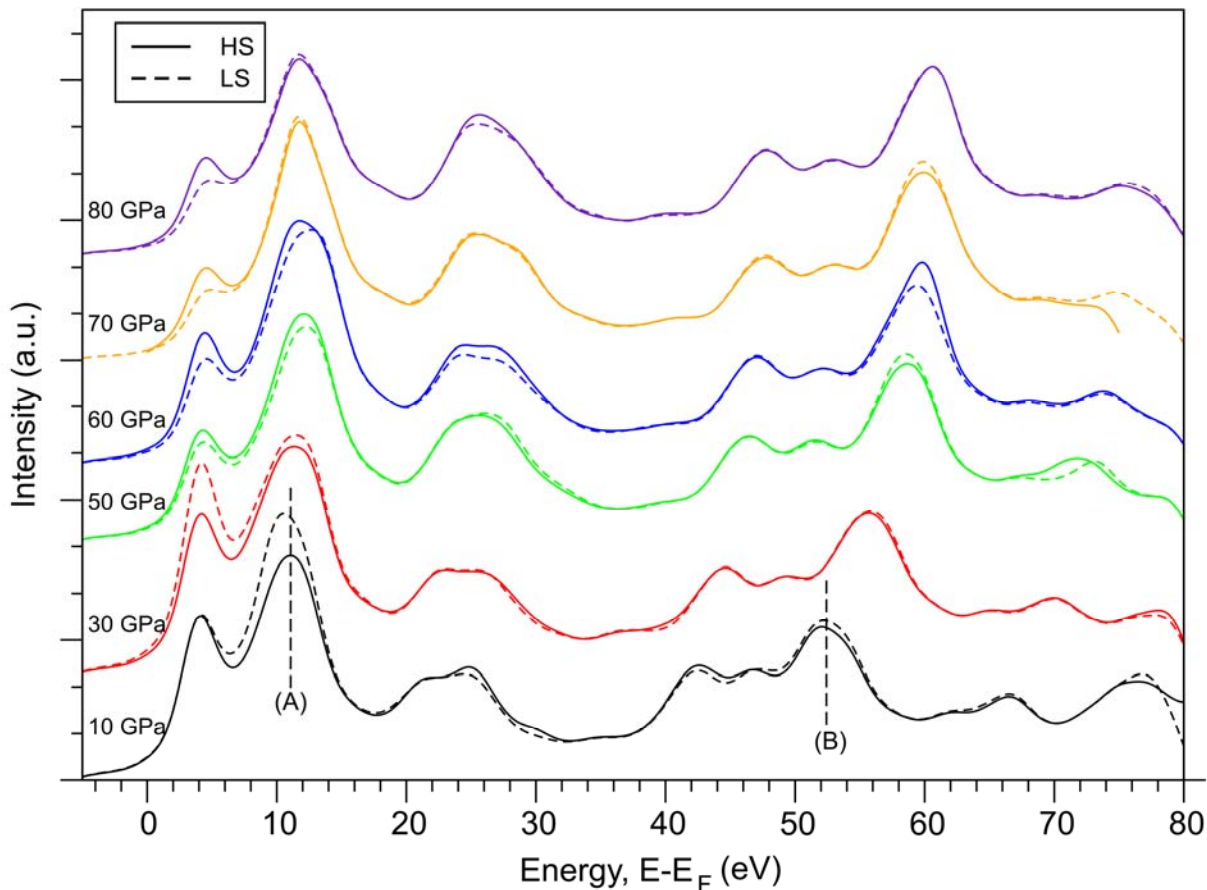


Figure 5.2-9 Theoretical Fe K-edges at different pressures by imposing a fixed spin occupation at the Fe d -states in the $(\text{Mg}_{0.80}, \text{Fe}_{0.20})\text{O}$ ferropericlase system. The onset energy of each spectrum was adjusted according to the variation in the Fermi energy and in the $1s$ core level energy shift.

The theoretical Fe K-edges obtained for a frozen Fe $3d$ shell at different pressure values for both HS and LS configurations are shown in Fig. 5.2-9. The $3d$ shell freezing was achieved by selecting a high value for the linearization energy of the Fe $3d$ -atomic orbitals. The vanishing occupied d -DOS at the absorber Fe site is then reintroduced in the calculation by manually fixing the occupation of the core-states. Particularly, we moved the Fe $3d^6$, either with a HS or LS configuration, inside the core states and shifted the potential by an appropriate constant. A value of 2.0 was found to be sufficient enough to maintain the entire set of eigenvalues at negative

5. Results: iron in silicate perovskite

values during the iterative SCF procedure. When the desired energy convergence criterion is reached ($\Delta E \leq 0.0001$ Ry), we save the corresponding potential. The final Fe K-edges were then obtained in a second unfrozen non SCF calculation, which allow the recovering of the Fe d-DOS at the frozen site. This procedure was applied for unit cell volumes corresponding to a pressure range of 0-80 GPa and by imposing a 1s core-hole for a divalent Fe configuration. The simulated spectra are able to reproduce the main features of the experimental spectra shown in Fig. 5.2-7, underlying the strength of modern *ab-initio* codes in modeling complex systems such as these.

From Fig. 5.2-9 we see that for each pressure, the theoretical comparison of the HS and LS calculations shows that the spin state mostly affects the amplitude of the spectral features close to the absorption edge, such as the pre-edge and the white line amplitude (feature A). This is reasonable and reflects the higher sensitivity of the probed p states, through hybridization effects, to the spin-polarized d states close to the Fermi level.

In order to confirm this, we have calculated unoccupied conduction band (CB) Fe partial density of states (pDOS) (Fig. 5.2-10) and the occupied (VB) partial Fe, O₁ and O₂ pDOS for (Mg_{0.88},Fe_{0.12})O ferropericlase (Fig. 5.2-11). These figures help to identify which features of the absorption spectra are more sensitive to local structural modifications, such as bond compression, and which features are more sensitive to spin state.

Fig. 5.2-10 shows that the spectroscopic signatures mentioned above originate mainly from the high-pressure behaviour of the Fe *p*-states, which represent the dominant contribution to the spectra at large values of photoelectron energy (i.e. away from the absorption edge region). Fig. 5.2-11 shows that the oxygen *s*- and *p*- orbitals hybridize well with the *s*-, *p*- and *d*-states of Fe, indicating that the spectral shapes shown in Fig. 5.2-7 are largely modulated by Fe-O electronic hybridization. The computed bandwidths for Fe and O states become larger and the electronic density of states get broader as pressure changes from 0 to 80 GPa.

5. Results: iron in silicate perovskite

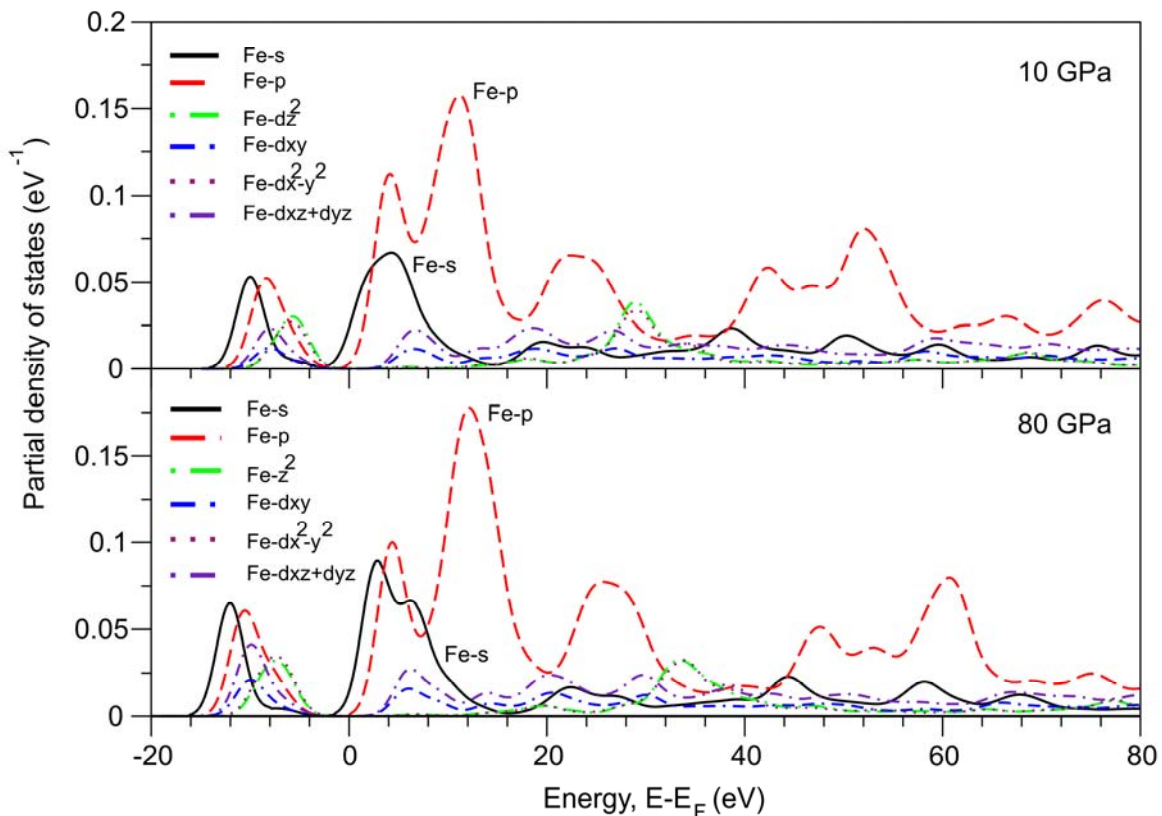


Figure 5.2-10 Calculated unoccupied (CB) Fe partial density of states (PDOS) for the $(\text{Mg}_{0.8},\text{Fe}_{0.2})\text{O}$ $2\times 2\times 2$ supercell.

Modifications in spin state are expected to affect mainly the occupied Fe-d pDOS. Therefore K-edge features, mainly sensitive to the unoccupied Fe-p pDOS, should not be very sensitive to changes in spin state. Spin state effects are readily observable using $\text{K}\beta$ emission spectroscopy, which directly probes the occupied Fe-d states. However, due to hybridization effects, K-edge spectroscopy becomes indirectly sensitive to the Fe-d pDOS through p-d hybridization. As shown in Fig. 5.2-11, the occupied d pDOS is localized around the Fermi level. Therefore we expect spin state modifications to affect mainly the region of the spectra close to the absorption edge. From Fig. 5.2-9 we note however that the calculation is not as yet able to reproduce quantitatively the important changes in the shape of the absorption spectra highlighted in Fig. 5.2-8. This is most certainly related to the fact that at very low kinetic energies the photoelectron is extremely sensitive to the details of the surrounding potential, setting enormous challenges to the precision of the *ab-initio* calculations.

5. Results: iron in silicate perovskite

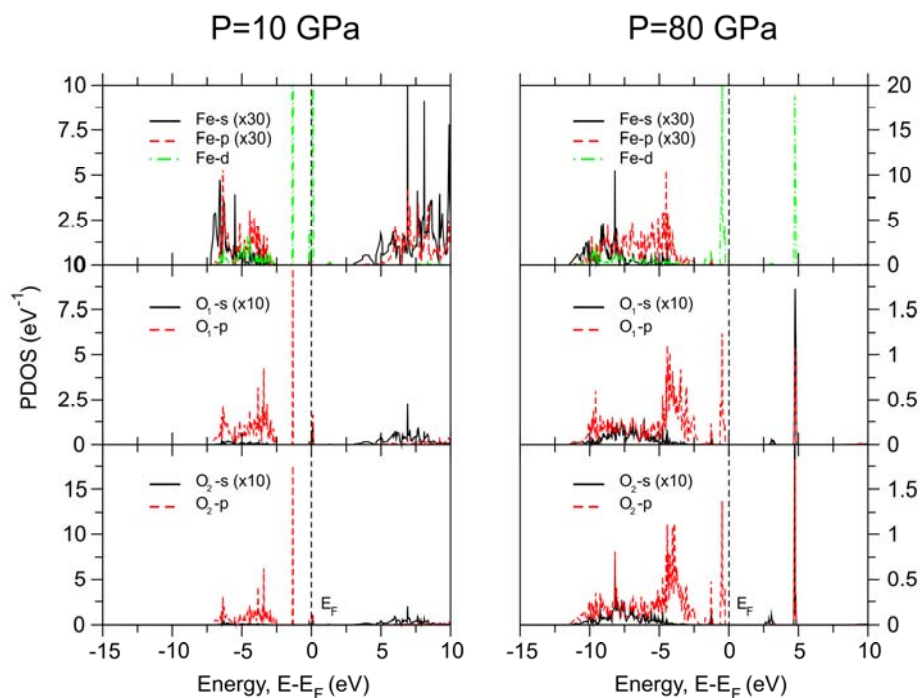


Figure 5.2-11 Calculated occupied (VB) partial Fe, O₁ and O₂ pDOS for (Mg_{0.8},Fe_{0.2})O ferropericlase. Note that the atom type O₁ and O₂ constitute the first coordination shell of the absorbing Fe atom.

5.2.4b.2. (Mg,Fe)(Si,Al)O₃ perovskite

5.2.4b.2.i Experimental

Our recent Mössbauer spectroscopic results for both (Mg,Fe)SiO₃ and (Mg,Fe)(Si,Al)O₃ perovskite phases demonstrate clear changes in the iron electronic state starting at 30-80 GPa (McCammon et al., 2008). Briefly, at 30 GPa we observe the appearance of a new component with an unusually large quadrupole splitting, close to 4 mm/sec, and a central shift about 1 mm/sec. We assign this component to an intermediate spin (IS) state of Fe²⁺. Thus our Mössbauer spectroscopic results suggest a gradual HS-IS crossover in Fe-bearing magnesium silicate perovskite at 30-80GPa.

Fig. 5.2-6b illustrates the HS and IS electronic configuration in the perovskite system. Fe²⁺ is located in 8+4-fold coordinated polyhedra, which in a first approximation can be considered as distorted cuboctahedra. The five 3d energy levels are split in two lower - e_g and three higher - t_{2g} energy levels which at ambient conditions are populated by two paired and four unpaired electrons – the high spin configuration. In the intermediate spin configuration four

5. Results: iron in silicate perovskite

electrons are paired and occupy the lower e_g levels while two unpaired electrons remain on the high t_{2g} energy levels. A crossover to the intermediate spin state increases the value of electric field gradient but does not generate any significant structural change. Therefore the spin crossover effect on the Fe absorption spectra of $(\text{Mg,Fe})(\text{Si,Al})\text{O}_3$ perovskite is expected to be less pronounced in this system than in the $(\text{Mg,Fe})\text{O}$ case.

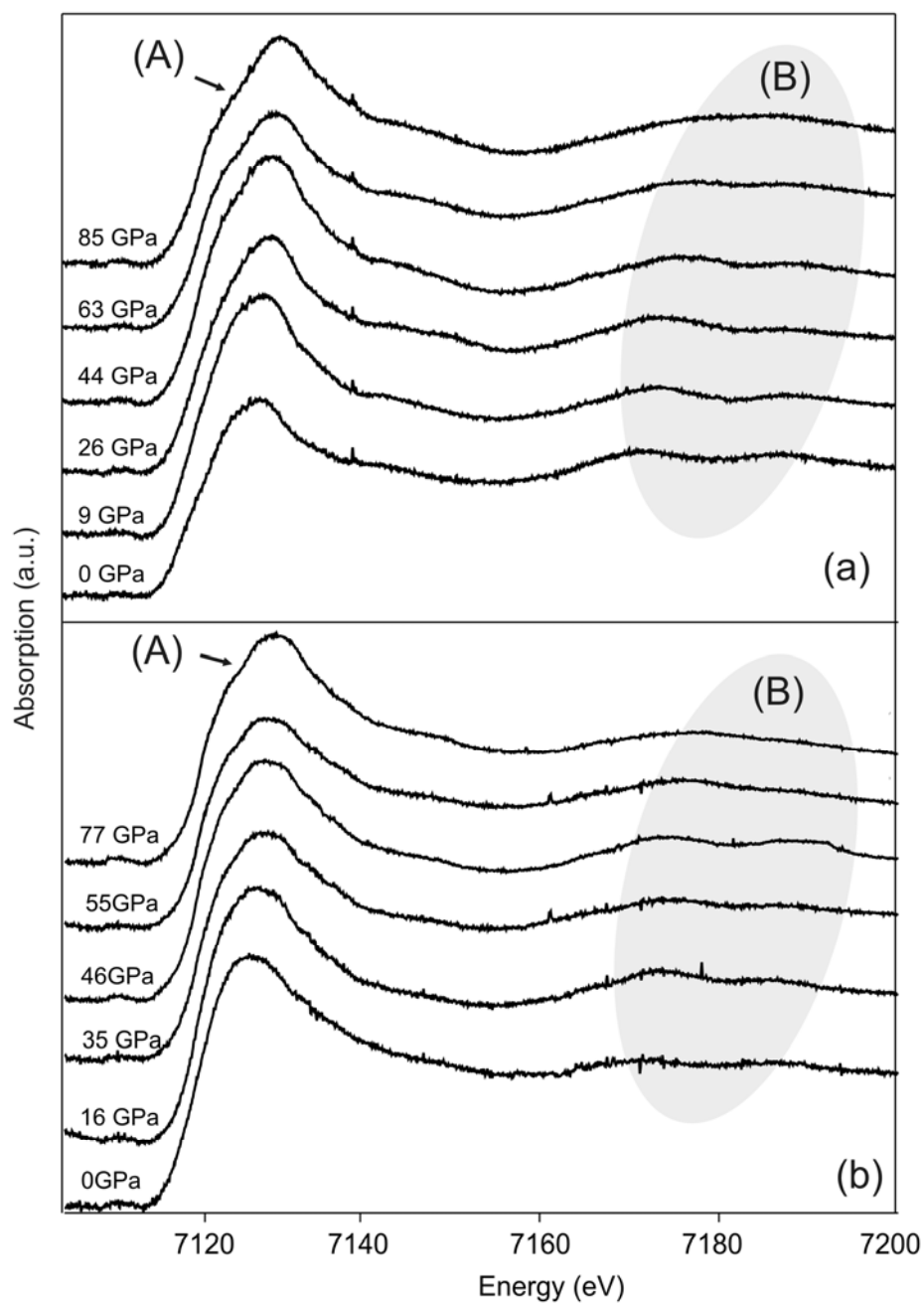


Figure 5.2-12 XANES spectra of $(\text{Mg,Fe})\text{SiO}_3$ (a) and $(\text{Mg,Fe})(\text{Si,Al})\text{O}_3$ (b) perovskites as a function of pressure.

5. Results: iron in silicate perovskite

Absorption spectra of the silicate perovskites, illustrated in Fig. 5.2-12, do indicate some changes in the 30-87 GPa range: (i) in the white-line region a small shoulder on the first broad peak appears with increasing pressure (feature A); (ii) in the high-energy region, the two maxima, resolved at low energy, merge forming a broad maximum at 80 GPa (feature B in the highlighted region).

As done for the ferropicrclase system above, here again we can try to highlight the changes in the shape of the spectra by following the pressure evolution of specific features that have different sensitivities to spin state and local structure. For example, we plot in Fig. 5.2-13 the amplitude ratio between the white line feature (at 7130 eV) and feature B (at 7170 eV), for both Al-free and Al-bearing perovskites as a function of pressure.

This figure shows a weak change in slope at about 35 GPa. We can conclude that Fe K absorption spectroscopy can probably detect the spin transition but it has much less sensitivity in perovskites than it does in ferropicrclase due to the different mechanism of the transition.

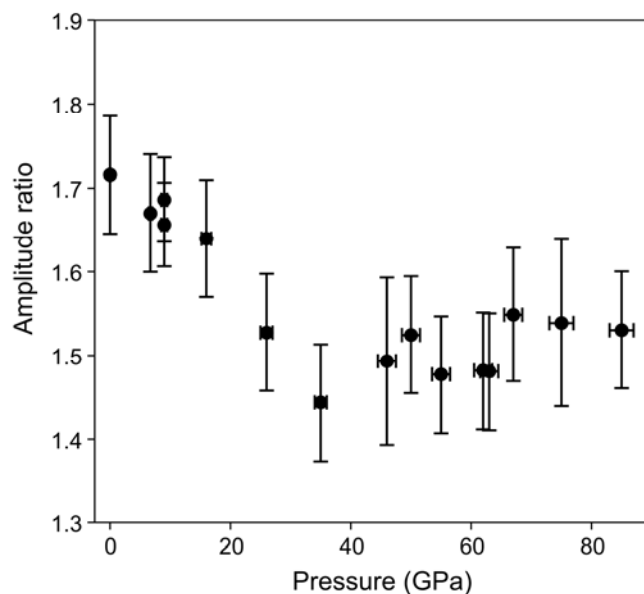


Figure 5.2-13 Pressure evolution of the amplitude ratio between white line at 7130 eV (feature A) and the peak at 7170 eV (feature B) of the XANES spectra of both Al-free and Al-bearing silicate perovskites shown in Fig. 5.2-12.

5.2.4.b.2.ii Ab initio calculation of X-ray absorption spectra

A similar theoretical spin-dependent method was applied for the $(\text{Mg}_{0.88}\text{Fe}_{0.12})\text{SiO}_3$ perovskite structure as was done for the $(\text{Mg}_{0.80}\text{Fe}_{0.20})\text{O}$ structure. To account for the effect of the

5. Results: iron in silicate perovskite

Fe $1s^1$ core-hole on the electronic band states, the excited iron atom (Fe^{ex}) was formally treated as an impurity inside a perovskite MgSiO_3 supercell of dimension $2 \times 2 \times 1$ and a background charge was used in order to keep the entire system neutral. The employed model system consists of an 80-atom orthorhombic supercell containing 16 Mg, 48 O and 16 Si atoms. To achieve the desired 12 wt-% Fe concentration one Mg atom was then substituted with Fe.

Fig.5.2-14 shows the theoretical Fe K-edge spectra calculated at 0 (HS) and 83 GPa (LS) using a self-consistent method to fill the Fe $3d$ -states. When applying pressure to $(\text{Mg}_{0.88}\text{Fe}_{0.12})\text{SiO}_3$ perovskite, two main features are seen in the calculated absorption spectra: (i) the onset peak gets broadened and its intensity maximum moves to higher energy values (cf. feature A_1 and A_2), and (ii) the two bumps labelled (B_1) and (B_1') convolute into a one single peak (B_2) when going towards high-pressure regimes. Similar changes were registered in the white-line region and in the high-energy part of the measured spectra shown in Fig. 5.2-12. This comparison confirms the power of such a calculational scheme in reproducing absorption spectra for band systems that are containing rather delocalized p-states.

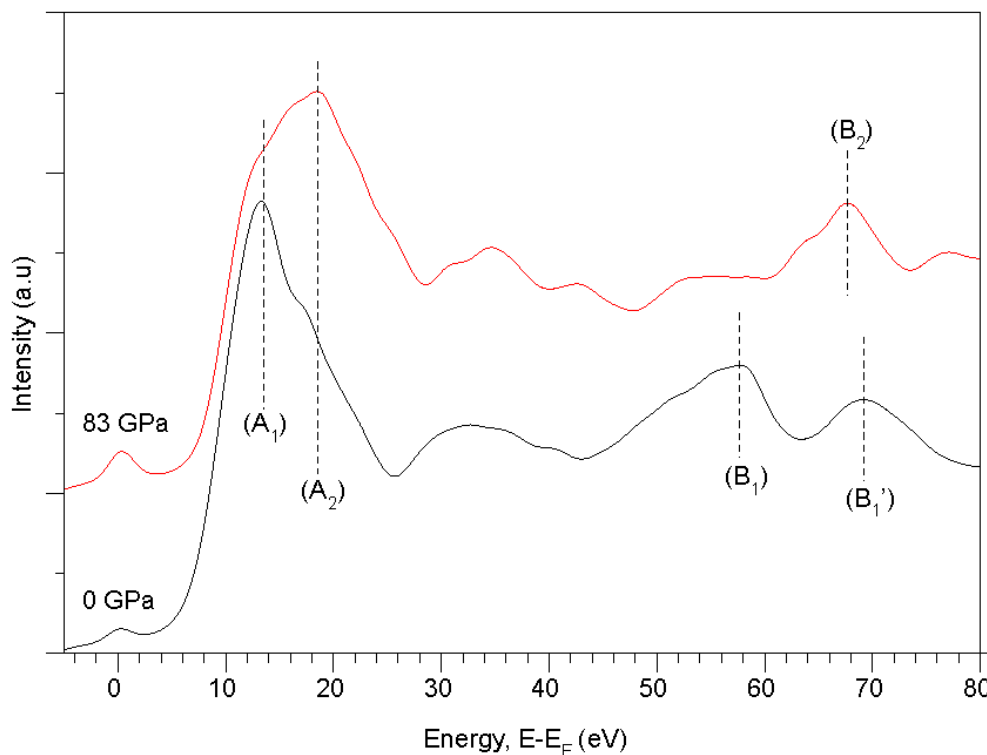


Figure 5.2-14 Calculated Fe K-edge for $(\text{Mg}_{0.88}\text{Fe}_{0.12})\text{SiO}_3$ perovskite at 0 and 83 GPa. The absorption spectra were computed using the experimental atomic positions and lattice parameters.

5. Results: iron in silicate perovskite

Fig. 5.2-15 represents the calculated unoccupied conduction band (CB) Fe partial density of states (pDOS) whereas Fig. 5.2-16 shows the calculated occupied (VB) partial Fe, O₁ and O₂ pDOS for (Mg_{0.88},Fe_{0.12})SiO₃ perovskite. Fig. 5.2-15 clearly shows that the spectroscopic signatures mentioned above originate mainly from the high-pressure behaviour of the Fe *p*-states. The evolution of features (A₁) and (A₂) in Fig. 5.2-14 reflect the relative change in the weight of the Fe-s and Fe-p pDOS with pressure. Whereas the former undergoes only a slight broadening with compression but does not shift significantly in energy, the latter is strongly affected, with an important broadening and energy shift.

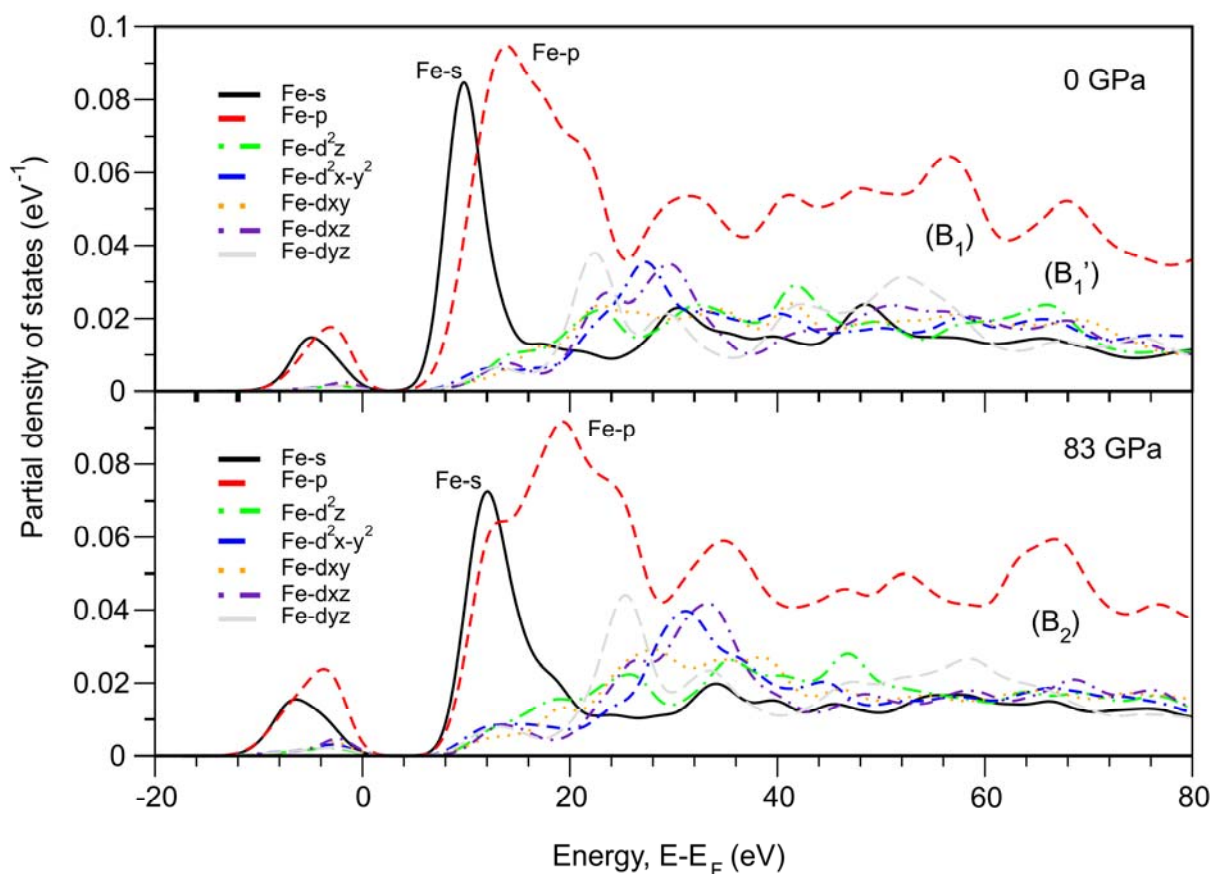


Figure 5.2-15 Calculated unoccupied (CB) Fe partial density of states (PDOS) for the (Mg_{0.88},Fe_{0.12})SiO₃ 2x2x1 supercell. The DOSs were broadened in order to facilitate comparison with the absorption spectra of Fig. 5.2-14.

Features (B₁), (B₁') and (B₂) are associated almost uniquely to variations of the Fe-p pDOS, and are therefore related to the structural variations that occur upon compression of the perovskite structure, i.e. to the reduction of the Fe-O distance. The high-pressure evolution of the Fe K-edge spectra is therefore attributed to the local geometrical modifications that are taking place around

5. Results: iron in silicate perovskite

the absorbing Fe atom. In particular, when going from 0 to 83 GPa the first coordination shell of iron, which consists of 8-oxygen ions, shrinks considerably, thus enhancing the degree of hybridization between the electronic states that are involved in the Fe-O bonds. We see from Fig. 5.2-16 that the oxygen *s*- and *p*- orbitals hybridize well with the *s*-, *p*- and *d*-states of Fe, indicating that the spectral shapes shown in Fig. 5.2-12 are largely modulated by Fe-O electronic hybridization. As observed for ferropervicase, the computed bandwidths for Fe and O states become larger and the electronic density of states get broader as pressure changes from 0 to 83 GPa. Here as well, the calculations show that we should expect spin state modifications to affect mainly the region of the spectra close to the absorption edge, where the occupied *d* pDOS is important.

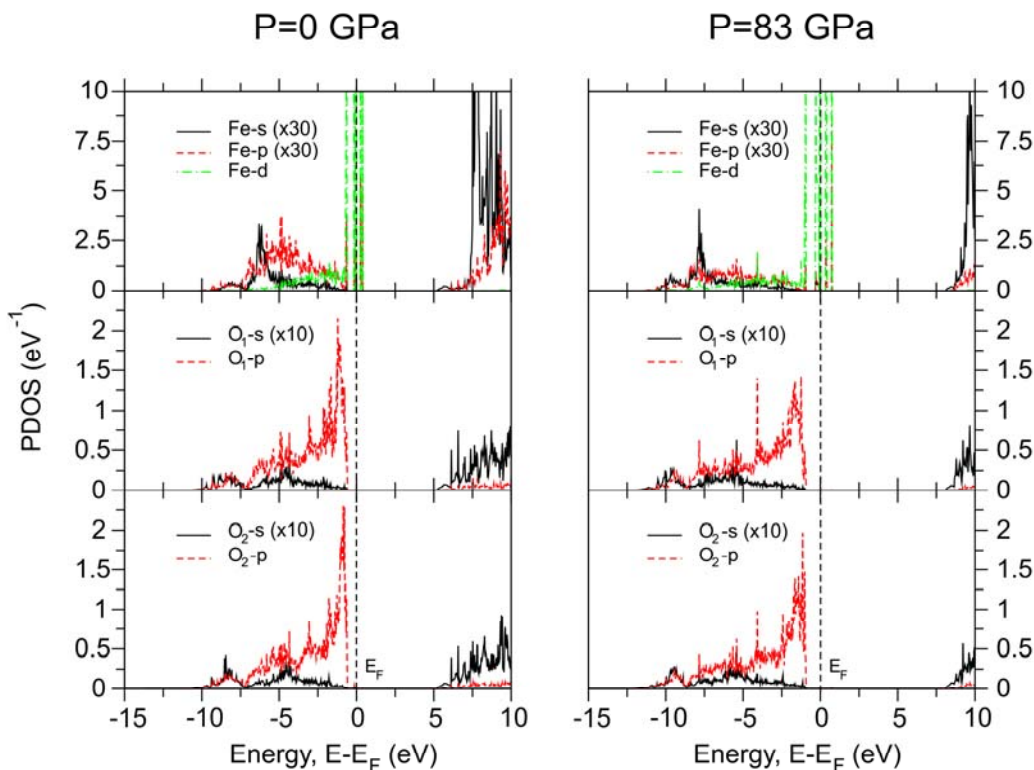


Figure 5.2-16 Calculated occupied (VB) partial Fe, O₁ and O₂ pDOS for (Mg_{0.88},Fe_{0.12})SiO₃ perovskite. Note that the atom type O₁ and O₂ constitute the first coordination shell of the absorbing Fe atom.

Spin-polarized 1s core-hole calculations of the (Mg_{0.88}Fe_{0.12})SiO₃ model system were also performed. Using a cell volume corresponding to ambient pressure we first obtained a magnetization of 5.00 μ_B /cell for a charge-converged spin-dependent calculation, thus describing

5. Results: iron in silicate perovskite

the low-pressure high-spin (HS) situation. We then performed a fixed spin calculation for the same geometry/volume by imposing a magnetic moment per cell of $1.00 \mu_B$ in order to reproduce a low-spin (LS) case. The obtained HS and LS spectra are shown in Fig. 5.2-17 with their relative spin-up and spin-down components. It is seen that the high-energy features (B_1 and B_1') are well reproduced in both spin channels for the two different HS and LS cases. Also, spin state is seen to affect (weakly) mainly the energy region close to the absorption edge.

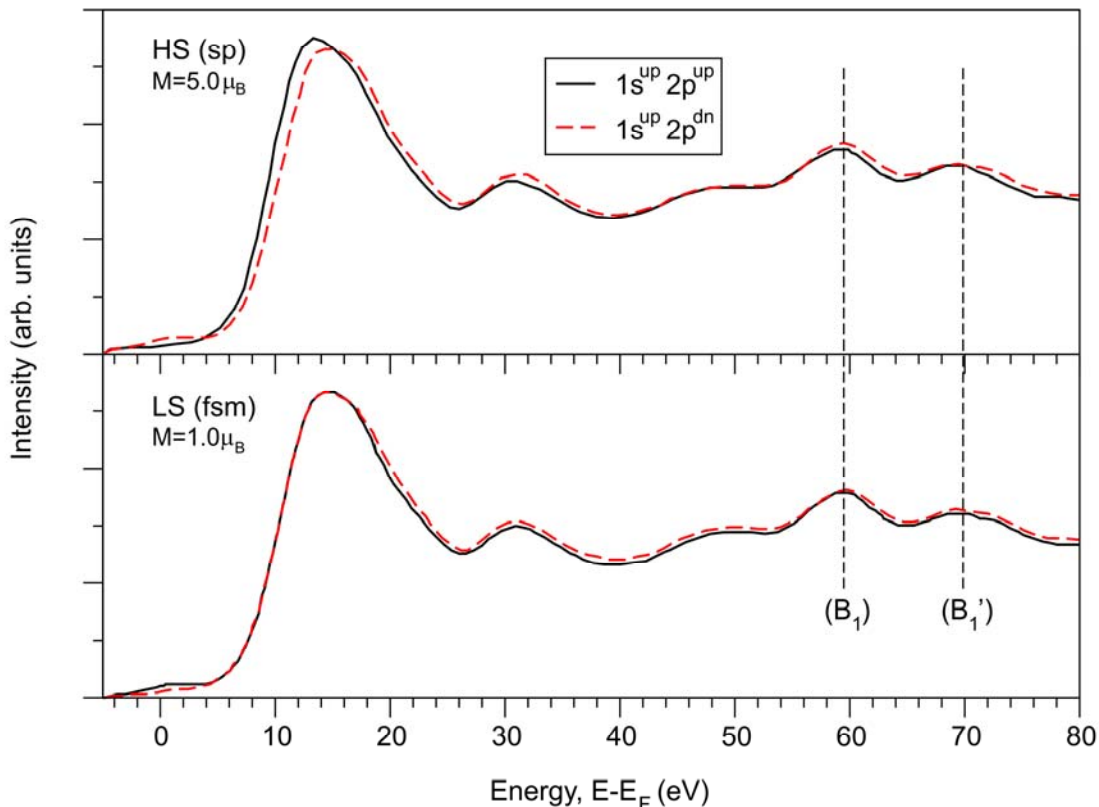


Figure 5.2-17 Theoretical Fe K-edge at ambient by fixing the Fe d -state occupations in the $(Mg_{0.88},Fe_{0.12})SiO_3$ perovskite model.

We further ran SCF calculations for a frozen Fe $3d$ shell by using the same theoretical scheme described earlier in Sec. 5.2.4.b.1.ii. This procedure was applied for unit cell volumes corresponding to a pressure range of 0-83 GPa and by imposing a $1s$ corehole for a divalent Fe configuration. We confirmed that the high-energy features labeled B_1 and B_1' are also spin-transition independent.

5. Results: iron in silicate perovskite

To summarize, for the perovskite system the ambient P theoretical calculations suggest that the effects of a spin transition on the Fe K-edge data are very weak. This is in qualitative agreement with our experimental results discussed above.

5.2.5. Conclusion

In this work we take advantage of recent experimental and theoretical improvements to perform for the first time a systematic Fe K-edge XANES study on several iron oxides and silicates under very high pressure. The aim is to establish the strengths and limitations of this technique in complementing information on oxidation and electronic state of iron in these compounds, and to define the abilities of the method to investigate spin transitions, particularly in the geophysically important systems ferropericlase and Al-free and Al-bearing perovskite.

Firstly, we demonstrate that the quality of the data allows to provide direct experimental validation for band-structure calculations. Modern *ab-initio* codes are found to be able to simulate the main features of the Fe K-edge XANES spectra in these complex Fe oxides, and their evolution with pressure. Concerning the sensitivity of XANES spectroscopy to the valence state of the absorber, by comparing data on a large variety of samples of known valence at the same pressure, we can conclude that whereas the centroid position of the first peak in the derivative of the XANES is a good fingerprint of Fe valence within the family of pure Fe oxides, it fails when attempting to include Mg and Ti containing Fe oxides. We attribute this failure to the modifications introduced in the local and electronic structure following the substitution of Fe with other elements. These are reflected in changes in the empty p density of states on Fe, directly probed by Fe K-edge XANES.

In addition, in perovskites, ilmenite and ferropericlase it is not possible to extract information on the valence of Fe from the pre-edge feature, because this feature is very weak at ambient pressure and remains weak as a function of pressure. The evolution with pressure of the energy value of the absorption onset is seen to be mainly affected by the effect of bond compression, which makes the edge drift towards higher energy with pressure at a constant rate. Modifications to this behaviour are indications of phase transitions, such as observed for ilmenite and ferropericlase.

Concerning the sensitivity of Fe K-edge XANES features to changes in spin state, we conclude that Fe K-edge XANES has variable sensitivity to the spin transition in different

5. Results: iron in silicate perovskite

systems. In ferropericlase, the HS-LS transition is clearly detected, whereas in the perovskites the effect of the HS-IS transition is visible but less pronounced.

Theoretical calculations are not as yet able to reproduce in a quantitative way the experimental trends observed on the Fe K-edge spectra upon the occurrence of spin transitions, but are extremely useful in helping to understand the origin of specific features of the spectra. Moreover, they provide invaluable explanations for the different sensitivity of spectral features to the underlying physics in such complex systems.

5.2.6. Acknowledgments

We acknowledge the European Synchrotron Radiation Facility for provision of synchrotron time and support. We thank the ID24 beamline technicians Sebastien Pasternak and Florian Perrin for valuable assistance in setting up the experiments. M.M. also wishes to acknowledge the Spanish Ministry of Science and Technology (MCyT) for financial support through the Ramón y Cajal program. The project was financially partly supported by funds from the German Science Foundation (DFG) Priority Programme SPP1236 under project Mc 3/16-1, and Eurocores EuroMinSci Programme.

5. Results: iron in silicate perovskite

5.3. XANES study of spin crossover in Fe-bearing silicate perovskite

Narygina O.¹, Kantor I.Yu.², Wu X.¹, Pascarelli S.³, Aquilanti G.³, McCammon C.¹, Dubrovinsky L.S.¹

¹*Bayerisches Geoinstitut, Universität Bayreuth, Germany;* ²*University of Chicago, CARS, Argonne, IL, USA ;* ³*European Synchrotron Radiation Facility, Grenoble, France*

Phase Transitions (2009) 82(4), 336-343

5.3.1. Abstract

(Mg_{0.88},Fe_{0.12})SiO₃, (Mg_{0.86},Fe_{0.14})(Si_{0.98},Al_{0.02})O₃ perovskites were studied using Fe K-edge X-ray Absorption Near Edge Spectroscopy (XANES) under pressure up to 85 GPa at ambient temperature. The amount and quality of the data collected allows to perform for the first time a systematic study of the absorption edge features as a function of pressure in this geophysically important system and permits to qualitatively confirm the presence of electronic transition in (Mg,Fe)(Si,Al)O₃ perovskite at 35-85 GPa, which according to Mössbauer data can be associated with the gradual high spin-intermediate spin crossover.

5.3.2. Introduction

The Earth's lower mantle is believed to consist predominantly of (Fe,Mg)(Si,Al)O₃ perovskite with a smaller amount of (Mg,Fe)O ferropericlasite and CaSiO₃ perovskite. The influence of iron on the properties of these phases is still not fully understood, but it is believed that properties such as elasticity, electrical and thermal conductivity, element partitioning between phases, etc. could be significantly affected by the electronic and structural behavior of iron in minerals under lower mantle conditions.

A number of studies have been carried out to investigate the spin and oxidation state of iron in (Fe,Mg)(Si,Al)O₃ perovskite under high pressures. It is known that in the perovskite structure iron can occur in the ferrous (Fe²⁺) or ferric (Fe³⁺) valence state. It is well established that ferrous iron occupies the large distorted 8-12-fold coordinated polyhedron, while ferric iron might also occupy the smaller octahedral site ([McCammon et al. 1992, 1998](#)). Electron energy

5. Results: iron in silicate perovskite

loss spectroscopy (EELS) and Mössbauer data suggest that the ferric iron fraction in (Fe,Mg)(Si,Al)O₃ perovskite depends on the aluminum content: with increasing aluminum concentration the amount of Fe³⁺ increases almost linearly ([Lauterbach et al. 2000](#); [McCammon et al. 2004](#); [Frost et al. 2004](#)).

Using K_β X-ray emission spectroscopy (XES) Badro et al. ([2004](#)) proposed that iron in (Fe,Mg)SiO₃ perovskite undergoes a spin crossover to the mix spin state at 70 GPa, with a following transition to the low-spin state at 120 GPa. Jackson et al. ([2005](#)) investigated the iron spin state in (Fe,Mg)SiO₃ perovskites with different iron contents using nuclear forward scattering (NFS), and inferred a high-spin to low-spin transition in Fe³⁺ at 70 GPa, with Fe²⁺ remaining in the high spin state throughout the studied pressure interval. Combining XES and NFS techniques to study (Mg,Fe)(Si,Al)O₃ perovskite, Li et al. ([2006](#)) inferred that Fe undergoes a transition from high-spin to low-spin state in the pressure range 20-100 GPa. From these results it appears that the use of only XES and NFS methods was not able to provide a conclusive answer to the question of the iron spin state in magnesium-bearing silicate perovskite at the megabar pressure range.

X-ray absorption near edge spectroscopy (XANES) directly probes the empty density of electronic states above the Fermi level around the absorber atom. Fe K-edge XANES, along with Electron Energy Loss Spectroscopy (EELS) and conventional and synchrotron Mössbauer spectroscopies (nuclear forward scattering: NFS), is one of the more precise experimental techniques to follow electronic and local structure around Fe and can be relatively easily combined with the diamond anvil cell (DAC) technique for making *in situ* measurements under high pressure and temperature conditions. In contrast to Mössbauer spectroscopy, XANES does not require ⁵⁷Fe-enrichment of the sample which simplifies the experimental procedure. While conventional Mössbauer spectroscopy gives information over a large region of the sample, it has recently become possible to obtain high quality XANES with the micron resolution ([Pascarelli et al. 2006](#)) enabling the analysis of individual regions within the DAC. Therefore micro-XANES spectroscopy can be a powerful experimental tool for *in situ* high-pressure and/or high-temperature measurements of the local electronic and crystallographic environment of iron. Consequently Fe K-edge micro-XANES can provide information that complements the results of other methods (XRD, conventional Mössbauer, NFS, and XES) for examining the spin and oxidation states of iron under Earth's lower mantle pressures.

5. Results: iron in silicate perovskite

Up to now, no systematic study has been performed on the evolution of Fe K-edge XANES in (Mg,Fe)(Si,Al)O₃ perovskite up to very high pressures. One of the reasons for this is related to the experimental difficulties in obtaining good quality data at such extreme conditions, due to the high absorption of the diamond anvils at low X-ray energy (the Fe K-edge is at ~ 7 KeV), and to the strong constraint on spot size and stability that these studies impose. Many of these difficulties have been overcome with the use of 3rd generation synchrotron sources, coupled to advances in X-ray optics and high pressure techniques.

The aim of this study was therefore to take advantage of these recent technical advances to perform for the first time a systematic Fe K-edge XANES study of Fe-bearing magnesium silicate perovskite under pressure in order to establish the strengths and limitations of this technique in complementing information on oxidation and electronic state of iron in (Mg,Fe)(Si,Al)O₃.

5.3.3. Sample description and preparation

Synthetic (Mg,Fe)SiO₃ and (Mg,Fe)(Si,Al)O₃ perovskite samples were studied by means of XANES spectroscopy. All samples were enriched with the ⁵⁷Fe isotope (in order to use the same samples for high-pressure Mössbauer spectroscopy). Al-bearing and Al-free silicate perovskite phases were synthesized in a laser-heated DAC at 30-35 GPa and approximately 2500°C from two orthopyroxene starting materials with compositions Mg_{0.86}Fe_{0.14}Si_{0.98}Al_{0.02}O₃ and Mg_{0.88}Fe_{0.12}SiO₃ (each 61% enriched in ⁵⁷Fe) that were described in Lauterbach et al. (2000). Run products were found using X-ray diffraction to consist almost exclusively of (Mg,Fe)SiO₃ or (Mg,Fe)(Si,Al)O₃ perovskite (in Al-bearing samples traces of SiO₂ stishovite were detected), and chemical compositions were found using the electron microprobe to be the same as the starting materials within experimental uncertainty. The relative concentration of Fe³⁺ was found by means of Mössbauer spectroscopy to be 0.10 (±0.02) and 0.25 (±0.07) for the Mg_{0.88}Fe_{0.12}SiO₃ and Mg_{0.86}Fe_{0.14}Si_{0.98}Al_{0.02}O₃ perovskite samples, respectively (Fig. 5.3-1a,b).

5. Results: iron in silicate perovskite

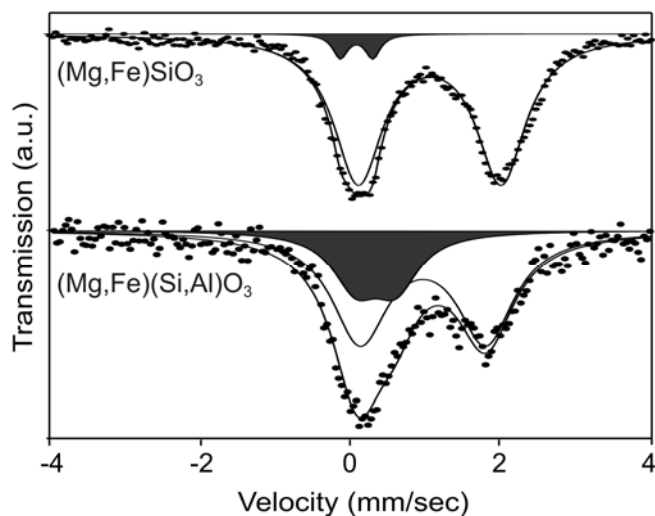


Figure 5.3-1. Mössbauer spectra of $(\text{Mg,Fe})\text{SiO}_3$ and $(\text{Mg,Fe})(\text{Si,Al})\text{O}_3$ perovskites at ambient conditions. The spectral area colored in black corresponds to Fe^{3+} .

5.3.4. Experimental method

For *in situ* high pressure micro-XANES and Mössbauer spectroscopy measurements in the DAC we used diamonds with 250 or 300 μm culet size. Samples were loaded into Re gaskets that had been preindented to $\sim 30 \mu\text{m}$ and then drilled with a hole of 125 μm diameter. No pressure transmitting medium was used that allowed to obtain high quality absorption data in high pressure range. For pressure calibration and evaluation of the pressure gradient we used small ruby chips that were loaded into the cell along with the sample. At the highest pressures ($\sim 80 \text{ GPa}$) the uncertainty in pressure measurements was estimated to be 5 GPa, while the pressure difference between the center and the edge of the pressure chamber was a maximum of 5 GPa. After each increase or decrease of pressure with step $\sim 5 \text{ GPa}$ above 30 GPa samples were annealed at 1700-1900 K by laser heating in order to release compression induced stresses in the sample and to decrease pressure gradient. K-edge XANES measurements were performed at the European Synchrotron Radiation Facility at the energy dispersive XAS beamline ID24. The beam was focused horizontally using a curved polychromator Si (111) crystal in Bragg geometry and vertically with a bent Si mirror placed at 2.8 mrad with respect to the direct beam ([Pascarelli et al. 2004](#)). The Bragg diffraction peaks arising from the diamond anvils were removed from the energy range of interest by changing the orientation of the diamond anvil cell and following in real time the intensity of the transmitted beam on a two-dimensional detector.

5. Results: iron in silicate perovskite

The measured XANES spectra were analyzed using the VIPER program ([Klementev 2001](#)). The flat part of the pre-edge region of the spectrum was fitted to the Victoreen function ($F = a + bE^{-3}$, where E is the absorption energy and a and b are fit parameters) and this baseline was extended over the entire energy region. The post-edge jump in X-ray absorption was then normalized to 1. Transmission Mössbauer spectra were recorded on a constant acceleration Mössbauer spectrometer at temperatures in the range 300-800 K and pressures in the range from ambient up to above 80 GPa. The experimental procedure is described in detail in Kantor et al. ([2004](#)) and McCammon et al. ([1992](#)).

5.3.5. Results and discussion

5.3.5a Oxidation state of iron

The most common way to extract information about oxidation state of iron from the XANES spectra is to analyze the pre-edge peak structure (e.g., [Berry et al. 2003](#)). But the intensity of the pre-edge features is very weak for both Al-free and Al-bearing perovskites (Fig. 5.3-2a, b). In this case the extraction of information about iron oxidation state is challenging, and it is necessary to identify other spectral features that are systematically correlated with the amount of ferric iron. In a previous XANES study of silicate glasses ([Berry et al. 2003](#)), the following features were proposed: (i) the energy of the main absorption edge, normalized to one at a height of 0.9; and (ii) the areas of the derivative peaks associated with the $1s \rightarrow 4s$ and $1s \rightarrow 4p$ transitions.

For our XANES experimental data the most well defined and reproducible spectral feature is the energy corresponding to the absorption edge, which one can determine from the centroid position of the first peak in the derivative (Fig. 5.3-3, inset). Even though Al-free and Al-bearing perovskites have different $\text{Fe}^{3+}/\Sigma\text{Fe}$ ratio (0.10 (± 0.02) for Al-free and 0.25 (± 0.07) Al-bearing perovskite samples), at any taken pressure energy position of the absorption Fe K-edge is almost the same in the range of uncertainty for both perovskites (Fig. 5.3-3). The fact that the difference in redox ratio almost does not effect the absorption edge position we address to the addition of Al that evidently modifies the density of empty states just above the Fermi level with respect to that of the pure Fe-bearing magnesium silicate perovskite. Therefore the centroid position of the first peak in the derivative could be considered as a good fingerprint of Fe valence

5. Results: iron in silicate perovskite

only within the family of pure Fe silicates, while it fails when attempting to include Al containing Fe silicates. Consequently we can not use absorption edge position as a feature correlated with the redox ratio, at least in this particular case.

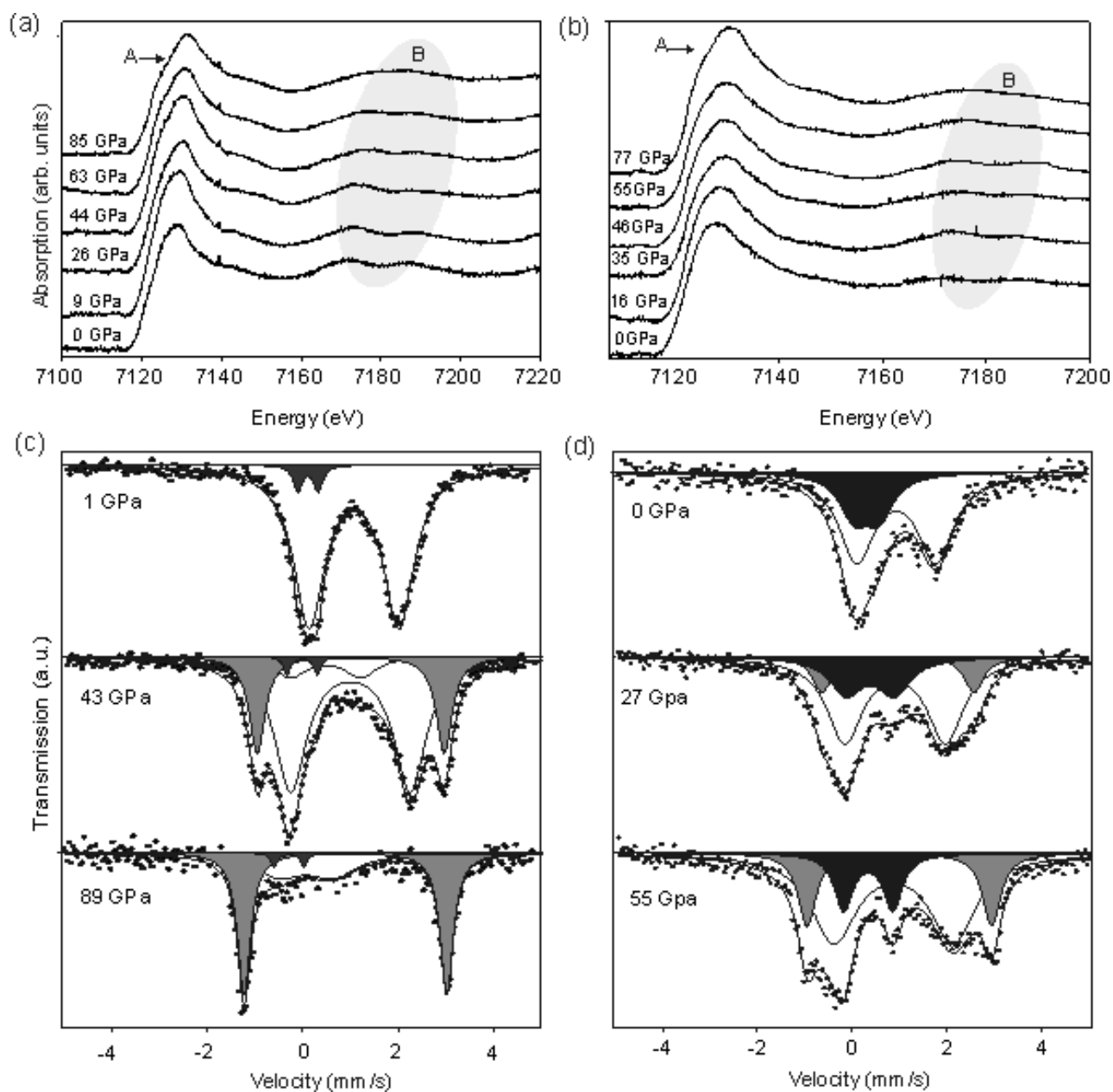


Figure 5.3-2. Room temperature XANES spectra of (Mg,Fe)SiO₃ (a) and (Mg,Fe)(Si,Al)O₃ (b) perovskites; evolution of Mössbauer spectra taken at room temperature for (Mg,Fe)SiO₃ (c) and (Mg,Fe)(Si,Al)O₃ (d) perovskites.

5. Results: iron in silicate perovskite

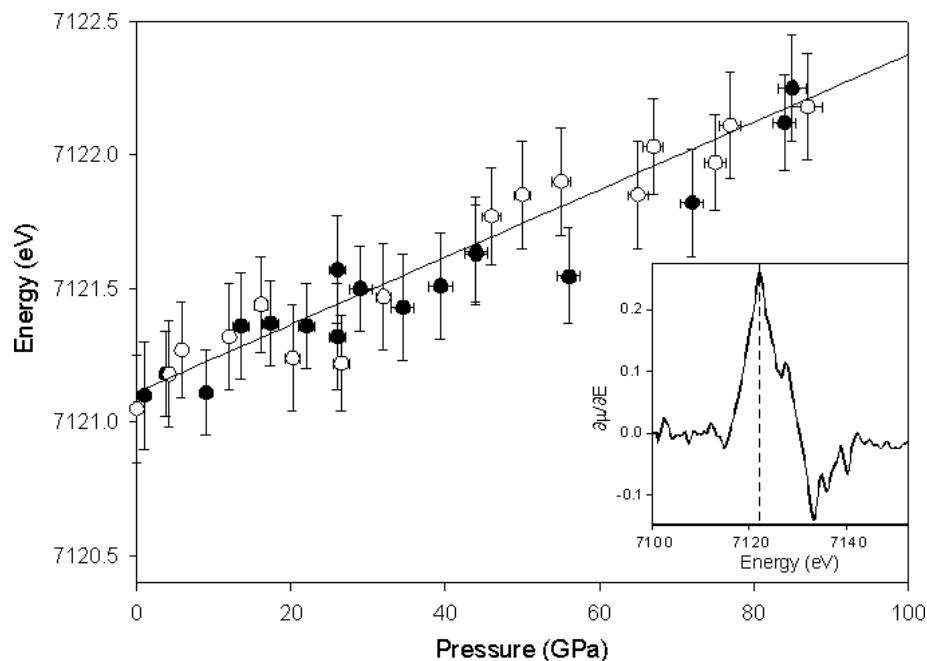


Figure 5.3-3 Pressure evolution of the Fe K-edge position for Al-free (●) and Al-bearing (○) perovskites. Straight line corresponds to the linear fit of the experimental points for both perovskites. Inset presents the derivative of the Fe K-edge of (Mg,Fe)SiO₃ at 44 GPa, room temperature.

5.3.5b Spin state of iron

The main motivation for the study is to examine the ability of XANES to detect spin transitions under high pressure. Our recent Mössbauer spectroscopic results for both (Fe,Mg)(Si,Al)O₃ and (Fe,Mg)(Si,Al)O₃ perovskite phases, which are discussed in detail in McCammon et al. 2008, demonstrate clear changes in iron electronic state in the perovskite structure starting at about 30 GPa (Figs. 5.3-2c,d). In brief, for both perovskites at pressures of about 25-30 GPa we observed the appearance of the new doublet (shown in dark gray on Figs. 5.3-2c, d) that has an isomer shift close to that of high-spin Fe²⁺ (about 1 mm s⁻¹) and an unusually large quadrupole splitting, close to 4 mm s⁻¹, which is probably the highest quadrupole splitting ever reported for an iron-containing material (Bancroft et al., 1967). The relative area of the new high-QS component increases with pressure for both the Al-free and the Al-bearing sample, whereas the relative area of the doublet corresponding to high-spin Fe²⁺ decreases and approaches zero at pressures about 80 GPa (Figs. 5.3-2c,d). X-ray diffraction data do not show any sign of structural transition in silicate perovskite within the 30-60 GPa pressure range (Komabayashi et al. 2008); therefore we suggest that the observed changes in iron behavior in the

5. Results: iron in silicate perovskite

Mössbauer spectra can be interpreted as pressure-induced spin crossover, specifically a high-spin to intermediate-spin transition in Fe^{2+} which is described in detail in McCammon et al. (2008).

Apart from the pressure induced gradual shift of the Fe K-edge (Fig. 5.3-3) XANES spectra of the silicate perovskites indicate also some changes at 30-87 GPa (Figs. 5.3-2a, b). In the white-line region a small bend on the first broad peak appears with increasing pressure (feature A). Also in the high-energy region, two peaks that are well resolved at low pressures converge and eventually form one broad peak at 80 GPa (feature B).

Carefully analyzing the pressure evolution of the absorption spectra of both perovskites we found out that the relative intensities of the two main peaks (at 7130eV and at 7170eV (Figs. 5.3-2a, b)) change with pressure. We extracted the amplitude ratios between these main peaks from the experimental XANES spectra and plotted them as a function of pressure for both Al-free and Al-bearing silicate perovskites (Fig. 5.3-4). As one can see from the plot (Fig. 5.3-4) the pressure dependence of amplitude ratio does change at 30-35 GPa, that corresponds to the pressure at which the crossover to intermediate spin state in Fe-bearing silicate perovskite starts, according to our recent Mössbauer results (McCammon et al., 2008).

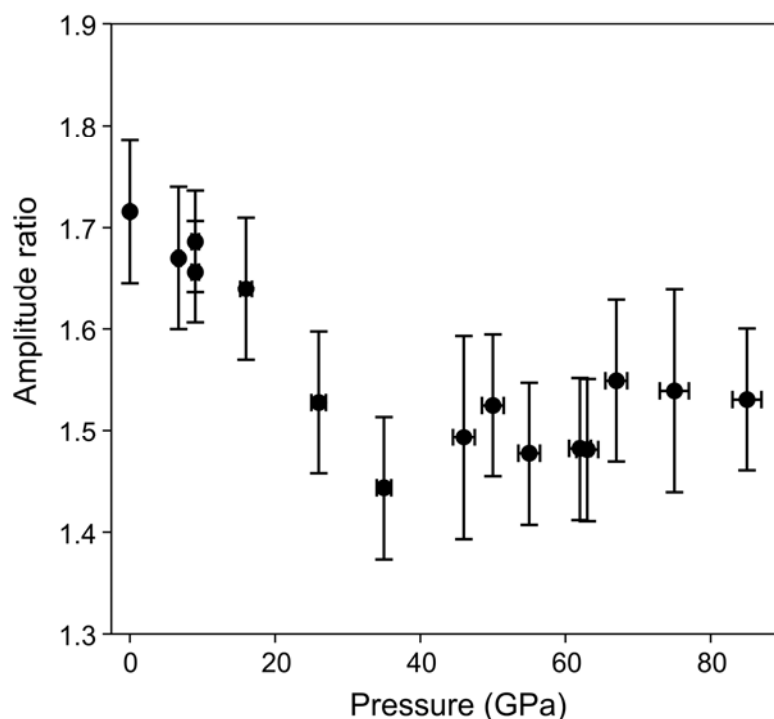


Figure 5.3-4. The amplitude ratio between peaks at 7130 eV and 7170 eV of the absorption spectra from both Al-free and Al-bearing silicate perovskites as a function of pressure.

5. Results: iron in silicate perovskite

Thus using micro-XANES technique we qualitatively confirm the presence of electronic transition in Fe-bearing silicate perovskite in the pressure range 35-80 GPa, which according to the Mossbauer data could be associated with the high spin - intermediate spin crossover.

5.3.6. Conclusion

In this work we take advantage of these recent technical advances to perform for the first time a systematic Fe K-edge XANES study of $(\text{Mg,Fe})\text{SiO}_3$ and $(\text{Mg,Fe})(\text{Si,Al})\text{O}_3$ perovskites under pressure in order to establish the strengths and limitations of this technique in complementing information on electronic state of iron in silicate perovskites.

We conclude that the pre-edge features of the Fe K-XANES in perovskites are very weak at ambient pressure and they remain weak as a function of pressure. This makes it impossible to extract information on oxidation state of Fe.

We showed that Fe K-edge XANES features are sensitive to the changes of the spin state in magnesium silicate perovskites and therefore can provide the complementing information on the behavior of iron in this system at elevated pressures.

5.3.7. Acknowledgements

We acknowledge the European Synchrotron Radiation Facility for provision of synchrotron time and support. The project was financially partly supported by funds from the German Science Foundation (DFG) SPP1236 Priority Programme, and Eurocores EuroMinSci Programme.

5. Results: iron in silicate perovskite

5.4. Electronic state of Fe²⁺ in (Mg,Fe)(Si,Al)O₃ perovskite and (Mg,Fe)SiO₃ majorite at pressures up to 86GPa and temperatures up to 800K

Narygina O.¹, Kantor I. Yu.², McCammon C.A.¹, Dubrovinsky L.S.¹

¹*Bayerisches Geoinstitut, Universität Bayreuth, 95440 Bayreuth, Germany;* ²*CARS, University of Chicago, IL 60437, USA*

Submitted to Physics and Chemistry of Minerals

5.4.1. Abstract

Using conventional Mössbauer spectroscopy we performed a comparative study of silicate perovskite (Fe_{0.12}Mg_{0.88}SiO₃) and majorite (with two compositions - Fe_{0.18}Mg_{0.82}SiO₃ and Fe_{0.11}Mg_{0.88}SiO₃) at pressures up to 81 GPa in the temperature range 296-800 K. Quadrupole splitting (QS) of the doublet associated with eight-coordinated Fe²⁺ (⁵⁷Fe²⁺) in majorite decreases with temperature at constant pressure and its behavior is described by Huggins model with the energy splitting between *e_g* levels equals to 1500 (50) cm⁻¹ for Fe_{0.18}Mg_{0.82}SiO₃ and 1680 (70) cm⁻¹ for Fe_{0.11}Mg_{0.88}SiO₃. Contrary, for the silicate perovskite at pressures above 30 GPa we observed appearance of the spectral component with QS about 4 mm/sec, temperature dependence of which can not be described in the framework of Huggins model, and amount of the component increases with temperature. Based on the differences in the high pressure high temperature behaviour of ⁵⁷Fe²⁺ in the perovskite and majorite phases we confirmed the presence of the gradual high spin – intermediate spin crossover in the lower mantle perovskite.

5.4.2. Introduction

Materials with the perovskite and garnet crystal structures are very common among dense oxides containing several cations. Iron-bearing magnesium silicate perovskite and majorite (garnet-structured silicate) are abundant minerals of the Earth's transition zone and lower mantle.

(Mg,Fe)(Si,Al)O₃ perovskite has an orthorhombic structure, with Si or Al in nearly symmetrical octahedral “B-site” (colored in green in Fig. 5.4-1a) and Mg²⁺ or Fe²⁺ in more distorted 8- to 12-fold coordinated “A-site” ([Horiuchi et al. 1987](#), [McCammon et al. 1992](#)). At

5. Results: iron in silicate perovskite

ambient conditions A-O distances range from 2.02 Å to 2.43 Å with average value 2.21 Å. A certain amount of Fe³⁺ can also probably occupy the smaller octahedral site (McCammon et al. 1992; McCammon, 1998; Jephcoat et al. 1999). Physical properties (elasticity, thermal and electrical conductivity, etc.) of the silicate perovskite are believed to be influenced by the electronic state of iron at high pressures and temperatures (Badro et al. 2004, McCammon et al. 2008, Goncharov et al. 2008, Keppler et al. 2009).

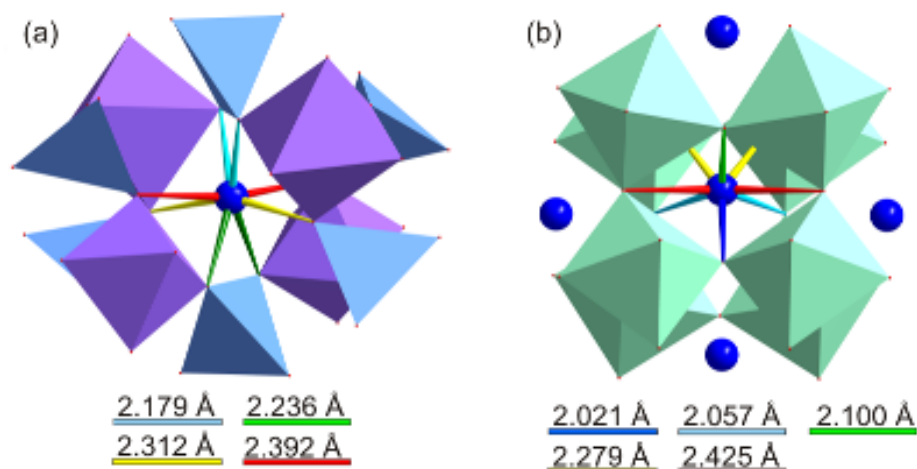


Figure 5.4-1. Coordination polyhedron of ferrous iron (large solid blue spheres) in the (a) perovskite (Ross and Hazen 1989) and (b) garnet (Angel 1989; McCammon and Ross 2003) structures. Green octahedra and blue tetrahedra represent the oxygen environment of Si, and the purple octahedra represent the Mg/Si site in the garnet structure.

(Mg,Fe)SiO₃ majorite has a tetragonal structure, with Mg²⁺ and Fe²⁺ cations in the dodecahedral (or distorted cubic) site and Si in the octahedral (colored in purple in Fig. 5.4-1b) and tetrahedral (colored in blue in Fig. 5.4-1b) sites; a small amount of Fe³⁺ can also occupy the octahedral site. The addition of Al to the end member tetragonal MgSiO₃ majorite stabilizes cubic symmetry (Hatch and Ghose 1989). At ambient conditions interatomic distances in dodecahedral position range from 2.18 Å to 2.39 Å with the average value 2.28 Å. Since the silicate garnet and perovskite structures have clear similarities in environment of Fe²⁺ located in 8-coordinated position, one can expect analogues in the iron behaviour in these two minerals.

There have been several experimental and theoretical studies on the iron spin state in magnesium silicate perovskite at high pressures, but the results are rather controversial. Badro et al. (2004), using K_β X-ray emission spectroscopy (XES), suggested that iron in perovskite first undergoes a high spin (HS) - intermediate spin (IS) crossover at 70 GPa and then the transition to

5. Results: iron in silicate perovskite

the low-spin (LS) state occurs at 120 GPa. Jackson et al. (2005), using nuclear forward scattering (NFS), observed a spin-pairing transition in ferric iron at 70 GPa, while ferrous iron remained HS through the entire studied region. Li et al. (2006), combining XES and NFS techniques, reported a gradual HS-LS crossover in iron at 20-100 GPa. Recently our group published results of Mössbauer spectroscopy studies of iron behaviour in (Mg,Fe)(Si,Al)O₃ perovskite at pressures up to 110 GPa (McCammon et al. 2008). We observed a gradual change of the electronic state of ferrous iron in perovskite at 30 – 65 GPa, which we interpreted as HS-IS crossover. In particular, at about 30 GPa a new Mössbauer component with an unusually large value of quadrupole splitting (QS) (about 4 mm s⁻¹) was detected, and the amount of the component increases with pressure and temperature. This new component was assigned to intermediate spin Fe²⁺ in the 8-12-fold coordinated site in the perovskite structure.

The QS of 4 mm s⁻¹ is nearly the highest value that has ever been reported for any iron containing material (Bancroft et al., 1967). A similar value (3.6 mm s⁻¹) was previously observed for 8-fold coordinated high spin ferrous iron in the garnet structure (Murad and Wagner, 1987; McCammon and Ross 2003). Since Fe²⁺ in perovskite has a similar oxygen environment to garnet (Fig. 5.4-1) we decided to compare the behaviour of “high-QS component” in (Mg,Fe)SiO₃ perovskite with that of (Mg,Fe)SiO₃ majorite as a function of pressure and temperature in order to understand whether the origin of the high QS value for ferrous iron in the perovskite is similar to that in majorite. This work compliments and extends the results published by McCammon et al. (2008).

5.4.3. Experimental procedure

In order to evaluate the influence of the synthesis procedure on the behavior of iron-bearing silicate perovskite at high pressure we investigated two types of samples: the first had been pre-synthesized in a multianvil press and the second was synthesized *in situ* in diamond anvil cell (DAC). The first set of samples of ⁵⁷Fe_{0.12}Mg_{0.88}SiO₃ perovskite were synthesized from ⁵⁷Fe-enriched clinopyroxene starting material in a Re capsule using a multianvil press at 25 GPa and 1650°C with heating duration 20 min. Further details are given in McCammon et al. (2004) and Frost et al. (2004). The second set of ⁵⁷Fe_{0.12}Mg_{0.88}SiO₃ perovskite was synthesized from the same starting material in a DAC at a pressure of 30-35 GPa and temperature about 2500°C which corresponds to lower mantle conditions. Chemical compositions of perovskite samples

5. Results: iron in silicate perovskite

synthesized in a DAC (after recovering to ambient conditions) and in the multianvil apparatus were checked by electron microprobe and within the uncertainties of measurements turned out to be the same. According to X-ray diffraction data, samples contain pure silicate perovskite although in some cases traces of SiO₂ stishovite were detected.

⁵⁷Fe_{0.18}Mg_{0.82}SiO₃ and ⁵⁷Fe_{0.11}Mg_{0.88}SiO₃ majorite samples were also synthesized from ⁵⁷Fe-enriched clinopyroxene starting material in a Re capsule using a multianvil press at 19 GPa and 1900°C with heating duration 25 min. The chemical composition of majorite samples was also checked by electron microprobe, and X-ray diffraction showed the presence of a single silicate majorite phase. Further details are given in McCammon & Ross (2003).

For the high-pressure high-temperature Mössbauer measurements in a DAC we used diamonds with 300 µm culet size. The sample was loaded in a Re gasket that was preindented to ~ 30 µm and then drilled with a hole of 125 µm diameter. For pressure calibration and evaluation of pressure gradient we used small ruby chips that were loaded into the cell along with the sample. At the highest pressures (~ 81 GPa) the uncertainty in pressure determination by ruby fluorescence was estimated to be below 4 GPa, while the pressure gradient between the center and border of the pressure chamber did not exceed 5 GPa. After each increase or decrease of pressure with step ~ 5 GPa above 30 GPa perovskite samples were annealed at 1700-1900 K by laser heating. Transmission Mössbauer spectra were recorded at temperatures 300-800 K in the pressure range from ambient up to 81 GPa on a constant acceleration Mössbauer spectrometer with a ⁵⁷Co point source. The experimental procedure of high-pressure Mössbauer spectroscopic measurements is described in detail in McCammon et al. (1992) and Kantor et al. (2004). In order to heat samples up to 800 K under pressure we used an external resistive heater mounted inside the DAC (Fig. 5.4-2). The heater consists of a ceramic plate wound with Pt wire of 0.5 mm diameter. The heater wire was isolated from other conductive parts of the cell by high-temperature ceramic glue (the layer of ceramic glue is not shown in Fig. 5.4-2). A S-type thermocouple (90%Pt10%Rh/Pt) is glued to another part of the cell as shown in Fig. 5.4-2. The temperature gradient within the pressure chamber was estimated to be a maximum of 20 K.

5. Results: iron in silicate perovskite

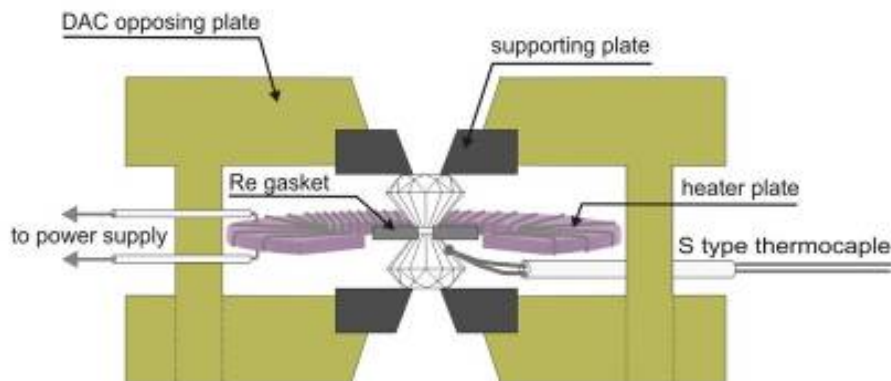


Figure 5.4-2. Schematic drawing of the DAC with an external resistive heating system.

5.4.4. Results

5.4.4a (Mg,Fe)SiO₃ perovskite

5.4.4a.i Pressure effect

Selected Mössbauer spectra of (Mg,Fe)SiO₃ perovskite collected on compression at room temperature are presented in Fig. 5.4-3. We chose a fitting model that is consistent with known constraints on the hyperfine parameters (central shift (CS) and quadrupole splitting (QS)) (McCammon, 1998, McCammon et al., 2008). At pressures up to ~ 30 GPa (Fig. 5.4-3a) the spectra were fitted to two quadrupole doublets with Lorentzian lineshape: (i) high spin Fe²⁺, shown in dark gray (CS is about 1 mm s⁻¹ and QS is about 2.4 mm s⁻¹); and (ii) Fe³⁺, the relative amount of which varies from 8% to 12% depending on the sample (shown in black). At a pressure of about 30 GPa we observed the appearance of a third doublet (shown in blue on the Figs. 5.4-3b,c), the relative area of which increases with pressure (Fig. 5.4-3 and Fig. 5.4-4c). The new doublet has CS close to that for HS Fe²⁺ and an unusually large QS, close to 4 mm s⁻¹. This component was assigned to IS Fe²⁺ by McCammon et al. (2008), but for now we will simply denote it as the high-QS component. Also during compression we observed an increase of the absorption at ~ 0.4 mm s⁻¹ (doublet shaded light gray in Figs. 5.4-3b,c). We suggest that this component is associated with charge transfer, the contribution of which increases with pressure (Fig. 5.4-4c) (Fei et al. 1994, McCammon, 1998).

5. Results: iron in silicate perovskite

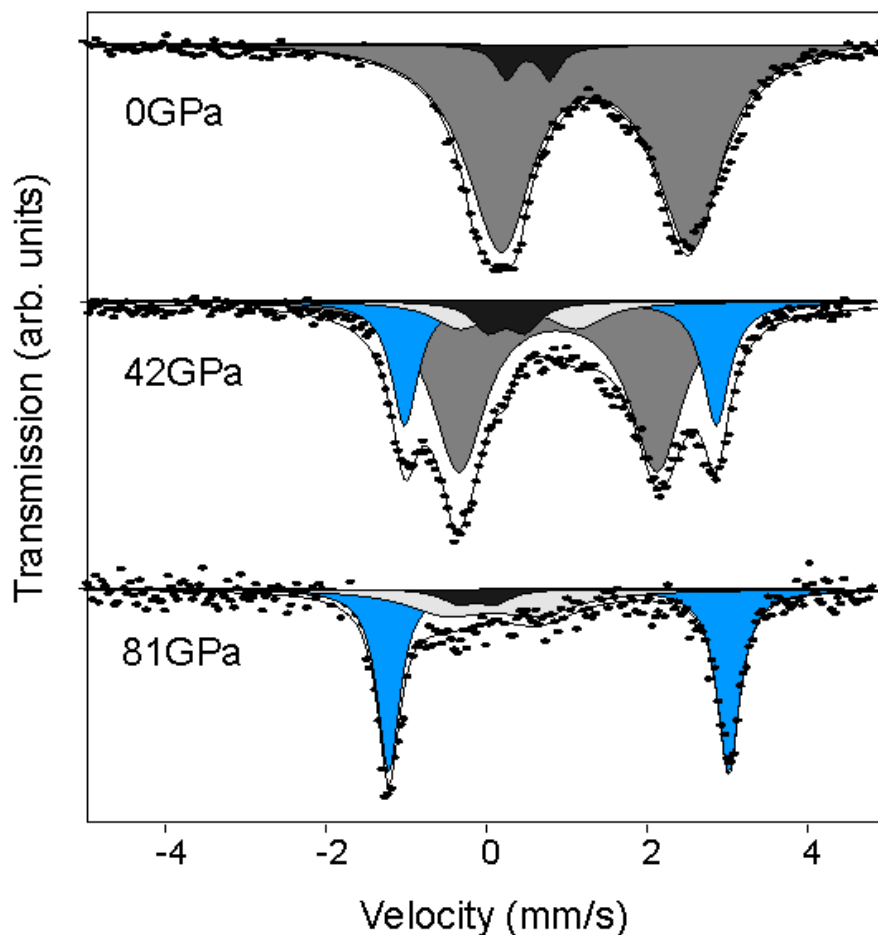


Figure 5.4-3. Selected Mössbauer spectra of Fe_{0.12}Mg_{0.88}SiO₃ perovskite at variable pressure collected at room temperature. The solid circles correspond to the experimental data. Components are shaded as follows: dark gray – HS Fe²⁺, black – Fe³⁺, blue – high-QS component, light gray – charge transfer component.

The hyperfine parameters and relative areas of all spectral components are presented in Fig. 5.4-4. The CS of HS Fe²⁺ and high-QS components decreases with pressure, while QS slightly increases (Figs. 5.4-4a,b).

There are no noticeable differences between the spectra of samples synthesized in a multianvil press and in a DAC, except for a small difference in Fe³⁺ content (silicate perovskite synthesized in a multianvil press contains 2-4% more Fe³⁺ than the sample synthesized in a DAC), but there is no observable influence on the hyperfine parameters of spectral components.

5. Results: iron in silicate perovskite

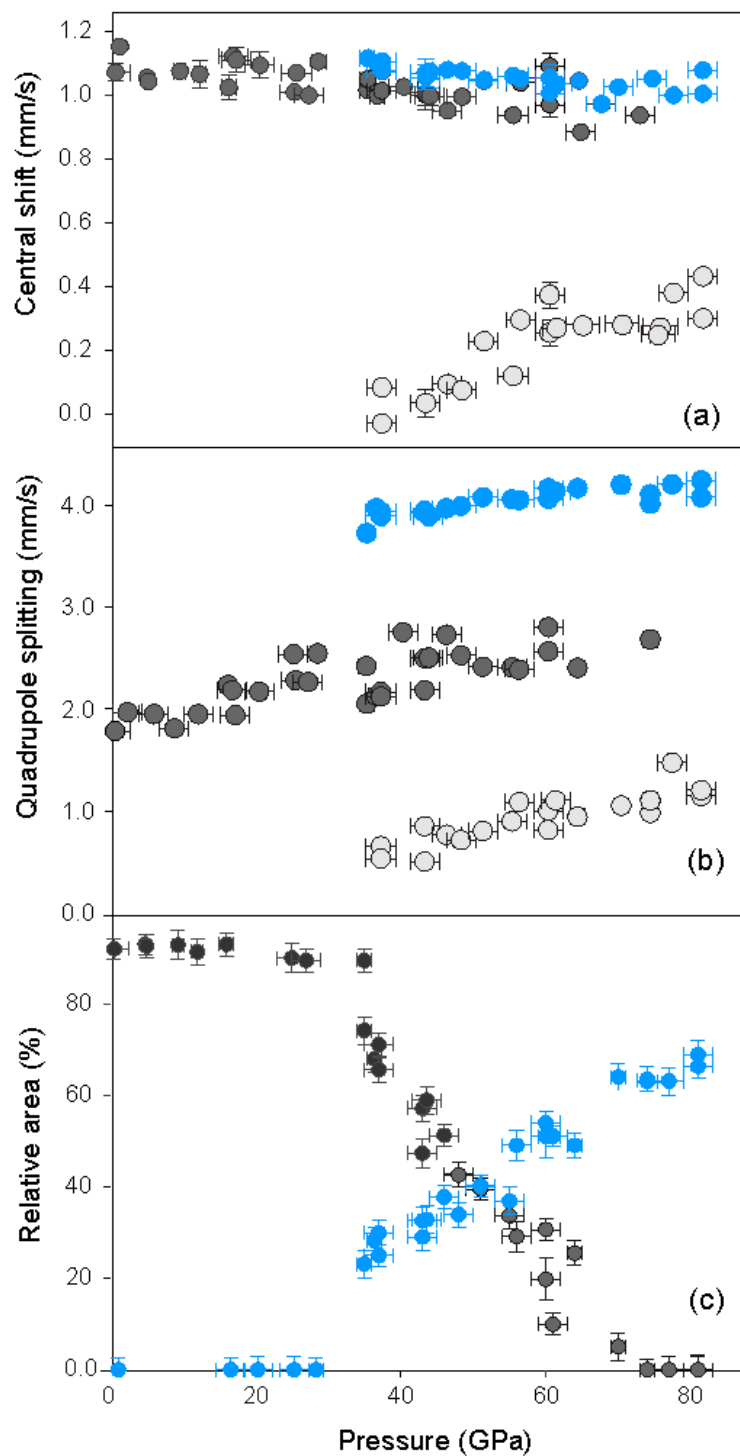


Figure 5.4-4. Central shift (a), quadrupole splitting (b) and relative area (c) as a function of pressure for $\text{Fe}_{0.12}\text{Mg}_{0.88}\text{SiO}_3$ perovskite HS Fe^{2+} (dark gray circles), high-QS component (blue circles) and the charge transfer component (light gray circles). For clarity the relative area of the charge transfer component is not shown.

5. Results: iron in silicate perovskite

5.4.4a.ii Temperature effect

Increase of temperature decreases the signal/noise ratio (Fig. 5.4-5) due to the fact that the recoil-free fraction is inversely proportion to the temperature ([Mössbauer and Wiedemann 1960](#)), which introduces additional uncertainty to the fitting procedure. Nevertheless we were able to resolve the hyperfine parameters of Mössbauer spectral components.

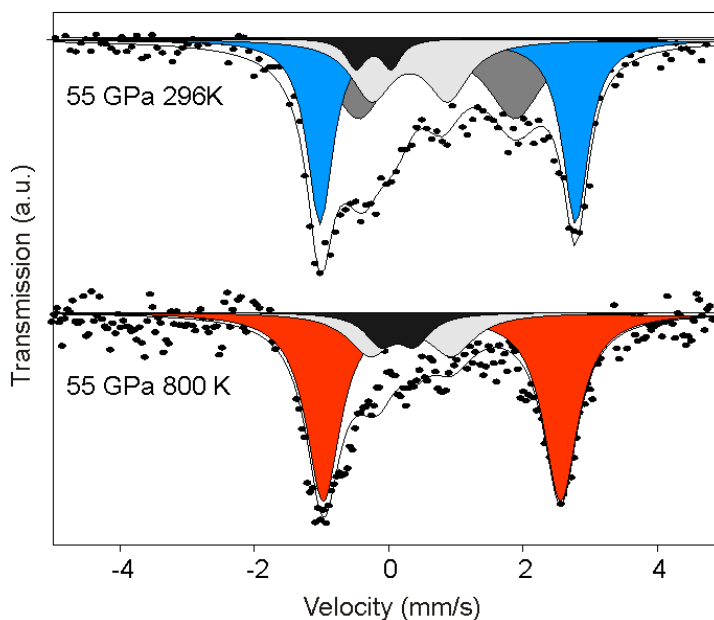


Figure 5.4-5. Mössbauer spectra of $\text{Fe}_{0.12}\text{Mg}_{0.88}\text{SiO}_3$ perovskite at 55 GPa collected at room temperature (on the top) and at 800K (on the bottom). Solid circles correspond to the experimental data. Components are shaded as follows: dark gray – HS Fe^{2+} , black – Fe^{3+} , light gray – charge transfer component, blue – high-QS component at room temperature, red – high-QS component at 800K.

In addition to the usual temperature induced decrease of QS and CS values for all components and intensification of charge transfer between ferrous and ferric iron (doublet shaded light gray in Fig. 5.4-5), we also detected a gradual increase of the amount of the high-QS component with temperature (Fig. 5.4-6). For example at 55 GPa the relative area of the component increases from 41 (1)% at room temperature to 69 (2)% at 800 K (Fig. 5.4-5). We will discuss the temperature effect on the high-QS component in more detail below.

5. Results: iron in silicate perovskite

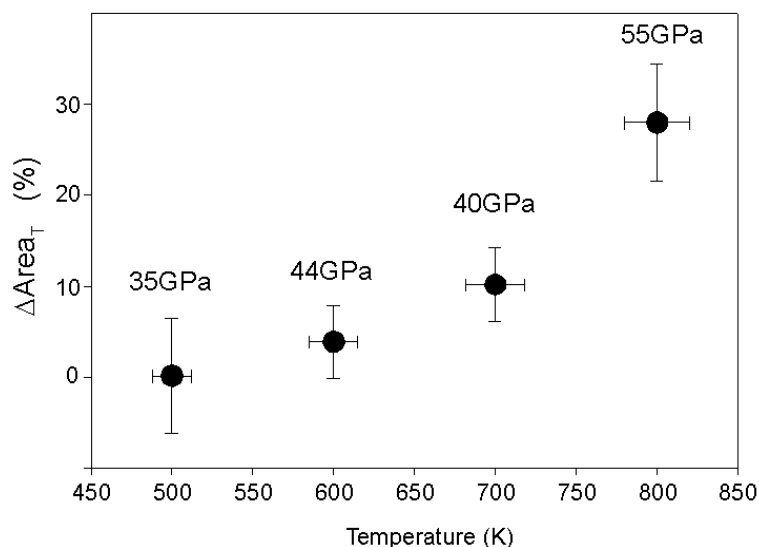


Figure 5.4-6. Change in the relative area of the high-QS component of $\text{Fe}_{0.12}\text{Mg}_{0.88}\text{SiO}_3$ perovskite with temperature relative to room temperature data collected at the same pressure.

5.4.4b (Mg,Fe)SiO₃ majorite

5.4.4b.i Pressure effect

The pressure evolution of Mössbauer spectra collected from $^{57}\text{Fe}_{0.18}\text{Mg}_{0.82}\text{SiO}_3$ majorite at room temperature is shown in Fig. 5.4-7. The main component (about 80% relative to the total amount of iron) represents HS Fe^{2+} in 8-fold coordinated polyhedra ($^{[8]}\text{Fe}^{2+}$) (doublet shaded blue), the quadrupole doublet shaded dark gray corresponds to HS Fe^{2+} in the octahedral site, and the black doublet represents ferric iron in an octahedral site, the amount of which varies from 8 to 12% depending on the sample (McCammon and Ross 2003). At ambient pressure the $^{[8]}\text{Fe}^{2+}$ component has CS around 1.2 mm s^{-1} and a large value of QS – 3.6 mm s^{-1} (which is comparable to the hyperfine parameters of the high-QS component in perovskite, which will be discussed in the following section). The CS of all three doublets slowly decreases with pressure while QS increases (Figs. 5.4-8a,b). However the relative amounts of all components remain the same within uncertainty through the entire studied pressure region (up to 52GPa) (Fig. 5.4-8c).

5. Results: iron in silicate perovskite

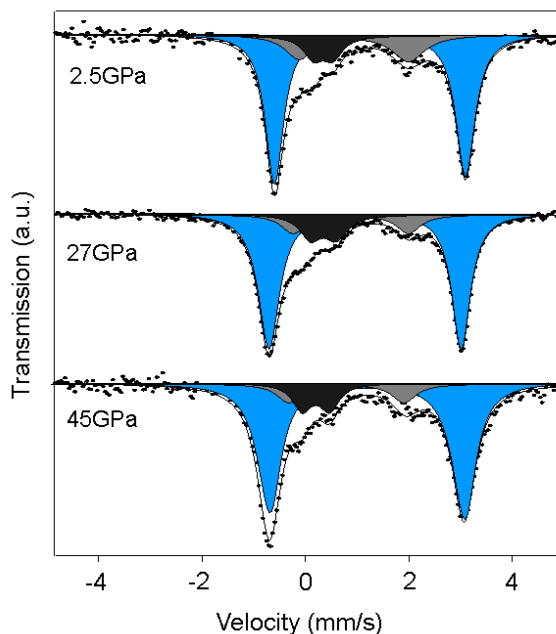


Figure 5.4-7. Selected Mössbauer spectra of $\text{Fe}_{0.18}\text{Mg}_{0.82}\text{SiO}_3$ majorite collected at room temperature. Solid circles correspond to the experimental data. Components are shaded as follows: blue – HS $^{[8]}\text{Fe}^{2+}$, dark gray – HS $^{[6]}\text{Fe}^{2+}$, black – Fe^{3+} .

5.4.4b.ii Temperature effect

Mössbauer spectroscopic measurements were performed at variable temperature for two majorite samples with different compositions: $^{57}\text{Fe}_{0.18}\text{Mg}_{0.82}\text{SiO}_3$ and $^{57}\text{Fe}_{0.11}\text{Mg}_{0.89}\text{SiO}_3$. The temperature dependence of hyperfine parameters obtained for both samples at 20 GPa are presented in Figs. 5.4-8d,e,f. An increase of temperature up to 670 K does not introduce any significant changes to the Mössbauer absorption spectra except for the usual decrease in the values of hyperfine parameters with temperature; the relative areas of individual components remain the same (Figs. 5.4-8d,e,f and Fig. 5.4-10).

5. Results: iron in silicate perovskite

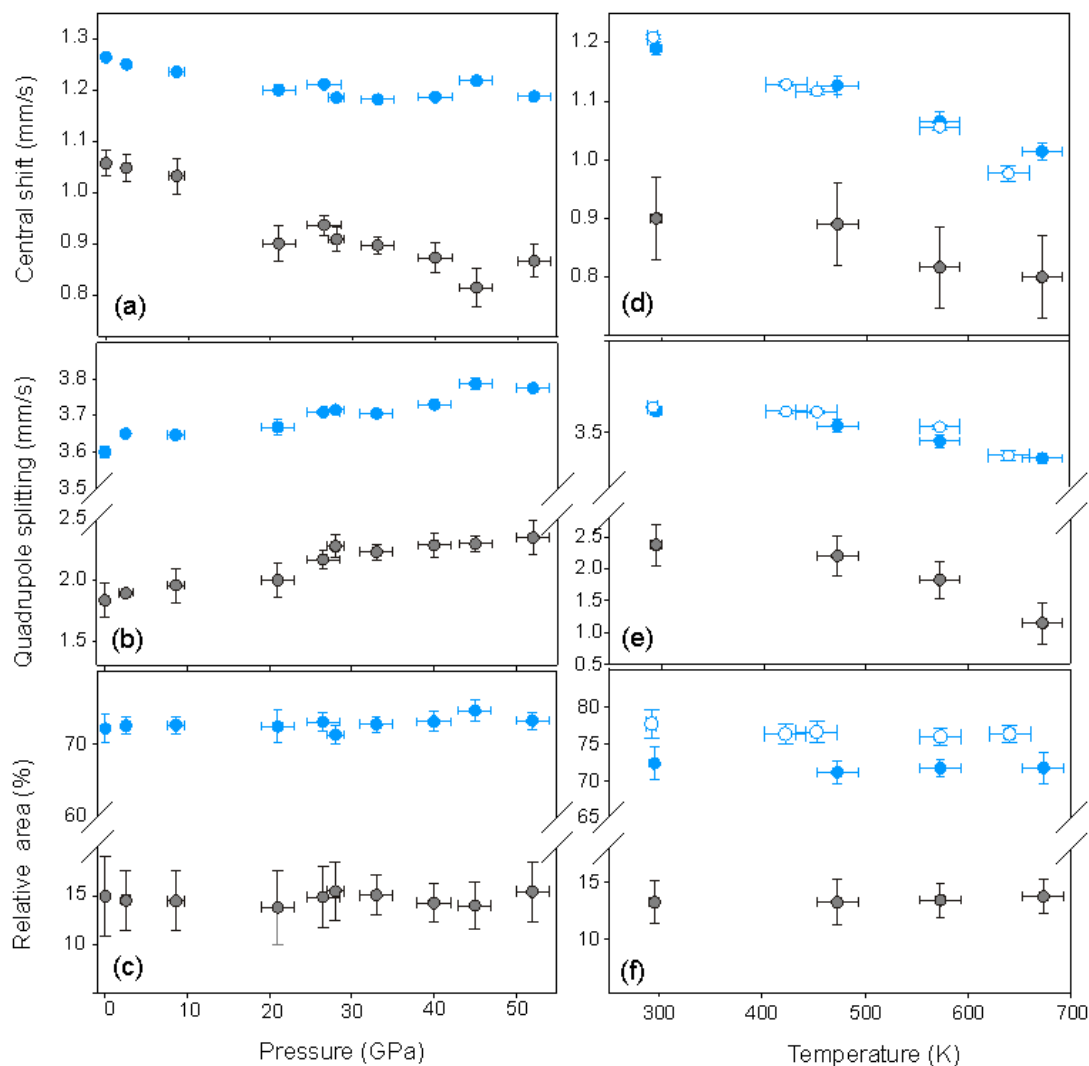


Figure 5.4-8. Central shift, quadrupole splitting and relative area as a function of pressure (**a**, **b**, **c**) and temperature (**d**, **e**, **f**) for $\text{Fe}_{0.18}\text{Mg}_{0.82}\text{SiO}_3$ majorite $^{57}\text{Fe}^{2+}$ (blue circles), $^{57}\text{Fe}^{2+}$ (light gray circles) and for $^{57}\text{Fe}^{2+}$ in $\text{Fe}_{0.11}\text{Mg}_{0.89}\text{SiO}_3$ majorite (open blue circles).

5.4.5 Discussion

5.4.5a (Fe,Mg) SiO_3 majorite

Let us now consider in details the high pressure and temperature behavior of $^{57}\text{Fe}^{2+}$ in majorite, and then compare it with the high-QS component in perovskite. In general the value of QS is determined by two factors: (i) lattice contribution, which is proportional to the electrical field gradient (EFG) produced by the charge distribution surrounding the absorbing nucleus (which is normally negligible and does not vary significantly with pressure and temperature) and

5. Results: iron in silicate perovskite

(ii) valence contribution, which is proportional to the EFG produced by the electrons distributed over the valence energy levels associated with the absorbing nucleus; therefore the valence contribution to the QS value is temperature and pressure dependent ([Ingalls 1964](#)).

In the case of $^{[8]}\text{Fe}^{2+}$ in majorite, the valence contribution to the EFG is determined by the Boltzmann distribution of six 3d-electrons over the five 3d levels, which are split into two levels with lower energy, e_g , and three levels of higher energy, t_{2g} , that are separated by the crystal field splitting energy, Δ_C , as illustrated in Fig. 5.4-9a ([Burns 1993](#)).

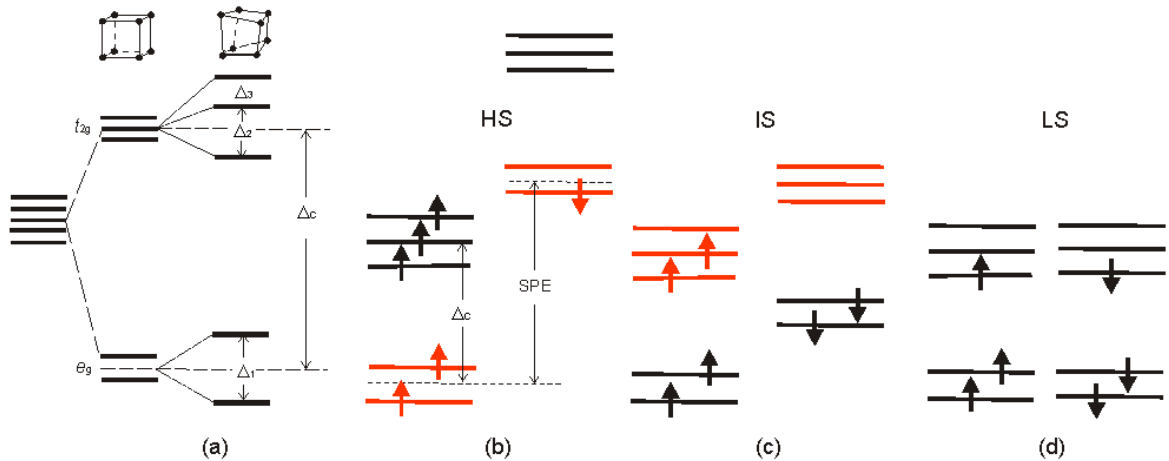


Figure 5.4-9. Splitting of Fe^{2+} energy levels (a) and possible spin state configurations (b, c, d) in a distorted cubic field (modified after [Burns, 1993](#)). The energy levels that predominantly contribute to EFG for a certain spin configuration are highlighted in red.

The lower energy levels correspond to the d_{z^2} and $d_{x^2-y^2}$ electronic orbitals and the high energy levels correspond to the d_{xy} , d_{yz} , d_{xz} orbitals. If the d_{z^2} and $d_{x^2-y^2}$ orbitals are equally populated, the magnitude of their contributions to the EFG would be the same, but opposite in sign. Consequently their total contribution to the EFG would be zero. The same is true in the case of the three t_{2g} orbitals. According to the Boltzmann distribution the population of

the i -th level $n_i = n_0 \cdot \exp\left(-\frac{\Delta_i}{kT}\right)$, where Δ_i is the energy of the i -th level and n_0 is a normalization constant, the values of Δ_i and therefore the population of energy levels depends on the relation between crystal field splitting (Δ_C) and spin pairing energy (SPE) as well as on temperature. The relative magnitudes of Δ_C and SPE determine which spin configuration is stable. In the case of high spin $^{[8]}\text{Fe}^{2+}$ in majorite ($\text{SPE} \gg \Delta_C$), five 3d electrons occupy each of

5. Results: iron in silicate perovskite

the five energy levels and the last sixth electron pairs with the one occupying the lowest energy level (Fig. 5.4-9b). For this configuration only e_g orbitals contribute to the EFG, because the t_{2g} orbitals are equally populated and compensate each other. Consequently the value of QS in this case is mainly determined by the energy difference between e_g levels – Δ_1 (Fig. 5.4-9a). Note that the larger the value of Δ_C and the lower the temperature, the higher the QS will be. The value of Δ_1 in this particular case (HS $^{[8]}\text{Fe}^{2+}$ in majorite) can be estimated through the temperature dependence of quadrupole splitting, as was shown by Huggins (1975). Based on the Ingalls model (1964), Huggins (1975) derived the following simple expression for the variation of quadrupole splitting, QS, with temperature, T, for the case of ferrous iron in garnet:

$$\text{QS}(T) = (\text{QS}(0) + F_{\text{lat}}) \left(\frac{1 - e^{-\Delta_1/kT}}{1 + e^{-\Delta_1/kT}} \right) - F_{\text{lat}}, \quad (5.4-1)$$

where QS(0) is the quadrupole splitting (in mm/sec) at 0K, Δ_1 is the separation of e_g levels (Fig. 5.4-9a), k is Boltzmann's constant and F_{lat} is the lattice contribution (in mm s^{-1}) to the QS.

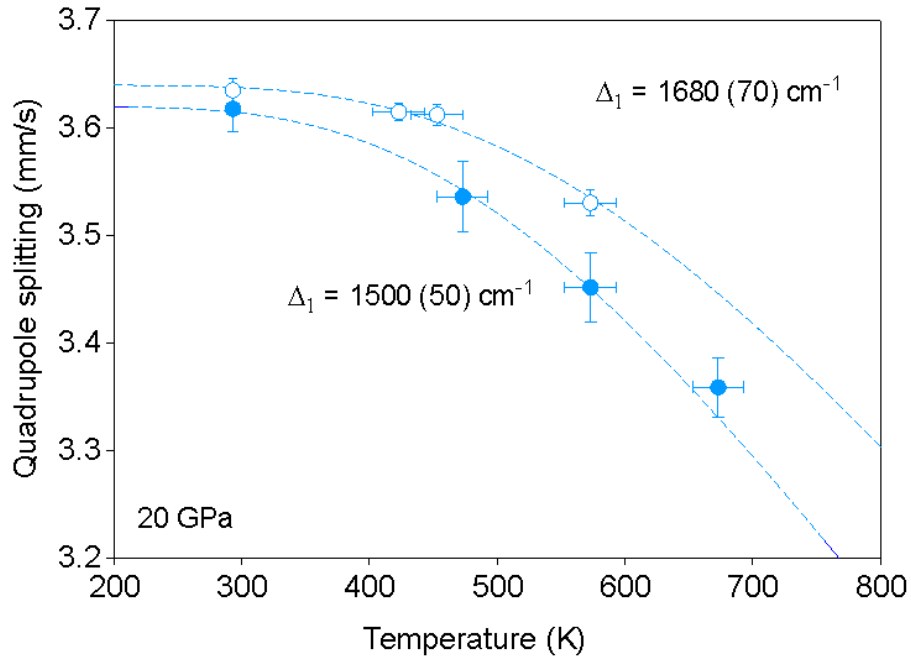


Figure 5.4-10. Variation of QS with temperature at 20 GPa for $^{57}\text{Fe}_{0.18}\text{Mg}_{0.82}\text{SiO}_3$ majorite (solid circles) and $^{57}\text{Fe}_{0.11}\text{Mg}_{0.89}\text{SiO}_3$ majorite (open circles). The dashed lines represent the fit of the experimental data with equation 5.4-1.

Applying this formula (5.4-1) to our variable temperature data for majorite (Fig. 5.4-10) and assuming $F_{\text{lat}} = 0$ (Huggins 1975), we obtained the results that at 20 GPa, Δ_1 is 1500 (50) cm^{-1}

5. Results: iron in silicate perovskite

¹ and 1680 (70) cm⁻¹ for ferrous iron in ⁵⁷Fe_{0.18}Mg_{0.82}SiO₃ and ⁵⁷Fe_{0.11}Mg_{0.89}SiO₃ majorites respectively (for comparison, an ambient pressure value of Δ_1 in garnets was estimated to be 1100 (50) cm⁻¹ ([Huggins 1975](#), [Burns 1993](#))). With these values of Δ_1 we were able to obtain a good fit of our data to equation (5.4-1), which is shown by the dashed lines in Fig. 5.4-10. Consequently, in the case of majorite we can account for the high value of the QS (about 3.6-3.7 mm s⁻¹) as a consequence of the large splitting between the lower energy levels e_g .

5.4.5b (Fe,Mg)SiO₃ perovskite

As a first approximation the energy diagram for ^[8-12]Fe²⁺ in silicate perovskite is similar to that for ^[8]Fe²⁺ in majorite (Fig. 5.4-9a), hence we can interpret the origin of the high QS-component in the Mössbauer spectrum of silicate perovskite (blue doublet in Figs. 5.4-2b,c) in the framework of the same theoretical model that was used for majorite. If we consider the pressure and temperature dependence of CS and QS of the high-QS and ^[8]Fe²⁺ components, they have the same trend without any abrupt changes (compare Figs. 5.4-4a,b and Figs. 5.4-8a,b,d,e). However the relative areas of the two components behave very differently at high pressure and temperature: in the case of majorite the amount of ^[8]Fe²⁺ almost does not change with pressure and temperature within the range of uncertainty (Figs. 5.4-8c,f), while in the case of perovskite we clearly observe an increase of the relative area of the high-QS component with pressure and temperature (Fig. 5.4-4c and Fig. 5.4-6). Therefore we suggest that the origin of the high-QS component in perovskite is different from that of majorite. In order to understand the origin of the high-QS component we come back to the energy diagram for ferrous iron in a distorted cubic site (Fig. 5.4-9a) to explore possible spin configurations. As already mentioned, the stability of a particular spin configuration is determined by the relation between crystal field splitting (Δ_C) and spin pairing energy (SPE). If SPE exceeds Δ_C the HS state is stable (Fig. 5.4-9b), and only e_g orbitals contribute to the EFG and therefore to the QS value. With increasing pressure Δ_C increases while SPE remains the same ([Sherman 1988](#)) and when at a certain point Δ_C becomes higher than SPE, the intermediate-spin state (IS) becomes energy favorable: the two lower levels are completely populated by four 3d-electrons and the other two valence electrons occupy two of the three upper levels (Fig. 5.4-9c). Hence in this case the EFG (and consequently the value of QS) is determined by the population of t_{2g} orbitals. Finally, with the further increase of Δ_C and if $\Delta_2 \neq 0$ the low-spin state (LS) becomes energy favorable: all valence electrons are spin-paired and

5. Results: iron in silicate perovskite

the EFG is equal to zero and does not contribute to the QS value (Fig. 5.4-9d). According to Keppler et al. (1994) in the case of $^{[8-12]}\text{Fe}^{2+}$ in the perovskite the energy difference between t_{2g} levels is much higher than between e_g levels, therefore the crossover from HS to IS would cause an increase of QS. This is what is experimentally observed (Figs. 5.4-3, 4).

5.4.6. Conclusions

Using conventional Mössbauer spectroscopy we performed a systematic study of the ferrous iron electronic state in magnesium-bearing silicate perovskite and majorite at pressures up to 81 GPa in the temperature range 300-800K. The high data quality allowed us to calculate the energy splitting between e_g levels of $^{[8]}\text{Fe}^{2+}$ in majorite at 20GPa and describe the effect of temperature on QS of this component in the framework of Huggins (1975) model. Based on comparison of the high-pressure high-temperature behaviour of $^{[8-12]}\text{Fe}^{2+}$ in perovskite and $^{[8]}\text{Fe}^{2+}$ in majorite, we conclude that the origin of the component with high QS in these two phases is different. Using a simplified energy diagram for $^{[8-12]}\text{Fe}^{2+}$ in perovskite, we confirmed that continuous changes in the relative area of the high-QS component in the pressure range 30-65 GPa can be interpreted as HS-IS crossover (consistent with McCammon et al. 2008). The gradual nature of this transition is not expected to cause any abrupt changes in elasticity, thermal or electrical conductivity, or elements partitioning in the Earth's lower mantle. However, physical and chemical properties of iron-bearing silicate perovskite could be affected by HS-IS crossover, and any extrapolations of the properties of Fe-free silicate perovskite to geophysically and geochemically relevant materials at conditions of the Earth's lower mantle should be made with caution.

5.4.7. Acknowledgments

The project was financially partly supported by funds from the German Science Foundation (DFG) Priority Programme SPP1236 under project Mc 3/16-1, and Eurocores EuroMinSci Programme.

5.5. Development of micro-XANES mapping in the diamond anvil cell

Aquilanti G.¹, Pascarelli S.¹, Mathon O.¹, Muñoz M.¹, Narygina O.² and Dubrovinsky L.²

5. Results: XANES mapping in DAC

¹European Synchrotron Radiation Facility, BP 220, F-38043 Grenoble Cedex, France; ²Bayerisches Geoinstitut, Universität Bayreuth, D-95440 Bayreuth, Germany

J. Synchrotron Rad. (2009) 16, 376–379

5.5.1 Abstract

Energy-dispersive X-ray absorption spectroscopy is now a well established method that has been applied to a broad range of applications. At the energy-dispersive EXAFS beamline of the ESRF, ID24, the recently achieved $5\ \mu\text{m} \times 5\ \mu\text{m}$ focal spot combined with fast acquisition has allowed complex and non-uniform samples to be mapped and images to be obtained where each pixel contains full XAS information. This method has been applied to a study under extreme conditions of pressure and temperature in a diamond anvil cell in transmission mode. The case study was the investigation of the Fe K-edge XANES of (Mg,Fe)SiO₃-perovskite and (Mg,Fe)O-ferropericlasite on decomposition of the spinel-structured olivine [γ -(Mg,Fe)₂SiO₄] at 78 (3) GPa after laser heating at 2200 (100) K.

5.5.2 Introduction

One of the major goals in geosciences is the study of the dynamics of the solid Earth and properties of each of the Earth's reservoirs. This requires a detailed knowledge of the properties of the main mineral phases which compose the Earth's mantle, core, subducting slabs and ascending plumes under pressure and temperature conditions that may exceed 150 GPa and 5000 K, respectively. The iron oxidation state, in particular, is an important factor governing the reservoir mineralogy, the material exchanges at the core–mantle boundary, and the exchange of oxygen between deep mantle and globe surface ([Wood et al., 2006](#); [Rohrbach et al., 2007](#)). The study of chemical reactions of complex systems close to natural rocks under the actual conditions of the Earth's interior is essential for modelling the mineralogy and the chemistry of our planet. Although diamond anvil cells (DACs) associated with laser heating techniques allow us to reach such thermodynamic conditions, experiments under these conditions are usually associated with significant challenges. These include limited sample amount in the DAC (of the order of 10^{-10} g), pressure and temperature gradients, and the fact that several phase transitions are not quenchable. Moreover, pressure and temperature gradients give rise to a complex spatial distribution even

5. Results: XANES mapping in DAC

inside the small volume of the DACs. A probe with micrometric spatial resolution, chemical sensitivity and allowing in situ investigation would fulfil the constraints of such types of experiments.

Visual observation, Raman and infrared spectroscopies, X-ray and neutron powder diffraction, and resistivity measurements are widely used for in situ sample characterization in DACs and they certainly could recognize chemical reactions at high pressure. Raman and infrared active bands as well as diffraction patterns change on account of a chemical reaction or phase transformation of a material, but are neither chemically specific nor particularly sensitive to changes in oxidation states. On the other hand, Mössbauer spectroscopy is very sensitive to the chemical state of elements but lacks the spatial resolution necessary for studies of materials in the laser-heated DAC. There are also other different laboratory methods capable of determining the composition, chemistry and structure of complex heterogeneous materials, such as beam methods or scanning probe techniques ([Adams et al., 2005](#)). These methods can achieve not only a nanometric lateral spatial resolution but also allow the analysis of a third dimension thanks to the depth resolution obtaining three-dimensional pictures that could describe the system taking into account the actual thermal gradient present in the laser heated DAC. Unfortunately, these methods do not enable the products of chemical reactions to be studied in situ under extreme conditions and therefore are not suitable for the study of unquenchable structures and even less for the characterizations of reagents and products of chemical reactions during their evolution. Other techniques, based on the use of synchrotron radiation, such as X-ray fluorescence microprobes, combine micrometric spatial resolution and chemical analysis with the possibility of in situ experiments thanks to the physical penetration of hard X-rays, allowing a highly absorbing sample environment, such as DACs, to be used. Nonetheless, using these techniques it is currently impossible to retrieve complete structural information. X-ray absorption spectroscopy (XAS) is a chemically selective spectroscopic technique and is able to provide information about structural and electronic properties such as number and distance of neighbours as well as oxidation state and chemical speciation (Rehr and Albers, 2000). The strength of XAS in dispersive geometry applied to science at high pressure is well documented in the literature ([Itié et al., 1989](#); [Sapelkin et al., 1996](#); [Aquilanti and Pascarelli, 2005](#); [San-Miguel et al., 2007](#); [Aquilanti, Trapananti et al., 2007](#); [Aquilanti, Libotte et al., 2007](#)). In fact, the inherent beam stability owing to the absence of movement of the optics during spectra acquisition and the small spot obtained, thanks to the focusing properties of the polychromator, match the size

5. Results: XANES mapping in DAC

requirements of samples at high pressures. Moreover, on ID24 at the European Synchrotron Radiation Facility (ESRF) the choice of the source (undulators) allows the severe X-ray beam attenuation through the high-pressure cells to be overcome, especially at energies below 8 keV. Recently, the energy-dispersive XAS (EDXAS) beamline, ID24, has been used for m-XAS applications with a micrometric spatial resolution obtaining two-dimensional XANES (X-ray absorption near-edge structure) maps where each pixel contains full XANES information ([Pascarelli et al., 2006](#)). μ -XAS two-dimensional mapping has been used so far in fluorescence mode to investigate the content, redox and speciation of iron on a natural rock thin section ([Muñoz et al., 2006](#)).

Potential future scientific opportunities include: (i) Studies of dilute systems in highly absorbing environments (i.e. DACs) using fluorescence detection. For example, the flux at the Fe K-edge [of the order of 10^{14} photons s^{-1} (0.01% bandwidth) $^{-1}$ on ID24] allows for XANES characterization of relatively dilute samples (down to 1 wt% of iron for about 30 mm-thick natural samples). Using specially designed DACs, where diffusion of X-rays from the environment are minimized, acquisition times of the order of seconds should be feasible. (ii) Studies at extreme pressures and temperatures in DACs using in situ laser heating techniques. In this article we illustrate a novel method for two-dimensional m-XAS mapping in transmission mode through a DAC. The test case concerns a geological relevant issue under extreme conditions of temperature and pressure in a DAC. We show how this method can provide information, with micrometric spatial resolution, on the behaviour of iron during the reaction of decomposition of the spinel-structured olivine (Ol) [γ -(Mg,Fe) $_2$ SiO $_4$] into (Mg,Fe)SiO $_3$ -perovskite (Pv) and (Mg,Fe)O-ferropericlaase (Fp). We underline that the aim of this article is to describe in detail the hardware set-up needed for performing such types of experiments. The analytical method for the data analysis is described by Muñoz et al. ([2008](#)). The interpretation of the results, together with the geological implications, will be given in a following paper.

5.5.3 Experimental details

The experiment was performed at the dispersive EXAFS (extended X-ray absorption fine structure) beamline of the ESRF, ID24. A sketch of the optical scheme can be found by Pascarelli et al. ([2006](#)). The X-ray source consists of three undulators with gaps adjusted to have the maximum of the first harmonic at the energy of the Fe K-edge (7112 eV). The X-ray source is

5. Results: XANES mapping in DAC

then coupled to two silicon mirrors in a Kirkpatrick–Baez geometry at a grazing incidence angle of 3 mrad and to a Si (220) polychromator crystal in the Bragg geometry that disperses and horizontally focuses the beam to 5 μm FWHM at the sample position. An additional Si mirror is placed downstream of the polychromator at a grazing angle of 4 mrad to vertically focus the beam down to 5 μm FWHM. Fe K-edge XANES spectra were recorded in transmission mode using a fast CCD-based position-sensitive detector developed at the ESRF, i.e. the FReLon camera ([Labiche et al., 2007](#)) in the energy range 7090–7210 eV. Pixel–energy calibration was based on the acquisition of XANES spectra of a metallic iron foil. Fig. 5.5-1 shows a photograph of the experimental hutch of ID24 with the required set-up for such XAS experiments at high pressure.

The DAC is mounted on a stack of motors allowing x–z alignment with respect to the beam as well as in the y direction in order for the sample to be positioned exactly at the horizontal and vertical focal plane. A well known shortfall of XAS experiments at high pressure using a DAC is the crystal structure of the single-crystal diamond anvils. In the specific case of an energy-dispersive XAFS experiment the polychromatic beam impinges on the sample with a wide energy bandpass (of about 100–500 eV presently at ID24 at the Fe K-edge, depending on the choice of the polychromator and focal length). These photons will inevitably cover energies that satisfy Bragg conditions for the crystal structure of the diamond. This causes X-rays to be diffracted off the polychromator–detector direction leading to large dips in the transmitted X-ray intensity I_1 . These dips, appearing as peaks in the spectrum as $\alpha = \ln(I_0/I_1)$, heavily spoil the data quality. For this reason the DAC often needs to be rotated along angles ω , χ and φ in order to shift the diamond Bragg peaks out of the energy region of interest. Whereas there are no research papers limitations for the angle φ , which can be rotated through 360° , both angles ω and χ are limited. Indeed, large values for ω and χ , on one side, would increase the effective thickness of the sample, not fulfilling the requirement for the EXAFS measurements, and on the other side decrease the effective gasket hole diameter. Acceptable values for these angles are up to $\pm 20^\circ$. For the angle χ this value further decreases down to ± 10 because of the nature of the goniometer.

5. Results: XANES mapping in DAC

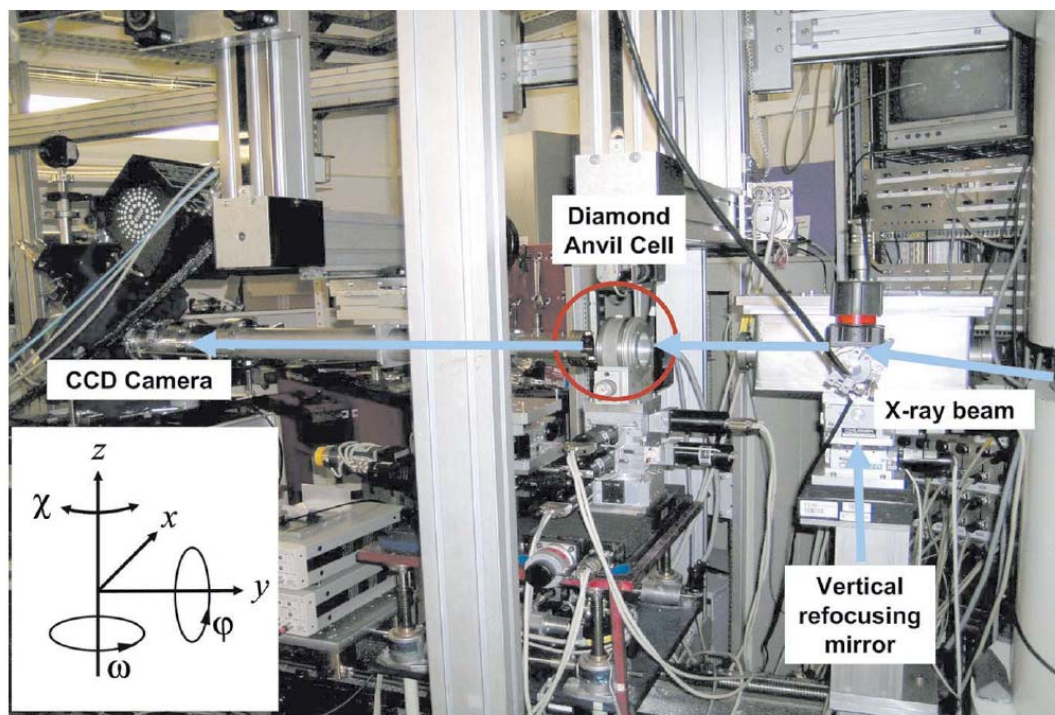


Figure 5.5-1 Experimental hutch of ID24 (ESRF) with the required set-up for μ -XAFS measurements at high pressure.

This procedure can be very time-consuming when using energy scanning XAS spectrometers. However, using EDXAS the transmitted intensity I_1 is visualized over the whole absorption spectrum energy range in ‘live’ mode. This allows the energy shift in the position of the Bragg peaks to be visualized in real time while rotating the DAC, until they are completely moved out of the energy range of interest.

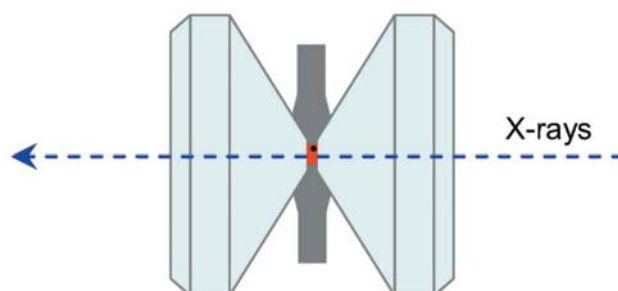


Figure 5.5-2. Schematic of the DAC. The dashed blue line represents the directions of the X-rays crossing the two diamond anvils. The sample (red rectangle) is held in place between the tips of the two diamond anvils by a metallic gasket. The diameter of the gasket is about 80 μm . The black dot represents a small ruby used for pressure calibration purposes.

5. Results: XANES mapping in DAC

As a starting material, a natural sample of San Carlos olivine with composition $(\text{Fe}_{0.12}\text{Mg}_{0.88})_2\text{SiO}_4$ was used. Its chemical and phase homogeneity were confirmed by X-ray powder diffraction and microprobe chemical analysis. A double-sided polished irregular-shaped sample of thickness 25 μm was loaded into a hole drilled in a Re gasket, together with two small (about 2 μm in diameter) rubies. As a pressure-transmitting medium, Ar loaded under a pressure of 1.4 kbar was used. We employed diamonds with culets of height 300 μm and 1.6 mm. Fig. 5.5-2 shows a schematic diagram of the DAC with respect to the beam. The transmission of the X-rays through 3.2 mm of diamond ($\rho = 3.52 \text{ g cm}^{-3}$) in the energy range 7000–7500 eV is between 4.5×10^{-4} and 2.0×10^{-3} . The sample in the DAC was initially compressed to 78 (3) GPa and a portion of the sample of about 50 $\mu\text{m} \times 75 \mu\text{m}$ was then double-side laser heated at 2300 (100) K using a YAG laser. Fig. 5.5-3 shows an optical image of the sample at 78 (3) GPa after the laser heating. The sample fills the gasket hole uniformly and the white part is the starting olivine pressurized to 78 (3) GPa while the dark rectangle represents the laser-heated portion of the sample. To record the XANES maps, the DAC was scanned horizontally and vertically in the focal plane of the X-ray beam with steps of 5 μm . Fe K-edge XANES were recorded over a 50 \times 50 step grid in order to cover an area of 250 $\mu\text{m} \times 250 \mu\text{m}$. Each map contains 2500 XANES spectra (one spectrum per pixel). Given the high absorbance of the diamond anvils, the acquisition time was 4 s per spectrum. XAFS data reduction, including energy calibration, normalization and edge position tracking, was performed using the XASMAP software (<http://www.esrf.eu/UsersAndScience/Experiments/TBS/SciSoft/OurSoftware/XASMAP>), allowing different kinds of targeted maps, such as absorbance maps, at given energy to be obtained (Muñoz et al., 2006). The analytical procedure to extract, from these maps, relevant information, such as the iron affinity for the different crystalline phases, is described by Muñoz et al. (2008).

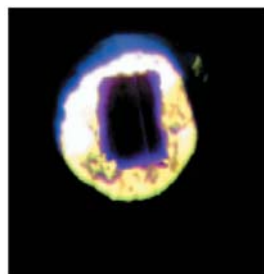


Figure 5.5-3 Optical image of the sample of San Carlos olivine compressed in Ar pressure-transmitting media at 78 (3) GPa. The dark rectangular area in the middle of the gasket hole is the part that is laser heated to 2300 (100) K.

5. Results: XANES mapping in DAC

5.5.3. Results and conclusions

Fig. 5.5-4 shows the two-dimensional maps of the normalized absorbance at $E = 7155$ eV after spectra normalization at 78 (3) GPa after laser heating. The choice of plotting the map of the absorbance at such an energy value is justified by the fact that at this energy the difference between the normalized absorbance of the different specimens within the sample (Ol, Pv, Fp) around the Fe K-edge is maximum. The change in colour in the central part of the sample evidenced in Fig. 5.5-3 demonstrates a change in the absorbance within the heated zone probably due to a transformation from Ol into Pv and Fp.

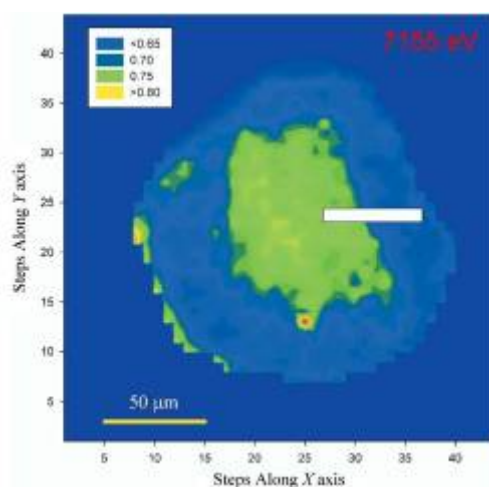


Figure 5.5-4 Absorbance maps at 7155 eV at 78 (3) GPa after the laser heating of the central part of the sample (green). The blue zone corresponds to the absorbance at 7155 GPa of the olivine compressed to 78 (3) GPa.

The red point corresponds to the position of one ruby sphere. Fig. 5.5-5 shows, from bottom to top, several normalized spectra of olivine in the non-heated area (blue spectra), the mixed region (red spectrum) and of Pv and Fp assemblage in the heated area (green spectra). The spectra are collected along the white line shown in Fig. 5.5-4 every $5 \mu\text{m}$, that is the spatial resolution currently available at ID24.

Only one spectrum shows the signature of a mixed phase between olivine and the Pv and Fp assemblage. The feature in the pre-edge region of the spectra recorded in the heated area cannot be assigned either to Pv or to Fp and this will be discussed in a following paper.

5. Results: XANES mapping in DAC

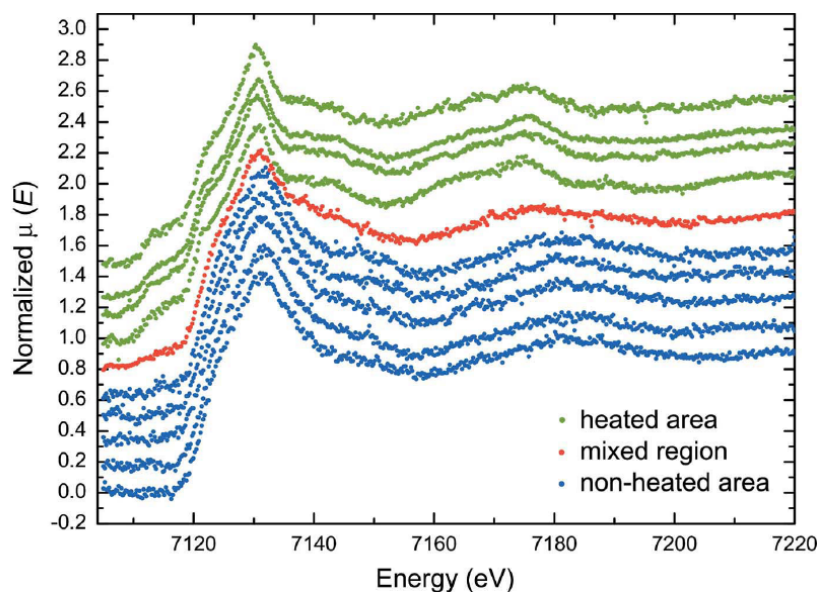


Figure 5.5-5 Normalized spectra of olivine in the non-heated area, in the mixed region, and of Pv and Fp assemblage in the heated area. The spectra are collected along the white line shown in Fig. 5.5-4 every 5 μm .

To conclude, we have shown that μ -XAS two-dimensional mapping recently developed at the energy-dispersive EXAFS beamline of the ESRF can be applied to study geological relevant issues under extreme conditions in a DAC, assessing, with micrometric spatial resolution, the chemistry of individual high-pressure phases under equilibrium conditions in complex chemical systems. As a further development of this technique, we envisage the characterization of diffusion processes under extremes conditions and access to metastable states, by exploiting the time resolution naturally offered by EDXAS. Finally, a modification of the geometry of the ID24 spectrometer foreseen in the near future will allow the energy bandpass to be increased at energies below 8 keV up to $k = 20 \text{ \AA}^{-1}$ enabling the important step from μ -XANES to μ -EXAFS two-dimensional mapping to retrieve the full structural information achievable from the EXAFS features.

5.6. Hyperspectral -XANES mapping in the diamond-anvil cell: analytical procedure applied to the decomposition of (Mg,Fe)-ringwoodite at the upper/lower mantle boundary

Muñoz M.^{1,2}, Pascarelli S.², Aquilantib G.², Narygina O.³, Kurnosov A.³ and Dubrovinsky L.³

¹LGCA-OSUG, UMR 5025, Université Joseph Fourier, Grenoble, France; ²European Synchrotron Radiation Facility, Grenoble, France; ³Bayerisches Geoinstitut, Universität Bayreuth, Bayreuth, Germany

High Pressure Research (2008) 28(4), 665–673

5.6.1 Abstract

We propose a new analytical approach to extract information from μ -X-ray Absorption Spectroscopy (XAS) based mapping techniques, where each pixel of a map contains full XANES (X-ray Absorption Near Edge Structure) information. Data reduction is performed thanks to specifically developed software, XASMAP, which allows automatic normalization, linear combination fits, map reconstruction and spectrum extraction. We illustrate an example of application on data acquired in a laser heated diamond-anvil cell, devoted to the investigation of the behavior of iron during the decomposition of (Mg,Fe)-ringwoodite into perovskite and ferropericlasite at conditions relevant to Earth upper/lower mantle boundary. The analysis of 1600 Fe K-edge XANES spectra allows the reconstruction of maps based on iron-speciation, but it also drives to iron-concentration maps in a complex mixture of three crystalline phases. This analytical procedure opens the way to *in situ* studies at extreme conditions of pressure and temperature for the geosciences, physics and chemistry communities.

5.6.2. Introduction

The potential of the energy-dispersive X-ray absorption spectroscopy (EDXAS) beamline ID24 of the European Synchrotron Radiation Facility (ESRF) was recently enhanced due to technical improvements in instrumentation and optics ([Pascarelli et al., 2004](#), [2006](#)), coupling fast data acquisition to a micrometer X-ray beam. This leads to the possibility of recording μ -XANES (X-ray absorption near edge structure) maps with a spatial resolution of a few microns, where

5. Results: XANES mapping in DAC

each pixel contains full XANES information (details on analytical principles are described in [\(Muñoz et al., 2006\)](#)). This first work was illustrated by the study of a natural geological sample at the Fe K-edge, for which the XANES data were collected in the fluorescence mode. To automate the analysis of large sets of XANES spectra, we specifically developed a dedicated software, namely the XASMAP package (<http://www.esrf.eu/computing/scientific/XASMAP/munoz.htm>). This led to the reconstruction of the first hyperspectral normalized μ -XANES maps, collected at the iron K-edge for geological samples ([\(Muñoz et al., 2006\)](#)). Since then, dispersive μ -XANES mapping in fluorescence mode has been exploited in a number of different ways, such as for the validation of thermodynamic properties applied to metamorphic rocks ([\(Vidal et al., 2006\)](#)), or for the understanding of the main factors responsible for the crystallization of the ‘inconspicuous’ polyhedral serpentine mineral ([\(Andréani et al., 2008\)](#)).

We have then extended these studies to investigations within a diamond-anvil cell (DAC) using EDXAS in the transmission mode (see Aquilanti et al. [\(2009\)](#) for technical description), to probe the potential of this method for *in situ* studies at extreme conditions of temperature and pressure. We present here a new procedure for the analysis of these first *in situ* μ -XANES maps. Particularly, the XASMAP software has been implemented with a multicomponent linear-combination fitting procedure, and statistical evaluation tools like standard deviation and principal component analysis. Applied to complex systems that present, for example, mixtures of crystalline phases, these tools allow for the reconstruction of quantitative concentration maps showing the distribution of the different structural environments (*i.e.* crystalline phases) in which the absorber is located. It is important to underline the difference between this ‘phase concentration’, which is chemically selective and is different for different absorber atoms (C^{abs}), and the real concentration of the crystalline phases (C^{xtal}), obtained, for example, from X-ray diffraction data. Note that all numerical tools used for this study derive from MATLAB®-based routines.

To illustrate the potential of this method, we investigate the behavior of iron during the decomposition of (Mg,Fe)-ringwoodite into silicate perovskite and ferropericlase, which occurs at the upper/lower mantle boundary. Indeed, because of its abundance and its possible changes in oxidation state, iron is known to be one of the major elements governing past and present of Earth as a planet (see for example a recent review in [\(Wood et al., 2006\)](#)), and knowledge of its speciation (*i.e.* phase affinity, oxidation state, etc.) in the different crystalline phases of the mantle is fundamental. The upper mantle is essentially constituted of olivine ($\text{Mg}_{1-x}\text{Fe}_x\text{)}_2\text{SiO}_4$ and

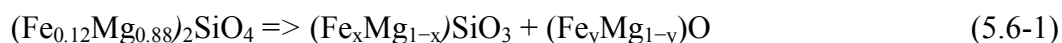
5. Results: XANES mapping in DAC

its high-pressure and high-temperature polymorphs, whereas the lower mantle mainly contains silicate perovskite (Mg,Fe)SiO₃ (further designated as Pv) and ferropericlase (Mg,Fe)O (Fp) minerals, as well as post-perovskite (Mg,Fe)SiO₃, most likely located in parts of the D'' layer. Olivine is known to transform to modified spinel (wadsleyite) and γ -spinel (ringwoodite, Rw) structures under high-pressure and high-temperature conditions, respectively, at \sim 13.5 GPa/1400 °C and 18 GPa/1500 °C. Additionally at 660 km depth (\sim 22 GPa and 1600 °C, [Katsura et al., 2003](#)), the chemical decomposition of ringwoodite into perovskite plus ferropericlase occurs, which corresponds to a strong seismic discontinuity ([Shim et al., 2001](#)). These results are based on studies of quenched materials obtained from high-pressure and high-temperature, as well as from *in situ* characterization of the phase transitions using either the multi-anvil press or the DAC ([Irifune et al., 1998](#); [Chudinovskikh and Boehler, 2001](#)).

As shown by their structural formula, each of the crystalline phases of the Earth's mantle allows iron–magnesium substitutions. Based on the results of quenched experiments, it is now generally believed that Fe incorporation in ringwoodite does not significantly influence the phase boundary between (Mg,Fe)₂SiO₄ and (Mg,Fe)SiO₃ + (Mg,Fe)O. However, from the best of our knowledge, no *in situ* studies of the decomposition of iron-bearing γ -spinel (with \sim 10% Fe-content, like the natural one) were reported in the literature. Until now, only Andrault ([2001](#)) has performed systematic angle dispersive X-ray diffraction measurements on natural San Carlos olivine (Mg_{1.68}Fe_{0.32}SiO₄), but its starting patterns were corresponding to a pressure of 35.5 GPa with increasing temperature, well above the pressure–temperature range of the chemical decomposition of olivine.

5.6.3. Experimental details

In the present study, we illustrate the potential of the μ -XANES mapping by exploring *in situ* the Rw to Pv and Fp reaction of geophysical interest,



(with $x = 0.24 - y$), which occurs above \sim 23 GPa and 1600 °C. The starting sample of ringwoodite was synthesized at BGI (Bayerisches Geoinstitut, Germany) in a multi-anvil apparatus at 19 GPa and 1900 °C. μ -XANES maps were collected on beamline ID24 of the ESRF in the DAC at different pressures, before and after laser heating. A full description of the experimental setup may be found in reference Aquilanti et al. ([2009](#)).

5. Results: XANES mapping in DAC

The DAC was scanned horizontally and vertically in the focal plane of the X-ray beam with steps of 5 μm . Fe K-edge XANES were recorded over a 40 by 40 step grid in order to cover an area of $200 \times 200 \mu\text{m}^2$. Each map contains 1600 XANES spectra (1 spectrum/pixel) and was recorded in ~ 100 min. A total of three μ -XANES maps were recorded at 26 GPa before and after laser heating, and at 37 GPa after laser heating. The laser heating process consisted of a single hot spot at 1600 $^\circ\text{C}$ performed in the center of the sample.

5.6.4. Analytical procedure

The application of dispersive μ -XANES mapping to investigate the complex heterogeneous system described in Equation (1) provides large data sets extremely rich in information, as each pixel of the images corresponds to a complete XANES spectrum. Therefore, choosing an appropriate way to extract the targeted information is challenging. To achieve this, we first selected three model compounds relevant for the characterization of the system, namely Rw, Pv, and Fp. Each model compound has been synthesized separately in three different DAC experiments, at 26 GPa after laser heating. For Rw, Pv, and Fp, the starting materials were, respectively, olivine, enstatite, and ferroperricite, each with an iron-number (noted Fe#), *i.e.* Fe/(Fe + Mg), of 0.12 in mol.

Fig. 5.6-1 reports Fe K-edge XANES spectra for these three model compounds, recorded at 26 GPa and ambient temperature. Features of these spectra reveal quite different shapes, in agreement with the different local environments of iron in the three crystalline structures.

In particular, feature A shows important shifts of the inflection point of the edge for the phases considered. Feature B, corresponding to the maximum of the ‘white-line’, presents major contrasts (from 7126 to 7132 eV with important changes in intensity), and feature C also appears to be extremely sensitive to the different crystalline structures. Because the spectral signatures of Rw, Pv, and Fp are clearly different, it is possible to analyze the collected Fe K-edge XANES using multicomponent linear-combination fits, in order to derive the amount of each component in the mixture system.

5. Results: XANES mapping in DAC

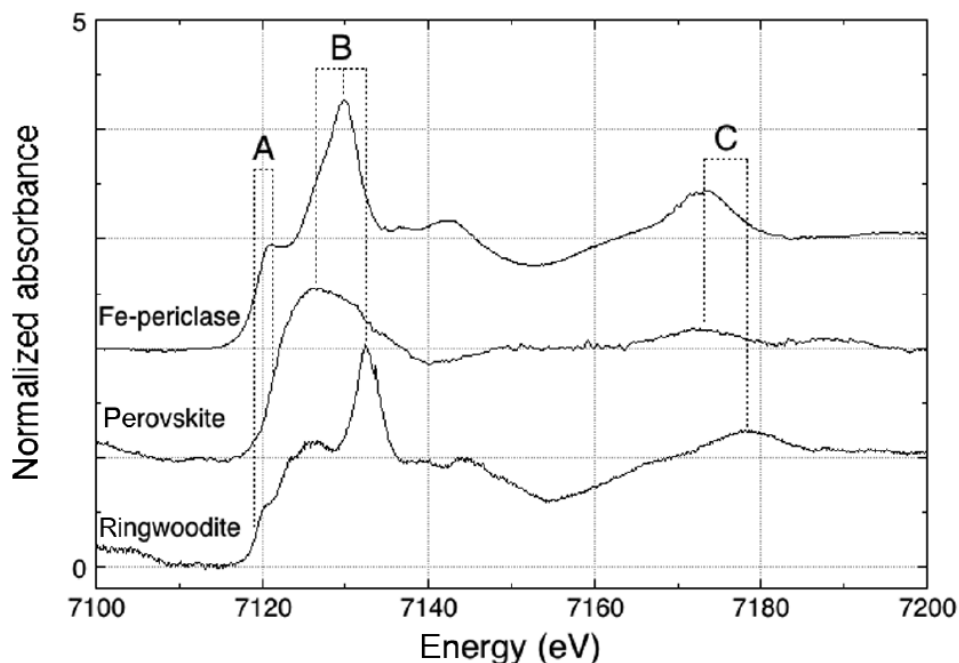


Figure 5.6-1 Fe K-edge XANES spectra collected at 26 GPa and ambient temperature for $(\text{Fe}_{0.12}\text{Mg}_{0.88})_2\text{SiO}_4$ – ringwoodite, $(\text{Fe}_{0.12}\text{Mg}_{0.88})\text{SiO}_3$ – perovskite, and $(\text{Fe}_{0.12}\text{Mg}_{0.88})\text{O}$ – ferropericlase.

Starting from the $(\text{Fe}_{0.12}\text{Mg}_{0.88})_2\text{SiO}_4$ ringwoodite sample, we collected a first μ -XANES map at 26 GPa before any laser heating of the sample. Fig. 5.6-2a shows the corresponding ‘edgejump’ map (Muñoz et al., 2006). According to the Beer–Lambert law, for a constant density and thickness of the sample, this criterion is only sensitive to variations in iron content. In the present case, we will only pay attention to the region surrounded in black, which highlights the sample region in the pressure chamber. We can ascertain that the surrounded region is quite homogeneous in the starting material (*i.e.* non-heated sample at 26 GPa), with edge-jump values of the XANES spectra close to 0.35. Additionally, the same homogeneity is observed in Fig. 5.6-2b,c, which correspond, respectively, to the sample at 26 GPa after a first laser heating and to the sample at 37 GPa after a second laser heating in the same region. We can then conclude that for our experimental conditions, and within the precision of the measurement, iron does not significantly migrate under the thermal gradient applied twice to the sample.

5. Results: XANES mapping in DAC

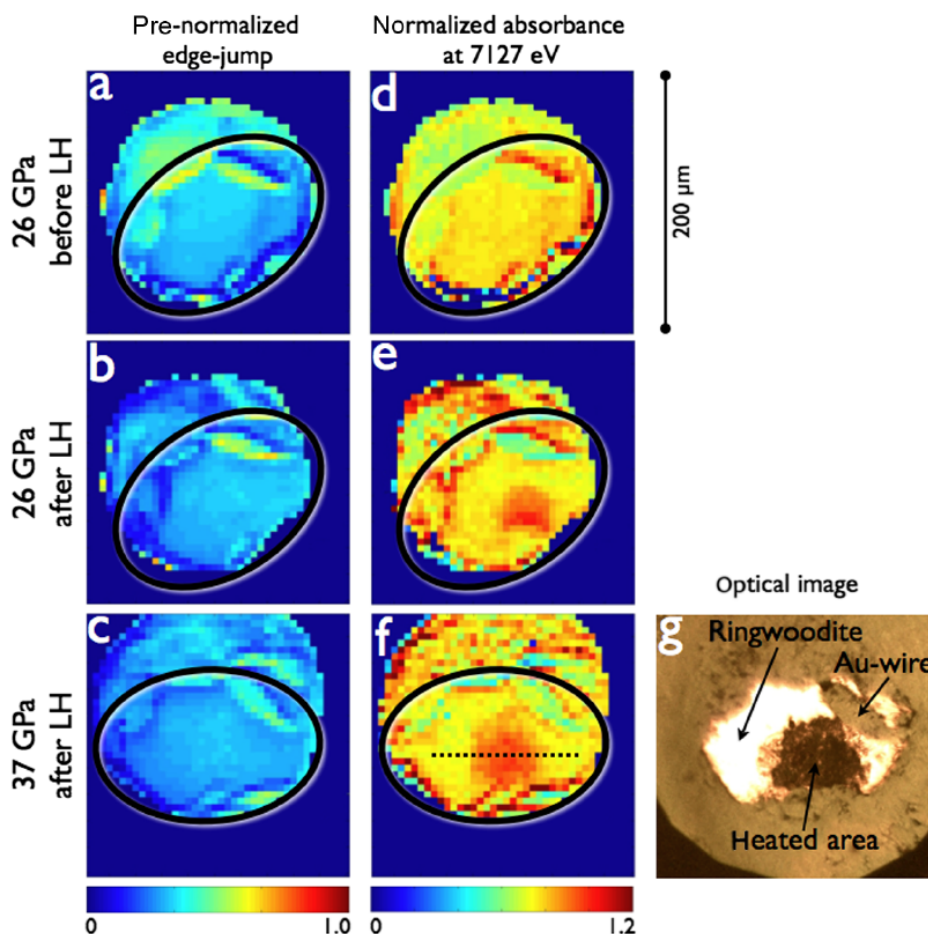


Figure 5.6-2 Pre-normalized XANES edge-jump maps collected in the DAC: **a**, at 26 GPa before laser heating, **b**, at 26 GPa after laser heating, and **c**, at 37 GPa after laser heating. Normalized XANES absorbance maps at 7127 eV collected in the DAC: **d**, at 26 GPa before laser heating, **e**, at 26 GPa after laser heating, and **f**, at 37 GPa after laser heating. The sample in the pressure chamber is surrounded by a black line, as shown in the optical image of the sample at 37 GPa after laser heating, **g**.

The second step of our data processing method consists of analyzing the set of XANES spectra corresponding to the pixels within the sample region of the pressure chamber. Taking into account this set of data, we first calculate the standard deviation spectrum in order to highlight the energies for which one can observe a maximum of variation for the normalized absorbance values (black curve in Fig. 5.6-3a). The standard deviation curve presents two main peaks, the first at 7127 eV and the second close to 7130 eV. This information is then directly used to reconstruct normalized absorbance maps (*i.e.* speciation maps) at given energy values. Figs. 5.6-2d–f represent, respectively, the normalized 7127 eV absorbance maps at 26 GPa before and after laser heating, and at 37 GPa after laser-heating. Focusing on the part of the map surrounded in

5. Results: XANES mapping in DAC

black, Figs. 5.6-2d presents a yellow to orange region that is quite homogeneous and corresponds to a normalized absorbance value of ~ 0.8 . However, Figs. 5.6-2e,f reveal a red spot in the same region where the normalized absorbance is close to 1, which traduces the thermal gradient applied to the sample during the successive laser-heating processes. The red region corresponds to the heated part of the sample, whereas the yellow region remains unchanged. The optical image of the sample at 37 GPa after laser heating, shown in Fig. 5.6-2g, rigorously confirms (i) the geometry of the pressure chamber delimited by the rhenium gasket and a gold wire, (ii) the unchanged ringwoodite region in white, and (iii) the heated area that appears darker. Therefore, this step in data processing allows localizing the maximum of contrasts in the set of XANES spectra, and thus allows localizing accurately the transformed regions in terms of changes in crystalline phases or any other heterogeneity in the sample. However, observations at this stage of data processing remain qualitative, and one cannot yet conclude as to the degree of phase transformation and/or the distribution of iron between the different phases.

In order to visualize the differences on the XANES spectra between the transformed and the unchanged regions of the sample at 37 GPa, we extracted a series of spectra following the profile materialized by the horizontal dashed line in Fig. 5.6-2f. The resulting series of spectra is presented in Fig. 5.6-3a. Blue spectra correspond to the non-transformed ringwoodite, whereas the two red ones correspond to the region with maximum degree of transformation. Green spectra are intermediates and most likely correspond to the region where the thermal gradient due to laser heating is significant. Note that since the distance between two pixels of the image is $5\ \mu\text{m}$, the central part of the heated region (*i.e.* corresponding to the two red spectra) appears relatively homogeneous within a surface of around $10\ \mu\text{m} - 15\ \mu\text{m}$ in diameter.

5. Results: XANES mapping in DAC

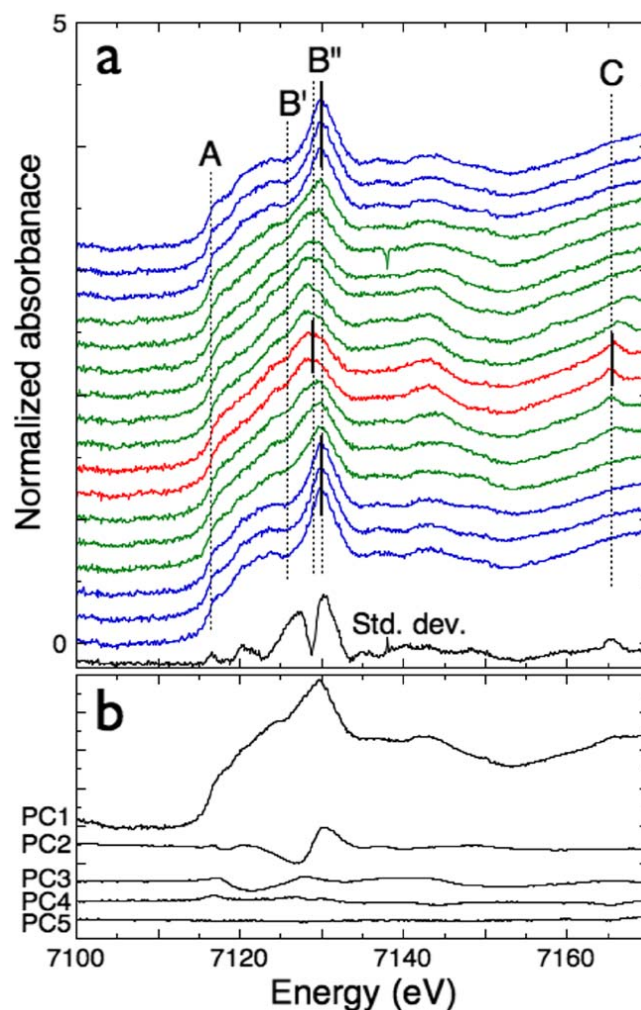


Figure 5.6-3 (a), Fe K-edge XANES spectra profile across the heated region at 37 GPa (dashed line in Fig. 5.6-2f) showing, in blue the XANES signatures for the non-transformed region, in green the intermediate region, and in red the more transformed region. The black curve corresponds to the standard deviation calculation. (b), First five principal components, respectively, noted PC1, PC2, PC3, PC4, and PC5, resulting from the PCA of the XANES data set.

One can first observe that the inflection point of the edge is not strongly affected by the phase transformation (see feature A in Fig. 5.6-3a), although the standard deviation curve, in black at the bottom of the figure, reveals a small peak at 7117 eV. The main changes in the XANES signatures appear in the white-line region. In particular, the small valley noted B', which characterizes the spectrum of ringwoodite, disappears progressively in the hot spot region. In parallel, feature B'' tends to decrease in intensity and slightly shift to lower energies while a small peak appears at higher energy (feature C). These different variations observed on the series

5. Results: XANES mapping in DAC

of XANES spectra are responsible for several significant features on the standard deviation curve.

The following step in the analytical process consists of exploring the set of data in terms of minimum number of independent components required to properly reproduce each spectrum of the series. To achieve this, we use the ‘principle component analysis’ (PCA) statistical tool from MATLAB®. The result of the PCA calculation is presented in Fig. 5.6-3b in which the first five principal components are represented and, respectively, noted PC1, PC2, PC3, PC4, and PC5. The first principal component (PC) reproduces the main part of the XANES spectra, whereas the second and third principal components also appear significant. Consequently, at least three standards are required to adjust the green and red spectra in Fig. 5.6-3a. However, although the fourth PC presents much lower amplitude compared with the first three, it presents slight features that are not negligible. Notably, this PC seems to be necessary for a fine adjustment of (i) the absorption edge ~ 7117 eV and (ii) the little peak in the XANES structure appearing in the hot spot region at 7165 eV. Finally, the fifth PC does not present any structure.

5.6.5. Results

The PCA shows that at least four standard spectra would be required for a robust adjustment of our data set. However, the fourth PC corresponds to $<5\%$ of the signal. Consequently, as a first approximation, we assume that three PCs are sufficient to reproduce the data in the heated region, and we choose the spectra of the three standards collected at 26 GPa presented in Fig.5.6-1, namely the ringwoodite, perovskite, and ferropericlase with an Fe# of 0.12. Note that the Fe# of the final products (*i.e.* crystals in the heated region) may differ from the starting material, and therefore from the Fe# of the standard compounds. This potentially introduces a systematic error in the analysis that needs to be carefully evaluated before deriving any quantitative result.

For each XANES spectrum of the map recorded at 26 GPa before laser heating, we performed a multicomponent linear combination fit based on the three standard spectra. We then reconstructed the maps based on the percentage of each standard required for the adjustment of each spectrum. Assuming that the system is correctly constrained, with the correct number of standards and the appropriate choice of standards, this process provides quantitative C^{Fe} maps, *i.e.* the distribution of iron within the different crystalline phases. Figs. 5.6-4a–c present,

5. Results: XANES mapping in DAC

respectively, the C^{Fe} maps of Rw, Pv, and Fp at 26 GPa, before laser heating. As shown in Fig. 5.6-2, a black line surrounds the sample in the pressure chamber. At this pressure and at ambient temperature, the sample is still not transformed. Thus, the iron is exclusively located in a ringwoodite structure ($\sim 100\%$), as shown by the homogeneous red region on the C^{Fe} map (Fig. 5.6-4a). In parallel, the same region appears in dark blue ($\sim 0\%$) for the perovskite and ferropericlasite C^{Fe} maps (Figs. 5.6-4b,c respectively).

The maps presented in Figs. 5.6-4d–f correspond to the distribution of iron in the different phases, *i.e.* C^{Fe} maps, obtained at the final stage of the experiment, after laser heating at 37 GPa. One clearly sees the impact point of the laser beam on the sample, which triggers an important decrease in the concentration of iron in the ringwoodite structure (Fig. 5.6-4d) coupled to an important increase in the perovskite and ferropericlasite phases (Figs. 5.6-4e,f respectively).

The averaged C^{Fe} values obtained from the transformed region of these maps (*i.e.* a 3 by 3 pixel region centered in the hot spot) are 47, 21, and $32 \pm 5\%$ for ringwoodite, perovskite, and ferropericlasite, respectively. These C^{Fe} values suffer from a systematic error, not included in our error bar, deriving from the use of models with Fe# equal to the starting sample. This error can be quantified only after performing a systematic analysis using Fe K-edge XANES data obtained at extreme conditions of P and T on standard samples with different Fe#.

The values obtained show that the phase transition is incomplete since the amount of Fe remaining in the ringwoodite structure is still close to 50%. Moreover, although the transformation of 1 mole of ringwoodite provides rigorously 1 mole of perovskite plus 1 mole of ferropericlasite (see Equation 1), the C^{Fe} values for perovskite and ferropericlasite differ by $11 \pm 5\%$. This difference likely traduces a redistribution of iron between the different mineral species, which suggests a higher Fe# in ferropericlasite compared with the one in perovskite. The same reasoning can be applied to the ringwoodite phase, in which the important C^{Fe} value obtained ($\sim 47\%$) could suggest an important affinity of iron for this phase. However, in order to interpret the C^{Fe} values obtained by Fe K-edge XANES spectroscopy, an accurate knowledge of the relative concentrations of each crystalline phase (C^{xtal}) is absolutely required, for example by complementary X-ray diffraction measurements. Indeed, the possible presence of axial thermal gradient, colder at the diamond surface than in the center of the sample, may also explain such important value obtained for the Rw phase. Once the real-phase concentration (C^{xtal}) is well established, and assuming that the chemical system is at thermodynamic equilibrium in the hot spot region, the coupling of X-ray absorption and diffraction data can provide a quantitative

5. Results: XANES mapping in DAC

description of the behavior of iron, which potentially yields the partitioning coefficients between the different crystalline phases.

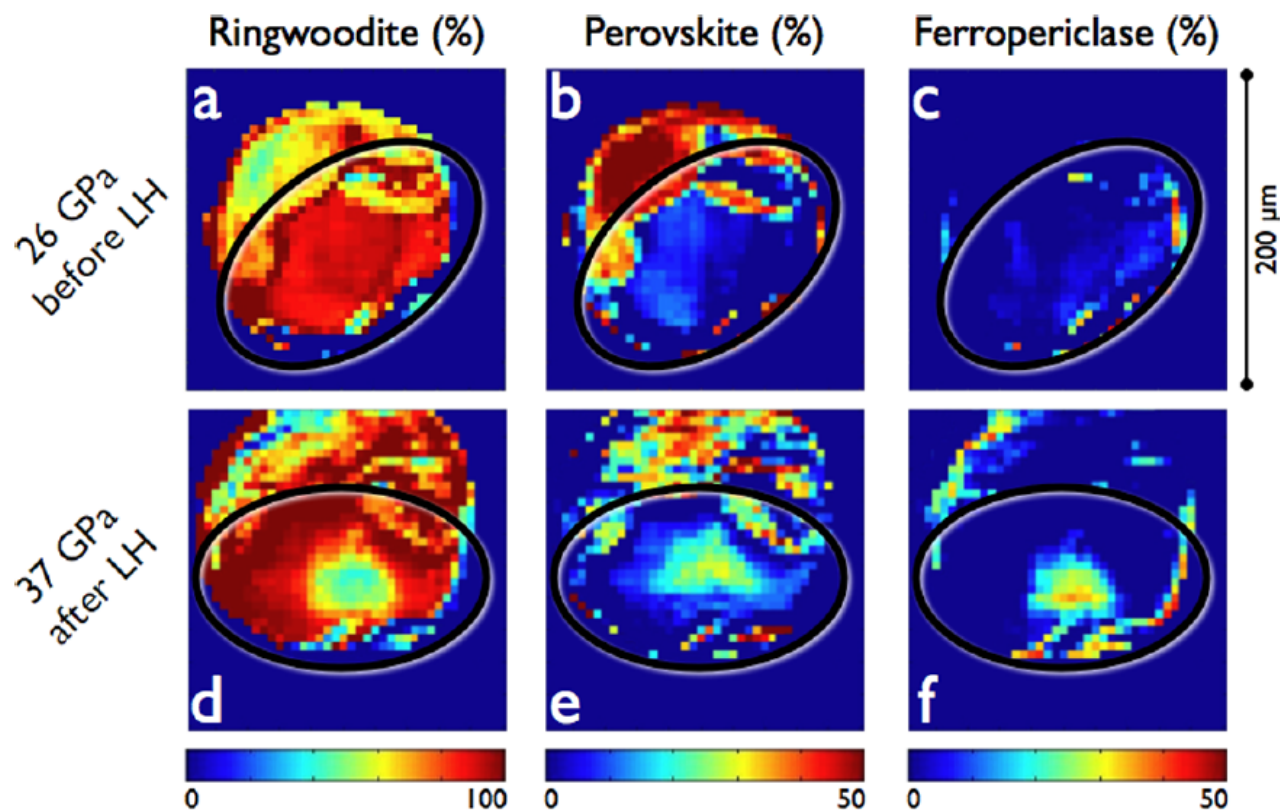


Figure 5.6-4 Iron concentration maps of ringwoodite, perovskite, and ferropericlase, for the sample at 26 GPa before laser heating (a, b, and c, respectively) and for the sample at 37 GPa after laser heating (d, e, and f, respectively). The sample in the pressure chamber is surrounded by a black line.

5.6.6. Conclusion

The analytical possibilities of μ -XANES mapping data sets have been implemented in the XASMAP package, including standard deviation, principal component analysis and multicomponent linear-combination fits. Such analytical tools make possible, for the first time, the reconstruction of quantitative concentration maps, seen from the point of view of a specific element (Fe in the case of this study). Since XANES spectroscopy is exclusively sensitive to the amount of absorber atoms probed and not directly to the amount of crystalline phases, the concentration maps yield the affinity of iron with each crystalline phase present in the system. This particularity offers a unique opportunity to characterize the behavior of the element probed and its affinity with the crystalline phases in a complex chemical system.

5. Results: XANES mapping in DAC

Our observations indicate that, at 37 GPa and after laser heating at 1600 °C, ~50% of the Fe is found in a crystallographic environment that differs from the initial ringwoodite phase and that can be described by a combination of ferropericlase and perovskite phases, where Fe shows a marked affinity for the ferropericlase.

The critical issues that may affect the quantitative results obtained from the analytical procedure described in this study are (i) the accurate normalization for the standards and the data set, (ii) the use of an appropriate number of standards, and (iii) the use of appropriate standards.

This work on a complex geophysical-relevant chemical system, coupling the performances of the dispersive μ -XANES mapping acquisition to a specific analytical procedure, is shown as an example to illustrate the potential of the method for a large domain of investigations for the high-pressure geosciences or physics and chemistry communities.

5.6.7. Acknowledgements

This work was supported by EuroMinSci ESF program and by the ESRF. L.D. acknowledges financial support by German Science Foundation (DFG). The authors especially thank the ID24 beamline staff, M.-C. Domingez for beamline control and acquisition software support, F. Perrin for support in electronics, and T. Mairs and S. Pasternak for support in mechanics.

5. Results: Fe-Mg partitioning

5.7. Chemically homogeneous spin transition zone in the Earth's lower mantle

Narygina O.¹, Dubrovinsky L.S.¹, McCammon C.¹, Pascarelli S.², Aquilanti G.², Kantor I.Yu.^{1,3}, Hanfland M.², Prakapenka V.³

¹Bayerisches Geoinstitut, Universität Bayreuth, 95440, Germany. ²European Synchrotron Radiation Facility, 38043, Grenoble, France. ³CARS, University of Chicago, IL 60437, USA.

To be submitted to Science

5.7.1. Abstract

The effect of spin crossover in lower mantle silicate perovskite (Pv) and ferropericlasite (Fp) on the iron partitioning between these two phases remains uncertain, mainly due to the lack of *in situ* experiments under the relevant pressure and temperature conditions. Combining *in situ* synchrotron X-ray absorption and diffraction measurements on natural (Mg_{0.88}Fe_{0.12})₂SiO₄ San Carlos olivine and synthetic ringwoodite at pressures between 22 GPa and 115 GPa treated at temperatures of 1950 K to 2300 K, we found that temperature promotes iron partitioning into Pv, while pressure acts oppositely. There is only a limited effect of spin crossover in co-existing Pv and Fp on iron partitioning which cannot produce an appreciable chemical inhomogeneity within the Earth's lower mantle spin transition zone.

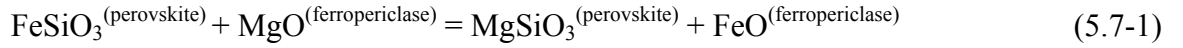
5.7.2. Introduction

Recently detected spin transitions in the Earth's lower mantle main constituents: (Mg,Fe)SiO₃ perovskite ([Badro et al., 2004](#); [Jackson et al., 2005](#); [Li et al., 2006](#); [McCammon et al., 2008](#); [Lin et al., 2008](#)) and (Mg,Fe)O ferropericlasite ([Van der Hilst and Kårason, 1999](#); [Lin et al., 2005](#); [2006](#); [Speziale et al., 2005](#); [Kantor et al., 2006a](#)), are believed to affect Fe-Mg partitioning between these phases and therefore form chemically distinct layers in the Earth's lower mantle which can be responsible for the seismic heterogeneities within 1000-2200 km layer ([Van der Hilst and Kårason, 1999](#)), named "spin transition zone" ([Lin et al., 2007b](#)). Such changes of electronic properties of iron may enhance Fe partitioning into the low-spin (LS)

5. Results: Fe-Mg partitioning

ferropericlase relative to the high-spin (HS) or intermediate-spin (IS) perovskite, almost entirely depleting perovskite of its iron (Badro et al., 2003), which would significantly affect lower mantle elasticity, rheology, electrical and thermal conductivity, and geodynamics.

Partitioning of Fe and Mg between co-existing Pv and Fp is characterized by the partition coefficient, K_D , corresponding to the following ion exchange reaction:



The apparent partition coefficient then is defined as:

$$K_D^{\text{app}} = \frac{\left(\frac{X_{\text{Fe}}}{X_{\text{Mg}}}\right)^{\text{Pv}}}{\left(\frac{X_{\text{Fe}}}{X_{\text{Mg}}}\right)^{\text{Fp}}}, \quad (5.7-2)$$

where X is the molar fraction of Fe (Fe^{2+} and Fe^{3+}) or Mg in Pv or Fp. Although Fe-Mg partitioning has been extensively studied neither absolute values, not even pressure-temperature trend (especially at conditions of spin crossover in co-existing phases) of K_D are well defined (Mao et al., 1997; Kobayashi et al., 2005; Auzende et al., 2008) (see Section 5.7.4c, Fig. 5.7-6). The reasons for discrepancies relate, particularly, to the lack of *in situ* partitioning experiments and difficulty in the performing of high-quality chemical analyses of the samples treated in a diamond anvil cells (DACs) at megabar pressure range.

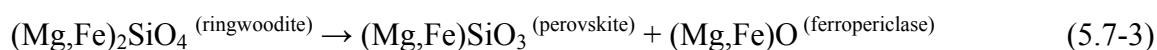
We have studied the iron partitioning between $(\text{Mg,Fe})\text{SiO}_3$ perovskite and $(\text{Mg,Fe})\text{O}$ ferropericlase *in situ* at pressures up to 115 GPa and temperatures up to 2300 K combining synchrotron radiation X-ray diffraction and Fe K-edge micro X-ray Absorption Near Edge Spectroscopy (μ -XANES) in a laser-heated DAC as described in our previous publications (Pascarelli et al, 2006; Muñoz et al., 2008; Aquilanti et al., 2009; Naryigna et al., 2009) (see also Section 5.7.4a).

5.7.3. Results and discussion

As a starting materials we used natural $(\text{Mg}_{0.88}\text{Fe}_{0.12})\text{SiO}_4$ San-Carlos olivine and ringwoodite, synthesized from it in multi-anvil apparatus at 19 GPa and 1900°C (the details regarding the preparation of the DAC experiments are given in Section 5.7.4a). We performed a

5. Results: Fe-Mg partitioning

series of DAC runs at different the pressure-temperature conditions for the synthesis and equilibration of a mixture of $(\text{Mg,Fe})\text{SiO}_3$ perovskite and $(\text{Mg,Fe})\text{O}$ ferropericlasite via the following reaction:



This reaction is supposed to take place in the Earth at bottom of transition zone (660 km seismic discontinuity) at pressures higher than 23 GPa and temperatures above 1600°C. In all runs ringwoodite had transformed completely to a mixture of perovskite and ferropericlasite in the heated area (as confirmed by XRD data, Fig. 5.7-2b) whereas surrounding unheated area remained as the starting phase. Before and after each laser heating at high pressure 2D μ -XANES mapping of the entire sample area with 5 μm step was performed (Fig. 5.7-1b,c). Each pixel of such a map provides the full XANES information at the Fe K-edge from a $5 \times 5 \mu\text{m}^2$ sample area (technical details are given in Muñoz et al. (2008) and Aquilanti et al. (2009)).

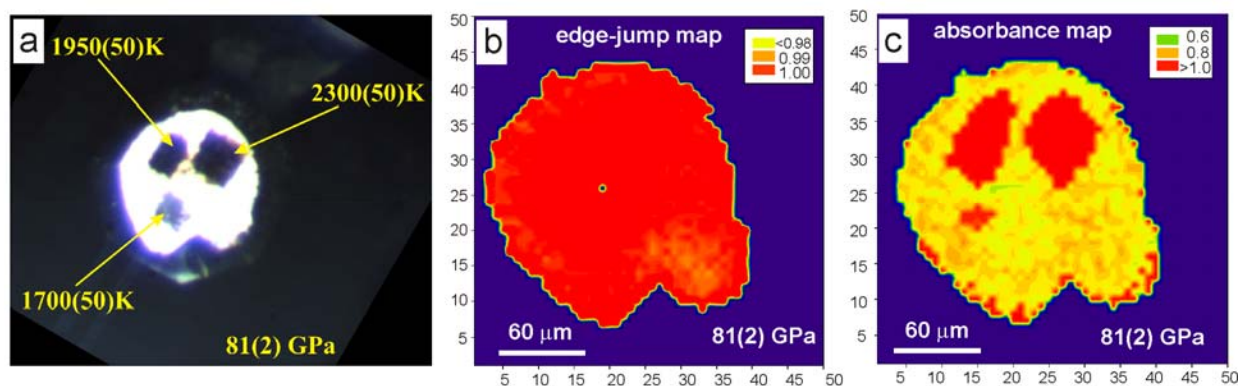


Figure 5.7-1. (a) Photo image of the ringwoodite, different parts of which were laser heated at 1700(50) K, 1950(50)K and 2300(50) K at 81(2) GPa. (b) Pre-normalized XANES edge-jump map collected after laser heating at 81(2) GPa and normalized absorbance map collected after laser heating at 81(2) GPa (c).

Value of edge-jump in XANES spectra is proportional to amount of the iron in sample (Muñoz et al., 2008). Homogeneity of the typical pre-normalized edge-jump map, collected after laser heating at 81(2) GPa and different temperatures (Fig. 5.7-1b) indicates that at the described experimental conditions and within the precision of the measurements we do not observe noticeable migration of the iron due to laser heating. Then, applying the same analytical method described in Muñoz et al. (2008), we obtain normalized absorbance map (Fig. 5.7-1c, areas with the absorbance higher than 1 correspond to the laser heated areas, compare with Fig. 5.7-1a),

5. Results: Fe-Mg partitioning

based on which we deconvolute the absorption spectra, collected in the laser-heated at 2300(100) K area, on the 25.1(5)% of “perovskite” and 74.9(5)% of “ferropericlase” absorption component at 81(2) GPa (Fig. 5.7-2a). Combining these values with the phases amounts (50(1)% according to result of full-profile refinement with GSAS program of X-ray diffraction data collected at the same P - T conditions at the same spot, Fig. 5.7-2b), we can calculate the apparent Fe-Mg partition coefficient between perovskite and ferropericlase (defined in Eq. 5.7-2), $K_D=0.29(6)$.

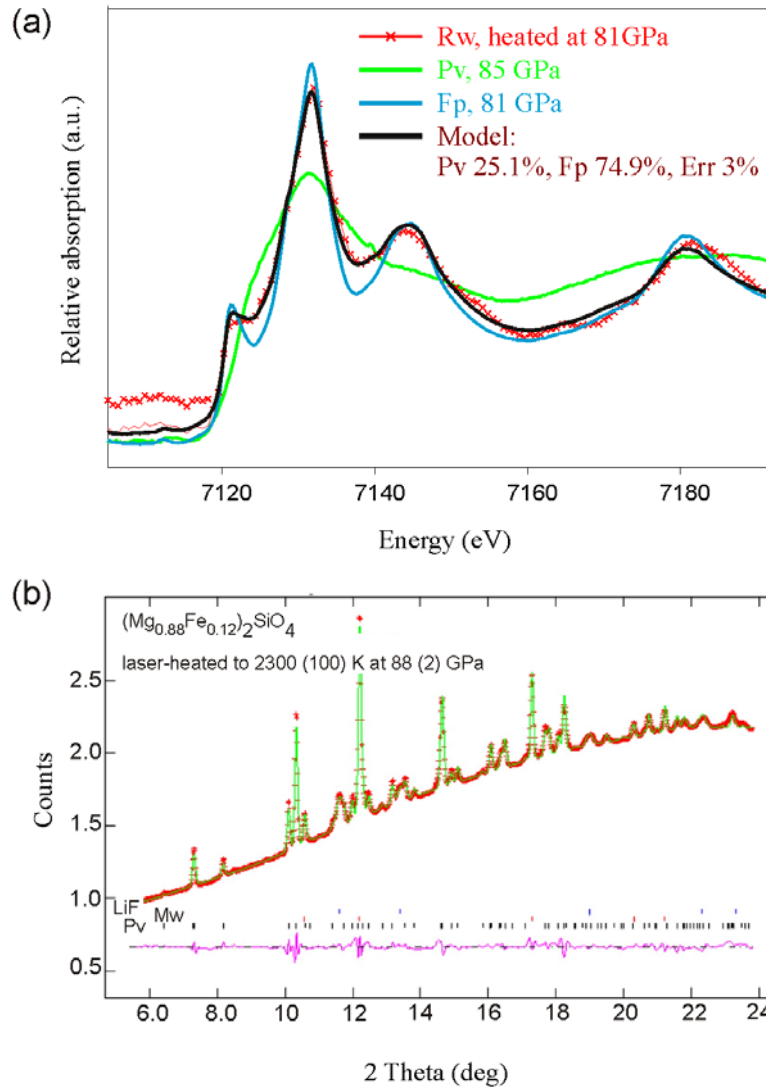


Figure 5.7-2 (a) Deconvolution of the XANES spectra, collected from the area laser-heated at 81(2)GPa, to the “perovskite” and “ferropericlase” XANES components, collected at the comparable pressures. (b) X-ray diffraction pattern collected at ID09A (ESRF) ($\lambda = 0.4141 \text{ \AA}$) from the $(Mg_{0.88}Fe_{0.12})_2SiO_4$ ringwoodite laser heated at 2300(100) K and 88(2) GPa. Apart from LiF only diffraction peaks from silicate perovskite and ferropericlase are presented which confirms complete decomposition of the ringwoodite to perovskite and ferropericlase via the breakdown reaction 5.7-3.

5. Results: Fe-Mg partitioning

Applying the same routine to the other pressure-temperature points (including the point collected on decompression, shown in blue in the Fig. 5.7-3) we obtained Fe-Mg partition coefficient between Pv and Fp as a function of pressure at 1950(50) and 2300(100) K (Fig. 5.7-3). As was expected with the increase of pressure (and hence with the increase of the amount of LS ferrous iron in ferropericlase) iron preferably partitions to ferropericlase in comparison with magnesium silicate perovskite (the same trend (dark green squares in Fig. 5.7-3) was observed by Auzende et al., 2008). Conversely with the increase of temperature, iron preferably partitions to silicate perovskite (coincides with Mao et al., 1999; Frost and Langenhorst, 2002).

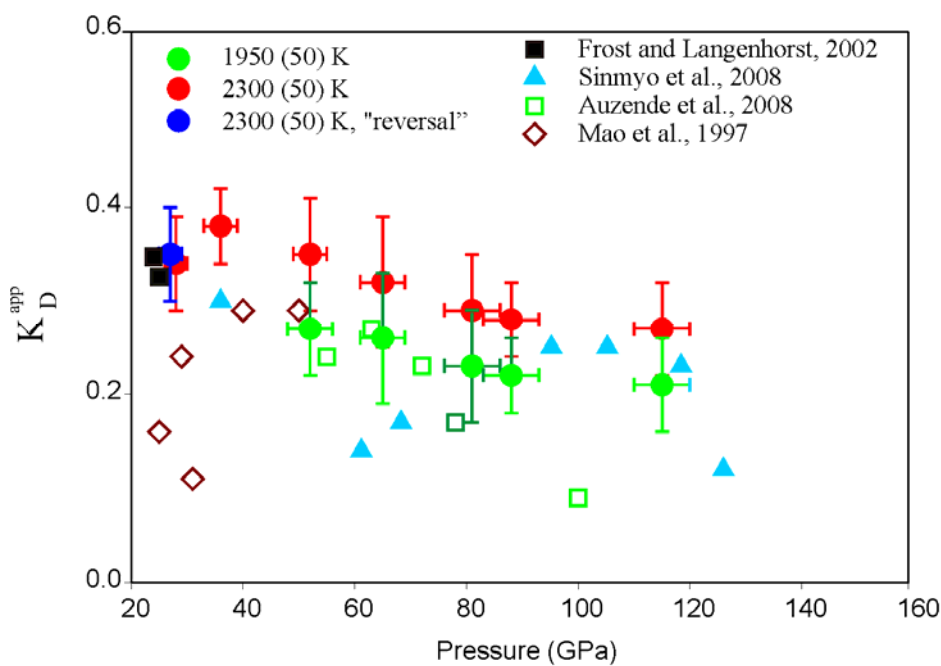


Figure 5.7-3 Fe-Mg partition coefficient between $(\text{Mg,Fe})\text{SiO}_3$ perovskite and $(\text{Mg,Fe})\text{O}$ ferropericlase (defined in Eq. 5.7-2) as a function of pressure at 1950 K (green closed circles) and 2300 K (red and blue closed circles), obtained in this study. For comparison some of previously published results are shown.

Our iron partitioning data is in good agreement with that obtained in multi-anvil experiments (closed light green circles in Fig. 5.7-3) (Frost and Langenhorst, 2002). Although there are quite a bit of discrepancies with the other results of the previous studies, which might be explained by both different starting materials (see Section 5.7.4b), methods of treatment, and difference in methodology of the chemical and phase analysis (“postmortem” characterization in all previous studies vs. *in situ* in this work).

5. Results: Fe-Mg partitioning

The effect of pressure and temperature on the K_D is subtle therefore we do not expect any significant change of the overall density and sound velocity of the Pv and Fp phase assemblage across the lower mantle.

The Earth's lower mantle mineral composition is certainly more complex than the one we investigated in the laboratory. Apart from pressure and temperature, Fe-Mg partitioning between Pv and Fp could be affected by the total amount of iron, iron oxidation state, oxygen fugacity, presence of Al in Pv, influence of other phases, etc. However, none of these factors could suppress the spin crossovers in Pv and Fp ([McCammon et al., 2008](#); [Speziale et al., 2005](#); [Kantor et al., 2006a](#)), which implies only a small change of Fe-Mg partitioning with depth, and therefore that the Earth's spin transition zone can be considered to be chemically homogeneous.

5.7.4. Supplementary materials

5.7.4a Experimental details

In situ experiments were conducted in DACs equipped with 250 or 300 μm culet size diamond anvils. At pressures above 70 GPa diamonds with laser-drilled hole (~ 100 μm in diameter and ~ 30 μm height) were used in order to increase thickness of thermal insulating layer and improve homogeneity and stability of laser heating. A confining gasket, made of a 200 μm thick rhenium foil was pre-indented to about 30 μm and then 125 μm was drilled in a gasket. A ringwoodite or San-Carlos olivine starting material along with ruby chips was placed in a sample chamber between two LiF layers, which were used as a thermal isolation, as a pressure-transmitting medium, and as an internal pressure calibrant (additional to the ruby fluorescence). At the highest reached pressure value of 115 GPa the pressure gradient between the center and the edge of the sample chamber did not exceed 5 GPa.

K-edge XANES measurements were performed at the European Synchrotron Radiation Facility at the energy dispersive XAS beamline ID24. The beam was focused horizontally using a curved polychromator Si (111) crystal in Bragg geometry and vertically with a bent Si mirror placed at 2.8 mrad with respect to the direct beam ([Pascarelli et al., 2004](#)). The Bragg diffraction peaks arising from the diamond anvils were removed from the energy range of interest by changing the orientation of the diamond anvil cell and following in real time the intensity of the

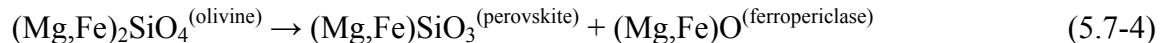
5. Results: Fe-Mg partitioning

transmitted beam on a two-dimensional detector. Further details regarding the experimental setup are given in Aquilanti et al. (2009).

To record the XANES maps, the DAC was scanned horizontally and vertically in the focal plane of the X-ray beam with steps of 5 μm . Fe K-edge XANES were recorded over a 50×50 step grid in order to cover an area of $250 \mu\text{m} \times 250 \mu\text{m}$. Each map contains 2500 XANES spectra (one spectrum per pixel). Given the high absorbance of the diamond anvils, the acquisition time was 4 s per spectrum. Data reduction, including energy calibration, normalization and edge position tracking, was performed using the XASMAP software (<http://www.esrf.eu/UsersAndScience/Experiments/TBS/SciSoft/OurSoftware/XASMAP>), allowing different kinds of targeted maps, such as absorbance maps, at given energy to be obtained (Muñoz et al., 2006). The analytical procedure to extract from these maps relevant information, such as the iron affinity for the different crystalline phases, is described by Muñoz et al. (2008). The measured XANES spectra were analysed using the VIPER program (Klementev, 2001). The flat part of the pre-edge region of the spectrum was fitted to the Victoreen function ($F = a + bE^{-3}$, where E is the absorption energy and a and b are fit parameters) and this baseline was extended over the entire energy region. The post-edge jump in X-ray absorption was then normalized to 1.

5.7.4b Effect of starting material

It is known that the main lower mantle phase assemblage (magnesium silicate perovskite and ferropericlasite) can be obtained by pressure-temperature induced decomposition of a magnesium silicate ringwoodite (this case is fully described in the manuscript) or olivine via the following reaction:



In order to evaluate the influence of the synthesis procedure on the value of Fe-Mg partition coefficient between silicate perovskite and ferropericlasite and its behaviour at high pressures and temperatures we performed the same experiment (as described in Section 5.7.3) but chose a natural San-Carlos $(\text{Mg}_{0.88}\text{Fe}_{0.12})_2\text{SiO}_4$ olivine as the starting material. The synthesis was conducted in a laser heated diamond anvil cell (DAC) equipped with 250-300 μm culet size

5. Results: Fe-Mg partitioning

diamond anvils. A confining gasket, made of a 200 μm thick rhenium foil, was pre-indented to 30 μm and then 125 μm hole was drilled in a gasket. The olivine sample, sandwiched between two layers of LiF, was then placed into the hole along with ruby chips used for pressure measurements. LiF layers were used as a thermal isolation for laser heating, as a pressure transmitting medium and as an additional internal pressure standard. The olivine sample in the DAC was initially compressed up to 52 GPa and a central portion of the sample then was double side laser heated at 2300(100) K using a YAG laser. Before and after laser heating the 2D Fe K-edge micro-XANES mapping of the entire sample area with 5 μm step was performed. Each pixel of such a map gives the full x-ray absorption information from a sample area of $5 \times 5 \mu\text{m}^2$ (further technical details are given in Muñoz et al. (2008) and Aquilanti et al. (2009)). Normalized edge-jump XANES map of the olivine (Fig. 5.7-4b), central portion of which was double-side laser heated at 52 GPa and 2300 K (Fig. 5.7-4a) is homogenous. This suggests that within the uncertainty of measurements we do not observe any significant migration of the iron within the pressure chamber after applied temperature treatment (Muñoz et al., 2008). Applying the analytical method described in Muñoz et al. (2008) we obtain normalized absorbance map (Fig. 5.7-4c), where one can clearly distinguish between the laser-heated area, where the breakdown reaction (5.7-4) occurred (absorbance values higher than 0.5) and the rest of the sample, where unheated material remains as the starting olivine (absorbance values lower than 0.5).

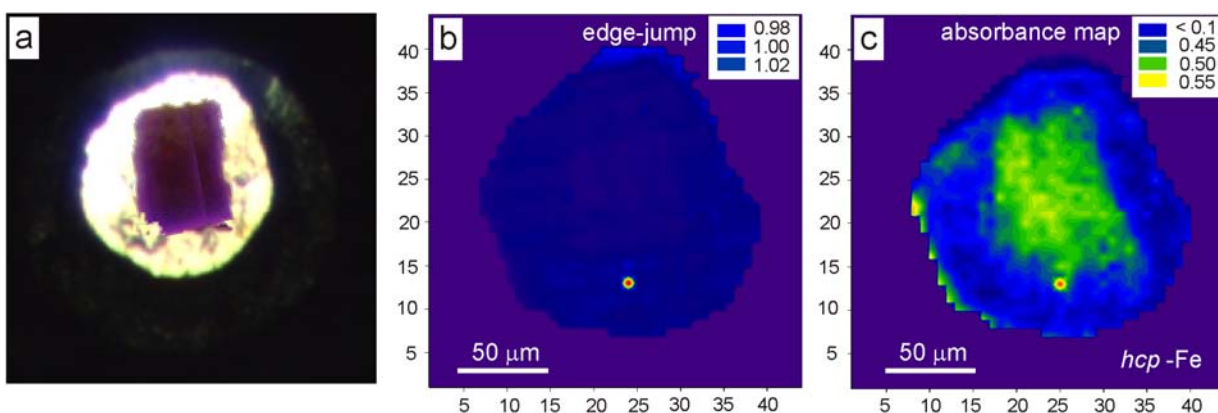


Figure 5.7-4 (a) Photo image of the $(\text{Mg}_{0.88}\text{Fe}_{0.12})_2\text{SiO}_4$ olivine, laser-heated to 2300 (100) K at 52(1) GPa. Edge-jump (b) and absorbance (c) maps, collected from the $(\text{Mg}_{0.88}\text{Fe}_{0.12})_2\text{SiO}_4$ olivine after laser heating at 52(1) GPa. Absorbance map is plotted at the 7112.7 eV, the energy corresponding to Fe K-edge at 52 GPa.

Average XANES spectrum from the laser-heated portion of the sample is shown by red crosses in Fig. 5.7-5a. For comparison XANES spectrum collected from $(\text{Mg,Fe})_2\text{SiO}_4$

5. Results: Fe-Mg partitioning

ringwoodite and $(\text{Mg,Fe})_2\text{SiO}_4$ olivine, both laser-heated at 52(1) GPa to 2300(100)K, are shown in Fig. 5.7-5b by black and red curves, respectively. The shape of the laser-heated olivine XANES spectrum can not be described by the superposition of only magnesium silicate perovskite and ferropericlasite components (as it should be according to the reaction (5.7-4) and as we observed in the case of ringwoodite, described in the section 5.7.3).

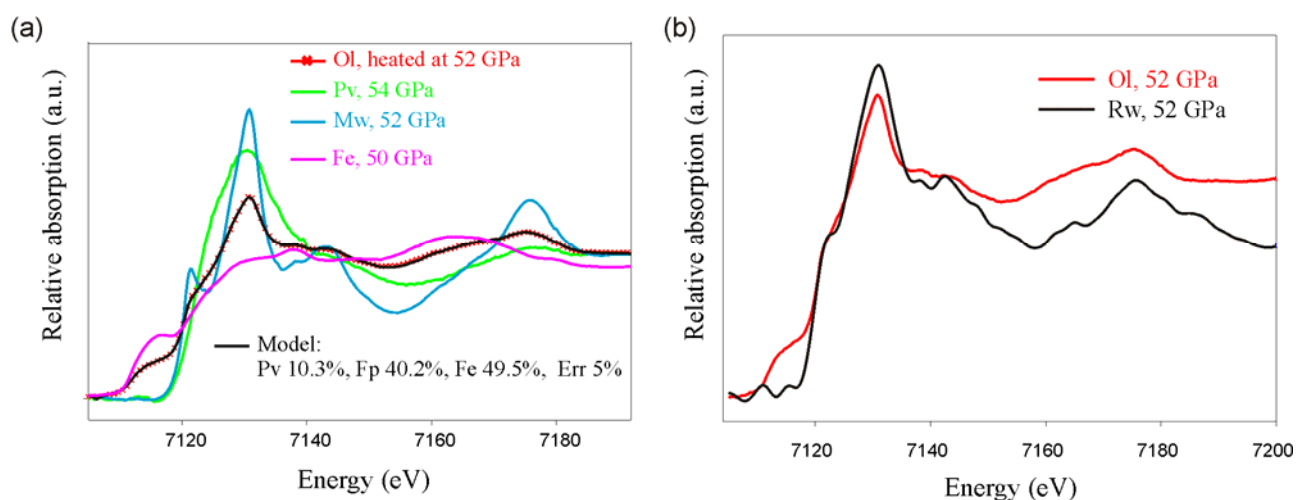


Figure 5.7-5 (a) Deconvolution of the XANES spectrum collected from laser heated $(\text{Mg}_{0.88}\text{Fe}_{0.12})_2\text{SiO}_4$ olivine (52 GPa and 2300K) (red crosses) to 10.3% magnesium silicate perovskite (green), 40.2% ferropericlasite (blue) and 49.5% of metallic iron (pink). (b) XANES spectra collected from $(\text{Mg}_{0.88}\text{Fe}_{0.12})_2\text{SiO}_4$ olivine (red) and $(\text{Mg}_{0.88}\text{Fe}_{0.12})_2\text{SiO}_4$ ringwoodite (black) laser heated at 52 GPa and 2300(100) K.

Previously it was reported that breakdown reaction of $(\text{Mg,Fe})_2\text{SiO}_4$ olivine (reaction 5.7-4) is accompanied by the precipitation of a metallic iron through the disproportionation of Fe^{2+} into Fe^{3+} and metallic iron (Fe^0) (Kobayashi et al., 2005; Frost et al., 2004a; Auzende et al., 2008). Indeed if we add metallic iron component to our deconvolution model (Fig. 5.7-5a) we can perfectly reproduce XANES spectrum collected from the laser-heated area by the superposition of 10.3% silicate perovskite, 40.2% ferropericlasite and 49.5% metallic iron XANES components collected at the almost the same P-T conditions (Fig. 5.7-5a).

Precipitation of metallic iron in the course of $(\text{Mg,Fe})_2\text{SiO}_4$ olivine decomposition to silicate perovskite and ferropericlasite suggests that several parallel reactions (oxidation of Fe^{2+} , reduction of Fe^{3+} , formation of vacancies in silicate perovskite, etc.) are taking place in the samples, which obviously affects the value of Fe-Mg partitioning between perovskite and ferropericlasite. This fact could explain the smaller (in comparison to the present study) partition coefficient values given by Kobayashi et al. (2005) and Auzende et al. (2008). Therefore we

5. Results: Fe-Mg partitioning

suggest that the starting conditions for the experimental studies of the iron partitioning between silicate perovskite and ferropericlase have to be chosen with the high caution.

5.7.4c Supplementary figures

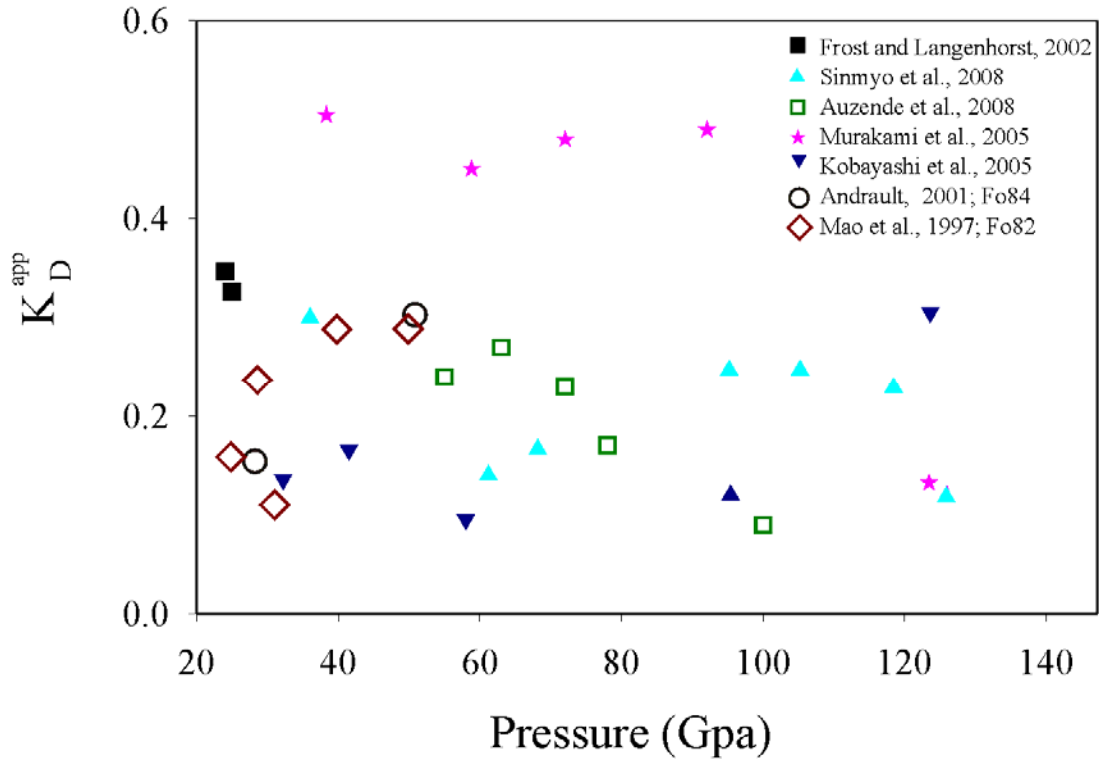


Figure 5.7-6 Previously reported values of Fe-Mg partition coefficient between $(\text{Mg,Fe})\text{SiO}_3$ perovskite and $(\text{Mg,Fe})\text{O}$ ferropericlase, obtained by multianvil and DAC experiments.

5.8. Phase relations in Fe-Ni-C system at high pressures and temperatures: implication for the Earth's Core

Narygina O.¹, Dubrovinsky L.¹, Miyajima N.¹, McCammon C.¹, Frost D.¹, Dubrovinskaia N.^{1,2}, Mezouar M.³, Kantor I.^{1,4}, Prakapenka V.⁴

¹Bayerisches Geoinstitut, Universität Bayreuth, D-95440 Bayreuth, Germany; ²Mineralphysik, Institut für Geowissenschaften, Universität Heidelberg, 69120 Heidelberg, Germany; ³European Synchrotron Radiation Facility, BP 220, F-38043 Grenoble Cedex, France; ⁴Center for Advanced Radiation Sources, University of Chicago, Chicago, Illinois 60637, USA

To be submitted to Physics of the Earth and Planetary Interiors

5.8.1. Abstract

We performed comparative study of phase relations in $\text{Fe}_{1-x}\text{Ni}_x$ ($0.10 < x < 0.22$) and $\text{Fe}_{0.90}\text{Ni}_{(0.10-x)}\text{C}_x$ ($0.1 < x < 0.5$) systems at pressures to 45 GPa and temperatures to 2600 K using laser-heated diamond anvil cell (LH-DAC) and large-volume press (LVP) techniques. We showed that laser heating of Fe-Ni alloys in DAC even to relatively low temperatures can lead to the contamination of the sample with the carbon coming from diamond anvils, which results in the decomposition of the alloy on iron- and nickel-rich components. Based on the results of LVP experiments with Fe-Ni-C system (the covered P-T area is 0.5-20.0(5) GPa and 2050-2300 K) we suggest decrease of carbon solubility in FeNi alloy with pressure (from 0.9 wt% at 9 GPa and 2300 K to 0.7 wt% at 20 GPa and 2300 K).

5.8.2. Introduction

Knowledge of the properties of the Earth's core (its structure and composition, temperature profile, etc) as well as understanding of the processes driving its dynamics is essential for reliable modeling of the deep Earth's interior. Due to its remoteness the only direct probe of the properties of the Earth's core is provided by seismic observations, requiring large earthquake events and highly sensitive seismometers, which are able to detect weak wave signals, propagated through the Earth's deepest interior. However seismic data along with estimations of

5. Results: phase relations in Fe-Ni-C system

the bulk silicate earth composition ([Ringwood, 1979](#); [Allégre et al., 1995b](#); [O'Neill and Palme, 1998](#); [McDonough and Sun, 1995](#)) and meteoritic records provide some insights in the structure and composition of the Earth's core. Nowadays it is well established that the core consists of the liquid outer and solid inner parts, which are mainly composed by $\text{Fe}_{1-x}\text{Ni}_x$ ($0.5 \text{ wt.\%} \leq x \leq 20 \text{ wt.\%}$) alloy with a certain amount of light element(s) (Si, S, O, H, C, etc.), required to fulfill the density deficit, which accounts for $\sim 6\text{-}10 \%$ between the outer core and liquid Fe, and $1\text{-}2 \%$ between inner core and crystalline Fe ([Birch, 1952](#); [McDonough and Sun, 1995](#); [Allégre et al., 1995](#); [Poirier, 1994a](#)).

Phase diagram of iron - the most abundant element in the core, has been extensively studied using both experimental and numerical approaches. Although melting curve of iron at high pressures is controversial ($\sim 2000 \text{ K}$ misfit between shockwave ([Yoo et al., 1993](#); [Brown and McQueen, 1986](#)) and diamond anvil cell ([Williams et al., 1987](#); [Boehler et al., 1993](#); [Shen et al., 1998](#)) experiments, with theoretical predictions laying in between ([Laio et al., 2000](#); [Alfe, 2009](#))) both experimentalist and theoreticians are agreed that at the Earth's core conditions the stable phase of pure iron more likely would be hexagonal closed packed (*hcp*) ε -phase ([Akimoto, 1987](#); [Boehler, 1986](#); [Mao et al., 1987](#); [Manghnani and Syono, 1987](#); [Dubrovinsky et al., 1998](#); [Schen et al., 1998](#); [Funamori et al., 1996](#); [Dewaele et al., 2006](#); [Vocadlo et al., 2000](#)). Although there are indications that at pressures around $300\text{-}360 \text{ GPa}$ face-centered cubic (*fcc*) γ -phase of iron may become as stable as ε -phase at high temperature close to melting ($5000\text{-}6000 \text{ K}$) ([Michaulushkin et al., 2007](#)). Since the core is not made out of pure iron, in order to constrain its structural properties one need to take into account alloying effect of nickel and light element(s) on the phase diagram of iron at the relevant P-T conditions. It is known that even small amount of nickel, alloyed with iron, significantly enlarges stability area of γ -phase to lower temperatures and higher pressures ([Huang et al., 1988, 1992](#); [Lin et al., 2002](#); [Mao et al., 2006](#); [Dubrovinsky et al., 2007](#)). As was suggested by Mao et al. (2006) 15 wt\% Ni is enough to stabilize γ -phase to the pressure relevant for the outer Earth's core. According to theoretical calculations small amount of impurities can stabilize body-centered cubic (*bcc*) α -iron phase in the inner core ([Belonoshko et al., 2003, 2008](#); [Vocadlo et al., 2003](#)). Experimentally formation of the so-called "high-pressure *bcc* -structured phase" in laser-heated diamond anvil cell was reported by Dubrovinsky et al. (2007) for $\text{Fe}_{0.9}\text{Ni}_{0.1}$ alloy at pressures above 225 GPa and temperatures over 3500 K . Alloying effect of the potential light core's components on the phase diagram of iron at elevated pressures and temperatures also has been extensively studied ([Badding et al., 1991](#); [Wood, 1993](#); [Fei and](#)

5. Results: phase relations in Fe-Ni-C system

[Mao, 1994](#); [Knittel and Williams, 1995](#); [Sanloup et al., 2000b](#); [Fei et al., 1995, 2000](#); [Scott et al., 2001](#); Lin J.-F., Heinz D.L., Campbell A.J., Devine J.M., Mao W.L., and Shen G (2002b) Iron-silicon alloy alloy in Earth's core? *Science* **295**, 313-315). However the question regarding the composition and structural phase of the Earth's core remains unsolved in significantly degree due to the lack of experiments under the relevant pressures and temperatures, which leads to inevitable extrapolations of experimental data set to the Earth's core conditions.

Pressures and temperatures comparable with that in the core can be achieved in diamond anvil cells with in situ laser heating (LH-DACs) ([Boehler, 1993](#), [Murakami et al., 2005](#); [Mao et al., 2006](#); [Dubrovinsky et al., 2007](#); [Ohta et al., 2008](#); etc.), but the price for this is the lack of control of the system, including possible significant pressure and temperature gradients, possible occurrence of chemical reactions, migration of the matter under study ([Heinz et al., 1991](#); [Prakapenka et al. 2003-2004](#), [Fialin et al., 2009](#)), which cause some uncertainties in the interpretation of the results and gives rise to the question whether or not the result obtained reflects the equilibrium of the system at the certain pressure and temperature. The large-volume press (LVP) technique (another method of static compression) on the other hand provides more controllable and equilibrated experimental conditions, due to the larger size of the pressure chamber. However the upper pressure limit is 25 GPa (in multianvil experiments with tungsten carbide anvils ([Kubo and Akaogi, 2000](#))), which is far below the Earth's core conditions.

Employing advantages of both LH-DAC and LVP experiments we performed comparative study of the phase relations in $\text{Fe}_{(1-x)}\text{Ni}_x$ ($0.10 < x < 0.22$ wt%) to 45 GPa and 2300 K and investigated the effect of carbon on the system at high pressures and temperatures.

5.8.3. Experimental details

Synthetic $\text{Fe}_{0.9}\text{Ni}_{0.1}$, $\text{Fe}_{0.85}\text{Ni}_{0.15}$ and $\text{Fe}_{0.78}\text{Ni}_{0.22}$ alloys used for LH-DAC and part of LVP experiments were synthesized from metallic rods by arc melting of appropriate amounts of iron (99.999% purity) and nickel (99.999 % purity) in an arc furnace in a pure argon atmosphere. The samples were homogenized in vacuum at 900°C for 150 hours. Their chemical and phase homogeneity were confirmed by electron-microprobe analyses and X-ray powder diffraction. Further details of synthesis and sample characterization are given in Dubrovinsky et al. ([2001](#)). A series of LVP runs were performed with the powder mixtures $\text{Fe}_{0.90}\text{Ni}_{(0.10-x)}\text{C}_x$ (where $0.1 < x < 0.5$ at.%). The powder were grated together under alcohol, dried and placed into a capsule. Two

5. Results: phase relations in Fe-Ni-C system

types of capsule were used: (i) “simple” capsule made out of MgO compressed powder; and (ii) “complex” capsule, composed by a single crystal of NaCl placed inside the MgO capsule. NaCl was used in order to eliminate oxygen from the system.

For LH-DAC experiments the opposed-plate DACs equipped with diamond anvils of 250 μm and 300 μm culet size. 10-15 μm -thick foils of synthetic $^{57}\text{Fe}_{0.9}\text{Ni}_{0.1}$ and $^{57}\text{Fe}_{0.78}\text{Ni}_{0.22}$ alloys, sandwiched between two 10 μm -thick pellets of LiF or NaCl, along with few ruby chips (used for pressure calibration according to ruby fluorescence scale by [Mao et al. \(1986\)](#)) were loaded in a 100 – 125 μm hole drilled in Re gasket pre-indented to 30-35 μm . LiF and NaCl were used as a pressure transmitting medium, thermal isolation from diamond anvils as well as an internal X-ray diffraction pressure marker (LiF and NaCl equation of states were taken from Liu et al. ([2006](#)) and Brown ([2000](#)), respectively).

The high-resolution angle dispersive X-ray diffraction (XRD) experiments with *ex situ* laser heating were performed with 0.3738 \AA radiation at beamline ID27 at the European Synchrotron Radiation Facility (ESRF). The MAR 345 image-plate system at 450 mm distance from the sample was used as a detector. The beam size on the sample was approximately 10 μm x 9 μm FWHM. As a source of laser light we use a Nd:YAG Quantronix 117 two-head laser (CW TEM00 mode, $\lambda = 1064$ nm) with a maximum power of 70 W.

The high-resolution XRD experiments with *in situ* double-side Nd:YLF laser heating system were carried out at Applied Photon Source APS (GSECARS, sector 13). The size of the laser beam varied from 20 to 30 μm in diameter with a temperature variation of ± 100 K within the beam at temperatures in the order of 3000 K. Heating duration in different experiments was from 10 to 30 minutes. Temperature was measured by means of multiwavelength spectroradiometry. The radiation with 0.3344 \AA wavelength and a CCD MAR detector were used. Two dimensional XRD images we integrated using Fit2D software ([Hammersley, 1997, 1998](#)) and then processed by means of GSAS package ([Larson and Von Dreele, 2004](#)).

For the quenched experiments the end-loaded piston-cylinder apparatus and 6-8 Kawai-type multianvil press installed in Bayerisches Geoinstitut (BGI) were used. Piston-cylinder experiments were performed in half-inch talc-Pyrex glass assembly, equipped with graphite heater. Temperature was controlled by a $\text{W}_{75}\text{Re}_{25}/\text{W}_{97}\text{Re}_3$ thermocouple (type D). For multianvil experiments the 10/5 (octahedral edge length / tungsten-carbide anvil truncation in mm) assembly with LaCrO_3 heater was employed in the 1200 tonne press. The pressure calibration curve is based on that developed by Frost et al. ([2001](#)). Time of LVP runs varied from 4 h to 14 h.

5. Results: phase relations in Fe-Ni-C system

Sample recovered from both LH-DAC and LVP experiments were analysed by X-ray powder diffraction, Mössbauer spectroscopy, Transmission Electron Microscopy (TEM) and Scanning Electron Microscopy (SEM). Powder X-ray diffraction measurements were performed at (i) high-brilliance X-ray diffractometer with Mo anod, providing the 0.7108 Å radiation, (ii) Swiss-Norwegian beamline (ESRF), with 0.7002 Å radiation and (iii) APS (GSCARS, sector 13), with 0.3344 Å.

5.8.4. Experimental results

5.8.4a XRD study of FeNi alloys, employing LH-DAC

5.8.4a.i Fe_{0.9}Ni_{0.1} alloy at pressures to 30 GPa

The thin (15 µm) foil of ⁵⁷Fe_{0.90}Ni_{0.10} alloy was compressed in DAC to 30 (1) GPa, the central part, ~ 20 µm × 40 µm, was laser heated to 2000 K (± 100 K) (see Fig. 5.8-1b). During the decompression from 30 GPa to the ambient pressure we collected XRD spectra from the heated and non-heated areas of the sample (ID27, ESRF). In the laser-heated spot we detected presence of *fcc*-structured phase along with *hcp*-FeNi. While in the non-laser-heated area only initial *hcp*-(Fe,Ni)-alloy was found (see Fig. 5.8-1a,c). The *fcc-hcp* phase assemblage was observed from 30 GPa to ~ 6 GPa, where it eventually transformed to the *bcc*-structured Fe-Ni phase. Since *fcc*-structured phase, detected in the heated area, accounts only for about 6 (1) wt%, it is impossible to extract XRD parameters of its *bcc*-structured polymorph, “hidden” by the strong reflections coming from the “main” (Fe,Ni) *bcc*-phase. At the same pressure (~ 6 GPa) the *hcp-bcc* structural transition occurred in the non-heated area (Fig. 5.8-1c). Molar volumes of the *hcp*-FeNi phase observed in the laser-heated area (closed black triangles) and that in the non-heated part (open triangles) are almost the same within the uncertainty of measurements (Fig. 5.8-1c). The same is valid for the *bcc*-phases, formed below 6 GPa in both areas.

Coexistence of *hcp* and *fcc* –structured phases of Fe,Ni-alloy at certain pressure-temperature (P-T) conditions was previously reported ([Lin et al., 2002a](#); [Mao et al., 2006](#)), however presence of *fcc*-Fe,Ni-alloy at room temperature in the LH-DAC experiments was never discussed before.

5. Results: phase relations in Fe-Ni-C system

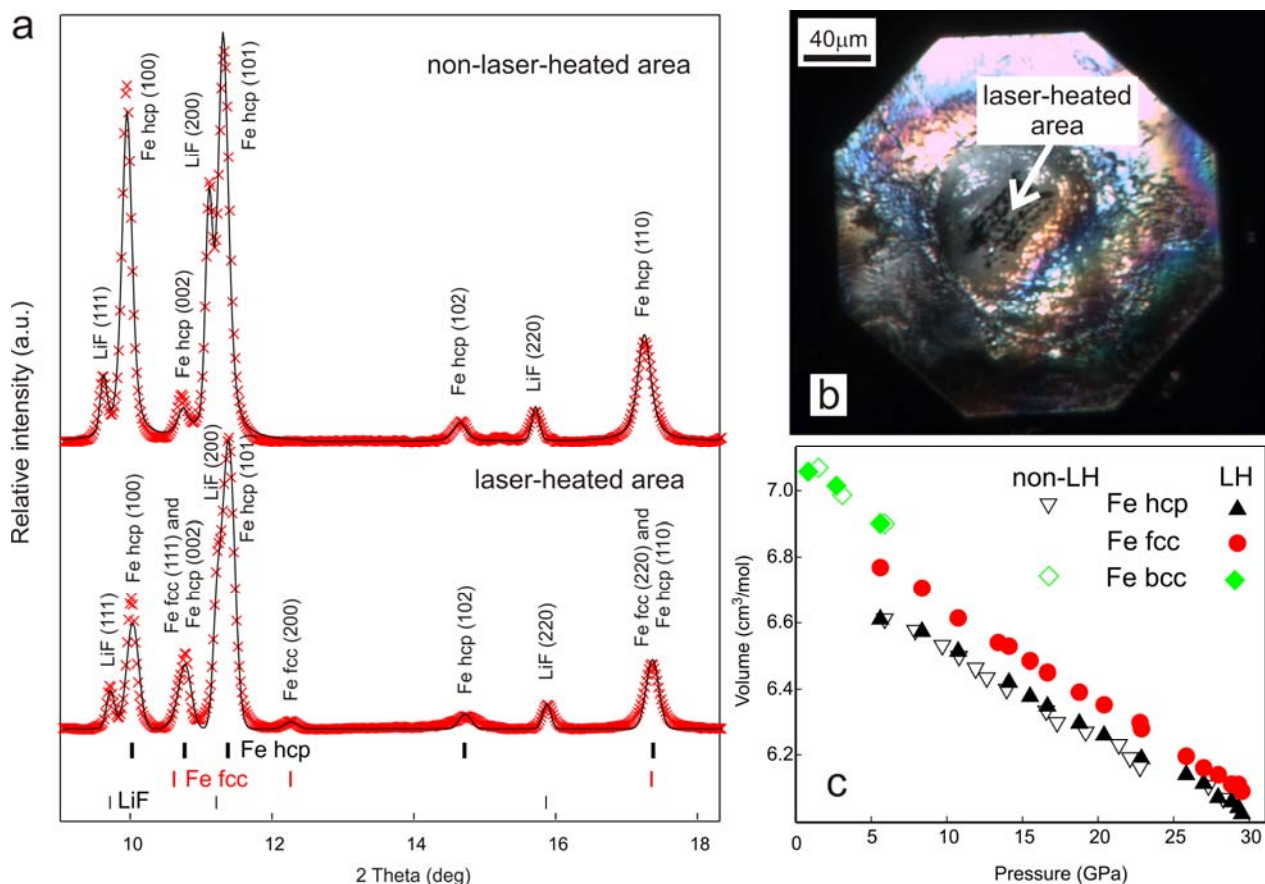


Figure 5.8-1 (a) XRD patterns ($\lambda = 0.3738 \text{ \AA}$) collected at 15.5 (0.1) GPa and room temperature from the heated and non-heated areas of the $\text{Fe}_{0.90}\text{Ni}_{0.1}$ sample, photo-image of which is given under (b). (c) Molar volumes of *hcp*-, *fcc*- and *bcc*-structured $\text{Fe}_{0.9}\text{Ni}_{0.1}$ phases.

5.8.4a.ii $\text{Fe}_{0.78}\text{Ni}_{0.22}$ at pressures to 52 GPa and temperatures to 2600 K

Another *in situ* X-ray diffraction experiment was carried out with $\text{Fe}_{0.78}\text{Ni}_{0.22}$ alloy at pressures to 44 (1) GPa and temperatures to 2600 (50) K (GSECARS, Sector 13, APS). $\text{Fe}_{0.78}\text{Ni}_{0.22}$ sample was compressed to 22 (1) GPa, then five series of laser-heating, quenching and compression were performed (Fig. 5.8-2). First, second and third series of the high temperature XRD data were collected during gradual decrease of temperature from 1800-2000 K to 1500-1450 K, while fourth and fifth series of data were collected upon gradual increase of temperature. The sequence of measurements is shown in Fig. 5.8-2 by arrows.

5. Results: phase relations in Fe-Ni-C system

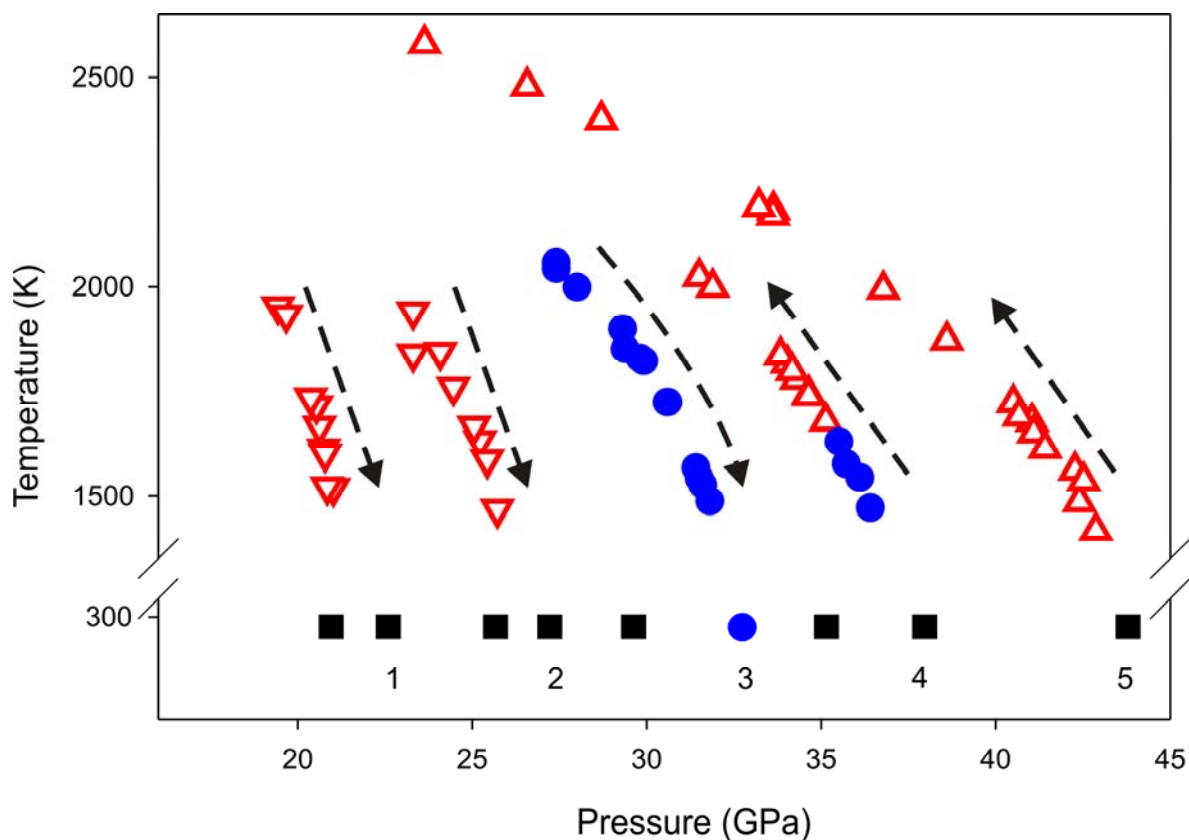


Figure 5.8-2 Diagram presenting pressure-temperature conditions, achieved in five series of compression, laser heating and quenching of $\text{Fe}_{0.78}\text{Ni}_{0.22}$ alloy, at which point in the diagram an XRD pattern was collected. Arrows show the sequence of the measurements. Blue closed circles correspond to the spectra with two coexisting *fcc*-structured phases.

Below 30 GPa all XRD spectra collected (first and second laser-heating series) suggest presence of the single *fcc*-structured Fe-Ni phase along with LiF, used as the pressure-transmitting medium (Fig. 5.8-3, bottom). During third laser heating of the $\text{Fe}_{0.78}\text{Ni}_{0.22}$ we detected appearance of another *fcc*-structured phase at $\sim 29.0(5)$ GPa and 2000 (20) K (Fig. 5.8-3, in the middle). The difference in molar volume between two *fcc*-phases is $1.16(1) \text{ cm}^3 \text{ mol}^{-1}$ at $29.0(5)$ GPa and 2000(20) K. Entire XRD data set, collected during third laser heating (30 ± 2 GPa and temperatures from 2000 (20) K to 1450 (20) K), four XRD spectra, obtained in the beginning of the fourth laser heating (36 ± 1 GPa and temperatures from 1450 (20) K to 1700 (20) K) as well as room temperature data collected in between suggest presence of two *fcc*-phases (blue closed circles in Fig. 5.8-2). At temperatures higher 1700 K and pressures over 35 GPa

5. Results: phase relations in Fe-Ni-C system

(high temperature part of fourth and entire fifth laser-heating series) again the single *fcc*-phase was detected (see Fig. 5.8-2 and Fig 5.8-3, top spectrum).

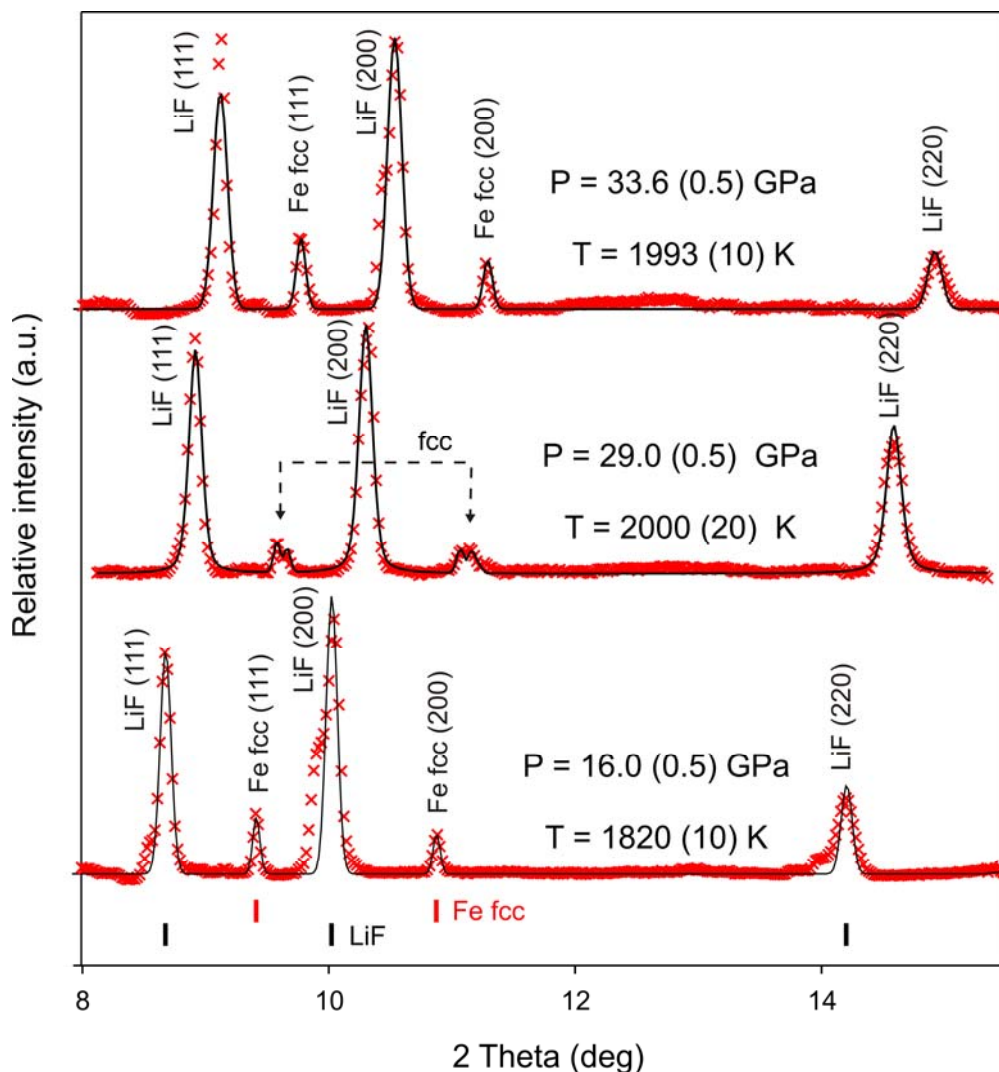


Figure 5.8-3 XRD patterns ($\lambda = 0.3344 \text{ \AA}$) collected upon *in situ* laser heating of the $\text{Fe}_{0.78}\text{Ni}_{0.22}$ sample. “Doubling” of “*fcc*” peaks is highlighted by arrows.

The first arising simple explanation for the observed doubling of “*fcc*” -peaks is inhomogeneous heating. For example the spectrum shown on the bottom in Fig. 5.8-3 with nice and narrow “*fcc*”-peaks indeed was collected from the area with high thermal gradient, which caused significant broadening of LiF -peaks. However in the case of spectrum with two *fcc*-phases (Fig. 5.8-3, in the middle) LiF -peaks are quite narrow, consequently the thermal gradient, if it exists, is negligibly small and obviously can not explain 0.03 \AA difference in lattice parameter between the two *fcc* -phases. Two other possible explanations are (i) iso-structural

5. Results: phase relations in Fe-Ni-C system

phase transition, occurring at high pressures and temperatures or (ii) chemical reaction during laser heating.

5.8.4b Comparative study of $Fe_{1-x}Ni_x$ ($0.10 < x < 0.22$) at high pressures and temperatures by means of LH-DAC and LVP techniques

$Fe_{1-x}Ni_x$ ($0.10 < x < 0.22$) alloy samples were subjected to the same P-T conditions in multianvil experiments like in LH-DAC experiments described above. The recovered products then were analysed by XRD, Mössbauer spectroscopy and SEM. For comparison the results of one of the paired LH-DAC and multianvil runs is shown in Fig. 5.8-4. In these two experiments $Fe_{0.90}Ni_{0.10}$ sample was heated to 2000 K at 20 GPa, the duration of heating in both cases was about 5 min.

XRD spectrum collected from the $Fe_{0.90}Ni_{0.1}$ recovered after laser-heating in DAC (Fig. 5.8-4c) shows weak reflections of *fcc* phase along with the reflections from the *bcc*-Fe,Ni phase, LiF (used as a pressure-transmitting medium and thermal isolation) and rhenium gasket. Mössbauer spectrum collected from this sample also suggests presence of two iron-bearing phases (see Fig. 5.8-4a, on the top): (i) the magnetic component (light gray sextet) with the hyperfine parameters typical for *bcc*-FeNi (central shift, CS, about 0.040 mm s^{-1} relative to α -iron and hyperfine magnetic field, B, is 34.18 T) and (ii) non-magnetic or anti-ferromagnetic component (blue singlet with CS = -0.07 (0.01) mm s^{-1}), which was assigned to the *fcc*-Fe,Ni phase, known to be antiferromagnetic ([Strixrude et al., 1994](#); [Cohen and Mukherjee, 2004](#); [Shallcross et al., 2006](#)). The observed value of the magnetic field of *bcc*-FeNi alloy (34.2(2)) T is higher than that for pure α -iron (~ 33 T). The same effect on the internal magnetic field of iron has the alloying of Co ([Greenwood and Gibb, 1977](#)), which was ascribed to the increased local exchange potential and the spin density.

The $Fe_{0.90}Ni_{0.10}$ sample recovered after multianvil run, performed at the same P-T conditions as the just discussed LH-DAC experiment, appeared to be single *bcc*-structured Fe,Ni phase with a trace amount of (Fe,Ni)O, as revealed by SEM (Fig. 5.8-4b,d on the bottom).

Thus, summarizing the results, in LH-DAC experiments with $Fe_{1-x}Ni_x$ ($0.1 < x < 0.22$ wt%) alloys (covered P-T area is 15 - 45 GPa 1450 – 2500 K) we observed formation of the “additional” *fcc*-structured Fe-bearing phase (additional to the main Fe-Ni alloy phase stable at the corresponding P-T conditions), which is stable at room temperature and even at room

5. Results: phase relations in Fe-Ni-C system

pressure in some experiments (Fig. 5.8-4a). While quenched products of multianvil runs, performed with the same samples at the same P-T conditions (covered P-T region is 15 – 20 GPa and 1700 – 2200 K), revealed the presence of the single initial *bcc*-structured Fe,Ni phase (Fig. 5.8-4b).

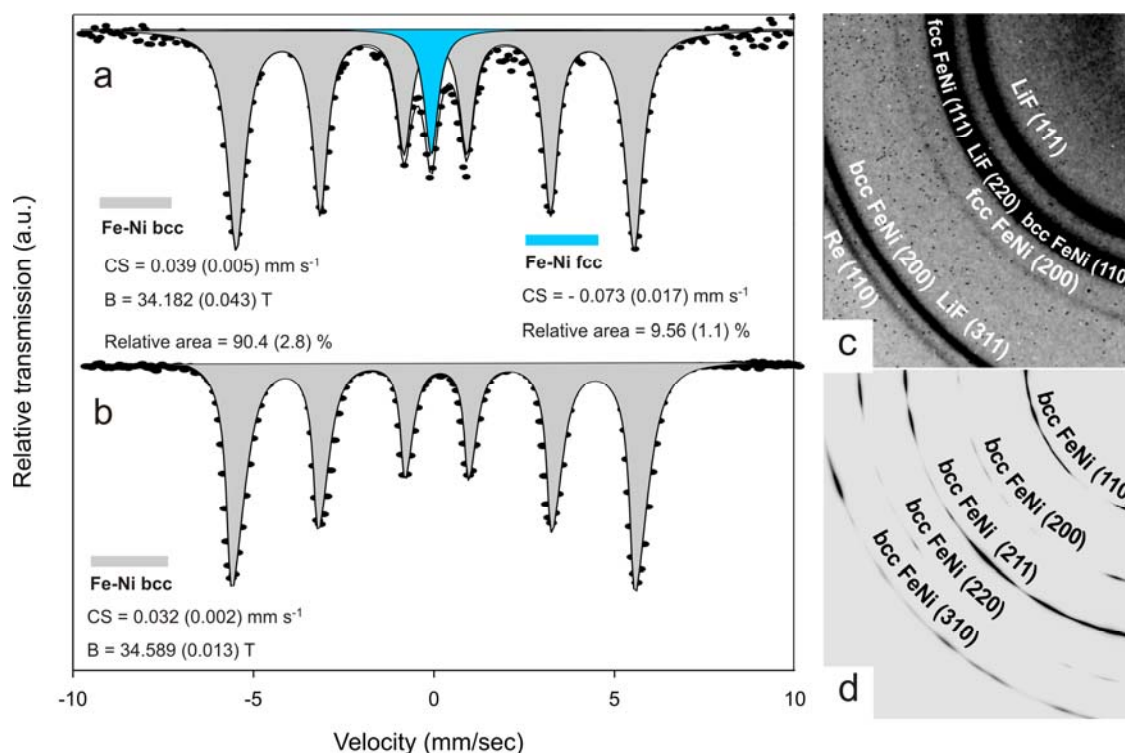


Figure 5.8-4 Mossbauer and XRD spectra collected from Fe_{0.90}Ni_{0.10} alloy recovered after heating to 2000 (50) K at 20 (1) GPa in LH-DAC (a,c) and in the multianvil (b,d).

5.8.5. Discussion

5.8.5a Fe_{1-x}Ni_x (0.1 < x < 0.22 wt%) alloys at pressures to 45 GPa and temperatures to 2500 K:

LH-DAC vs. multianvil experiments

The only plausible explanation for the observed discrepancy between results obtained with two different high-pressure techniques (Fig. 5.8-4) is the presence of contaminating material in LH-DAC experiments which reacts with the sample and leads to its decomposition. Careful preparation of a DAC experiment allows to eliminate any possible contamination excluding one, which cannot be removed by the definition – it is carbon in the form of diamond. Indeed as was previously reported by [Prakapenka et al. \(2003-2004\)](#) and [Rouquette et al. \(2008\)](#) carbon from diamond anvils can react with a sample material during laser-heating.

5. Results: phase relations in Fe-Ni-C system

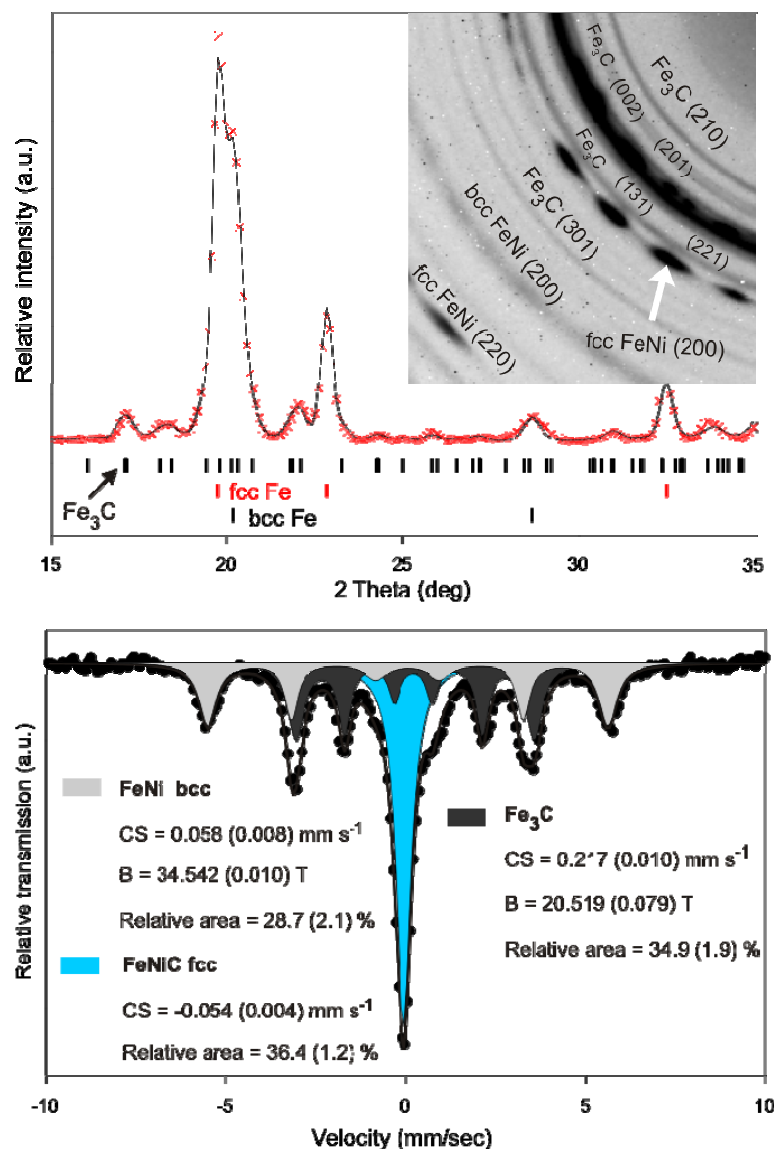


Figure 5.8-5 XRD (on the top) and Mossbauer spectra (on the bottom) collected from $\text{Fe}_{0.90}\text{Ni}_{0.10}$ alloy recovered after heating to 2000 (100) K at 20 (1) GPa in multianvil in the presence of 1wt. % diamond powder.

In order to check this hypothesis we simulated conditions of a DAC experiment in multianvil press, adding diamond powder (40-60 μm) into the pressure chamber. Dissolution of 1 wt. % diamond powder (relative to the weight of the sample) in $\text{Fe}_{0.9}\text{Ni}_{0.1}$ alloy at 20 (1) GPa and 2000 (100) K leads to the formation of carbon bearing *fcc*- structured Fe,Ni phases (blue singlet and light gray sextet respectively), *bcc*-structured Fe,Ni phase (which could also contain some trace amount of carbon) as well as to the precipitation of Fe_3C carbide (dark gray sextet) (Fig. 5.8-5).

5. Results: phase relations in Fe-Ni-C system

Comparing the result of the “DAC simulating” multianvil runs (Fig. 5.8-5) with that obtained in LH-DAC quenched experiments (Fig. 5.8-4a,c) we conclude that the discrepancy between the results of the LH-DAC and multianvil quenched experiments (Fig. 5.8-4) as well as the coexistence of *hcp*- and *fcc* –FeNi phases and “doubling” of “*fcc*”-peaks observed, in *in situ* XRD experiments with LH-DAC (Fig. 5.8-1 and Fig. 5.8-3), is related to contamination of Fe-Ni alloy by carbon. Namely, upon laser heating to the significantly high temperatures (2000-2500 K) carbon from diamond anvils diffused through the thermal isolation layers of LiF (or NaCl) and eventually was incorporated by the fraction of the *fcc*-FeNi, which necessarily changed the *fcc*-phase lattice parameter and shifted the *fcc*-*bcc* phase boundary towards lower temperatures.

5.8.5b Effect of carbon on the phase relations in Fe-Ni system at elevated pressures and temperatures. Martensitic transformation

According to the equilibrium Fe-C phase diagram at ambient pressure carbon solubility in *fcc*-structured phase of iron can be as high as 2.06 wt% at ~ 1400 K. The *bcc*-iron can incorporate only about 0.0022 wt% carbon at ~ 1000 K. Since atomic radius of carbon is almost two times smaller than that of iron in both *bcc* and *fcc* –structured iron phases carbon atoms occupy tetrahedral or octahedral interstices (Fig. 5.8-6).

Pressure effect on the carbon solubility in Fe and Fe-Ni alloys is poorly constrained. Theory predicts decrease of carbon solubility upon compression ([Wood, 1993](#); [Huang et al., 2005](#); [Lord et al., 2009](#)). However this conclusion has been challenged by Fei et al ([2007](#)), where the increase of carbon solubility in iron with the increase of pressure was suggested.

5. Results: phase relations in Fe-Ni-C system

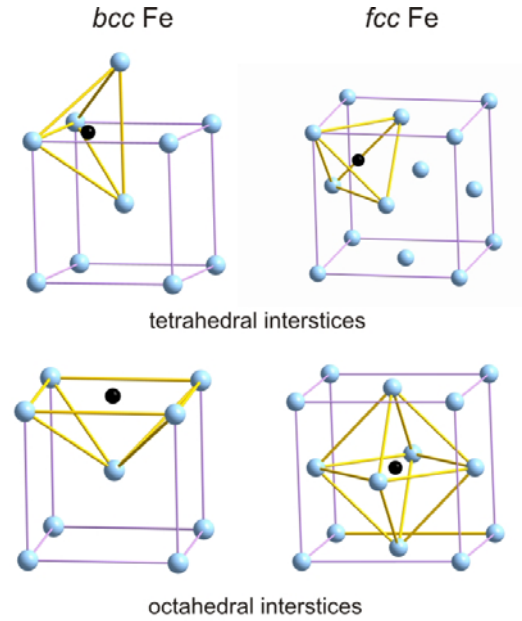


Figure 5.8-6 Location of carbon (black spheres) in octahedral and tetrahedral interstices of *bcc*- and *fcc*-Fe.

Due to the significantly higher ability of *fcc*-Fe to incorporate carbon in compare with *bcc*-Fe phases transformation of carbon bearing *fcc*-structured phase to the *bcc*-phase leads to the precipitation of the excess carbon in the form of Fe_3C . However in the case of LH-DAC and LVP experiments described in the present work the rapid cooling of the *fcc*-structured $\text{Fe}_{1-x}\text{Ni}_x$ alloys containing a certain amount of carbon results in the non-equilibrium diffusionless martensitic transformation, discovered by German metallurgist and engineer Adolf Martens ([Martens, 1878a,b,c; 1880](#)). This transformation is well known in metallurgy and widely used to increase the hardness of steels. Martensite is a metastable supersaturated carbon solid solution in iron with a body-centered tetragonal (*bct*) structure, slightly distorted form of *bcc* iron; the degree of distortion is linked to the carbon concentration ([Kurdjumov and Kaminsky, 1928, 1929; Kurdjumov, 1960; Mazur, 1950; Roberts, 1953; Xiao et al., 1995b](#)) and can be described by the following formula:

$$a = a_0 - \beta \cdot \rho_C, \quad c = c_0 + \alpha \cdot \rho_C, \quad c/a = 1 + \gamma \cdot \rho_C, \quad (5.8-1)$$

where a_0 and c_0 are the lattice parameters of *bcc*-Fe, a and c are the lattice parameters of Fe-C martensite, ρ_C is carbon content in wt%, $\alpha = 0.116$ (0.002), $\beta = 0.013$ (0.002) and $\gamma = 0.046$ (0.001). Martensitic transformation occurs over a certain temperature interval, defined by a

5. Results: phase relations in Fe-Ni-C system

martensitic start temperature, M_s , and a martensitic final temperature, M_f , at which the entire *fcc* - phase should have transformed into martensite. Both M_s and M_f temperatures of Fe-Ni-C system are significantly decreased by the alloying of Ni or/and C even at low concentrations ([Stevens and Haynes, 1956](#); [Gulyaev, 1977](#); [Troiano and Greninger, 1946](#); [Shackelford, 2001](#)). Therefore a certain amount of the *fcc*-structured phase can remain untransformed at room temperature. The effect of alloying on the M_f temperature can be estimated based on the empirical relation, developed by Stevens and Haynes ([1956](#)) and Gulyaev ([1977](#)) for low-carbon steels:

$$M_f \text{ (K)} = 639 - 17 \cdot \rho_{\text{Ni}} - 474 \cdot \rho_{\text{C}}, \quad (5.8-2)$$

where ρ_{Ni} and ρ_{C} are the percentage weight concentrations of Ni and C respectively. Other investigators suggest that the effect of Ni and C alloying is even higher ([Shackelford, 2001](#)). Thus for Fe-Ni alloys, used in this work, the values of M_f temperature were decreased at least to 496 (15) K, 384 (15) K and 321 (15) K at 10, 15 and 22 wt% of Ni concentration respectively. Addition of 0.2-0.3 wt% C would lower these values of M_f below the room temperature. This explains the presence of the *fcc* -structured Fe₃Ni phase at room temperature in the case of both the LH-DAC experiments (Fig. 5.8-1 and Fig. 5.8-4a,c) and the “DAC-simulating” LVP runs (Fig. 5.8-5). The reason why in the LH-DAC experiments, contrarily to the “DAC simulating” LVP runs, we did not detect the precipitation of Fe₃C carbide most probably is related to the significantly smaller amount of carbon dissolved in the former case.

5.8.5c Carbon solubility in Fe-Ni system at elevated pressures and temperatures

To define the maximum amount of carbon, which can dissolve in Fe-Ni alloy at elevated pressures and temperatures without Fe₃C formation we carried out another series of LVP quenched experiments (piston-cylinder and multianvil press) with Fe_{0.90}Ni_(0.10-x)C_x (0.01 < x < 0.05 at%, corresponding to approximately 0.02 < x < 0.11 wt.%) powder mixtures at 0.5 – 20 GPa and 2050-2300 K. Quenched products of LVP runs were analysed by the XRD and Mössbauer spectroscopies, as well as by SEM and TEM.

All LVP runs performed at pressures from 0.5 to 20 GPa and temperatures from 2050 (10) K to 2300 (20) K with Fe₉₀Ni_(10-x)C_x, containing up to 3 at% C as well as runs with 4 at% C at

5. Results: phase relations in Fe-Ni-C system

pressures to 9 GPa revealed formation of *bcc* – structured Fe-Ni-C phase with a certain amount of retained *fcc*-structured Fe-Ni-C alloy. No evidence of Fe₃C carbide precipitation was detected.

According to the formulas 5.8-1 at the maximum achieved carbon content, 4 at % (or ~0.9 wt%), the deviation from the *bcc* crystal lattice due to the carbon interstices is only about 4%, therefore the XRD spectra were fitted with the model consisting of *bcc*- (not *bct*) and *fcc*-iron. Previous studies of Fe-C martensite obtained by the rapid quenching (Génin and Flinn, 1966; [Gielin and Kaplow, 1967](#); [Ino et al., 1982](#); [Génin, 1987](#); [Dabrowski et al., 1994](#)) suggest that its Mössbauer spectrum consists of as many as three types of components: (i) high intensity ferromagnetic sextet attributed to iron atoms far away from carbon atom; (ii) low intensity weak sextet(s) ascribed to the iron atoms in the neighborhood of carbon atom(s); and (iii) central peak(s) associated with an antiferromagnetic retained *fcc* -phase. The number of the type-(ii) sextets varies depending upon the sample purity, processing conditions, test temperature, etc. Génin ([1987](#)), using a curve fitting approach, suggested that up to six type-(ii) sextets might be distinguished in the spectrum of the martensite quenched to room temperature. In the present work, however, we obtained a good fit of Mössbauer data using model, which contains one sextet (CS = 0.03 (0.01) mm s⁻¹, B = 34.2 (0.3) T) to fit the *bcc* –structured Fe-bearing component (colored in light gray in the Fig. 5.8-7) and one singlet (CS = -0.07 (0.01) mm s⁻¹) to fit the antiferromagnetic *fcc* –structured Fe-bearing component (colored in blue in Fig. 5.8-7a).

While at pressures to 9 GPa Fe-Ni alloy can still incorporate 4 at% C, at 20 GPa presence of this amount of carbon leads to the formation of Fe₃C carbide (dark grey sextet in Fig. 5.8-7b). This agreed with the previously reported compression induced decrease of carbon solubility in iron ([Wood, 1993](#); [Huang et al., 2005](#); [Lord et al., 2009](#)). All LVP runs performed with 5 at% carbon (1 - 20 GPa) also reveals formation of Fe₃C carbide.

Note that in all LVP runs performed in the MgO capsule formation of a trace amount of (Fe,Ni)O was also detected. In order to check whether or not the presence of oxygen affects the phase relations in the Fe-Ni-C system, we repeated some of the LVP runs using NaCl as an internal capsule, and obtained the same results as in the case of MgO capsule.

5. Results: phase relations in Fe-Ni-C system

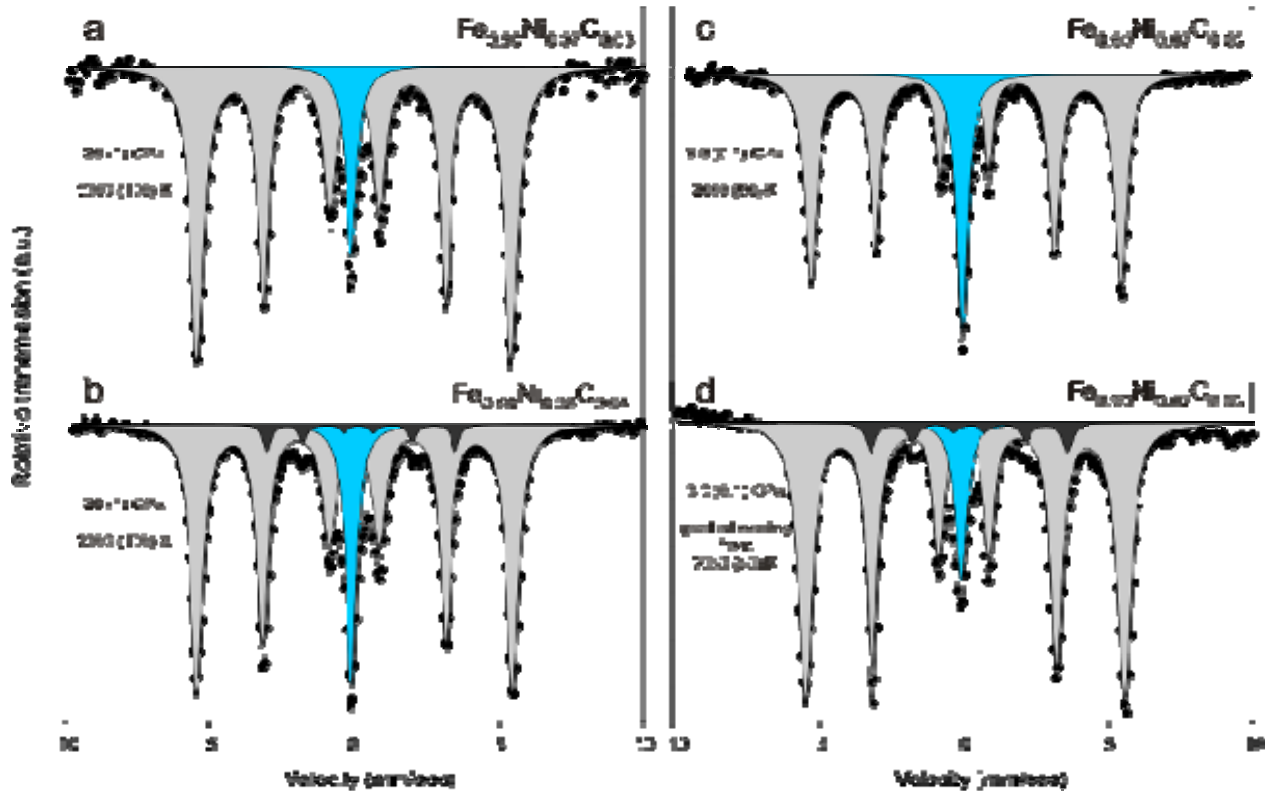


Figure 5.8-7 Mössbauer spectra collected from (a) $\text{Fe}_{0.90}\text{Ni}_{0.07}\text{C}_{0.03}$ and (b) $\text{Fe}_{0.90}\text{Ni}_{0.06}\text{C}_{0.04}$ quenched from 2300 (100) K at 20 GPa (1); $\text{Fe}_{0.90}\text{Ni}_{0.07}\text{C}_{0.03}$ quenched from 2050 (50) K and 3.0 (0.1) GPa (c) and gradually cooled from 2050 (50) K to 1000 (50) K at 3.0 (0.1) GPa (d). Components are colored as follows: light gray – *bcc*-structured FeNiC phase, light blue – *fcc*-structure FeNiC phase, and dark gray – Fe_3C carbide.

Indirect confirmation of the fact that the observed coexistence of *bcc*- and *fcc*-structured Fe-Ni-C alloy is the result of the martensitic (diffusionless) transformation induced by rapid cooling comes from the TEM analyses of the microstructure of the quenched products, which consists of the needle-shape grains of *bcc*-structured Fe-Ni-C phases with length of tens nanometers (Fig. 5.8-8a). Such fine structure of the low-carbon iron alloys is well known in metallurgy as the lath martensite, the morphology and crystallography of which has been extensively investigated by optical microscopy and transmission electron microscopy (TEM), the review can be found in Morito et al. (2006) and references therein.

5. Results: phase relations in Fe-Ni-C system

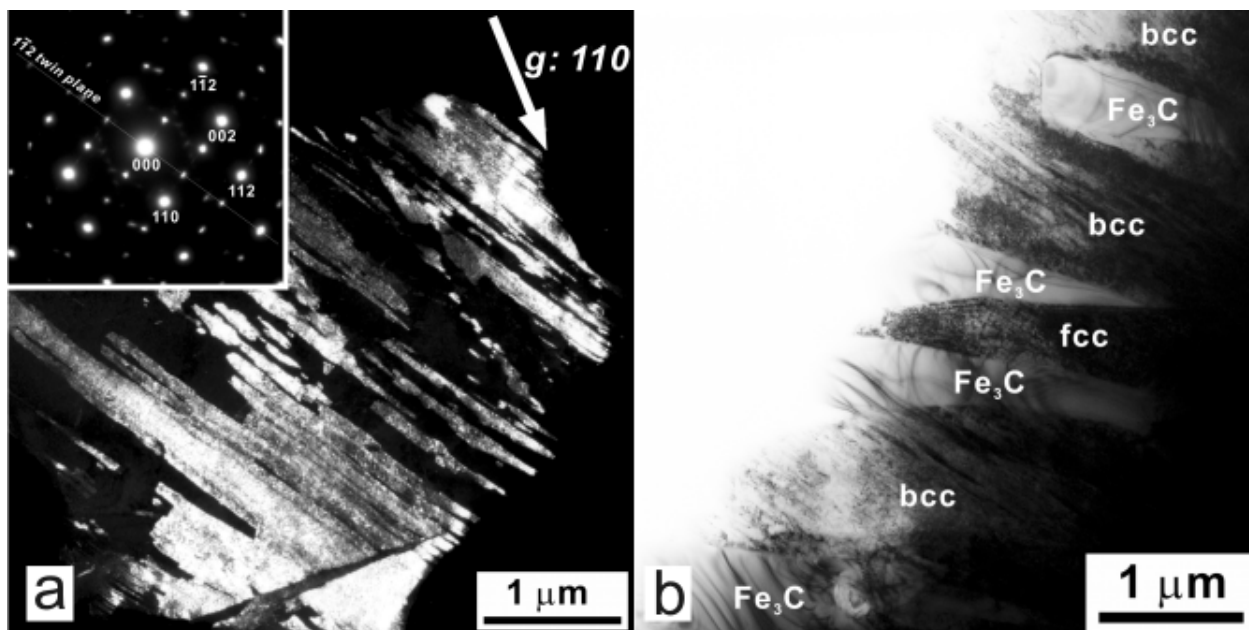


Figure. 5.8-8. Dark-field and bright-field TEM images obtained from (a) $\text{Fe}_{0.90}\text{Ni}_{0.08}\text{C}_{0.02}$ recovered after heating to 2100 (20) K at 9 (1) GPa and (b) $\text{Fe}_{0.90}\text{Ni}_{0.07}\text{C}_{0.03}$ gradually cooled to from 2050 (10) K to 1000 (10) K at 2.0 (0.1) GPa. The inset in (a) indicates a $\{112\}$ twin of the *bcc* phase.

In order to confirm that all above described results are the consequence of the non-equilibrium cooling of Fe-Ni-C system, which promotes martensitic transformation, in several LVP runs the FeNiC samples were gradually cooled to 1000 K with the speed $1.75 \text{ deg min}^{-1}$ and then immediately quenched to room temperature. XRD and Mössbauer spectroscopic analyses of the recovered Fe-Ni-C samples revealed the presence of Fe_3C carbide along with *bcc*- and *fcc*-structured Fe-Ni-C (Fig. 5.8-7d). TEM analyses of one of the quenched experiment, performed with $\text{Fe}_{0.90}\text{Ni}_{0.07}\text{C}_{0.03}$ stoichiometric mixture at 2.0(1) GPa (Fig. 5.8.8b), confirms presence of *bcc*- $\text{Fe}_{0.91}\text{Ni}_{0.09}$ and *fcc*- $\text{Fe}_{0.83}\text{Ni}_{0.17}$ alloys along with $(\text{Fe}_{0.97}\text{Ni}_{0.03})_3\text{C}$ carbide (the chemical compositions were estimated by means of energy-dispersive X-ray analyses).

5.8.6. Conclusion

We carried out the systematic comparative study of $\text{Fe}_{1-x}\text{Ni}_x$ ($0.1 < x < 0.22 \text{ wt\%}$) alloys at pressures to 45 GPa in temperature range 296 K – 2600 K, using LH-DAC and LVP techniques. We showed that laser heating in DAC even to relatively low temperatures, 1700 – 1800 K, can induce diffusion of carbon from the diamond anvils, which can eventually contaminate the sample. Therefore the experimental results obtained in LH-DAC experiments

5. Results: phase relations in Fe-Ni-C system

should be interpreted with great caution especially in the case of systems which readily react with carbon (like iron in the present case). Laser heating induced diffusion of carbon can be considered, as a plausible reason for systematic lowering of the melting curve of iron obtained in LH-DAC experiments in respect to theoretical predictions and shock-wave measurements.

Our LVP experiments with $\text{Fe}_{0.90}\text{Ni}_{(0.10-x)}\text{C}_x$ ($0.01 < x < 0.05$ at%, corresponding to approximately $0.02 < x < 0.11$ wt.%) at pressures 0.5 – 20.0(5) GPa and temperatures 2050 (10) – 2300 (20) K suggest that *fcc*-structured Fe-Ni alloy can incorporate as much as 0.9 wt% carbon at pressures to 9 GPa; and via diffusionless martensitic transformation this alloy can be quenched to ambient conditions without formation of Fe_3C carbide. Our results also confirm previously suggested decrease of carbon solubility in Fe-Ni alloy with increase of pressure ([Wood, 1993](#); [Huang et al., 2005](#); [Lord et al., 2009](#)).

5.8.7. Acknowledgments

We acknowledge the European Synchrotron Radiation Facility for provision of synchrotron radiation facilities (ID27) and we would like to thank V. Dmitriev for the X-ray diffraction measurements performed at the SNBL beamline. Use of the Advanced Photon Source (beamline 13-ID-D) was supported by the U.S. Department of Energy, Office of Science, Office of Basic Energy Sciences, under Contract No. DE-AC02-06CH11357. We are grateful to Hubert Schulze and Uwe Dittmann for the sample preparation (Bayerisches Geoinstitut). The project was financially partly supported by funds from the German Science Foundation (DFG) Priority Programme SPP1236 under project Mc 3/16-1, and Eurocores EuroMinSci Programme.

References:

- Adams F., Van Vaeck L., and Barret R. (2005) Advanced analytical techniques: platform for nano materials science. *Spectrochim. Acta* **B60**, 13–26
- Agnor C.B., Canup R.M., and Levison H.F. (1999) On the character and consequences of large impacts in the late stage of terrestrial planets formation. *Icarus* **142**, 219-237
- Akimoto S. (1987) High-pressure research in geophysics: past, present, and future, pp. 1-13. In *High-pressure Research in Mineral Physics* (eds. Manghnani M.H. and Syono Y.) Terra Scientific Publishing Company, Tokyo
- Alfè D. (2009) Temperature of the inner-core boundary of the Earth: Melting of iron at high pressure from first-principles coexistence simulations. *Phys. Rev. B (Rapid)* **79**, 060101(R)
- Allègre C.J., Poirier J.-P., Humler E., and Hofmann A.W. (1995b) the chemical composition of the Earth. *Earth Planet. Sci. Lett.* **134**, 515-526
- Anderson D.L. (1989) *Theory of the Earth*. Blackwell Scientific Publications Oxford, pp. 11-15
- Anderson O.L. and Isaak D.G. (2002) Another look at the core density deficit of the Earth's outer core. *Phys. Earth Planet. Inter.* **131**, 19-27
- Anderson W.W. and Ahrens T.J. (1994) An equation of state for liquid iron and implications for the Earth's core. *J. Geophys. Res.* **99**, 4273-4284
- Andrault D. (2001) Evaluation of (Mg,Fe) partitioning between silicate perovskite and magnesiowustite up to 120 GPa and 2300K. *J. Geophys. Res.* **106** (2001), 2079–2087
- Andréani M., Grauby O., Baronnet A., and Muñoz M. (2008) Occurrence, composition and growth of polyhedral serpentine. *Eur. J. Mineral.* **20**, 159–171
- Angel R.J., Finger L.W., Hazen R.M., Kanzaki M., Weidner D.J., Liebermann R.C., and Veblen D.R. (1989) Structure and twinning of single-crystal MgSiO₃ garnet synthesized at 17 GPa and 1800C. *Am. Mineral.* **74**, 509-512
- Aquilanti G. and Pascarelli S. (2005) EXAFS study of the local structure of InAs up to 80 GPa. *J. Phys. Cond. Matter* **17** 1811–1824
- Aquilanti G., Libotte H., Crichton W. A., Pascarelli S., Trapananti A. and Itié J.-P. (2007a) High-pressure phase of GaP: Structure and chemical ordering. *Phys. Rev. B* **76**, 064103-7
- Aquilanti G., Trapananti A., Minicucci M., Liscio F., Twaróg A., Principi E., and Pascarelli S. (2007b) Electronic topological transition in zinc under pressure: An x-ray absorption spectroscopy study. *Phys. Rev. B* **76**, 144102-6

- Aquilanti G., Pascarelli S., Muñoz M., Narygina O., and Dubrovinsky L. (2009) Development of μ -XANES mapping in the diamond anvil cell. *J. Synch. Rad.* **16**, 376–379
- Aragón R., Buttrey D.J., Shepherd J.P., and Honig J.M. (1985) Influence of nonstoichiometry on the Verwey transition. *Phys. Rev. B* **31**, 430-436
- Auzende A.-L., Badro J., Ryerson F.J., Weber P.K., Fallon S.J., Addad A., Siebert J., Fiquet G. (2008) Element partitioning between magnesium silicate perovskite and ferropericlase: New insights into bulk lower-mantle geochemistry. *Earth Planet. Sci. Lett.* **269**, 164-174
- Badding J.V., Mao H.-K., and Hemley R.J. (1991) High-pressure chemistry of hydrogen in metals: in-situ study of iron-hydride. *Science* **253**, 421-424
- Badro J., Fiquet G., Guyot F., Rueff J.-P., Struzhkin V.V., Vankó G., and Monaco G. (2003) Partitioning in Earth's mantle: toward a deep lower mantle discontinuity. *Science* **300**, 789–791
- Badro J., Rueff J.-P., Vankó G., Monaco G., Fiquet G., and Guyot F. (2004) Electronic transitions in perovskite: Possible non-convecting layers in the lower mantle. *Science* **305**, 383-386
- Badro J., Fiquet G., and Guyot F. (2005) Thermochemical state of the lower mantle: new insights from mineral physics, pp. 241-260. In *Earth's Deep Mantle: Structure, Composition, and Evolution* (eds. van der Hilst R.D., Bass J., Matas J., and Trampert J.) American Geophysical Union, Washington
- Bancroft G.M., Maddock A.G., and Burns R.G. (1967) Applications of the Mössbauer effect to silicate mineralogy — I. Iron silicates of known crystal structure. *Geochim. et Cosmoch. Acta* **31**, 2219-46
- Belonoshko A.B., Ahuja R., and Johansson B. (2003) Stability of the body-centred-cubic phase of iron in the Earth's inner core. *Nature* **424**, 1032-1034
- Belonoshko A.B., Skorodumova N.V., Rosengren A., and Johansson B. (2008) Elastic Anisotropy of Earth's Inner Core. *Science* **319**, 797-800
- Bengtson A., Persson K., and Morgan D (2008) Ab initio study of the composition dependence of the pressure induced spin crossover in perovskite ($\text{Mg}_{1-x}\text{Fe}_x$) SiO_3 . *Earth Planet. Sci. Lett.* **265**, 535–545
- Bergmann M.I. (1997) Measurements of elastic anisotropy due to solidification texturing and implication to the Earth's inner core. *Nature* **489**, 60-63

- Berry A.J., O'Neill H.St.C., Jayasuriya K.D., Campbell S.J., and Foran G.J. (2003) XANES calibrations for the oxidation state of iron in a silicate glass. *Am. Mineral.* **88**, 967-977
- Bianconi A. (1988) XANES spectroscopy, p.573. In *X-Ray Absorption: Principles, Applications, Techniques of EXAFS, SEXAFS, and XANES* (ed. Prins D. C. K. a. R.) Vol. 92, Wiley, New York
- Billen M. I. (2008) Modeling the dynamics of subducting slabs. *Annu. Rev. Earth Planet. Sci.* **36**, 325–356
- Bina C.R. (2003) Seismological constraints upon mantle composition. pp. 39-59. In *The Mantle and Core* (ed. R.W. Carlson) Vol. 2 Treatise on Geochemistry (eds. Holland H.D. and Turekian K.K.), Elsevier-Pergamon, Oxford
- Bina C.R. and Helffrich G. (1994) Phase transition: Clapeyron slope and transition zone seismic discontinuity topography. *J. Geophys. Res.* **99**, 15853-15860
- Birch F. (1952) Elasticity and constitution of the Earth's interior. *J. Geophys. Res.* **57(2)**, 227–286
- Blaha P., Schwarz K., Madsen G.K.H., Kvasnicka D., and Luitz J. (2001) WIEN2k, An Augmented Plane Wave Plus Local Orbitals Program for Calculating Crystal Properties, Vienna University of Technology, Austria, 2001
- Boehler R. (1986) The phase diagram of iron to 430 kbar. *Geophys. Res. Lett.* **13**, 1153-1156
- Boehler R. (1993) Temperatures in the Earth's core from melting-point measurements of iron at high static pressures *Nature* **363**, 534–536
- Bower D. J., Gurnis M., Jackson J.M., Sturhahn W. (2009) Enhanced convection and fast plumes in the lower mantle induced by the spin transition in ferropericlase. *Geophys. Res. Lett.* **36**, L10306.1-4
- Boyd F.R. and England J.L. (1960) Apparatus for phase-equilibrium measurements at pressures up to 50 kilobars and temperatures up to 1750°C. *Journal Geoph. Res.* **65(2)**, 741-748
- Brand R.A. (1990) NORMOS programs, version 1990. The NORMOS program is available from Wissel GmbH, D-82319 Starnberg, Germany
- Brown J.M. and Shankland T.J. (1981) Thermodynamic parameters in the Earth as determined from seismic profiles. *Geophys. J. R. Astron. Soc.* **66**, 579–596
- Brown J.M. and McQueen R.G. (1986) Phase transitions, grüneisen parameter, and elasticity for shocked iron between 77 GPa and 400 GPa. *J. Geophys. Res.* **91**, 7485-7494

- Brown Jr. G.E., Calas G., Waychunas G.A., and Petiau, J. (1988) X-ray absorption spectroscopy and its applications in mineralogy and geochemistry, p. 431 In *Spectroscopic Methods in Mineralogy and Geology* (ed. Hawthorne F. C.) Vol. 18. Mineralogical Society of America, Chelsea, MI
- Brown J.M. (2000) The NaCl pressure standard. *J. Appl. Phys.* **86**, 5801-5808
- Burns R.G. (1970) Crystal-field spectra and evidence of cation ordering in olivine minerals. *Am. Mineral.* **55**, 1608-1632
- Burns R.G. (1993) Mineralogical applications of crystal field theory. 2nd edition. Cambridge University Press
- Carrez P., Ferré D., and Cordier P. (2007) Implications for plastic flow in the deep mantle from modeling dislocations in MgSiO₃ minerals. *Nature* **446**, 68–70
- Chambers J.E. (2003) Planet formation, pp. 461-475. In *Meteorites, Comets and Planets* (ed. Davis A.M.) Vol. 1 Treatise on Geochemistry (eds. Holland H.D. and Turekian K.K.), Elsevier-Pergamon, Oxford
- Chudinovskikh L. and Boehler R. (2001) MgSiO₃ phase boundaries measured in the laser-heated diamond cell. *Nature* **411**, 574–577
- Claussen W.F. (1960) Detection of the α - γ iron phase transformation by differential thermal analyses. *Rev. Sci. Instr.* **31**, 878-881
- Cohen R.E. and Mukherjee S. (2004) Non-collinear magnetism in iron at high pressures. *Phys. Earth Planet. Int.* **143–144**, 445–453
- Condie K.C. (2005) Earth as an evolving planetary system. Elsevier Academic Press, London
- Dabrowski L., Suwalski J., Sidzhimov B., and Christov V. (1994) Investigations of ordering dynamics in carbon martensite. *Acta Metall. Mater.* **42(7)**, 2375-2380
- Dewaele A., Loubeyre P., Occelli F., Mezouar M, Dorogokupets P.I., and Torrent M. (2006) Quasihydrostatic Equation of State of Iron above 2 Mbar. *Phys. Rev. Lett.* **97**, 215504
- Duba A., Peyronneau J., Visocekas F., and Poirier J.-P. (1997) Electrical conductivity of magnesiowüstite/perovskite produced by laser heating of synthetic olivine in the diamond anvil cell. *J. Geophys. Res.* **102(B12)**, 27,723–27,728
- Dubrovinskaia N. and Dubrovinsky L. (2003) Whole-cell heater for the diamond anvil cell. *Rev. Sci. Instrum.* **74**, 3433-3437

- Dubrovinsky L.S., Saxena S.K., and Lazor P. (1998) High-pressure and high-temperature X-ray diffraction study of iron and corundum to 68 GPa using an internally heated diamond anvil cell. *Phys. Chem Mineral.* **25**, 434-441
- Dubrovinsky L.S., Saxena S.K., Tutti F., and Rekhı S. (2000) In situ X-ray study of thermal expansion of iron at multimegabar pressure. *Phys. Rev. Lett.* **84**, 1720-1723
- Dubrovinsky L.S., Dubrovinskaia N.A., Abrikosov I.A., Vennström M., Westman F., Carlson S., Van Schilfgaarde M., and Johansson B. (2001) Pressure induced Invar effect in Fe-Ni alloys. *Phys. Rev. Lett.* **86**, 4851-4854
- Dubrovinsky L., Dubrovinskaia N., Narygina O., Kantor I., Kuznetsov A., Prakapenka V.B., Vitos L., Johansson B, Mikhaylushkin A.S., Simak S.I., Abrikosov I.A. (2007) Body-centered Cubic Iron-Nickel Alloy in Earth's Core. *Science* **316**, 1880-1883
- Dziewonski A.M and Anderson D.L (1981) Preliminary Reference Earth Model. *Phys. Earth Planet. Int.* **25**, 297 – 356
- Fei Y. and Mao H.-K. (1994) In situ determination of the Ni-As phase of FeO at high pressure and temperature. *Science* **266**, 1678-1680
- Fei Y., Virgo D., Mysen B. O., Wang Y., and Mao H.-K. (1994) Temperature dependent electron delocalization in (Mg,Fe)SiO₃ perovskite. *Am. Mineral.* **79**, 826–837
- Fei Y., Prewitt C.T., Mao H.K., and Bertka C.M. (1995) Structure and density of FeS at high pressure and high temperature and internal structure of Mars. *Science* **268**, 1892-1894
- Fei Y., Bertka C.M., and Prewitt C.T. (2000) Structure type and bulk modulus of Fe₃S, a new iron-sulfur compound. *Am. Mineral.* **85**, 1830-1833
- Fei Y., Wang Y., and Deng L. (2007) Melting relations in the Fe–C–S system at high pressures: implications for the chemistry of the cores of the terrestrial planets. *Lunar and Planetary Science Conference (2007) XXXVIII abstract 1231*
- Fialin M., Catillon G., and Andrault D. (2009) Disproportionation of Fe²⁺ in Al-free silicate perovskite in the laser heated diamond anvil cell as recorded by electron probe microanalysis of oxygen. *Phys. Chem Min.* **36**, 183-191
- Fiquet G., Dewaele A., Andrault D., Kunz M., and Le Bihan T. (2000) Thermoelastic properties and crystal structure of MgSiO₃ perovskite at lower mantle pressure and temperature conditions. *Geophys. Res. Lett.* **27**, 21–24

- Frost D.J., Langenhorst F., and van Aken P.A. (2001) Fe-Mg partitioning between ringwoodite and magnesiowüstite and the effect of pressure, temperature and oxygen fugacity. *Phys. Chem. Miner.* **28**, 455-470
- Frost D.J. and Langenhorst F. (2002) The effect of Al₂O₃ on Fe–Mg partitioning between magnesiowüstite and magnesium silicate perovskite. *Earth Planet. Sci. Lett.* **199**, 227–241
- Frost D.J., Liebske C., Langenhorst F., McCammon C.A., Trønnes G.R., and Rubie D.C. (2004a) Experimental evidence for the existence of iron-rich metal in the Earth's lower mantle. *Nature* **428**, 409-412
- Frost D.J., Poe B.T., Trønnes R.G., Liebske C, Duba A., and Rubie D.C. (2004b) A new large-volume multianvil system. *Phys. Earth Planet. Int.* **144**, 507-514
- Frost, D.J. (2008) The Upper Mantle and Transition Zone. *Elem. Mag.* **4**, 171-176
- Funamori N., Yagi T., and Uchida T. (1996) High-pressure and high-temperature in-situ X-ray diffraction study of iron to above 68 GPa using MA8-type apparatus. *Geophys. Res. Lett.* **23**, 953-956
- Fyfe, W.S. (1960) The possibility of d-electron coupling in olivine at high pressures. *Geochim. Cosmochim. Acta* **19**, 141–143
- Gaffney E.S. and Anderson D.L. (1973) Effect of low-spin Fe²⁺ on the composition of the lower mantle. *J. Geophys. Res.* **78**, 7005-14
- Gavrilenko P. (2008) Water solubility in diopside. Ph.D. Thesis. Bavarian Geoinstitut, University of Bayreuth
- Génin J.-M. and Flinn P.A. (1966) Mössbauer effect evidence for the clustering of carbon atoms in iron-carbon martensite during aging at room temperature. *Phys. Lett.* **22**, 392-393
- Génin J.-M. (1987) The clustering and coarsening of carbon multiplets during the aging of martensite from mössbauer spectroscopy: The preprecipitation stage of epsilon carbide. *Metallur. Mater. Trans. A* **18(8)**, 1371-1388
- Gielen P.M. and Kaplow R (1967) Mossbauer effect in iron-carbon and iron-nitrogen alloys. *Acta Metall.* **15**, 49-63
- Goldreich P. and Ward W.R. (1973) The formation of planetesimals. *Astrophys. J.* **183**, 1051-1062
- Goncharov A.F., Struzhkin V.V., Jacobsen S.D. (2006) Reduced radiative conductivity of low spin (Mg,Fe)O in the lower mantle. *Science* **312**, 1205–1208

- Goncharov A.F., Haugen B.D., Struzhkin V.V., Beck P., and Jacobsen S.D. (2008) Radiative conductivity in the Earth's lower mantle. *Nature* **456**, 231-234
- Goodman J. and Pindor B. (1999) Secular instability and planetesimal formation in the dust layer. *Icarus* **148**, 537-549
- Greenwood N.N. and Gibb T.C. (1971) Mossbauer Spectroscopy, pp. 314–315, and the references therein, Chapman and Hall, London
- Grossman L. (1972) Condensation in primitive solar nebula. *Geochim. Cosmochim. Acta* **36**, 597-619
- Gulyaev A. (1977) Metallurgy. Metallurgiya, Moscow
- Hammersley A.P. (1997) FIT2D: An Introduction and Overview. *ESRF Internal Report*, **ESRF97HA02T** (unpublished)
- Hammersley A.P. (1998) FIT2D V9.129 Reference Manual V3.1 *ESRF Internal Report* **ESRF98HA01T** (unpublished)
- Hart S.R. and Zindler A. (1986) In search of a bulk Earth composition. *Chem. Geology* **57**, 247-267
- Hatch D.M. and Ghose S. (1989) Symmetry analysis of the phase transition and twinning in MgSiO₃ garnet: Implications to mantle mineralogy. *Am. Mineral.* **74**, 1221-1224
- Hedlin M.A.H., Shearer P.M., and Earle P.S. (1997) Seismic evidence for small-scale heterogeneity throughout the Earth's mantle. *Nature* **387**, 145-150
- Heinz D.L., Sweeney J.S., Miller P. (1991) A laser-heating system that stabilizes and controls the temperature – diamond anvil cell applications. *Rev. Sci. Instrum.* **62**, 1568-1575
- Hofmeister A.M. (2006) Is low-spin Fe²⁺ present in Earth's mantle? *Earth Planet. Sci. Lett.* **243**, 44–52
- Holzheid A., Sylvester P., O'Neill H.St.C., Rubie D.C., and Palme H (2000) Evidence for a late chondritic veneer in the Earth's mantle from high-pressure partitioning of palladium and platinum. *Nature* **406**, 396-399
- Horiuchi H., Ito E., and Weidner D.J. (1987) Perovskite-type MgSiO₃: single-crystal X-ray diffraction study. *Am. Mineral.* **72**, 357-360
- Huang E., Bassett W., and Weathers M.S. (1988) Phase relationships in Fe-Ni alloys at high pressures and temperatures. *J. Geophys. Res.* **93**, 7741-7746
- Huang E., Bassett W., and Weathers M.S. (1992) Phase diagram and elastic properties of Fe 30% Ni alloy by synchrotron radiation. *J. Geophys. Res.* **97**, 4497-4502

- Huang L., Skorodumova N.V., Belonoshko A.B., Johansson B., and Ahuja R. (2005) Carbon in iron phases under high pressure. *Geophys. Res. Lett.* **32**, L21314-5
- Huggins F. (1975) The 3d levels of ferrous iron in silicate garnets. *Am. Mineral.* **60**, 316-319
- Ingalls R. (1964) Electric-field gradient tensor in ferrous compounds. *Phys. Rev.* **133A**, 787-795
- Ino H., Ito T., Nasu S., and Gonser U. (1982) A study of interstitial atom configuration in fresh and aged iron-carbon martensite by Mössbauer spectroscopy. *Acta Metall.* **30**, 9-20
- Irifune T. and Ringwood A.E. (1987) Phase transformations in primitive MORB and pyrolite compositions to 25 GPa and some geophysical implications, pp. 221-230. In *High-pressure research in mineral physics* (eds. Manghnani M. and Syono Y.) Terra/American Geophysical Union, Tokyo/Washington
- Irifune T., Nishiyama N., Kuroda K., Inoue T., Isshiki M., Utsumi W., Funakoshi K.-I., Urakawa S., Uchida T., Katsura T., and Ohtaka O. (1998) The postspinel phase boundary in Mg₂SiO₄ determined by in situ X-ray diffraction. *Science* **279**, 1698–1700
- Itié J. P., Polian A., Calas G., Petiau J., Fontaine A., and Tolentino H. (1989) *Phys. Rev. Lett.* **63**, 398–401
- Ito E., Katsura T., Aizawa Y., Kawabe K., Yokoshi S., Kubo A., Nozawa A., and Funakoshi K. (2005) High-pressure generation in the Kawai-type apparatus equipped with sintered diamonds anvils: application to the wurzite-rocksalt transformation in GaN, pp. 451-460. In *High-Pressure Technology for Geophysical Applications Advance* (eds. Chen J., Wang Y., Duffy T.S., Shen G., Dobzhineskaya L.F.), Elsevier B.V.
- Ito E., Katsura T., Yamazaki D., Yoneda A., Tado M., Ochi T., Nishibara E., and Nakamura A. (2008) A new 6-axis apparatus to squeeze the Kawai-cell of sintered diamond cubes. *Phys. Earth Planet. Interior.* **174**, 264-269
- Jackson J.M., Sturhahn W., Shen G., Zhao J., Hu M.Y., Errandonea D., Bass J.D. and Fei Y. (2005) A synchrotron Mössbauer spectroscopy study of (Mg,Fe)SiO₃ perovskite up to 120 GPa. *Am. Mineral.* **90**, 199-205
- Jagoutz E, Palme H, Baddenhausen H, Blum K, Cendales M, Dreibus G, Spettel B, Lorenz V, Wänke H (1979) The abundance of major, minor and trace elements in the earth's mantle is derived from primitive ultramafic modules. pp. 2031-2050. In: *Proceedings of the 10-th Lunar and Planetary Science Conference*. Elmsford, NY, Pergamon Press
- Jepchoat A. and Olson P. (1987) Is the inner core of the Earth pure iron? *Nature* **325**, 332-335

- Jepchoat A.P., Hriljac J.A., McCammon C.A., O'Neill H.St.S., Rubie D.C. and Finger L.W. (1999) High-resolution X-ray powder diffraction and Rietveld refinement of two (Mg_{0.95}Fe_{0.05})SiO₃ perovskite samples synthesized under different oxygen fugacity conditions. *Am. Mineral.* **8**, 214-220
- Kaneshima S. and Helffrich G. (1999) Dipping low-velocity layer in the mid-lower mantle: Evidence for geochemical heterogeneity. *Science* **283**, 1888-1891
- Kantor I.Yu., McCammon C.A., and Dubrovinsky L.S. (2004) Mössbauer spectroscopic study of pressure-induced magnetisation in wüstite (FeO). *J. of Alloys and Compounds* **376**, 5-8
- Kantor I., Dubrovinsky L.S., and McCammon C.A. (2006a) Spin crossover in (Mg,Fe)O: A Mössbauer effect study with an alternative interpretation of x-ray emission spectroscopy data. *Phys. Rev. B* **73**, 100101-4
- Karato S.I. (1999) Seismic anisotropy of the Earth's inner core resulting from flow induced by Maxwell stresses. *Nature* **402**, 871-873
- Kato T. (1986) Stability relation of (Mg,Fe)SiO₃ garnets, major constituents in the Earth's interior. *Earth Planet. Sci. Lett.* **77**, 399-408
- Katsura T., Yamada H., Shinmei T., Kubo A., Ono S., Kanzaki M., Yoneda A., Walter M.J., Ito E., Urakawa S., Funakoshi K., and Utsumi W. (2003) Post-spinel transition in Mg₂SiO₄ determined by high P-T in situ X-ray diffractometry. *Phys. Earth Planet. Inter.* **136**, 11–24
- Kawai N., Endo S. (1970) The generation of ultrahigh hydrostatic pressures by split sphere apparatus. *Rev. Sci. Instrum.* **41**, 1178-1181
- Keppler H., McCammon C.A., and Rubie D.C. (1994) Crystal-field and charge-transfer spectra of (Mg,Fe)SiO₃ perovskite. *Am. Mineral.* **79**, 1215-1218
- Keppler H., Kantor I., and Dubrovinsky L.S. (2007) Optical absorption spectra of ferropericlasite to 84 GPa. *Am. Mineral.* **92**, 433-436
- Keppler H., Dubrovinsky L.S., Narygina O.V., Kantor I. (2009) Optical absorption and radiative thermal conductivity of silicate perovskite to 125 Gigapascals. *Science* **322**, 1529-1532
- Kimura K., Lewis R.S., and Anders E. (1974) Distribution of gold and rhenium between nickel-iron and silicate melts: implications for the abundances of siderophile elements on the Earth and Moon. *Geochim. Cosmochim. Acta* **38**, 683–701
- Klementev K.V. (2001) Extraction of the fine structure from x-ray absorption spectra, *J Phys D Appl. Phys.* **34**, 209-217

- Knittel E. and Williams Q. (1995) Static compression of ϵ -FeSi and evolution of reduced silicon as a deep Earth constituent. *Geophys. Res. Lett.* **22**, 445-448
- Kobayashi Y., Kondo T., Othani E., Hirao N., Miyajima N., Yagi T., Nagase H., Kikegawa T. (2005) Fe–Mg partitioning between (Mg,Fe)SiO₃ postperovskite, perovskite, and magnesiowüstite in the Earth's lower mantle. *Geophys. Res. Lett.* **32**, L19301.1-4
- Komabayashi T., Hirose K., Sugimura E., Sata N., Ohishi Y., and Dubrovinsky L.S. (2008) Simultaneous volume measurements of post-perovskite and perovskite MgSiO₃ and their thermal equations of state, *Earth Planet. Sci. Lett.* **265**, 515-52
- Krot A.N., Keil K., Goodrich C.A., Scott E.R.D., and Weisberg M.K. (2003) Classification of meteorites, pp. 83-128. In *Meteorites, Comets and Planets* (ed. A.M. Davis) Vol. 1 *Treatise on Geochemistry* (eds. Holland H.D. and Turekian K.K.), Elsevier-Pergamon, Oxford
- Kubo A. and Akaogi M. (2000) Post-garnet transitions in the system Mg₄Si₄O₁₂–Mg₃Al₂Si₃O₁₂ up to 28 GPa: phase relations of garnet, ilmenite, and perovskite. *Phys. Earth Planet. Interior.* **125**, 105–112
- Kudoh Y., Ito E., and Takeda H. (1987) Effect of pressure on the crystal structure of perovskite-type MgSiO₃. *Phys. Chem. Miner.* **14**(4), 350-353
- Kurdjumov G. and Kaminsky E. (1928) X-ray studies of the structure of quenched carbon steel *Nature* **122**, 475-476
- Kurdjumov G. and Kaminsky E. (1929) Eine röntgenographische Untersuchung der Struktur des gehärteten Kohlenstoffstahls. *Z. Phys.* **53**, 696-707
- Labiche J.-C., Mathon O., Pascarelli S., Newton M.A., Guilera Ferré G., Curfs C., Vaughan G., and Homs A. (2007) The fast readout low noise camera as a versatile x-ray detector for time resolved dispersive extended x-ray absorption fine structure and diffraction studies of dynamic problems in materials science, chemistry, and catalysis. *Rev. Sci. Instrum.* **78**, 91301–91312
- Lagarec K., Rancourt D.C. (1998) Recoil, Mössbauer spectral analysis software for Windows, version 1.0
- Laio A., Bernard S., Chiarotti G.L., Scandolo S., and Tosatti E. (2000) Physics of iron at Earth's core conditions. *Science* **287**, 1027–1030
- Larimer J.W. (1967) Chemical fractionation in meteorites - I. Condensation of elements, *Geochim. Cosmochim. Acta* **31**, 1215-1238

- Larson A.C. and Von Dreele R.B. (2004) General Structure Analysis System (GSAS). *Los Alamos National Laboratory Report LAUR 86, 748*
- Lauterbach S., McCammon C.A., van Aken P, Langenhorst F., and Seifert F. (2000) Mössbauer and ELNES spectroscopy of (Mg,Fe)(Si,Al)O₃ perovskite: a highly oxidised component of the lower mantle. *Contrib. Mineral. Petrol.* **138**, 17-26
- Leng W. and Zhong S. (2008) Controls on plume heat flux and plume excess temperature. *Geophys. Res. Lett.* **113**, B04408
- Li J., Struzhkin V.V., Mao H.-K., Shu J., Hemley R.J., Fei Y., Mysen B., Dear P., Prakapenka V.B., and Shen G. (2004) Electronic spin state of iron in lower mantle perovskite. *Proced. Nat. Acad. Sci.* **101**, 14027-14030.
- Li J., Sturhahn W., Jackson J.M. Struzhkin V.V., Lin J.-F., Zhao J., Mao H.-K. and Shen G. (2006) Pressure effect on the electronic structure of iron in (Mg,Fe)(Si,Al)O₃ perovskite: a combined synchrotron Mössbauer and X-ray emission spectroscopy study up to 100 GPa. *Phys. Chem. Minerals.* **33**, 575-585
- Liebske C., Schmickler B., Terasaki H., Poe B.T., Suzuki A., Funakoshi K., Ando R., and Rubie D.C. (2005) Viscosity of peridotite liquid up to 13 GPa: Implications for magma ocean viscosities. *Earth Planet. Sci. Lett.*, **240**, 589-604
- Lin J.-F., Heinz D.L., Campbell A.J., Devine J.M., Mao W.L., and Shen G (2002a) Iron-Nickel alloy in the Earth's core. *Geophys. Res. Lett.* **29(10)**, 109-111
- Lin J.-F., Heinz D.L., Campbell A.J., Devine J.M., Mao W.L., and Shen G (2002b) Iron-silicon alloy alloy in Earth's core? *Science* **295**, 313-315
- Lin J.-F., Struzhkin V.V., Sturhahn W, Huang E., Zhao J, Hu M.Y., Alp E.E., Mao H.-K., Boctor N., and HemleyR.H. (2003) Sound velocities of iron–nickel and iron–silicon alloys at high pressures. *Geophys. Res. Lett.* **30(21)**, 2112-2115
- Lin J.-F., Struzhkin V.V., Jacobsen S.D., Hu M.Y., Chow P., Kung J., Liu H., Mao H.K., and Hemley R.J. (2005) Spin transition of iron in magnesiowüstite in the Earth's lower mantle. *Nature* **436**, 377-380
- Lin J.-F., Gavriluk A.G., Struzhkin V.V., Jacobsen S.D., Sturhahn W, Hu M.Y., Chow P., and Yoo C.S. (2006) Pressure-induced electronic spin transition of iron in magnesiowüstite-(Mg,Fe)O. *Phys. Rev. B* **73**, 113107-4
- Lin J. F., Jacobsen S. D., and Wentzcovitch R. M. (2007a) Electronic spin transition of iron in the Earth's deep mantle. *Eos* **88**, 13–17

- Lin J.-F., Vankó G., Jacobsen S.D., Iota V., Struzhkin V.V., Prakapenka V.B., Kuznetsov A., and Yoo C.S. (2007b) Spin transition zone in Earth's lower mantle. *Science* **317**, 1740-1743
- Lin J.-F. and Tsuchiya T. (2008) Spin transition of iron in the Earth's lower mantle. *Phys. Earth Planet. Int.* **170**, 248-259
- Lin J.-F., Watson H., Vankó G., Alp E.E., Prakapenka V.B., Dera P., Struzhkin V.V., Kubo A., Zhao J., McCammon C.A., and Evans W.J. (2008) Intermediate-spin ferrous iron in lowermost mantle post-perovskite and perovskite. *Nature Geosci.* **1**, 688-691
- Liu J., Dubrovinsky L., Boffa Ballaran T., and Crichton W. (2007) Equation of state and thermal expansivity of LiF and NaF. *High Press. Res.* **27**, 483 - 489
- Lord O.T., Walter M.J., Dasgupta R., Walker D., and Clark S.M. (2009) Melting in the Fe-C system to 70 GPa. *Earth Planet. Sci. Lett.* **284**, 157-167
- Ma Y., Mao H.-K., Hemley R.J., Gramsch S.A., Schen G., and Spmayazulu M. (2001) Two-dimensional energy dispersive X-ray diffraction at high pressures and temperatures. *Rev. Sci. Instr.* **72**, 1302-1305
- Manghnani M. and Syono Y. (1987) High pressure research in Mineral Physics. Terra Scientific Publishing Company, Tokyo
- Mao H.-K., Xu J., and Bell P.M. (1986) Calibration of the ruby pressure gage to 800 kbar under quasi-hydrostatic conditions. *J. Geophys. Res.* **91**, 4673-6
- Mao H.-K., Bell P.M., and Hadidiacos C. (1987) Experimental phase relations of iron to 360 kbar, 1,400°C, determined in and internally heated diamond-anvil apparatus, pp. 135-138. In *High pressure Research in Mineral Physics* (eds. Manghnani M.H. and Syono Y.) Terra Scientific Publishing Company, Tokyo
- Mao H.-K., Wu Y., Chen L.C., Shu J.F., and Jephcoat A.P. (1990) Static compression of iron to 300 GPa and Fe_{0.8}Ni_{0.2} alloy to 260 GPa: implications for composition of the core. *J. Geophys. Res.* **95**, 21737-21742
- Mao H.-K., Shen G., Hemley R (1997) Multivariable dependence of Fe-Mg partitioning in the lower mantle *Science* **278**, 2098-2100
- Mao W., Campbell A.J., Heinz D.L., and Shen G. (2006) Phase relations of Fe-Ni alloys at high pressure and temperature. *Phys. Earth Planet. Int.* **155**, 146-151
- Martens A. (1878a) Ueber die mikroskopische Untersuchung des Eisens. *Z. Vereines Deutscher Ingenieure* **22**, 11-18

- Martens A. (1878b) Zur Mikrostruktur des Spiegeleisens – Die Erscheinungen auf den Bruchflächen. *Z. Vereines Deutscher Ingenieure* **22**, 205-214
- Martens A. (1878c) Zur Mikrostruktur des Spiegeleisens – Die Erscheinungen auf den Schliiffflächen. *Z. Vereines Deutscher Ingenieure* **22**, 481-488
- Martens A. (1880) Ueber das mikroskopische Gefüge und die Krystallisation des Roheisens, speciell des grauen Eisens. *Z. Vereines Deutscher Ingenieure* **24**, 397-406
- Matas J., Bass J., Ricard Y., Mattern E., and Bukowinski M.S.T. (2007) On the bulk composition of the lower mantle: Predictions and limitations from generalized inversion of radial seismic profiles. *Geophys. J. Int.* **170**, 764–780
- Mattern E., Matas J., Ricard Y., and Bass J. (2005) Lower mantle composition and temperature from mineral physics and thermodynamic modelling. *Geophys. J. Int.* **160**, 973–990
- Mazur J. (1950) Lattice Parameters of Martensite and of Austenite. *Nature* **166**, 828
- McCammon C.A. and Liu L.-g. (1984) The effects of pressure and temperature on nonstoichiometric wüstite, Fe_xO : The iron-rich phase boundary *Phys. Chem. Minerals* **10**, 106-113
- McCammon C.A., Rubie D.C., Ross II C.R., Seifert F. and O'Neill H.St.C. (1992) Mössbauer spectra of $^{57}\text{Fe}_{0.05}\text{Mg}_{0.95}\text{SiO}_3$ perovskite at 80 and 298 K. *Am. Mineral.* **77**, 894-897
- McCammon C.A. (1997) Perovskite as a possible sink for ferric iron in the lower mantle. *Nature* **387**, 694-696
- McCammon C.A. (1998) The crystal chemistry of ferric iron in $\text{Fe}_{0.05}\text{Mg}_{0.95}\text{SiO}_3$ perovskite as determined by Mössbauer spectroscopy in the temperature range 80-293 K. *Phys. Chem. Minerals* **25**, 292–300
- McCammon C.A. and Ross N.L. (2003) Crystal chemistry of ferric iron in $(\text{Mg,Fe})(\text{Si,Al})\text{O}_3$ majorite with implications for the transition zone. *Phys. Chem. Min.* **30**, 206-216
- McCammon C.A., Lauterbach S., Seifert F., Langenhorst F., and van Aken P.A. (2004) Iron oxidation state in lower mantle mineral assemblages I. Empirical relations derived from high-pressure experiments. *Earth Planet. Sci. Lett.* **222**, 435-449
- McCammon C.A. (2005a) The paradox of mantle redox. *Science* **308**, 807-808
- McCammon C.A. (2005b) Mantle oxidation state and oxygen fugacity: Constraints on mantle chemistry, structure and dynamics, pp. 221-242. In *Earth's Deep Mantle: Structure, Composition, and Evolution* (eds. Hilst R.D., Bass J., Matas J., and Trampert J.), American Geophysical Union, Washington D.C.

- McCammon C.A., Kantor I.Yu., Narygina O., Rouquette J., Ponkratz U., Sergueev I., Mezouar M., Prakapenka V., Dubrovinsky L.S. (2008) Stable intermediate-spin ferrous iron in lower-mantle perovskite. *Nature Geoscience* **1**, 684-687
- McDonough W.F. and Sun S.-S. (1995) The composition of the Earth. *Chemical geology* **120**, 223-253
- Mierdel K. (2006) Wasserlöslichkeit in Enstatit. Ph.D. thesis, University of Tübingen
- Mikhaylushkin A.S., Simak S.I., Dubrovinsky L., Dubrovinskaia N., Johansson B., and Abrikosov I.A. (2007) Pure iron compressed and heated to extreme conditions. *Phys. Rev. Lett.* **99** 165505.1-4
- Mirwald P.W. and Kennedy G.C. (1979) The Curie point and the α - γ transition of iron to 53 kbar – a reexamination. *J. Geophys. Res.* **84**, 656-658
- Mitchell M.H. (2000) Perovskites. Almaz Press Inc., Thunder Bay, Canada
- Morito S., Huang X., Furuhashi T., Maki T., and Hansen N. (2006) The morphology and crystallography of lath martensite in alloy steels. *Acta Mater.* **54(19)**, 5323-5331
- Mössbauer R.L. (1958) Kernresonanzfluoreszenz von gammastranzfluoreszenz in IR-191. *Z. Phys.* **151**, 124
- Mössbauer R.L. and Wiedemann W.H. (1960) Kernresonanzabsorption nicht Doppler-verbeiteter Gammastrahlung in Re^{187} . *Z Phys.* **159**, 33-48
- Muñoz M., Andrade V.D., Vidal O., Lewin E., Pascarelli S., and Susini J. (2006) Redox and speciation micro-mapping using dispersive X-ray absorption spectroscopy: application to iron in chlorite mineral of a metamorphic rock thin section. *Geochem. Geophys. Geosyst.* **7**, Q11020
- Muñoz M., Pascarelli S., Aquilanti G., Narygina O., Kurnusov A. and Dubrovinsky L. (2008) Hyperspectral -XANES mapping in the diamond-anvil cell: analytical procedure applied to the decomposition of (Mg,Fe)-ringwoodite at the upper/lower mantle boundary. *High Press. Res.* **28**, 665–673
- Murad E. and Wagner F.E. (1987) The mössbauer spectrum of almandine. *Phys Chem Minerals* **14**, 264-269
- Murakami M., Hirose K., Kawamura K., Sata N., and Ohishi Y. (2004) Post-perovskite phase transition in MgSiO_3 . *Science* **304**, 855-858
- Murakami M., Hirose K., Sata N., and Ohishi Y. (2005) Post-perovskite phase transition and mineral chemistry in the pyrolitic lowermost mantle. *Geophys. Res. Lett.* **32**, L033004.1-4

- Müller J.E. and Wilkins J.W. (1984) Band-structure approach to the X-ray spectra of metals. *Phys. Rev. B* **29**, 4331-4348
- Naliboff J.B. and Kellogg L.H. (2007) Can large increases in viscosity and thermal conductivity preserve large-scale heterogeneity in the mantle? *Phys. Earth Planet. Inter.* **161**, 86–102
- Narygina O., Mattesini M., Pascarelli S., Kantor I., Wu X., Aquilanti G., McCammon C., and Dubrovinsky L. (2009) High-pressure experimental and computational XANES studies of the Earth's lower mantle (Mg,Fe)(Si,Al)O₃ perovskite and (Mg,Fe)O ferropericlasite. *Phys. Rev. B* **79(17)**, 174115.1-10
- Nguyen J.H. and Holmes N.C. (2004) Melting of iron at the physical conditions of the Earth's core. *Nature* **427**, 339-342
- O'Neill H.St.C, McCammon C.A., Canil D.C., Rubie D.C., Ross II C.R., and Seifert F. (1993a) Mossbauer spectroscopy of transition zone phases and determination of minimum Fe³⁺ content. *Am. Mineral.* **78**, 456-460
- O'Neill H.St.C, Rubie D.C., Canil D.C., Geiger C.A., Ross II C.R., Seifert F., and Woodland A.B. (1993b) Ferric iron in the upper mantle and in transition zone assemblages: implications for relative oxygen fugacities in the mantle, pp. 73-88. In *Evolution of the earth and planets* (eds. Takahashi T., Jeanloz R., and Rubie D.C.), American Geophysical Union, Washington DC
- O'Neill H.St.C and Palme H. (1998) Composition of the Silicate Earth: Implications for Accretion and Core formation. pp. 3-127. In: *The Earth's mantle* (ed. Jackson I.), Cambridge University Press
- Ohta K., Onoda S., Hirose K., Sinmyo R., Shimizu K., Sata N, Ohishi Y, Yasuhara A. (2008) The electrical conductivity of post-perovskite in Earth's D" layer. *Science* **320**, 89-91
- Omel'chenko A.V., Soshnikov V.I., and Estrin E.I. (1969) Effect of pressure on the Curie point and α - γ transformation of iron. *Fiz. Metal. Metalloved.* **28**, 77-83
- Palme H. and Jones A. (2003) Solar system abundances of the elements, pp. 41-61. In *Meteorites, Comets and Planets* (ed. Davis A.M.) Vol. 1 *Treatise on Geochemistry* (eds. Holland H.D. and Turekian K.K.), Elsevier-Pergamon, Oxford.
- Palme H. and Nickel K.G. (1985) Ca/Al ratio and the composition of the Earth's upper mantle. *Geochem. Cosmochem. Acta* **49**, 2123-2132

- Palme J. and O'Neill H.St.C. (2003) Cosmochemical estimates of mantle composition, pp. 1-38. *In The Mantle and Core* (ed. Carlson R.W.) Vol. 2 Treatise on Geochemistry (eds. Holland H.D. and Turekian K.K.), Elsevier-Pergamon, Oxford
- Pascarelli S., Mathon O., and Aquilanti G. (2004) New opportunities for high-pressure X-ray absorption spectroscopy using dispersive optics. *J. Alloys Comp.* **362**, 33-40
- Pascarelli S., Mathon O., Munoz M., Mairs T., and Susini J. (2006) Energy-dispersive absorption spectroscopy for hard-X-ray micro-XAS applications. *J. Synchrotron. Rad.* **13**, 351-358
- Perdew J.P., Burke K., and Ernzerhof M. (1996) Generalized gradient approximation made simple. *Phys. Rev. Lett.* **77**, 3865-3868
- Poirier J.-P. (1994a) Light elements in the Earth's outer core: a critical review. *Phys. Earth Planet. Inter.* **85**, 319-337
- Prakapenka V.B., Shen G., and Dubrovinsky L. (2003/2004) Carbon transport in diamond anvil cells. *High Temp. High Press.* **35/36**, 237-249
- Rehr J.J. and Albers R.C. (2000) Theoretical approaches to x-ray absorption fine structure. *Rev. Mod. Phys.* **72**, 621-654
- Rekhi S., Dubrovinsky L.S., Saxena S.K. (1999) Temperature-induced ruby fluorescence shifts up to a pressure of 15 GPa in an externally heated diamond anvil cell. *High Temp.-High Press.* **31**, 299-305
- Ringwood A.E. (1975) Composition and petrology of the Earth's mantle. McCraw-Hill, New York
- Ringwood A.E. (1979) Origin of the Earth and Moon. Berlin: Springer-Verlag
- Ringwood A.E. (1989) Constitution and evolution of the mantle. *Spec. Publ. Geol. Soc. Australia* **14**, 457-485
- Ringwood A.E. (1991) Phase transformations and their bearing on the constitution and dynamics of the mantle. *Geochim. Cosmochim. Acta* **55**, 2083-2110
- Roberts C.S. (1953) Effect of carbon on the volume fractions and lattice parameters of retained austenite and martensite. *Trans. Am. Inst. Metall. Eng.* **197**, 203-204
- Rohrbach A., Ballhaus C., Golla-Schindler U., Ulmer P., Kamenetsky V.S., and Kuzmin D.V. (2007) Metal saturation in the upper mantle. *Nature (London)* **449**, 456
- Ross N.L. and Hazen R.M. (1989) Single crystal X-ray diffraction study of MgSiO₃ perovskite from 77 to 400 K. *Phys Chem Minerals* **16**, 415-420

- Ross N.L. and Hazen R.M. (1990) High-pressure crystal chemistry of MgSiO₃ perovskite. *Phys. Chem. Miner.* **17**, 228-237 (1990)
- Rouquette J., Dolejš D., Kantor I., McCammon C.A., Frost D.J., Prakapenka V.B., Dubrovinsky L.S. (2008) Iron-carbon interactions at high temperatures and pressures. *Appl. Phys. Lett.* **92**, 121912.1-3
- Rubie D.C. (1999) Characterising the sample environment in multianvil high-pressure experiments. *Phase Transitions.* **68**, 431-451
- Ruffer, R. & Chumakov, A. I. (1996) Nuclear resonance beamline at ESRF. *Hyperfine Interact.* **97/98**, 589–604
- Safranov V.S. (1969) Evolution of the protoplanetary cloud and formation of the Earth and planets (English translation NASA TTF-667, 1972)
- San-Miguel A., Libotte H., Gauthier M., Aquilanti G., Pascarelli S., and Gaspard J.-P. (2007) New Phase Transition of Solid Bromine under High Pressure. *Phys. Rev. Lett.* **99**, 015501.1-4
- Sanloup C., Guyot F., Gillet P., Fiquet G., Mezouar M., and Martines I. (2000b) Density measurements of liquid Fe-S alloys at high-pressure. *Geophys. Res. Lett.* **27**, 811-814
- Sapelkin A.V., Bayliss S.C., Lyapin A.G., Brazhkin V.V., Itié J.P., Polian A., Clark S.M., and Dent A.J. (1996) Structural studies of bulk amorphous GaSb under high pressures. *Phys. Status Solidi B* **198**, 503–508
- Scott H.P., Williams Q., and Knittle E. (2001) Stability and equation of state of Fe₃C to 73 GPa: Implications for carbon in the Earth's core. *Geophys. Res. Lett.* **28**, 1875-1878
- Shackelford J. (2001) CRC Materials Science and Engineering handbook. CRC Press, Boca Raton, FL
- Shallcross S., Kissavos A.E., Sharma S., and Meded V. (2006) Noncollinear order in the γ -Fe system: Generalized Heisenberg approach. *Phys. Rev. B* **73**, 104443-8
- Shearer P. and Masters G. (1990) The density and shear velocity contrast at the inner core boundary. *Gheopys. J. Int.* **102**, 408-491
- Sherman D.M. (1988) Structural and magnetic phase transitions in minerals, pp. 113-128, In: *Advances in physical geochemistry* (eds. Ghose S, Coey J.M.D. and Salje E.) Springer, New York 7
- Schen G., Mao H.-K., Hemley R.J., Duffy T.S., and Rivers M.L. (1998) Melting and crystal structure of iron at high pressures and temperatures. *Geophys. Res. Lett.* **25**, 373-376

- Sherman D.M. (1988) pp. 113–128. In *Structural and magnetic phase transitions in minerals, advances in physical geochemistry*, Vol. 7, (eds. Ghose S., Coey J.M.D., and Salje E.), Springer, New York
- Shim S.-H., Duffy T.S., and Shen G. (2001) The post-spinel transformation in Mg_2SiO_4 and its relation to the 660-km seismic discontinuity. *Nature* **411**, 571–574
- Shterenberg L.E., Slesarev V.N., Korsunskaya I.A., and Kamenetskaya D.S. (1975) The experimental study of the interaction between the melt carbides and diamond in the iron-carbon system at high pressures. *High Temp.-High-Press.* **7**, 517-522
- Sinmyo R., Hirose K., Nishio-Hamane D., Seto Y., Fujino K., Sata N., and Ohishi Y. (2008) Partitioning of iron between perovskite/post-perovskite and ferropericlase in the lower mantle. *J. Geophys. Res.* **113**, B11204
- Smirnov G. V. (1999) General properties of nuclear resonant scattering. *Hyperfine Interact.* **123/124**, 31–77
- Speziale S., Milner A., Lee V.E., Clark S.M., Pasternak M.P., and Jeanloz R. (2005) Iron spin transition in Earth's mantle. *Proced. Nat. Acad. Sci.* **102**, 17918-17922
- Stackhouse S., Brodholt J.P., and Price G.D. (2007) Electronic spin transitions in iron-bearing $MgSiO_3$ perovskite. *Earth Planet. Sci. Lett.* **253**, 282–290
- Stevens W. and Haynes A.G. (1956) The temperature of forming martensite and bainite in low-alloy steels. *J. Iron Steel Inst.* **183**, 349-359
- Stevenson D.J. (1981) Models of the Earth's core. *Science* **214**, 611-619
- Stixrude L., Cohen R.E., and Singh D.J. (1994) Iron at high pressure: Linearized-augmented-plane-wave computations in the generalized-gradient approximation. *Phys. Rev. B* **50**, 6442-6445
- Stixrude L., Wasserman E. and Cohen R.E. (1997) Composition and temperature of the Earth's inner core. *J. Geophys. Res.* **102**, 24729-24739
- Stixrude L. and Lithgow-Bertelloni C. (2005) Mineralogy and elasticity of the oceanic upper mantle: origin of the low-velocity zone. *J. Geophys. Res.* **110**, B03204
- Stoyanov E. (2006) Valence state, coordination and incorporation of Ti and Cr into lower mantle phases: new insight from electron energy-loss spectroscopy. Ph.D. thesis, University of Jena
- Strong H.M. (1959) Fusion curve of iron to 96,000 atmospheres. *J. Geophys. Res.* **64**, 653-659

- Strong H.M. Tuft R.E., and Hanneman R.E. (1973) The iron fusion curve and γ - δ - λ triple point. *Rep. 73CRD017*, Gen. Elec. Corp., Schenectady, New York
- Sturhahn W., Jackson J.M., and Lin J. (2005) The spin state of iron in minerals of the Earth's lower mantle. *Geophys. Res. Lett.* **32**, L12307
- Tonks W.B. and Melosh H.J. (1992) Core formation by giant impacts. *Icarus* **100**, 326-346
- Troiano A and Greninger A. (1946) The martensite transformation. *Metal Progress* **50**, 303-307
- Van der Hilst R. and Karason S. (1999) Compositional heterogeneity in the bottom 1000 kilometers of Earth's mantle: Toward a hybrid convection model. *Science* **283**, 1885-1888
- Vidal O., De Andrade V., Lewin E., Muñoz M., Parra T., and Pascarelli S. (2006) P-T-deformation-Fe³⁺/Fe²⁺ mapping at the thin section scale and comparison with XANES mapping: application to a garnet-bearing metapelite from the Sambagawa metamorphic belt. *J. Metamorph. Geol.* **24**, 669-683
- Vocadlo L., Alfè D., Brodholt J., Gillan M. J., and Price G. D. (2000) Ab-initio free energy calculations on the polymorphs of iron at core conditions. *Phys. Earth Planet. Int.* **117**, 123-137
- Vocadlo L., Dario A., Gillan M.J., Wood I.G., Brodholt J.P., and David P.G. (2003) Possible thermal and chemical stabilization of body-centred-cubic iron in the Earth's inner core. *Nature* **424**, 536-539
- Vocadlo L. (2007) Ab initio calculations of the elasticity of iron and iron alloys at inner core conditions: Evidence for a partially molten inner core? *Earth and Planet. Sci Lett.* **254**, 227-232
- Wänke H., Dreibus G., and Jagoutz E. (1984) Mantle chemistry and accretion history of the Earth. pp. 1-24. In: *Archean Geochemistry* (ed. Kröner A.), Berlin, Springer-Verlag
- Wetherill G.W. and Stewart G.R. (1993) Formation of planetary embryos: effects on fragmentation, low relative velocity, and independent variation of eccentricity and inclination. *Icarus* **106**, 190-209
- Williams Q., Jeanloz R., Bass J., Svendsen B., and Ahrens T.J. (1987) The melting curve of iron to 250 gigapascals: A constraint on the temperature at the Earth's center. *Science* **236**, 181-182
- Wood B. (1993) Carbon in the core. *Earth Planet. Sci. Lett.* **117**, 593-607
- Wood B.J., Walker M.J., and Wade J. (2006) Accretion of the earth and segregation of its core. *Nature (London)* **441**, 825-833

- Wu X., Steinle-Neumann G., Narygina O., Kantor I.Yu., McCammon C.A., Pascarelli S., Aquilanti G., Prakapenka V., and Dubrovinsky L.S. (2009) Iron oxidation state of FeTiO_3 under high pressure. *Phys. Rev. B* **79**, 094106.1-7
- Xiao L., Fan Z., and Jinxiu Z. (1995b) Lattice-parameter variation with carbon content of martensite. I. X-ray-diffraction experimental study. *Phys. Rev. B* **52**, 9970-9978
- Yoshida S.I, Sumita I, and Kumazawa M (1996) Growth model of the inner core coupled with the outer core dynamics and the resulting elastic anisotropy. *J. Geophys. Res.* **101**, 28085-28103
- Yoo C.S., Holmes N.C., Ross M., Webb D.J., and Pike C. (1993) Shock temperatures and melting of iron at Earth core conditions. *Phys. Rev. Lett.* **70**, 3931-3934
- Zhang F. and Oganov A.R. (2006) Valence state and spin transitions of iron in Earth's mantle silicates. *Earth Planet. Sci. Lett.* **249**, 436–443

Erklärung

Hiermit erkläre ich, dass ich die vorliegende Arbeit selbständig verfasst und keine anderen als die von mir angegebenen Quellen und Hilfsmittel benutzt habe.

Ferner erkläre ich, dass ich nicht anderweitig versucht habe, mit oder ohne Erfolg, eine Dissertation einzureichen und auch keine gleichartige Doktorprüfung an einer anderen Hochschule endgültig nicht bestanden habe.

Bayreuth, im Oktober 2009

Olga Narygina